ABSTRACT

Title of thesis: AERODYNAMIC DESIGN OPTIMIZATION OF PROPROTORS FOR CONVERTIBLE-ROTOR CONCEPTS

Conor William Stahlhut, Master of Science, 2012

Thesis directed by: Professor J. Gordon Leishman
Department of Aerospace Engineering

Trades in the aerodynamic design of proprotors that could be used to power convertible-rotor aircraft have been examined. The key design challenge is to maximize overall aerodynamic efficiency of the proprotor in both hover and forward flight, while preserving adequate stall margins for maneuvering flight and compressibility margins for high speed flight. To better assess proprotor performance, a new formulation of the blade element momentum theory for high-speed propellers and proprotors was developed. This approach uses an efficient and robust numerical method to solve simultaneously for the axial and swirl induced velocity components in the wake of the proprotor. The efficacy of the approach was validated against measurements of the performance of two NACA high-speed propellers at advance ratios up to 2.5 and tip Mach numbers up to supersonic conditions. The importance of calculating accurately the swirl component of the induced velocity is emphasized. Parametric studies and design optimization studies were performed for different convertible-rotor aircraft platforms with the goal of developing a better understanding of the tradeoffs that would be needed for the development of advanced

proprotors to power such convertible-rotor aircraft. The effects that solidity, diameter, rotational speed, blade twist and taper, number of blades, tip sweep, and airfoil characteristics have on proprotor performance were all explored. Particular importance was given to proprotors that may have variable tip speed, and assessing the relative advantages of variable diameter versus variable rotational shaft speed concepts. Proprotors with variable blade twist were also considered. It was found that significant improvements in proprotor performance may only be practically realized by varying one or more of diameter, shaft speed, or blade twist during flight.

AERODYNAMIC DESIGN OPTIMIZATION OF PROPROTORS FOR CONVERTIBLE-ROTOR CONCEPTS

by

Conor William Stahlhut

Thesis submitted to the Faculty of the Graduate School of the
University of Maryland, College Park in partial fulfillment
of the requirements for the degree of
Master of Science
2012

Advisory Committee:
Professor J. Gordon Leishman, Chair/Advisor
Associate Professor James Baeder
Associate Professor Kenneth Yu

Acknowledgments

First and foremost, I would like to thank my advisor, Professor J. Gordon Leishman, for his continued motivation and guidance during my time here at the University of Maryland. His extensive knowledge and experience in rotorcraft aerodynamics have greatly helped me to grow my understanding of the field. I would also like to acknowledge my committee members, Dr. James Baeder and Dr. Kenneth Yu, for their support and encouragement.

I would also like to thank the Office of Naval Research (ONR), who partly supported this work. Judah Milgram was the technical monitor.

In particular, I would like to thank my colleagues Bharath Govindarajan and Dr. Monica Syal for their valuable assistance with the programming aspects of my research. Becoming acquainted with the more intricate aspects of Fortran would have been a much more brutal experience without their help.

I would also like to thank the rest of my friends and colleagues in the Department of Aerospace Engineering for helping to make my time here at Maryland an enjoyable experience, namely, Jillian Alfred, Erica Hocking, Jeremy Knittel, Joseph Schmaus, William Staruk, and Kate Strickland.

Lastly, I would like to express my deepest gratitude for my mother, father, and sister, for always being there to cheer me on in all of my endeavors, and for filling my head with the idea that I was capable of anything. I would not be where I am today if not for them.

Table of Contents

List of Tables

List of Figures

Nomenclature

a	Speed of sound
A	Rotor disk area
AR	Wing aspect ratio
c	Blade chord
C_d	Sectional drag coefficient
C_{D_0}	Average zero-lift drag coefficient of wing
C_l	Sectional lift coefficient
C_{l_α}	Sectional lift curve slope
C_P	Rotor power coefficient, = $P/\rho A\Omega^3 R^3$
C_T	Rotor thrust coefficient, = $T/\rho A\Omega^2 R^2$
D	Drag
e	Oswald's spanwise efficiency factor
f_e	Effective parasitic drag area
F	Prandtl's tip-loss factor
FM	Figure of merit
h	Altitude
L	Sectional lift
$\dot{m}$	Mass flow rate (through rotor annulus)
M	Mach number
M_{dd}	Drag divergence Mach number
N_b	Number of blades

r	Nondimensional radial position, = y/R
R	Rotor radius
$\mathcal{R}$	Flight range
p	Pressure
P	Rotor power
q_∞	Free-stream dynamic pressure
s_p	Distance between vortex sheets in rotor wake
S	Wing area
T	Rotor thrust
u_i	Induced swirl velocity at rotor disk
u_w	Induced swirl velocity in rotor wake
U	Sectional resultant velocity
U_P	Sectional out-of-plane velocity, = $V_\infty + w_i$
U_T	Sectional in-plane velocity, = $\Omega y - u_i$
V_∞	Free-stream velocity or true airspeed
V_i	Resultant induced velocity at rotor disk
V_w	Resultant induced velocity in rotor wake
w_i	Induced axial velocity at rotor disk
w_w	Induced axial velocity in rotor wake
W	Vehicle weight
y	Distance along blade from rotational axis

Greek Symbols

α	Angle of attack
β	Blade pitch angle
γ	$\tan^{-1}(C_d/C_l)$
Γ	Circulation
η_p	Propulsive efficiency
λ	Out-of-plane velocity (inflow) ratio, $= U_P/\Omega R$
λ_i	Out-of-plane induced velocity (induced inflow) ratio, $= w_i/\Omega R$
Λ	Tip sweep angle
μ	Advance ratio, $= V_\infty/\Omega R$
ξ	In-plane velocity ratio, $= U_T/\Omega R$
ξ_i	In-plane induced velocity (swirl) ratio, $= u_i/\Omega R$
ρ	Air density
σ	Solidity, $= N_b c/\pi R$
ϕ	Inflow angle
ϕ_∞	Free-stream inflow angle, $= \tan^{-1}(V_\infty/\Omega y)$
Ω	Rotational speed

Abbreviations

BEMT	Blade element momentum theory
BET	Blade element theory
CR	Convertible rotor
ISA	International Standard Atmosphere
SFC	Specific fuel consumption
SMA	Shape memory alloy
VDPR	Variable diameter proprotor
VDTR	Variable diameter tiltrotor
VSDPR	Variable speed and diameter proprotor
VSPR	Variable speed proprotor
VSTR	Variable speed tiltrotor

Chapter 1

Introduction

1.1 Background

Increasingly demanding military and civil vertical-lift aircraft requirements often lead to the consideration of vehicles that can combine the merits of a helicopter with those of an airplane. Convertible-rotor (CR) aircraft have been developed as one way of fulfilling this need [1–6]. CR aircraft rely on one or two pairs of rotor-propeller concepts, called proprotors, to sustain flight. When tilted level, the proprotors provide lift to overcome aircraft weight and allow for hovering flight. When tilted forward, the proprotors provide propulsion with the lift being carried on a fixed-wing. In principle, CR aircraft can take off vertically and hover like a helicopter, convert to airplane mode by progressively tilting their rotors, and then fly at forward airspeeds approaching those of some turboprop airplanes. The cyclic blade pitch controls needed for control of the rotor in hover are typically locked out in airplane mode, and the proprotors function more as conventional propellers with collective pitch control only.

The hybrid nature of the design of CR aircraft can give them several advantages over conventional helicopters. By tilting their proprotors forward, CR aircraft avoid most of the aerodynamic problems that are inherent to edgewise rotors, such as retreating blade stall and reverse flow, so they can usually achieve higher maximum airspeeds and flight ranges than helicopters. Their increased range is especially useful in a military environment,

allowing them to operate out of safer locations that are further away from their targets. CR aircraft, with their faster maximum speeds, are able to perform rescue missions in considerably less time than traditional helicopters, easily meeting the requirements of the "Golden Hour." CR aircraft also generate less noise in forward flight than comparably sized helicopters, helping them to avoid detection, as well as reducing annoyance levels near populated areas.

Although no certified civil CR aircraft are in production at this time (although the AgustaWestland AW-609 tiltrotor is slated for civil certification by 2016), they continue to be considered for their potential ability to meet certain regional transportation requirements [7, 8]. Because CR aircraft do not require a runway for takeoff or landing, they would be able to operate closer to city centers, which would also serve to help reduce congestion at larger hub airports. However, even if such CR aircraft are technically realizable, it is the economics of operation and passenger acceptance that will be the ultimate tests for any civil CR aircraft.

Historically, numerous challenges have been encountered during the design of CR aircraft. They have become rather compromised aircraft with several significant design trades being needed that often adversely impact their desired fight capabilities, e.g., see Refs. 8–12. While CR aircraft may not necessarily ever attain the high levels of hovering efficiency of conventional helicopters or reach the same airspeed, payload, and range capabilities of many airplanes, they offer the ability to vertically lift payload to greater distances and at higher cruise speeds than is possible with helicopters. With the growing importance of tiltrotors in both the military and civil sectors, an increased emphasis has been placed on research into improving their performance, efficiency, and overall flight

Figure 1.1: The Bell Boeing V-22 Osprey tiltrotor with its rotors tilted partially forward. Source: `http://www.navy.mil/view_photos_top.asp`

capabilities.

1.2 Types of CR Aircraft

The two primary CR configurations are the tiltrotor and tiltwing; see Figs. 1.1 and 1.2 for examples of these aircraft. With a tiltrotor, the proprotors are tilted relative to the wing to convert between hover and cruise modes of operation. On a tiltwing, both the wings and the rotors are tilted together in unison. From an aerodynamic perspective, tiltrotors generally have a lower hovering efficiency because of the aerodynamic download and other flow interactions on the airframe that are produced by the wakes from the proprotors. Tiltwing aircraft experience lower download penalties and interactional ef-

Figure 1.2: The Ling-Temco-Vought XC-142 tiltwing in hover. Source: `http://lisar.larc.nasa.gov/`

fects, but they can show adverse susceptibility to crosswinds and ground effect conditions when in helicopter or transition flight modes. During conversion from helicopter to airplane mode operation, tiltwings tend to have narrower conversion corridors to avoid wing stall and aeroelastic instabilities such as pylon whirl flutter [13]. Tiltwings also have a structural advantage over tiltrotors because they can be designed with thinner and more aerodynamically efficient wings for cruising flight; they can use relatively thin wings because the wing is oriented vertically in hover and, therefore, has higher bending stiffness to carry the weight of the aircraft [1]. In practice, however, the tiltrotor configuration has been a preferred design option, with the military V-22 Osprey and the civil AW-609 (see Fig. 1.3) being two CR aircraft that are currently flying.

In addition to tiltrotor and tiltwing aircraft, other CR aircraft configurations have been considered, either as design concepts or being built as demonstrators or experimen-

Figure 1.3: The AgustaWestland AW-609 tiltrotor in transitional flight mode. Source: http://www.agustawestland.com/product/aw609

tal aircraft. One such configuration is the tailsitter [14], so named because it lands and takes off with its tail on the ground and its nose pointed upward, as shown in Fig. 1.4. Rather than tilting only its rotors and/or its wings, the entire vehicle is tilted to transition between hover and forward flight modes of operation. The major disadvantage of this configuration is that the backward orientation of the pilot to the ground makes it difficult to land. Another configuration, the monotiltrotor [15], uses a pair of coaxially arranged proprotors. The monotiltrotor (see Fig. 1.5) has a smaller footprint than a tiltrotor and, hypothetically at least, can realize relatively large payload fractions. However, the drag and dynamics of the externally suspended load limits the airspeed and maneuver capability of the monotiltrotor.

1.3 Proprotor Efficiency

Proprotors are required to have high levels of aerodynamic performance over much broader ranges of flight conditions than would be encountered with either a helicopter rotor or with a propeller. Consequently, their net performance can become compromised between their two primary modes of operation [16–20]. For example, a proprotor operating in hover is generally less efficient than a helicopter rotor (i.e., it has a lower power loading and a lower figure of merit), and a proprotor operating in forward flight is typically less efficient than a propeller (i.e., it has lower propulsive efficiency). In hover, the proprotors provide thrust to overcome the weight of the vehicle (plus any airframe download), and generous blade areas and higher tip speeds are needed in this case. In cruise mode, the thrust must only overcome the drag of the aircraft; good propulsive efficiency

Figure 1.4: The Lockheed XFV-1 tailsitter.

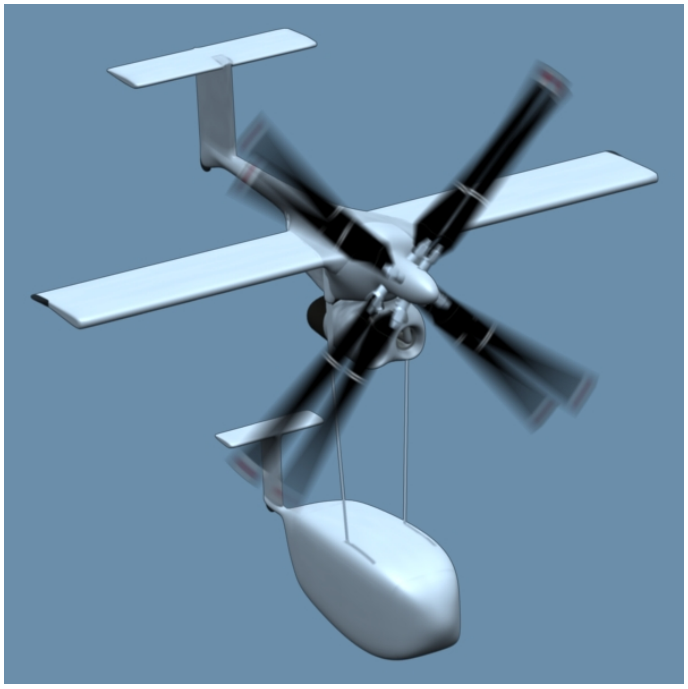

Figure 1.5: The monotiltrotor concept in airplane mode. Source: http://en.wikipedia.org/wiki/Baldwin_Mono_Tiltrotor

in this case requires low profile losses and the minimization of adverse compressibility effects, which demands the use of less blade area and lower tip speeds on the proprotor. Blade twist is also a trade between the two primary modes of flight operation, with significantly less blade twist being needed in hover to avoid inboard blade stall; generous stall margins are always needed with proprotors so that they can provide the aircraft with sufficient control capability and maneuverability at low airspeeds.

In light of the foregoing, it is not unexpected that a proprotor designed for high cruise speeds, which unlike a propeller must have very good static thrust (i.e., hover) efficiency, will be more difficult to design to avoid significantly compromised levels of performance. It has been suggested that the economic productivity of a civil tiltrotor can be better maximized at cruise speeds of between 360 to 380 kts [21], which is near the

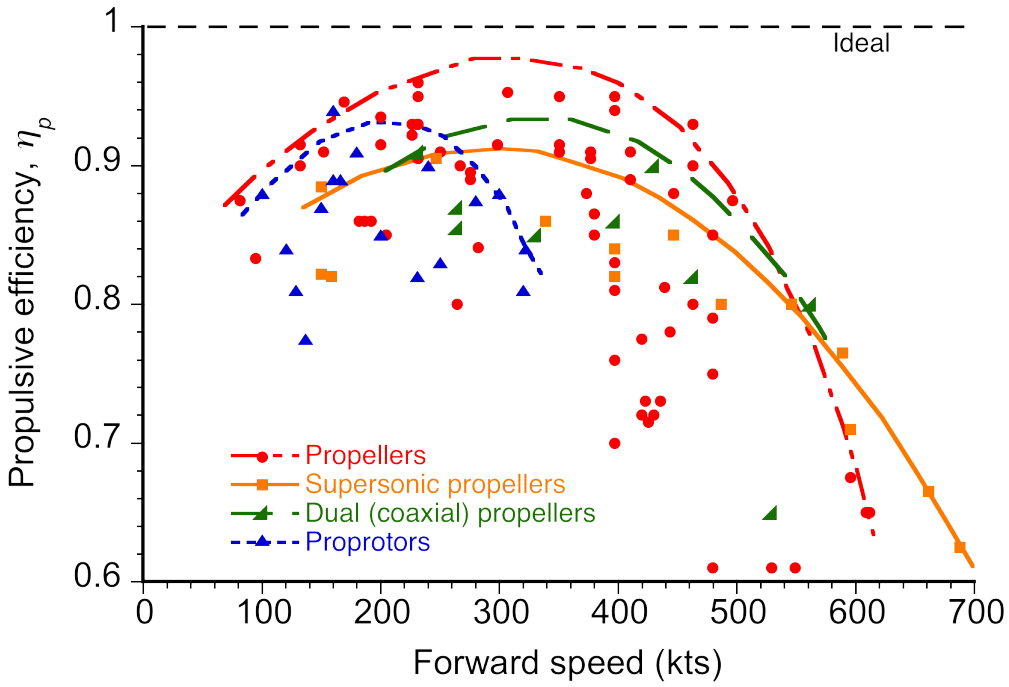

Figure 1.6: Measurements of the propulsive efficiencies of propellers and proprotors. Lines represent the estimated envelope of maximum efficiency for each concept. (Results are from various published sources including the NACA, NASA and the RAE, e.g., Refs. 22–25.)

speeds of contemporary turboprop airplanes. However, the compendium of results shown in Fig. 1.6 suggests that substantial improvements need to be realized if new generations of proprotors are ever to approach the propulsive efficiencies of the best propellers, especially at cruise speeds in excess of 350 kts. In particular, increasing the efficiency of CR aircraft at airspeeds close to where contemporary turboprop aircraft currently fly will be critical for establishing their performance and economic viability as civil transport vehicles. Reaching this goal clearly sets down many technical challenges, aerodynamic and otherwise.

Another aspect of the design of proprotors is the need to include high levels of robustness for off-design operations [26]. For example, sufficient stall margins must be designed into the proprotor to allow for maneuvers, gusts, altitude effects, and vehicle empty weight growth. Empty weight growth is inevitable because of new operational demands, future equipment upgrades, etc. Robustness of design is especially important for proprotors because the performance characteristics of CR aircraft are not as well established as for helicopters or for airplanes. Because of these relatively high levels of uncertainty, the proprotors should be designed so as to minimize losses in both efficiency and operating margins in the event that the predicted performance of the aircraft has been overestimated. In practice, good stall margins may only be achieved by trading other aspects of performance and/or efficiency, highlighting one of the key challenges in the aerodynamic design of more advanced proprotors. Design parameters such as disk loading, solidity, twist, and rotational speed, all need to be balanced between the performance requirements of both hovering and high-speed forward flight, as well as between the requirements of high efficiency, good performance and operating margins, and so giving an overall robustness to the design.

1.4 Approaches toward Aerodynamic Improvement

One approach to significantly increasing the performance of CR aircraft is to judiciously control the tip speed of the proprotors by varying either their rotational speed or diameter, or perhaps both together. Variable speed proprotor (VSPR) or variable diameter proprotor (VDPR) concepts can significantly delay the onset of compressibility effects to

higher forward speeds by reducing the helical Mach numbers on the blades as airspeed increases. Reducing tip speed in forward flight also can increase propulsive efficiency by allowing proprotor blade sections to operate at higher and more efficient angles of attack.

On one hand, the VSPR concept uses a gearbox to reduce the rotational speed while maintaining engine speed, thereby avoiding losses in engine efficiency. The so-called Optimum Speed Tilt Rotor (OSTR) [27] is one type of VSPR design that is intended to offer continuously variable rotational speeds to better optimize aerodynamic efficiency over the flight envelope. On the other hand, the VDPR concept maintains shaft speed and uses a retraction mechanism to draw the blades in toward the hub [28–30]. After retraction, the blade root is sheathed inside the outboard blade sections, reducing the blade area and total blade twist, see Fig. 1.7. However, in either case, reducing tip speed by too much can erode the compressibility/stall margins for the proprotor and produce a "coffin-corner" effect [26] similar to that experienced on high performance airplanes at transonic speeds and high altitudes. The U-2 spyplane is a classic example in this respect. This latter problem is also known to occur on some propellers, which can have very narrow operating margins near their peak propulsive efficiency, e.g., Refs. 31, 32. A proprotor can have both variable speed and variable diameter in a VSDPR concept, although the benefits of such a configuration would have to be carefully balanced against the added weight and mechanical complexity of the additional gearbox and retractable blade mechanism.

Proprotor aerodynamic performance may also be improved by using blades with variable twist, if this could be practically realized. This approach would allow the blade twist rates to be altered during flight, making the twist distribution less of a compromise

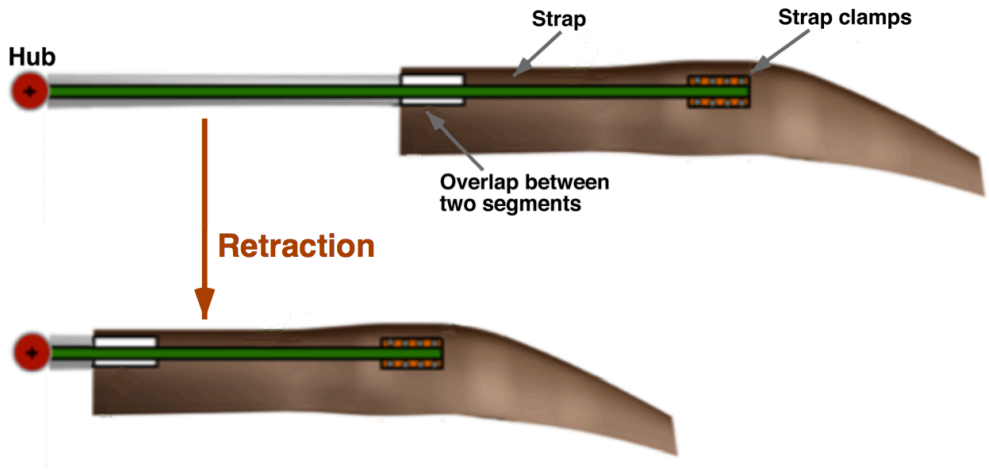

Figure 1.7: A variable diameter proprotor sheathes the inboard blade section inside the outboard section.

between the hover and airplane mode of operation. It has been shown that variable twist can be achieved passively by elastically deforming the blades through an extension-twist-coupling [33]. Using this method, the amount of blade twist is dictated by the centrifugal force so that twist is controlled by the rotor rotational speed. Even without a gearbox, the rotational speed can be decreased by about 10–20% in forward flight without incurring significant increases in engine SFC [34, 35]. Variable twist can also be achieved using shape memory alloys (SMA), where blade twist can be actively controlled through the application of heat [36]; twist is varied by using electroresistivity to heat SMA wires embedded into the blade that run along the chord direction. SMA approaches also may allow active control, allowing changes in twist to be decoupled from the rotor operational state, unlike extension-twist-coupling.

1.5 Objectives of the Present Work

The ability to confidently achieve better design compromises with proprotors will be fundamental to realizing future CR aircraft concepts that can operate at higher cruise speeds, have increased flight range, and offer better payload fractions. At the very least, achieving much better hovering efficiency (i.e., higher power loading approaching the values for a helicopter) simultaneously with better cruise efficiency (i.e., approaching the values of efficiency of contemporary turboprop-powered airplanes) must be a fundamental goal. In this regard, it is not necessarily inevitable that the proprotor that subsequently materializes is as much of an aerodynamic compromise as it has been in the past. While at least some compromises in proprotor performance may still be inevitable, they obviously cannot be allowed to manifest as unanticipated shortcomings in aircraft flight capabilities. Ultimately, it may be that the judicious tuning of vehicle speed, proprotor tip speed, blade pitch (perhaps also blade twist), and engine power setting by a vehicle management system will be needed to extract the best levels of performance from future CR aircraft [26].

The foregoing design challenges can only be solved successfully by using modeling tools with properly verified predictive capabilities [26]. To this end, this thesis discusses a numerically efficient approach that can be used to predict proprotor performance over broad ranges of operating conditions. This modeling framework can be used to expeditiously find the blade and proprotor designs that would fulfill the requirements of a CR aircraft while achieving the highest levels of operating efficiency, as well as meeting the constraints imposed by practical flight operations. Though some prior work has been performed on the aerodynamic optimization of proprotors [11, 17, 19, 37], the current work

addresses a more comprehensive methodology (with validation) and uses this methodology to develop a better understanding of the tradeoffs involved in the design of more efficient proprotors. The results show that there are still many challenges in proprotor design but also exciting opportunities in the development of proprotors with substantially improved capabilities that can be used to power new generations of CR aircraft.

1.6 Organization of Thesis

The first chapter of this thesis has discussed the factors affecting the aerodynamic efficiency of the proprotors used to power convertible-rotor (CR) aircraft, and has provided the general goals of the current research. Chapter 2 describes a predictive methodology that is used for determining the aerodynamic loads and induced velocity distributions on a proprotor in hover and forward flight. A description is provided of the assumed airfoil characteristics used in the predictive model. The formal optimization approach used in this thesis for the purposes of design is also explained. Results obtained using the modeling framework, including validation, are given in Chapter 3. The mathematical model is validated against wind-tunnel data for proprotors and high-speed propellers, as well as against published performance data for CR aircraft. The modeling is then used within the framework of a parametric study to investigate trades in the various design parameters as they will affect both the hovering and propulsive performance of the proprotor. The optimization approach is then used to examine proprotor airfoil requirements, as well as the benefits that could be realized from variable diameter, variable rotational speed, and variable twist proprotor designs. Finally, Chapter 4 discusses the conclusions

drawn from the present work and provides suggestions for future research that could be performed to further improve the aerodynamic efficiencies of proprotors.

Chapter 2

Methodology

Validated mathematical models can be used to help understand the limiting performance issues encountered by proprotors and to expose the levels of performance expected from new proprotor designs. To this end, validation with measurements of propeller and/or proprotor performance characteristics over appropriately broad ranges of operating conditions is critical.

The method used in the present work is a new development of the well-known blade element momentum theory (BEMT), but specifically formulated for propellers and proprotors. In general, the BEMT is mathematically parsimonious and computationally expedient, but has been previously validated only to a limited extent for propellers and proprotors [19, 26, 38]. The BEMT combines the principles of the blade element and momentum theory approaches of thrust generation [39–42]. The sectional aerodynamics are modeled by using assumed (canonical) aerodynamic airfoil models with the option for tables of coefficients, for which several optional sets of airfoils can be incorporated. In the present work, the BEMT approach was formally generalized to large angles and included a better method for simultaneously solving for the inflow and swirl induced velocity components in the wake of the proprotor.

2.1 Large Angle Approach

Figure 2.1 shows the angles, velocities, and force vectors acting on a blade element of a proprotor. The airfoil sections, which are at pitch angles β to the rotor plane, are at effective angles of attack α to the local flow, which has a relative velocity of U to the blade sections. The blade pitch varies along the span of the blade, and by convention is defined relative to the zero-lift angle of the airfoil(s) being used. The out-of-plane velocity component, U_P, is the sum of the forward velocity (i.e., airspeed), V_∞, and the induced axial velocity, w_i. The in-plane velocity component, U_T, is the difference between the rotational tangential speed, Ωy, and the induced swirl velocity, u_i. Notice that all of the velocity components are defined with respect to the leading edge of the blade, which may be swept with respect to a spanwise reference axis.

It is apparent that the inflow angle, ϕ, at each blade section, is affected by both the w_i and u_i components of the induced velocity. For a proprotor in high-speed forward flight the inflow angles can be large, often exceeding 45° near the blade tips. Therefore, the lift vectors on the blade sections may induce flow velocities in the in-plane direction that are even greater than the inflow components, so both the thrust and torque components will determine the induced flow field.

The approach used in the present study differs from the classical BEMT approach in three ways: 1. The removal of all small angle assumptions, 2. Formal inclusion of the in-plane or swirl velocity components, and 3. A large angle modification to the classic Prandtl tip-loss function. BEMT without the assumption of small inflow angles has been established to some extent for proprotors and propellers, as well as for wind turbines [43–

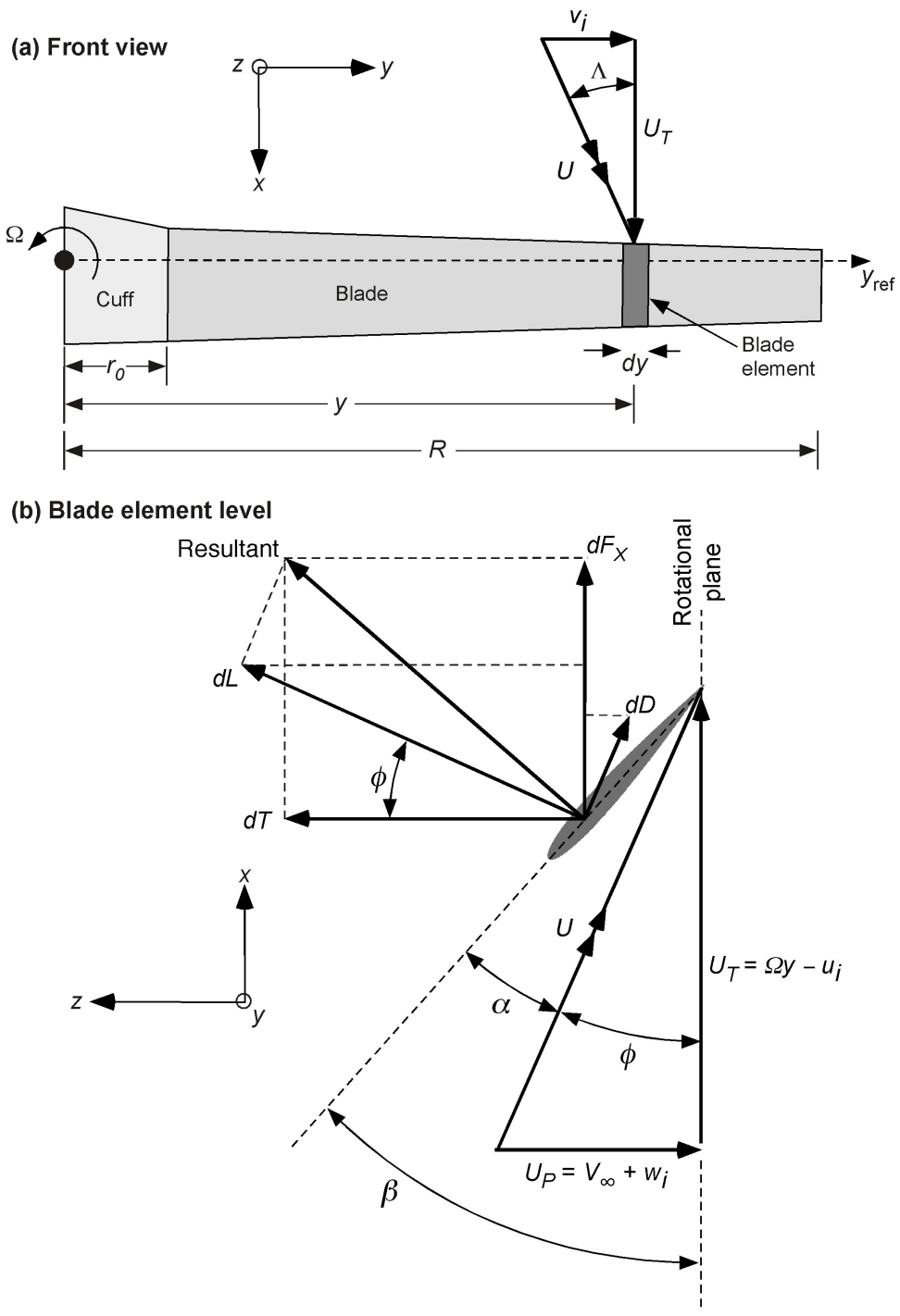

Figure 2.1: The blade element convention used for the proprotor analysis.

45]; however, such work often makes several assumptions meant to simplify the numerical solution. The method presented in this thesis is a more comprehensive approach, and includes a range of validation beyond what has been done in prior work.

Without using any small angle assumptions, the incremental thrust coefficient generated by a blade element is

$$dC_T = \frac{dT}{\rho A\left(\Omega R\right)^2} = \frac{N_b\left(dL\cos\phi - dD\sin\phi\right)}{\rho A\left(\Omega R\right)^2} \tag{2.1}$$

$$= \frac{N_b\left(\frac{1}{2}\rho U^2 c\right)\left(C_l\cos\phi - C_d\sin\phi\right)dy}{\rho A\left(\Omega R\right)^2} \tag{2.2}$$

$$= \frac{1}{2}\sigma\frac{\sqrt{U_T^2+U_P^2}\left(C_l U_T - C_d U_P\right)}{\left(\Omega R\right)^2}\, d\left(\frac{y}{R}\right) \tag{2.3}$$

$$\text{i.e.,}\quad dC_T = \frac{1}{2}\sigma\sqrt{\xi^2+\lambda^2}\left(C_l\xi - C_d\lambda\right)dr \tag{2.4}$$

The inflow ratio $\lambda = (V_\infty + w_i)/\Omega R$ and azimuthal flow ratio $\xi = (\Omega y - u_i)/\Omega R$ are the components of the total velocity perpendicular and parallel to the rotor plane, respectively, both being nondimensionalized by rotational tip speed, ΩR. The incremental power coefficient required by a blade element is

$$dC_P = \frac{dP}{\rho A\left(\Omega R\right)^3} = \frac{N_b\left(dL\sin\phi + dD\cos\phi\right)\Omega y}{\rho A\left(\Omega R\right)^3} \tag{2.5}$$

$$= \frac{N_b\left(\frac{1}{2}\rho U^2 c\right)\left(C_l\sin\phi + C_d\cos\phi\right)\Omega y\, dy}{\rho A\left(\Omega R\right)^3} \tag{2.6}$$

$$= \frac{1}{2}\sigma\frac{\sqrt{U_T^2+U_P^2}\left(C_l U_P + C_d U_T\right)}{\left(\Omega R\right)^2}\frac{y}{R}\, d\left(\frac{y}{R}\right) \tag{2.7}$$

$$\text{i.e.,}\quad dC_P = \frac{1}{2}\sigma\sqrt{\xi^2+\lambda^2}\left(C_l\lambda + C_d\xi\right)r\, dr \tag{2.8}$$

Table 2.1 summarizes the blade element equations with and without the small angle assumptions and the swirl velocity.

Table 2.1: Comparison of blade element terms with and without the small angle assumption and swirl velocity.

	Allowance for large inflow angles	Assumption of small inflow angles
dT	$N_b\left(dL\cos\phi - dD\sin\phi\right)$	$N_b dL$
dP	$N_b\left(dL\sin\phi + dD\cos\phi\right)\Omega y$	$N_b\left(\phi dL + dD\right)\Omega y$
dC_T	$\frac{1}{2}\sigma\sqrt{\xi^2+\lambda^2}\left(C_l\xi - C_d\lambda\right)dr$	$\frac{1}{2}\sigma C_l r^2 dr$
dC_P	$\frac{1}{2}\sigma\sqrt{\xi^2+\lambda^2}\left(C_l\lambda + C_d\xi\right)r\,dr$	$\frac{1}{2}\sigma\left(C_l\lambda + C_d r\right)r^2 dr$
ϕ	$\tan^{-1}\left(\lambda/\xi\right)$	λ/r

The BEMT also uses differential momentum theory to determine the aerodynamics at the blade element. The rotor disk is divided into a number of annuli of area $2\pi y dy$. Conservation of momentum gives $dT = \dot{m}w_w$ and $dF_X = \dot{m}u_w$, where $\dot{m}$ is the mass flow rate through the annulus, and w_w and u_w are the induced axial and azimuthal velocities in the wake. The conservation of energy is also applied, giving the result that $w_w = 2w_i$ and $u_w = 2u_i$. The thrust and power coefficients at each annulus then become

$$dC_T = 4\left|\lambda\right|\lambda_i r\,dr \tag{2.9}$$

and

$$dC_P = 4\left|\lambda\right|\xi_i r^2\,dr\,, \tag{2.10}$$

respectively, where $\lambda_i = w_i/\Omega R$ and $\xi_i = u_i/\Omega R$. The absolute values of λ in Eqs. 2.9 and 2.10 are necessary for the case where an upflow through the rotor annulus is predicted,

which can sometimes occur on a proprotor in the normal working state, such as in hover or at low forward speeds.

2.2 Tip-Loss for Large Angles

A Goldstein/Prandtl tip-loss model was used to account for the increased induced losses at the blade tips. Goldstein [46] established a method for tip-loss by using the velocity potential of a series of helical vortex sheets in the rotor wake. The vortex sheets form a pitch helical angle ϕ with the rotor plane. The sheets move perpendicular to their plane at a speed V_w, where $V_w = \sqrt{w_w^2 + u_w^2}$ is the resultant induced velocity in the wake. A simplified version of the Goldstein result was first developed by Prandtl [47], who approximated the helical surface as a series of two-dimensional planar sheets (see Fig. 2.2) that convect at the slipstream velocity, which is a more practical mathematical realization of Goldstein's approach [48].

Assuming the flow around the blade is irrotational, then the bound circulation Γ of a blade element is equal to the difference in velocity potential between the top and bottom surfaces of the blade section [49]. For a series of two-dimensional sheets then

$$\Gamma = \frac{2V_w s_p}{\pi} \cos^{-1}\left[\exp\left(\frac{-\pi a}{s_p}\right)\right] \tag{2.11}$$

where a is the distance between a blade section and the blade tip and $s_p = (2\pi y/N_b)\sin\phi$ is the normal distance between adjacent sheets, as shown in Fig. 2.2. Defining $V_w = 2V_i$, where $V_i = \sqrt{w_i^2 + u_i^2}$ is the resultant induced velocity at the rotor plane, then

$$\Gamma = \frac{4\pi y V_i F}{N_b} \sin\phi \tag{2.12}$$

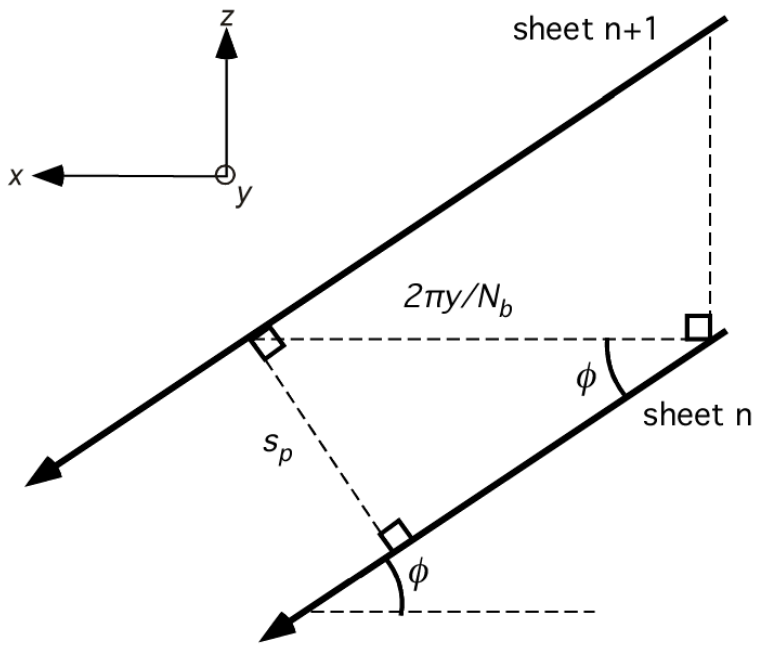

Figure 2.2: Adjacent vortex sheets in a proprotor wake.

where

$$F = \frac{2}{\pi}\cos^{-1}\left[\exp\left(\frac{N_b\,(r-1)}{2r\sin\phi}\right)\right] \tag{2.13}$$

Notice that F, Prandtl's tip-loss factor, decreases with increasing r, indicating that the tip vortices have a greater effect closer to the blade tip. The value of F also decreases as ϕ is increased and N_b is reduced, showing that the effect of the tip vortices becomes stronger as the spacing decreases between the vortex sheets. However, Prandtl's assumption of two-dimensional vortex sheets becomes less accurate as s_p increases. Strictly speaking, F should be a function of the vortex sheet spacing at the blade tip, i.e., the term in the exponent in Eq. 2.13 should be $N_b(r-1)/(2\sin\phi_{\text{tip}})$. However, it is sufficiently accurate to use the local inflow angles, which are also more convenient [43].

To incorporate tip-loss effects into the BEMT, the Kutta-Joukowski theorem is used

with the blade element expressions in Eqs. 2.4 and 2.8, i.e.,

$$\frac{1}{2}\rho U^2 c\left(C_l\cos\phi - C_d\sin\phi\right) = \rho U_T \Gamma \tag{2.14}$$

and

$$\frac{1}{2}\rho U^2 c\left(C_l\sin\phi + C_d\cos\phi\right) = \rho U_P \Gamma \tag{2.15}$$

Using the relations from Eqs. 2.12, 2.14, and 2.15, the circulation, Γ, is then substituted into Eqs. 2.4 and 2.8 to give

$$dC_T = \frac{1}{2}\left(\frac{N_b c}{\pi R}\right)\frac{U^2\left(C_l\cos\phi - C_d\sin\phi\right)}{\left(\Omega R\right)^2}dr \tag{2.16}$$

$$= \frac{N_b U_T \Gamma}{\pi R\left(\Omega R\right)^2}dr = \frac{4FV_i U_T r\sin\phi}{\left(\Omega R\right)^2}dr \tag{2.17}$$

$$\text{i.e.,}\quad dC_T = 4F\lambda\frac{V_i\cos\phi}{\Omega R}rdr \tag{2.18}$$

and

$$dC_P = \frac{1}{2}\left(\frac{N_b c}{\pi R}\right)\frac{U^2\left(C_l\sin\phi + C_d\cos\phi\right)\Omega y}{\left(\Omega R\right)^3}dr \tag{2.19}$$

$$= \frac{N_b U_P \Gamma \Omega y}{\pi R\left(\Omega R\right)^3}dr = \frac{4FV_i U_P r^2\sin\phi}{\left(\Omega R\right)^2}dr \tag{2.20}$$

$$\text{i.e.,}\quad dC_P = 4F\lambda\frac{V_i\sin\phi}{\Omega R}r^2 dr \tag{2.21}$$

Equations 2.18 and 2.21 are the same as Eqs. 2.9 and 2.10 except for the inclusion of the tip-loss factor F and the replacement of λ_i with $V_i\cos\phi/\Omega R$ and ξ_i with $V_i\sin\phi/\Omega R$.

Because an inviscid theory is used to obtain Eqs. 2.18 and 2.21, they are only completely valid when the directions of w_i and u_i are opposite to that of the corresponding force vectors. Equation 2.18 is only strictly valid when $\phi = 0^\circ$, and Eq. 2.21 is only valid when $\phi = 90^\circ$. At $\phi = 90^\circ$ for dC_T and $\phi = 0^\circ$ for dC_P, the tip vortices do not contribute to the induced velocities w_i and u_i.

To reconcile Eqs. 2.18 and 2.21 with the expected physical behavior, the expressions for the decreases in thrust and power, the terms $4\lambda\lambda_i r dr(1-F)$ and $4\lambda\xi_i r^2 dr(1-F)$, should gradually decrease to zero as the angles decrease between the tip vortex axes and the blade force vectors. To model this behavior, the differential momentum theory equations for the thrust and power coefficients can be modified to read

$$dC_T = 4K_T\,|\lambda|\,\lambda_i r\,dr \tag{2.22}$$

and

$$dC_P = 4K_P\,|\lambda|\,\xi_i r^2\,dr \tag{2.23}$$

respectively, where $K_T = [1-(1-F)\cos\phi]$ and $K_P = [1-(1-F)\sin\phi]$.

It is necessary to account for tip-loss effects because only some of the induced flow arises from momentum conservation, the remainder being from the presence of the tip vortices. The value of F can be viewed as the ratio of V_i that is directly induced by the rotor to the total V_i. Likewise, K_T and K_P are the ratios of the w_i and u_i that are directly induced by the rotor to the total w_i and u_i, respectively.

2.3 Numerical Solution for Inflow Components

To solve for the induced flow components, the blade element expressions for the incremental thrust and power coefficients are equated to those from momentum theory, i.e.,

$$dC_T = \frac{1}{2}\sigma\sqrt{\xi^2+\lambda^2}\,(C_l\xi - C_d\lambda)\,dr = 4K_T\,|\lambda|\,\lambda_i r\,dr \tag{2.24}$$

and

$$dC_P = \frac{1}{2}\sigma\sqrt{\xi^2+\lambda^2}\,(C_l\lambda + C_d\xi)\,r\,dr = 4K_P\,|\lambda|\,\xi_i r^2 dr \tag{2.25}$$

One way to solve this system of equations for λ and ξ is by fixed-point iteration, which is the conventional approach. The forms of Eqs. 2.24 and 2.25 with the best fixed-point convergence characteristics are

$$\lambda_{n+1} = \frac{V_\infty}{\Omega R} + \frac{\sigma\sqrt{\xi^2+\lambda_n^2}\,(C_l\xi - C_d\lambda_n)}{8K_T\lambda_n r} \tag{2.26}$$

and

$$\xi_{n+1} = r - \frac{\sigma\sqrt{\xi_n^2+\lambda^2}\,(C_l\lambda + C_d\xi_n)}{8K_P\lambda r} \tag{2.27}$$

When solving for λ and ξ in this fashion, convergence is usually rather slow. Additionally, successive iterations of Eqs. 2.26 and 2.27 tend to diverge away from the desired solution, requiring the use of relaxation to encourage the method to converge. Relaxation is a technique wherein the value of the variable in the new iteration is set to be between its previous value and its predicted updated value, e.g.,

$$\lambda_{n+1} = a\,\lambda_{n+1} + (1-a)\,\lambda_n \tag{2.28}$$

where a is a relaxation coefficient. The more the iterative method tends to diverge, the lower a needs to be to encourage convergence; too much relaxation will result in slower convergence, while too little may result in divergence.

Different rotor configurations and blade sections may require different relaxation coefficients to converge on an inflow ratio or azimuthal flow ratio using fixed-point iteration. Smaller relaxation coefficients are necessary to ensure that convergence occurs for

all configurations; however, a relaxation coefficient that is too low can dramatically slow the convergence process.

Rather than concurrently solving Eqs. 2.26 and 2.27, the thrust and power equations can be expressed in terms of the inflow angle ϕ and combined into a single transcendental equation, as shown by Winarto [50]. In this case, only one equation needs to be solved. Recognizing that $\lambda = U\sin\phi/\Omega R$ and $\xi = U\cos\phi/\Omega R$, Eq. 2.24 can be rewritten as

$$\frac{1}{2}\sigma\frac{U^2\left(C_l\cos\phi - C_d\sin\phi\right)}{\left(\Omega R\right)^2}dr = 4K_T\left|\lambda\right|\lambda_i r\,dr \tag{2.29}$$

Defining $\tan\gamma = C_d/C_l$ and substituting $C_l\tan\gamma$ for C_d, while also dimensionalizing by $(\Omega R)^2$ gives

$$\frac{1}{2}\sigma U^2 C_l\sec\gamma(\cos\gamma\cos\phi - \sin\gamma\sin\phi) = 4K_T U\sin\left|\phi\right| w_i r \tag{2.30}$$

Using the identity $\cos(\phi+\gamma) = \cos\phi\cos\gamma - \sin\phi\sin\gamma$, and recognizing that $w_i = U\sin\phi - V_\infty$, the above equation can be rearranged into the form

$$\frac{1}{8K_T}\sigma\frac{1}{r}UC_l\sec\gamma\csc\left|\phi\right|\cos\left(\phi+\gamma\right) = U\sin\phi - V_\infty \tag{2.31}$$

A function $B_1(\phi)$ is now defined as

$$B_1(\phi) = \frac{V_\infty}{U} = \sin\phi - \frac{1}{8K_T}\sigma\frac{1}{r}C_l\sec\gamma\csc\left|\phi\right|\cos\left(\phi+\gamma\right) \tag{2.32}$$

A similar method is used rewrite Eq. 2.25 to obtain a function $B_2(\phi)$, i.e.,

$$B_2(\phi) = \frac{\Omega y}{U} = \cos\phi + \frac{1}{8K_P}\sigma\frac{1}{r}C_l\sec\gamma\csc\left|\phi\right|\sin\left(\phi+\gamma\right) \tag{2.33}$$

Equations 2.32 and 2.33 can then be combined into a single transcendental equation, i.e.,

$$g\left(\phi\right) = \left[B_1(\phi)\,\Omega y - B_2(\phi)\,V_\infty\right]\sin\phi = 0 \tag{2.34}$$

or

$$g(\phi) = (\Omega y \sin\phi - V_\infty \cos\phi)\sin\phi \\ -\mathrm{sgn}(\phi)\frac{\sigma C_l \sec\gamma}{8r}\left[\frac{\Omega y}{K_T}\cos(\phi+\gamma) + \frac{V_\infty}{K_P}\sin(\phi+\gamma)\right] \tag{2.35}$$

The signum function is introduced into Eq. 2.35 because the absolute values in Eqs. 2.32 and 2.33 have cancelled out in the derivation of $g(\phi)$.

In Eq. 2.35, the inflow angle, ϕ, is the only unknown. The values of C_l, C_d, K_T, and K_P are themselves functions of several variables of which ϕ is the only unknown. If the lift coefficient is zero, then $g(\phi) = (\Omega y \sin\phi - V_\infty \cos\phi)$ should be solved instead of Eq. 2.35. The inflow ratio and azimuthal flow ratio can then be calculated and introduced into Eqs. 2.4 and 2.8 to obtain the incremental thrust and power at that particular blade section. The inflow and swirl velocity ratios can be obtained using

$$\xi = r\frac{\cos\phi}{G(\phi)} \tag{2.36}$$

and

$$\lambda = \xi\tan\phi \tag{2.37}$$

respectively.

One way to arrange Eq. 2.35 for solution by means of fixed-point iteration is

$$\phi_{n+1} = \sin^{-1}\left[\mathrm{sgn}(\phi)\frac{\sigma C_l \sec\gamma\left[\frac{\Omega y}{K_T}\cos(\phi_n+\gamma) + \frac{V_\infty}{K_P}\sin(\phi_n+\gamma)\right]}{8r(\Omega y\sin\phi_n - V_\infty\cos\phi_n)}\right] \tag{2.38}$$

Figure 2.3 shows an example of a fixed-point iteration history using Eq. 2.38. Even though the initial prediction is very close to the solution, the method diverges away from

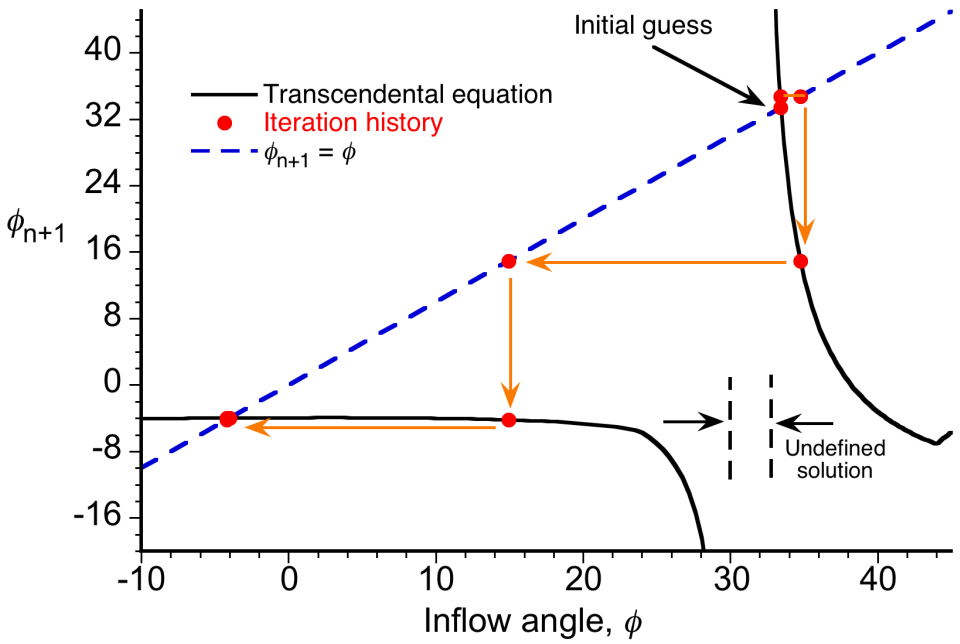

Figure 2.3: Iteration history for the fixed-point method to solve for the inflow ratio using Eq. 2.38.

the solution and eventually converges on a negative inflow angle, which is a physically unrealistic solution. Furthermore, there exists a range of values for ϕ_n that results in an undefined value of ϕ_{n+1}. If the initial prediction or any subsequent iterations generate a ϕ which falls in this undefined range, then the method will fail. As before, relaxation may be used to prevent the method from diverging or from converging on the wrong solution. However, the range of undefined solutions is still an issue in using fixed-point iteration to solve Eq. 2.35, making this particular method unsuitable for the BEMT applied to a propotor. All forms of Eq. 2.38 will have this undefined range because of the trigonometric terms.

The solution to the transcendental equation (2.35) can be found using other root-finding methods, although derivative-based methods such as Newton's method are not

helpful either because the derivative of Eq. 2.35 has a nonlinearity from the C_l and C_d terms; if reading data from airfoil tables then the derivative can only be approximated anyway.

The bracketed bisection method was found to be suitable for solving Eq. 2.35 because of its guaranteed convergence. This method works by realizing that a single solution for ϕ is located within a range bracketed between two points, and then halving this range with each iteration.

Figure 2.4 shows an example of an iteration history for the bisection method applied to solve the transcendental equation in Eq. 2.35 to obtain the inflow angle. A suitable convergence criteria is to end the iterations once the relative difference between successive iterations falls below a threshold, in this case 0.05%. Although the bisection method is among the slowest of root-finding methods, it can solve for ϕ in Eq. 2.35 roughly three times faster than solving for the induced velocity components separately by using Eqs. 2.26 and 2.27, and has the added benefit of not requiring any numerical relaxation. The bisection method is also very robust, and if there is only one solution then it is impossible for the method to fail to converge.

A complication arises in the implementation of the bisection method for a hovering rotor, because occasionally there are multiple solutions to ϕ, one positive and one negative. To determine the correct solution, $g(\phi)$ in Eq. 2.35 is first calculated for $\phi = 0$. If $g(0) > 0$, then ϕ is negative. If $g(0) \leq 0$, then ϕ is positive. The boundaries for the bracketed solution are then adjusted accordingly.

Solving for the spanwise aerodynamic loadings on a proprotor according to the method outlined in this section is fast, robust, and cost-efficient. A code containing the

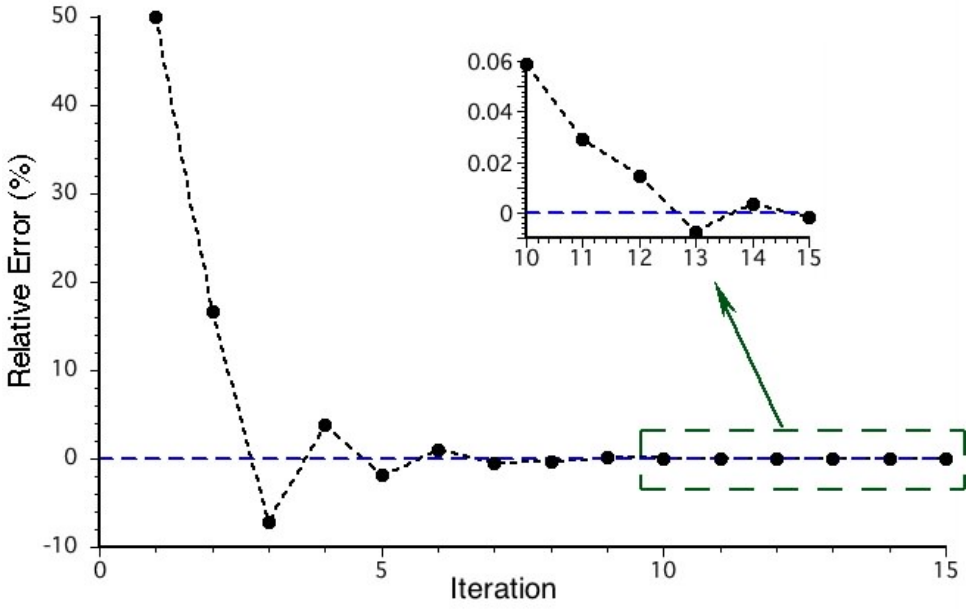

Figure 2.4: Iteration history for bisection method used to solve for ϕ in the transcendental equation, Eq. 2.35.

BEMT equations discussed previously can run several orders of magnitude faster than one containing a comparable free-vortex wake model. The BEMT methodology can be especially useful for preliminary design of a proprotor (or propeller) in axial flight, before more elaborate analysis is performed using less cost-efficient methods.

2.4 Airfoil Characteristics

Airfoil characteristics can be read in the conventional way from a collection of "C-81" like tables listing values of sectional C_l and C_d for ranges of angles of attack, Mach numbers, and Reynolds numbers. The data from these airfoil tables can come from sources such as experimental measurements or CFD generation [51]. However, such data are often unavailable for proprotor airfoils, and so other approaches must be used

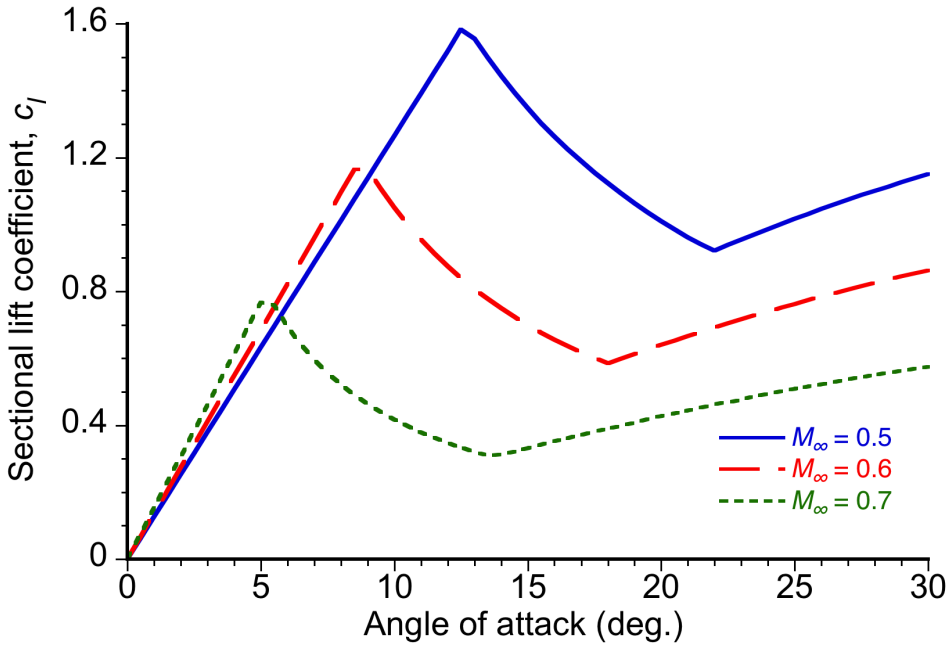

Figure 2.5: Canonical representation of sectional lift coefficients at different Mach numbers.

to specify the airfoil characteristics. Whatever models are used, it is imperative that they include stall and post-stall characteristics; in this regard, the compromised blade twist used on proprotors means that a significant portion of the blade may stall in hover and/or over some range of forward flight speeds.

The sectional lift and drag model that was assumed in the present study is shown in Figs. 2.5 and 2.6. After the blade stalls, drag increases as flow separation occurs. Lift decreases with further increases in angle of attack until the airfoil begins to act more as a flat plate. Figure 2.7 shows the lift-to-drag ratios obtained with the assumed airfoil model. As shown, airfoils can achieve higher, more efficient values of c_l/c_d at higher Mach numbers, but stall at lower angles of attack.

Modeling compressibility effects at higher Mach numbers is also necessary. In the

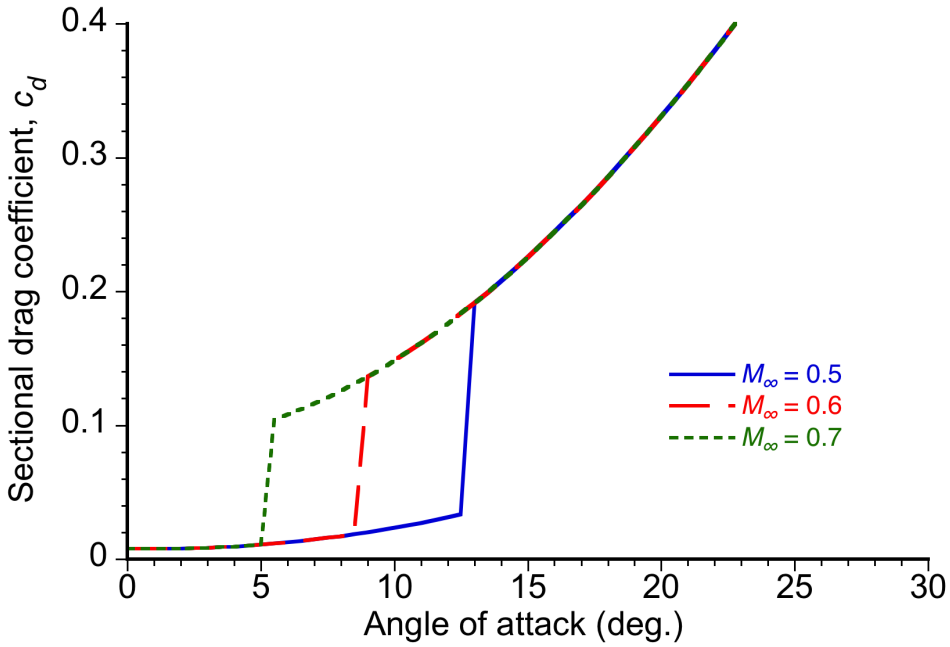

Figure 2.6: Canonical representation of sectional drag coefficients at different Mach numbers.

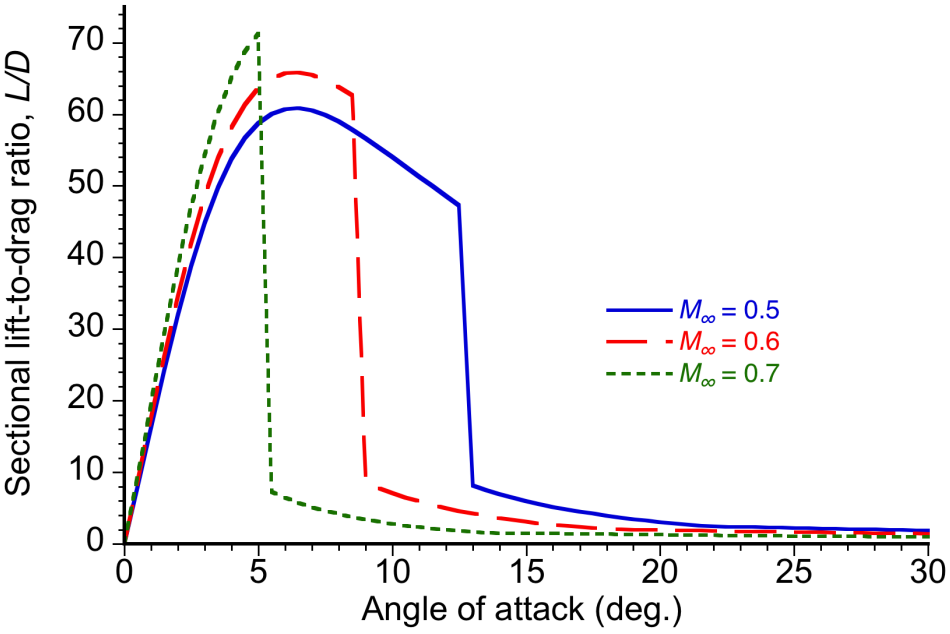

Figure 2.7: Canonical representation of sectional airfoil L/D at different Mach numbers.

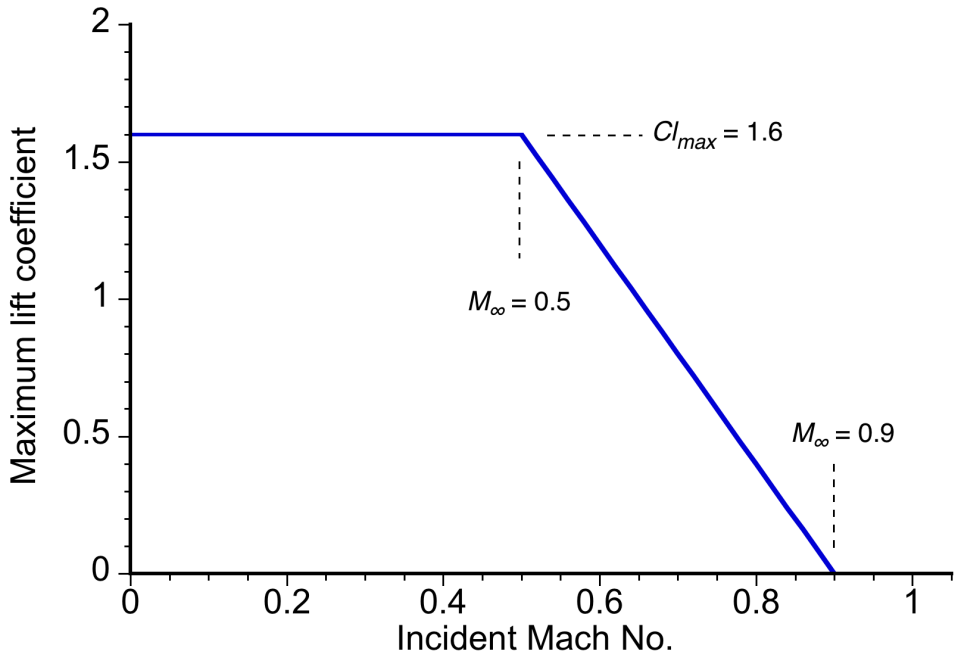

Figure 2.8: Canonical model for maximum lift coefficient versus Mach number.

attached flow regime, the lift curve slope, C_{l_α}, can be adjusted by using the Glauert rule, i.e.,

$$C_{l_\alpha} = \frac{C_{l_\alpha}|_{M=0.1}}{\sqrt{1-M^2}} \tag{2.39}$$

where $C_{l_\alpha}|_{M=0.1}$ is the lowest value for the lift curve slope. The maximum lift coefficient of an airfoil is also a function of Mach number. One canonical representation, shown in Fig. 2.8, is that $C_{l_{\max}}$ remains constant up to a certain value of M, at which point it decreases linearly with further increases in M.

Compressibility also has an effect on drag. In particular, the drag on an airfoil begins to increase rapidly as the oncoming flow reaches the drag divergence Mach number, M_{dd}. One approximation that has been used for the increase in drag approaching drag

divergence is [52]

$$\Delta C_d = \begin{cases} 12.5\,(M - M_{\text{dd}} + 0.08) & \text{if} \quad M \geq (M_{\text{dd}} - 0.08) \\ 0 & \text{otherwise} \end{cases}$$

2.5 Tip Relief

A compressibility tip relief model was also used in the present work, which acts to delay the onset of drag divergence at the blade tip sections. Because of three-dimensional flow at the tip, the effects of compressibility are relaxed. When a blade section within one chord-length of the tip exceeds M_{dd}, there is a reduced effective local Mach number, which can be approximated by [52], i.e.,

$$M_{\text{eff}} = M\left[\frac{M_{\text{dd2}}}{M_{\text{dd3}}} + \left(1 - \frac{M_{\text{dd2}}}{M_{\text{dd3}}}\right)(1 - r)\,AR_{\text{blade}}\right] \tag{2.40}$$

where AR_{blade} is the blade aspect ratio, M_{dd2} is the 2-dimensional drag divergence Mach number, and M_{dd3} is the assumed 3-dimensional drag divergence Mach number.

The effects of tip relief are shown in Fig. 2.9. As the ratio $M_{\text{dd3}}/M_{\text{dd2}}$ increases, the local effective Mach numbers near the tip decrease, thereby relieving the adverse effects of drag divergence.

2.6 Spinner Effects

The presence of a spinner can result in high supervelocities near the blade roots, which are caused by the oncoming flow accelerating as it passes over the spinner. This behavior is shown in Fig. 2.10. For proprotors, where the spinner diameter can be a significant fraction of the proprotor diameter, the supervelocity can have a significant

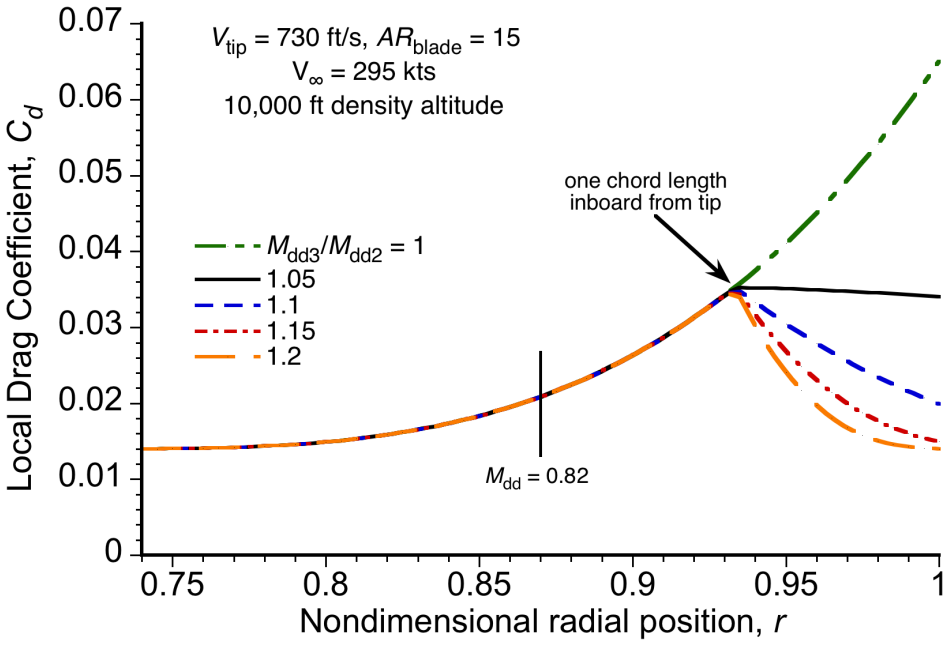

Figure 2.9: Effects of drag divergence and tip relief on the drag for a proprotor in forward flight.

effect on the blade aerodynamics by increasing the Mach number and altering the inflow angle distribution. This effect can be an issue, in particular, with a variable diameter proprotor design because the rotor diameter is reduced in forward flight and the spinner needs to be large enough to contain the blade retraction mechanisms.

If the spinner effects are approximated as an equivalent sphere, then potential flow theory gives the supervelocity, V_{sup}, as [53]

$$V_{sup} = \frac{V_\infty}{2}\left(\frac{R_{spinner}}{y_{blade}}\right)^3 \tag{2.41}$$

The increment in supervelocity is equal to half the free-stream velocity where the spinner meets the blade root, and then drops off quickly with distance outboard of the spinner. As shown in Fig. 2.11, the distribution of supervelocity depends greatly on the diameters of the proprotor and spinner. For configurations where the spinner is relatively large, such

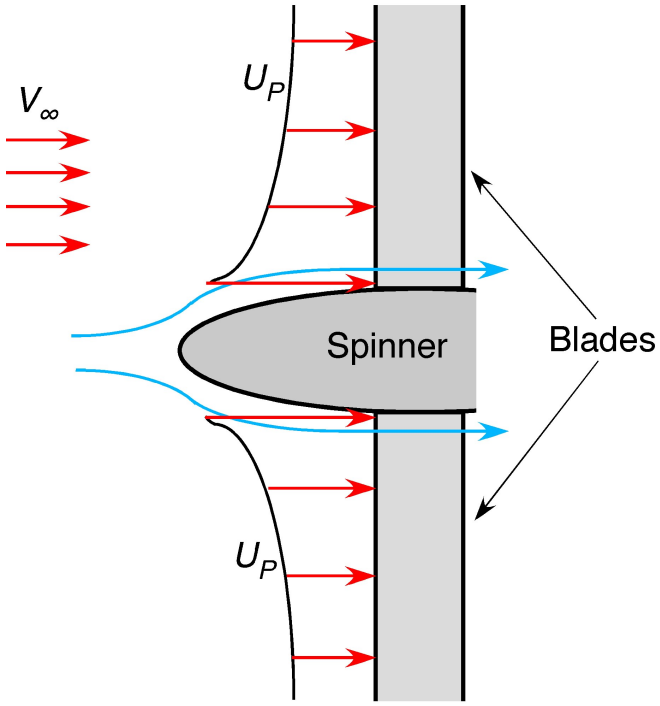

Figure 2.10: The presence of the spinner results in supervelocities near the blade roots.

as found on some propellers, the supervelocity can have a significant effect even at the mid-span of the blade.

2.7 Tip Sweep

Tip sweep can be employed on proprotor blades to delay the onset of compressibility by reducing the effective Mach number normal to the blade leading edge. The sweep angle, Λ, is implemented into the calculations by reducing the velocity of the flow component perpendicular to the leading edge by the factor $\cos\Lambda$.

Ignoring the induced velocity but accounting for both sweep and supervelocities,

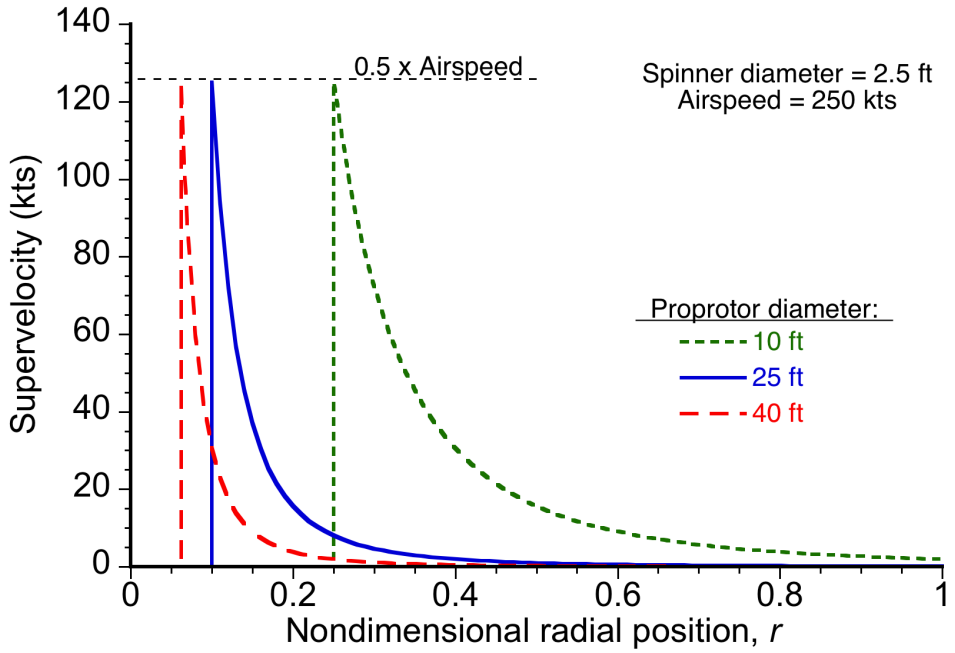

Figure 2.11: Distribution of supervelocity across the blade span depends on ratio of proprotor diameter to spinner diameter.

the effective Mach number at a blade section is then

$$M = \frac{1}{a}\sqrt{U_T^2 + U_P^2} \tag{2.42}$$

where

$$U_T^2 = (\Omega y)^2 \left[\cos^2\beta\cos^2\Lambda + \sin^2\beta\right]$$

and

$$U_P^2 = V_\infty^2 \left[1 + \frac{1}{2}\left(\frac{R_{\text{spinner}}}{y_{\text{blade}}}\right)^3\right]^2 \left[\cos^2\beta + \sin^2\beta\cos^2\Lambda\right]$$

2.8 Optimization Approach

Some of the results reported in this thesis were obtained using a formal optimization approach. The optimizer was validated by optimizing the efficiency of the proprotor

by using up to six design variables, and then performing parametric studies to confirm that the optimizer gave physically correct results and successfully minimized the stated objective function(s).

At its most elementary level, the optimizer functions by applying small perturbations to each of the design variables to obtain a profitable search direction, and then minimizes an objective function along this direction. This process continues until convergence occurs. Side constraints (i.e., the upper and lower boundaries of the design variables) are specified prior to the start of the optimization. If no inequality constraints (e.g., engine power available or transmission limits) are imposed, then the optimizer uses the Broydon-Fletcher-Goldfarb-Shanno (BFGS) algorithm.

The basic optimization approach is described as follows:

1. An initial vector $\mathbf{X}^0$ for the design variables is established, as well as the resulting initial objective function, $F(\mathbf{X}^0)$.

2. A small perturbation is sequentially applied to each design variable and the resulting gradients of the objective function, $\nabla F(\mathbf{X}^k)$, are calculated.

3. From the results of the previous step, a multi-dimensional search direction $\mathbf{S}^k$ is calculated.

4. A point along the search direction, designated as α^*, is found which minimizes $F(\mathbf{X})$.

5. The design variables are updated according to $\mathbf{X}^{k+1} = \mathbf{X}^k + \alpha^* \mathbf{S}^k$.

6. Steps 2–5 are repeated until $F(\mathbf{X})$ converges on a minimum. The convergence

criteria is defined by $\nabla F(\mathbf{X}^k)$ falling below a certain threshold, set by the user.

If inequality constraints are imposed, then the method of feasible directions (MFD) is used. The MFD seeks the lowest possible value of the objective function that does not violate the inequality constraints. The steps are similar to those outlined above, except the search direction $\mathbf{S}^k$ is calculated so that it both decreases $F(\mathbf{X})$ and avoids violating the constraints (i.e., it avoids the infeasible region). Additional convergence criteria, the Kuhn-Tucker conditions, are also in place [54].

2.9 Summary

This chapter has discussed the theory used to predict the loads and induced flow distributions on proprotors, both in hover and axial forward flight. Classical BEMT used for helicopter rotors has been modified to account for the high axial velocities and large inflow angles found on propellers and proprotors, as well as a new implementation for Prandtl's tip-loss factor. The induced flow distribution is most easily solved by combining the BEMT thrust and power equations into a single transcendental equation; the bisection method (or other, similar bracketed root-finding algorithms) proved to be the quickest and most robust approach for solving this transcendental equation. Also discussed were canonical airfoil characteristics that were used in lieu of complete airfoil tables, and how sectional loads are affected by the presence of tip relief, blade sweep, and spinner super-velocities. The formal optimization approach, used to generate some of the results in this paper, was also explained.

Chapter 3

Results and Discussion

The results in this thesis are discussed in eight parts: 1. A description of the proprotor designs and the convertible-rotor (CR) aircraft for which results were obtained; 2. Validation of the proprotor model with propeller measurements, isolated proprotor measurements, and CR vehicle performance; 3. Parametric studies of proprotor and CR vehicle performance; 4. A discussion of alternative metrics for evaluating proprotor efficiency; 5. Validation of the optimization methodology; 6. Requirements for the proprotor airfoils; 7. Optimization for variable tip speed operations, and 8. Optimization of hovering and propulsive efficiency for variable twist operations.

3.1 Aircraft Used in this Study

The results discussed in this thesis were obtained by using proprotors designed for three different CR configurations, namely: 1. A representative medium-lift tiltrotor [55]; 2. The Sikorsky VDTR concept [28]; and 3. The *Excalibur*, which is also a VDTR concept and was the University of Maryland's winning entry in the 2011 Annual AHS Design Competition [56]. These proprotors were used for the purposes of validation of the modeling, and also to show the sensitivities in performance to variations in the design parameters.

Some of the relevant vehicle specifications are given in Table 3.1. Notice that the

Table 3.1: Essential characteristics of the convertible-rotor configurations used in the present study.

	Medium-Lift Tiltrotor	VDTR	*Excalibur*
Max. VTOL GTOW	51,000 lb	–	18,000 lb
Installed power, P_{install}	2 x 6,150 hp	–	2 x 1,908 hp
Proprotor diameter, D	38.1 ft	49.2 ft	30.5 ft
Shaft speed, Ω	412 rpm	264 rpm	505 rpm
Proprotor solidity, σ	0.102	0.085	0.070
Vehicle parasitic drag area, f_e	26.0 ft^2	–	6.0 ft^2
Wing aspect ratio, AR	6.97	–	6.0
Wing profile drag coefficient, C_{D_0}	0.01	–	0.008
Oswald's efficiency factor, e	0.8	–	0.87
Wing area, S	301.6 ft^2	–	267.2 ft^2

VDTR and *Excalibur* are both variable-diameter proprotor concepts, the blades in this case retracting to 2/3 of their maximum extended diameter. The net performance of the proprotors for the medium-lift tiltrotor and *Excalibur* were evaluated when coupled to a representation of their respective airframes, including the performance limits imposed by the engines and/or the transmission. The thrust needed from the proprotors in hover was assumed to be equal to aircraft weight plus an increment to account for the download on the wings, this being 12% of aircraft weight in the present work.

The thrust needed in forward flight depends on the vehicle drag (i.e., its lift-to-drag ratio), so the thrust required in this case becomes a function of forward speed. The total drag can be split into a wing component and a non-wing (i.e., fuselage and empennage)

component, i.e.,

$$D_{\text{veh}} = q_\infty S C_{D_{\text{wing}}} + q_\infty f_e \tag{3.1}$$

where $q_\infty = 0.5\rho_\infty V_\infty^2$ is the freestream dynamic pressure. The drag on the non-wing surfaces is expressed as an equivalent parasitic drag area, f_e. The drag on the wing is the sum of profile and induced drag components and can be written as

$$C_{D_{\text{wing}}} = C_{D_0} + \frac{C_L^2}{\pi AR\, e} \tag{3.2}$$

where AR is the aspect ratio of the wing. The vehicle drag in Eq. 3.1 can then be rewritten as the sum of profile and induced components, i.e.,

$$D_{\text{veh}} = q_\infty (S C_{D_0} + f_e) + \frac{q_\infty S C_L^2}{\pi AR\, e} \tag{3.3}$$

Assuming that wing lift is equal to vehicle weight, W, then the lift coefficient can be expressed as

$$C_L = \frac{W}{q_\infty S} \tag{3.4}$$

Equation 3.3 is then expressed in the form used in the present work, i.e.,

$$D_{\text{veh}} = q_\infty (S C_{D_0} + f_e) + \frac{W^2}{q_\infty S \pi AR\, e} \tag{3.5}$$

3.2 Validation of the Modeling

Validation of the proprotor aerodynamic model described in Chapter 2 is necessary before using the model to generate any meaningful results. By validating the proprotor model against performance measurements of propellers and proprotors, as well as published CR vehicle performance data, a good level of confidence can be established in the

predictive capabilities of the model. In general, however, there are limited experimental data available for proprotors, and the existing data tend to be available for a relatively small range of operating conditions. For this reason, performance measurements of high-speed propellers are especially important for validation purposes.

3.2.1 Validation with Propeller Measurements

The proprotor model was initially validated against wind-tunnel data for two NACA "high-speed" propellers. While some proprotor measurements are also available [16, 57, 58], such measurements do not cover the wide range of operating conditions that are needed to validate all aspects of the modeling. Therefore, the two propellers identified by Harris [59], which are representative of both the geometry of a proprotor and of the wide operating conditions that may be encountered by an advanced high-speed proprotor, were used instead.

The performance characteristics of these two propellers were measured in the NACA wind tunnels, one propeller being 2-bladed with a 4 ft diameter [60] and the other being 3-bladed with a 9.75 ft diameter [61]. The 2-bladed propeller had a 2:1 blade taper from root to tip, and the 3-bladed propeller had constant chord untapered blades. Each propeller had approximately 32° of nose-down twist over the blade, and the boss (for the spinner and blade attachments) in each case extended out to 27% of the propeller radius. The 3-bladed propeller is shown in Fig. 3.1 in the wind tunnel test section.

Parametric measurements for the 2-bladed propeller were taken by varying the rotational speed while keeping constant the tunnel wind speed and the blade pitch. For

Figure 3.1: NACA propeller mounted in the wind tunnel test section [61].

the 3-bladed propeller, measurements were taken by fixing the rotational speed and blade pitch while the wind speed was varied. The net result in either case (i.e., of systematic variations of wind speed at a constant blade pitch and/or blade pitch variations at a constant wind speed) are sets of propeller thrust, power, and efficiency curves as a function of the operating advance ratio [39]. In some of the operating conditions for the 3-bladed propeller, the thinner blades were reported to have experienced stall flutter and so could not operate continuously at these conditions [61].

Predictions from the present model versus the propeller measurements are shown in Figs. 3.2 through 3.5 for the 2-bladed propeller, and in Figs. 3.6 through 3.9 for the 3-bladed propeller, in each case as sets of thrust, power, and propulsive efficiency curves. Airfoil tables were not available for either propeller, so the canonical sectional airfoil

characteristics in the forms described in Section 2.4 were used to represent the lift and drag coefficients in the BEMT.

The reported measurements in Refs. 60 and 61 were converted from conventional propeller nomenclature into conventional helicopter rotor nomenclature, in this case in the form of C_T/σ and C_P/σ coefficients (see Appendix). The advance ratio is defined conventionally for helicopters as $\mu = V_\infty/\Omega R$; when multiplied by a factor of π, the forward speed ratio is equivalent to the advance ratio "J" used for propeller performance evaluations. The propulsive efficiency is defined using the helicopter nomenclature as $\eta_p = C_T\mu/C_P$, which gives the same numerical result when using the conventional propeller nomenclature.

The results in Figs. 3.2 through 3.5 are for the 2-bladed propeller, which show good

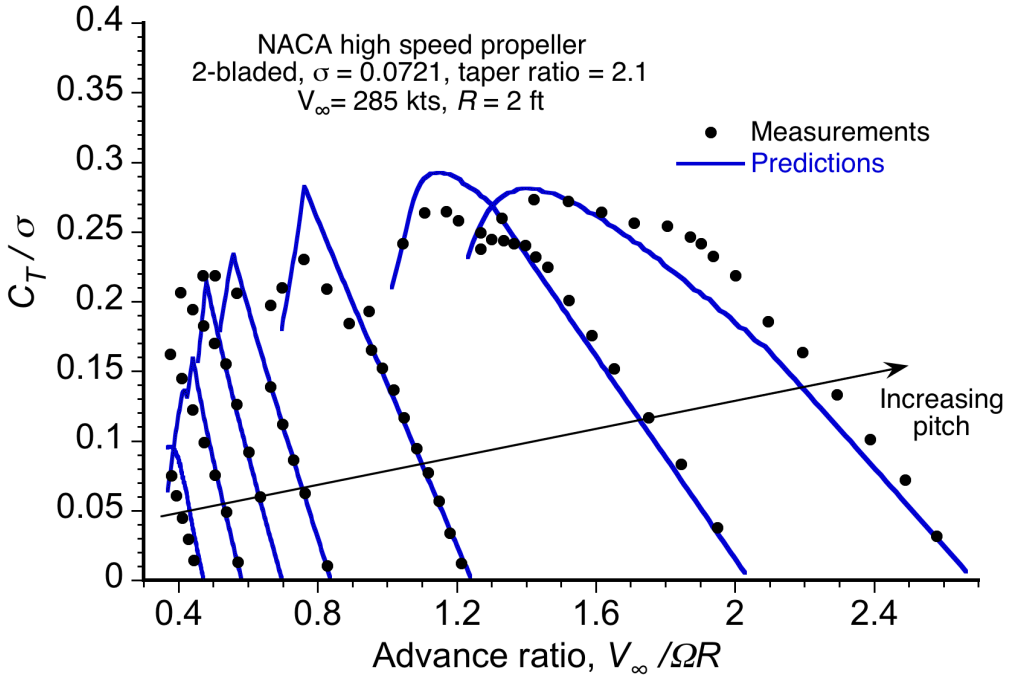

Figure 3.2: Thrust in the form of C_T/σ versus advance ratio for the 2-bladed NACA propeller.

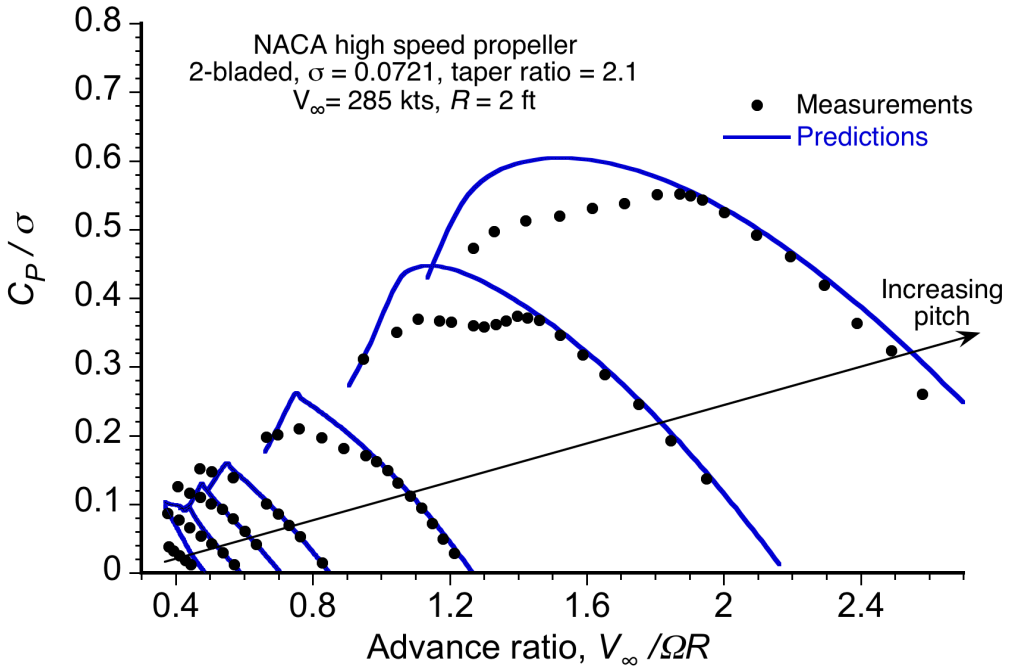

Figure 3.3: Power in the form of C_P/σ versus advance ratio for the 2-bladed NACA propeller.

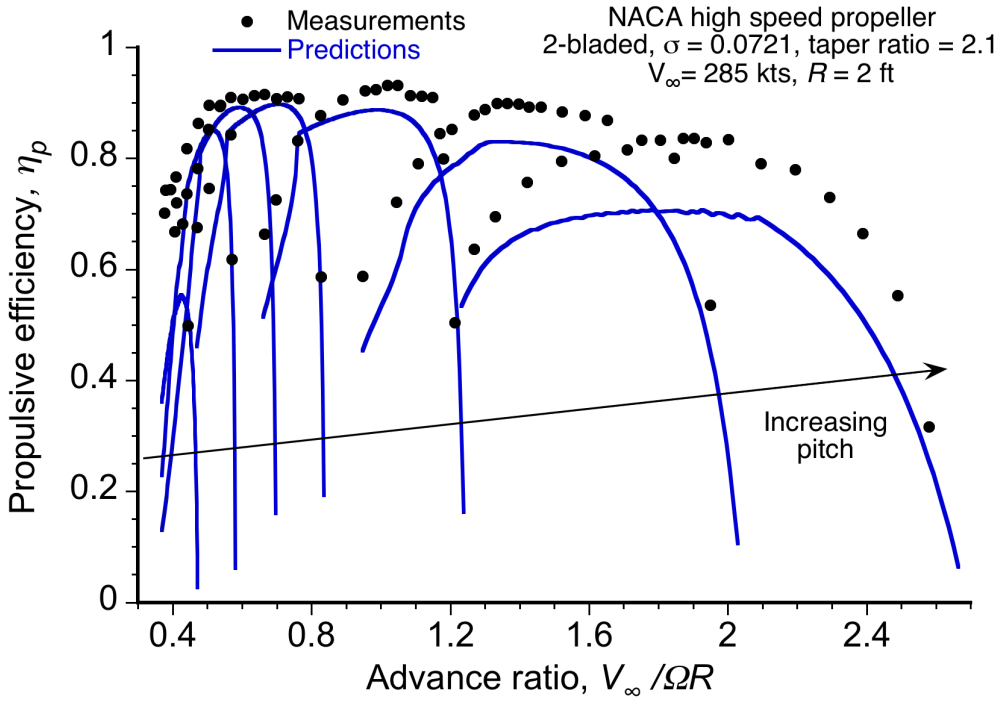

Figure 3.4: Propulsive efficiency versus advance ratio for the 2-bladed NACA propeller.

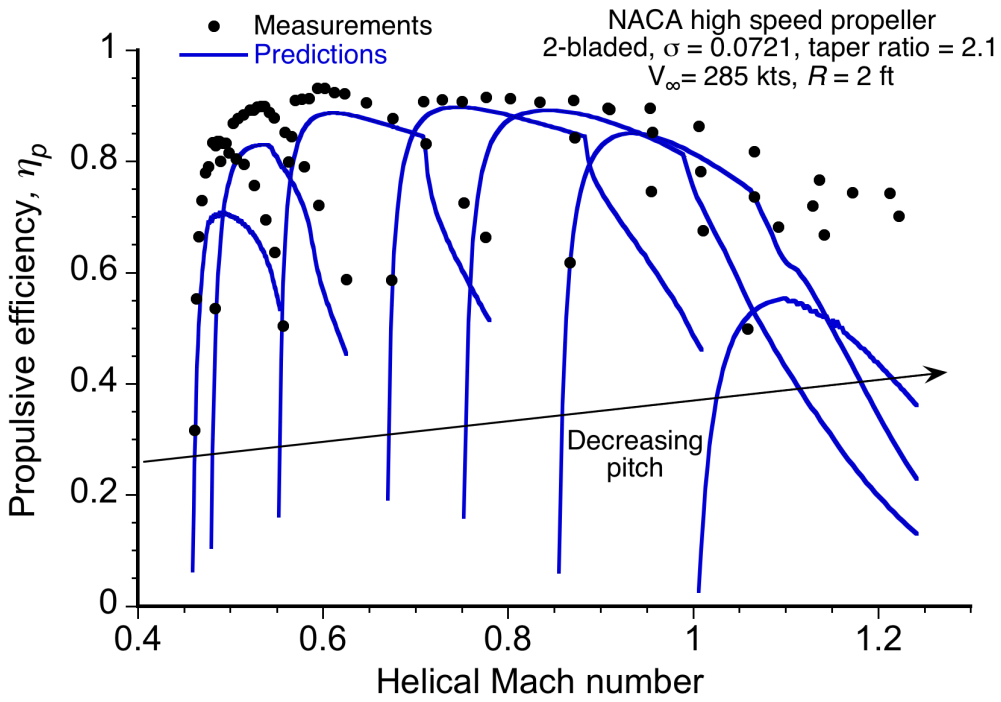

Figure 3.5: Propulsive efficiency versus helical tip Mach number for the 2-bladed NACA propeller.

overall agreement between the modeling and the measurements; in many cases the agreement is excellent. General predictions of propeller performance over such wide ranges of operating conditions is very challenging, and the results shown here are actually very good relative to what would be obtained by using *any* model of propeller performance. Recall that these particular propeller data are useful for the validation of the present model because they encompass the operating conditions where an advanced proprotor may operate, i.e., at high tip speed ratios and high helical Mach numbers.

Figures 3.2 through 3.5 expose several general aspects of propeller performance. At low values of operating advance ratio the blades become partly stalled, so the propellers generate some thrust but need relatively high power. Increasing advance ratio for a fixed blade pitch causes the flow on the blades to progressively attach, causing the propellers to

produce more thrust, the corresponding initial power requirements also reaching a peak. Thereafter, the thrust and power both decrease with increasing values of advance ratio at a constant blade pitch. Eventually, as the advance ratio increases to higher values, the propeller produces near zero or negative thrust as the brake state is reached. Repeating the process for increasing values of blade pitch produces a set of curves where the brake state is reached at progressively higher values of advance ratio. Figure 3.5 illustrates how compressibility effects cause a rapid reduction in peak propulsive efficiency as the blade tips approach and exceed a helical Mach number of unity.

Overall, the predictions made for the 2-bladed propeller showed good agreement with the measurements except for at the very lowest and highest blade pitch settings. At the lowest blade pitch, this propeller actually operates with some supersonic flow, so at least some of the differences shown can be attributed to the efficacy of the assumed airfoil model (Section 2.4) in the transonic and supersonic flow regimes. The supersonic flow in this case arises because in the tunnel the wind speed was held constant while the rotational speed of the propeller was progressively increased to relatively higher values, and so low pitch settings correspond to relatively high tip speeds that reach into the supersonic regime. At the highest blade pitch settings, it can be seen that the thrust on the propeller (see Fig. 3.2) was somewhat underpredicted, and the power requirements (see Fig. 3.3) were overpredicted, which also causes the propulsive efficiency to be underpredicted (see Fig. 3.4). However, the overall performance trends shown for this 2-bladed propeller are well represented by the present level of modeling.

In addition to operating partially in the supersonic range and also at very high advance ratios, which each pose challenges for the modeling, this propeller had sectional

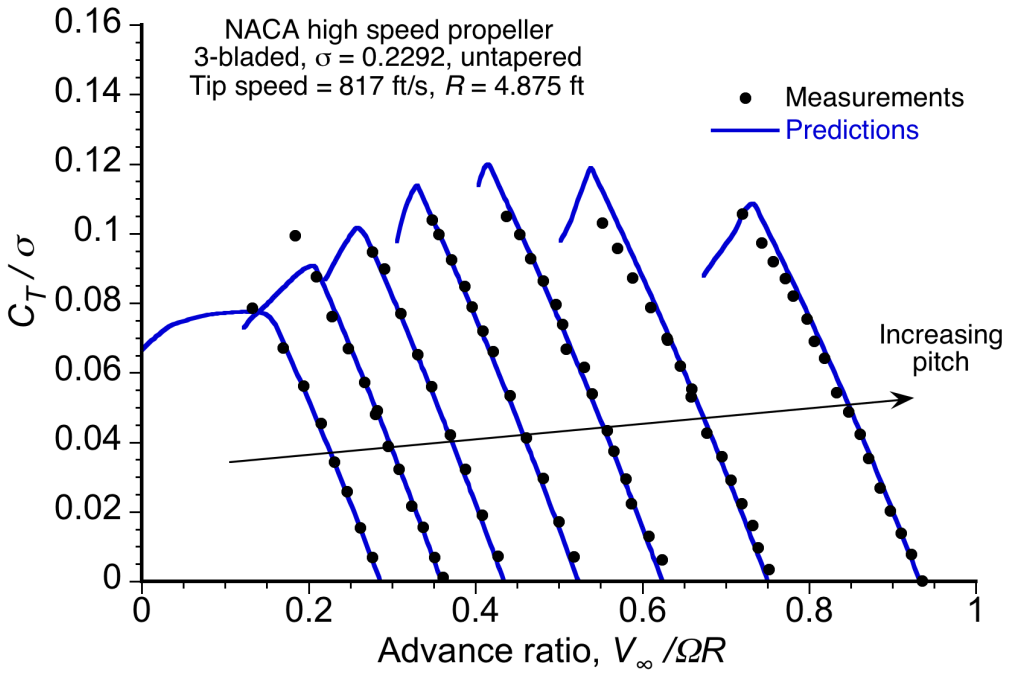

Figure 3.6: Thrust in the form of C_T/σ versus advance ratio for the 3-bladed NACA propeller.

Reynolds numbers that were lower than for the 3-bladed propeller (considered next) and so uncertainties in modeling the sectional characteristics are also higher. At lower chord Reynolds numbers, the effects of rotation of the three-dimensional boundary developments can be more pronounced, and often tend to manifest as modeling deficiencies at the higher operating thrusts [62]. However, based on the validation results shown here, the inclusion of such effects is not necessary and so no representation of rotational augmentation effects has been included into the present level of modeling.

In general, the results from the model were found to be in somewhat better overall agreement for the 3-bladed propeller, as shown in Figs. 3.6 through 3.9. In this case, the propeller operates at higher sectional Reynolds numbers, and was not tested such that it encountered significant supersonic flow at the blade tips. Therefore, the 3-bladed

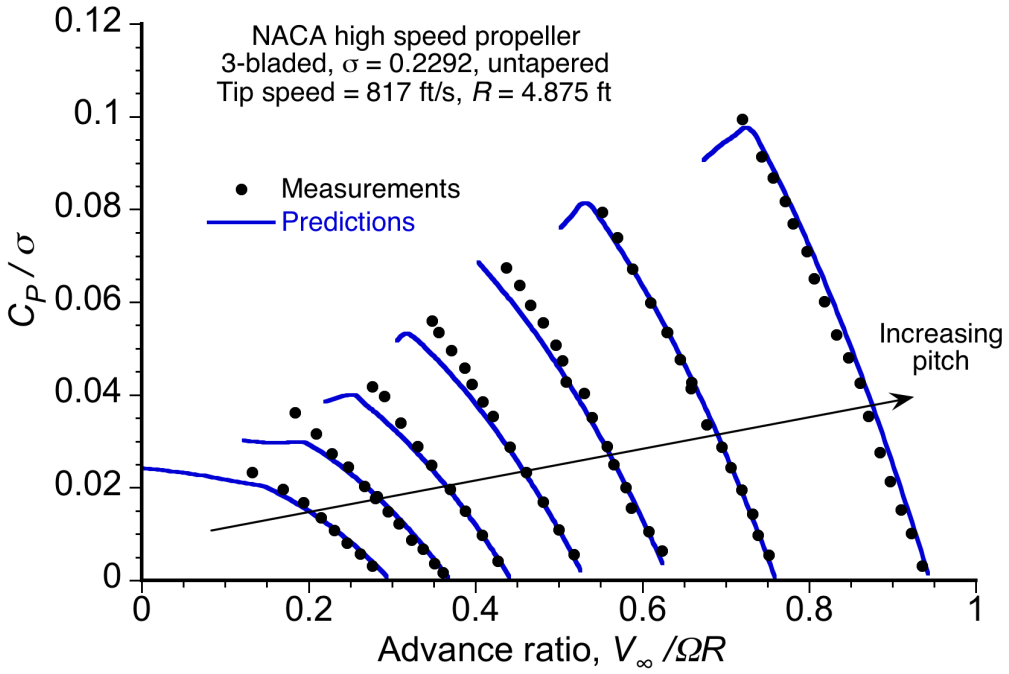

Figure 3.7: Power in the form of C_P/σ versus advance ratio for the 3-bladed NACA propeller.

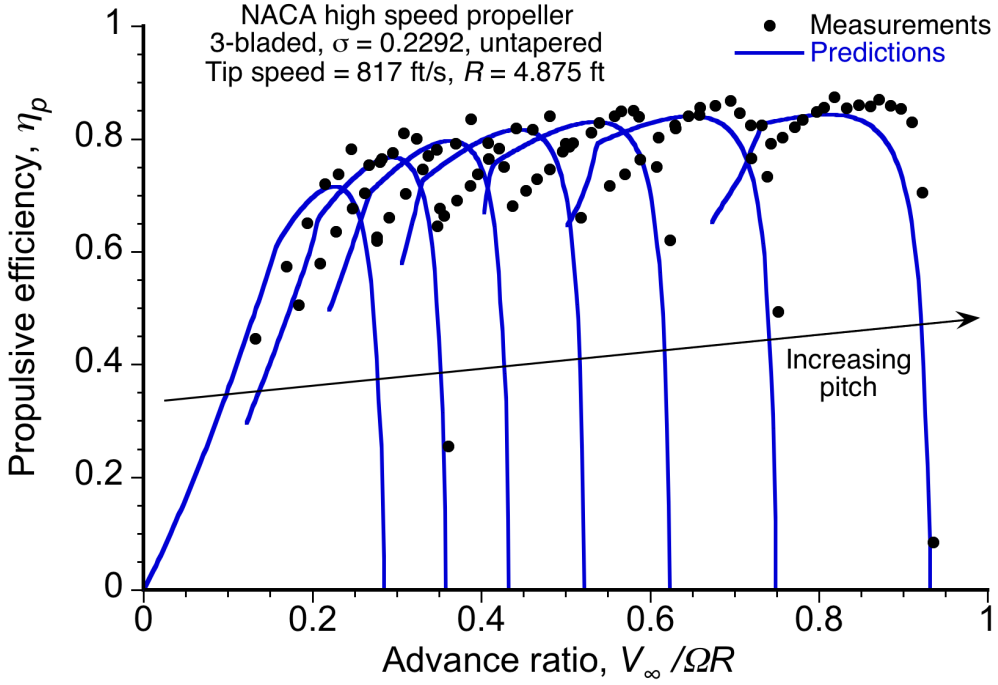

Figure 3.8: Propulsive efficiency versus advance ratio for the 3-bladed NACA propeller.

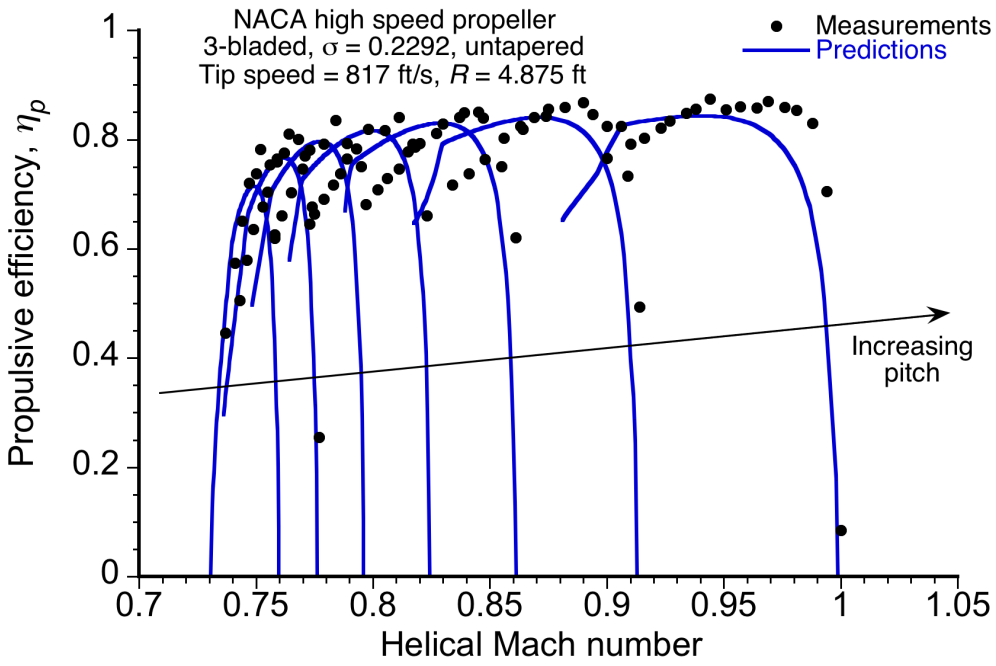

Figure 3.9: Propulsive efficiency versus helical tip Mach number for the 3-bladed NACA propeller.

propeller measurements probably serve as a better indicator of the capabilities of the present model over the expected range of its normal usage.

Notice again in this case, the sensitivity of the propulsive efficiency (shown in Fig. 3.8) to small differences in the prediction of thrust and power. This outcome arises because the predictions of the sectional airloads are sensitive to the angles of attack of the local blade sections. It is also apparent that, in this case, the measured efficiency curves in Fig. 3.8 tend to be fairly peaky compared to those seen for the 2-bladed propeller (c.f., Fig. 3.4). For a fixed blade pitch, these peaks are bounded on one side (i.e., at lower values of advance ratio for a given blade pitch) by losses of efficiency resulting from some sections that operate away from their best lift-to-drag ratios and other sections that begin to encounter blade stall, and on the other side (i.e., at higher values of advance ratio) by

the build up of compressibility effects from the growing helical Mach numbers over the blade tips.

The differences shown in the previous plots between the outcomes from the model and the measurements can be attributed to several sources, and are not just limited to the assumptions and/or simplifications that are involved in the aerodynamic modeling of the airfoil sections. For example, discrepancies can obviously arise because of deficiencies in predicting the magnitude and distribution of inflow and swirl velocities, as well as inadequate models of tip loss and tip relief effects. However, parametric studies and overall experience with the modeling has shown that the errors in the prediction of the inflow and swirl velocities will generally have the largest effects on overall performance.

For example, Figs. 3.10 and 3.11 show the effects on the thrust and power when the induced velocity components are systematically excluded. In this case, results for several values of blade pitch have been omitted to preserve clarity. When both the induced inflow, w_i, and the swirl, u_i, are removed from the inflow angle calculations, it is clear that both the thrust and power are significantly overpredicted at all blade pitch values and advance ratios. At lower advance ratios, the effects of the inflow velocities tend to be more important than swirl. However, at higher advance ratios, the need to include both the inflow and the swirl velocity components is clearly critical if good quantitative predictions of performance are to be obtained. In this regard, neglecting the swirl velocities [26], or assuming uniform induced inflow velocity, or both [63], is clearly inappropriate even at higher airspeeds where the induced velocities become a smaller fraction of the total sectional velocities.

Although neglecting certain components of the induced velocity and/or their distri-

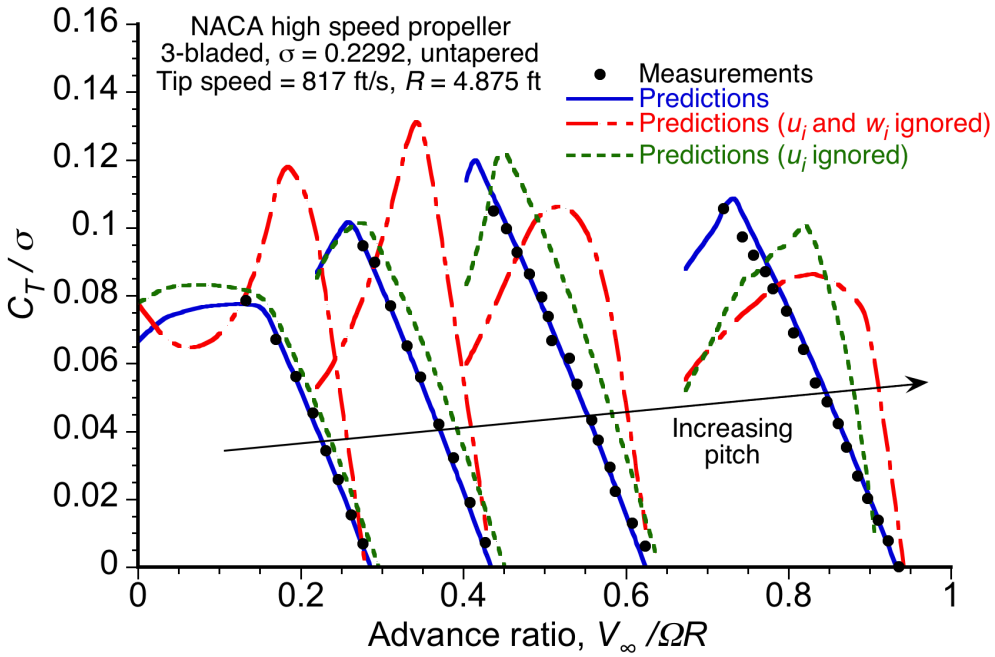

Figure 3.10: Effect of inflow and swirl velocities on the predicted thrust of the NACA 3-bladed propeller.

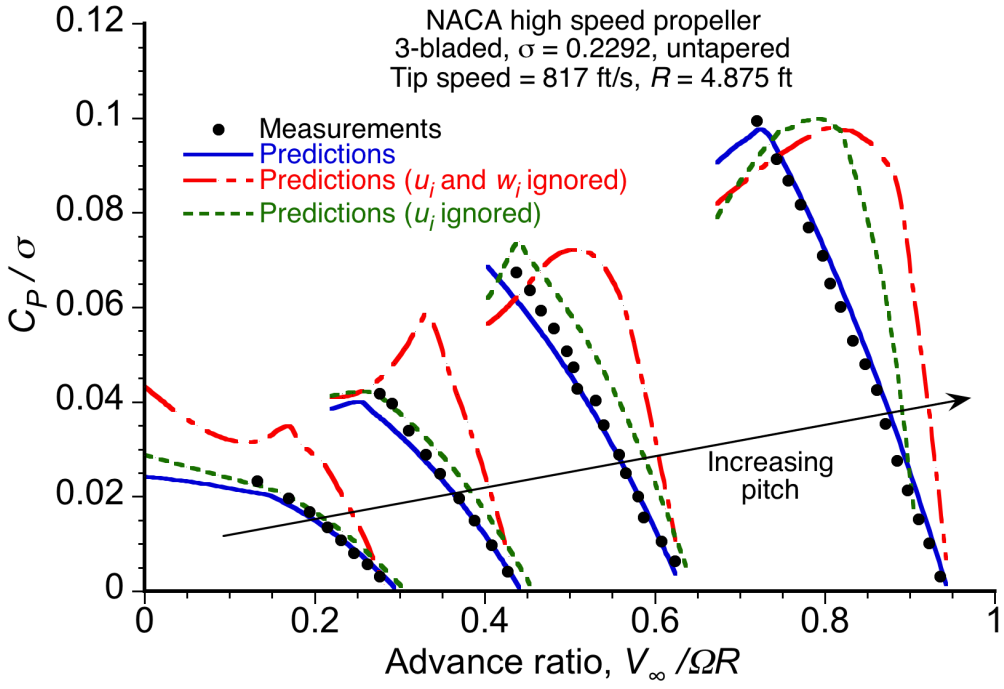

Figure 3.11: Effect of inflow and swirl velocities on the predicted power of the NACA 3-bladed propeller.

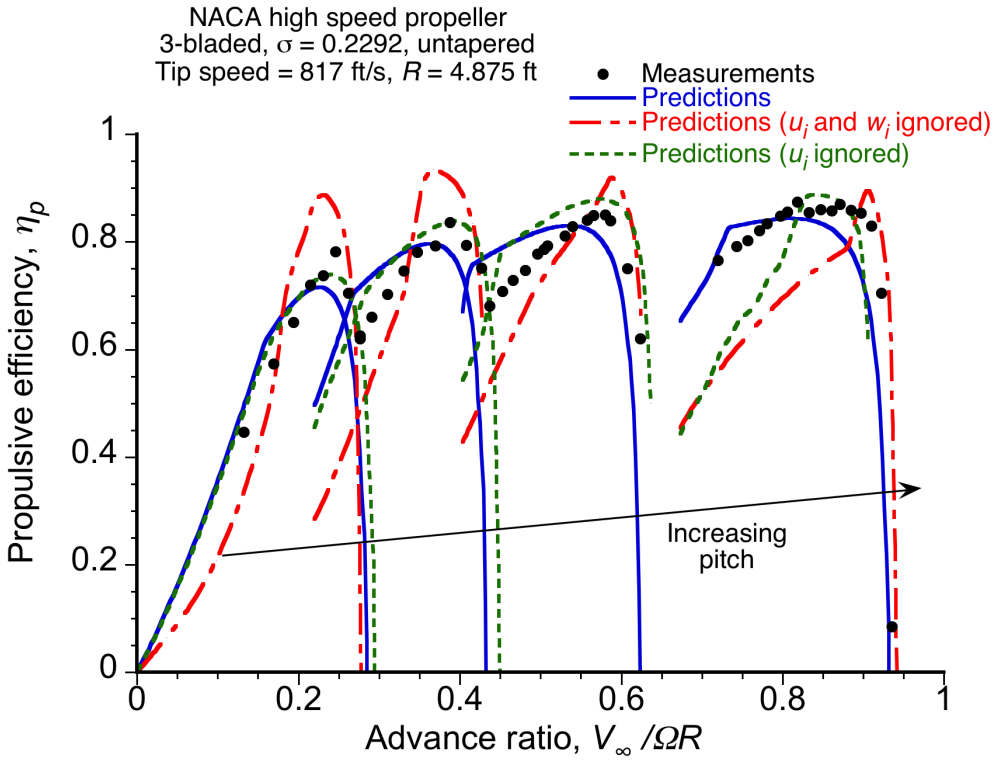

Figure 3.12: Effect of inflow and swirl velocities on the predicted propulsive efficiency of the NACA 3-bladed propeller.

butions results in overpredictions of thrust and power, reasonable efficiency predictions may still be obtained. Propulsive efficiency, i.e., $\eta_p = TV_\infty/P$, may be insensitive to overpredictions of thrust and power if they are both overpredicted by the same relative amount. Figure 3.12, however, shows that this outcome is not the case, at least when the induced velocity is completely removed from the calculations of inflow angle. If only the swirl component, u_i, of the induced flow is ignored, then the predictions are still in good agreement with the measurements, but only for advance ratios lower than about 0.7.

Figure 3.13 helps to explain the sensitivity of the predictions to the induced flow components. When the induced velocities are completely removed, the inflow angle at the blade is the free-stream inflow angle $\phi_\infty = \tan^{-1}(V_\infty/\Omega y)$. In practice, ϕ is between ϕ_∞

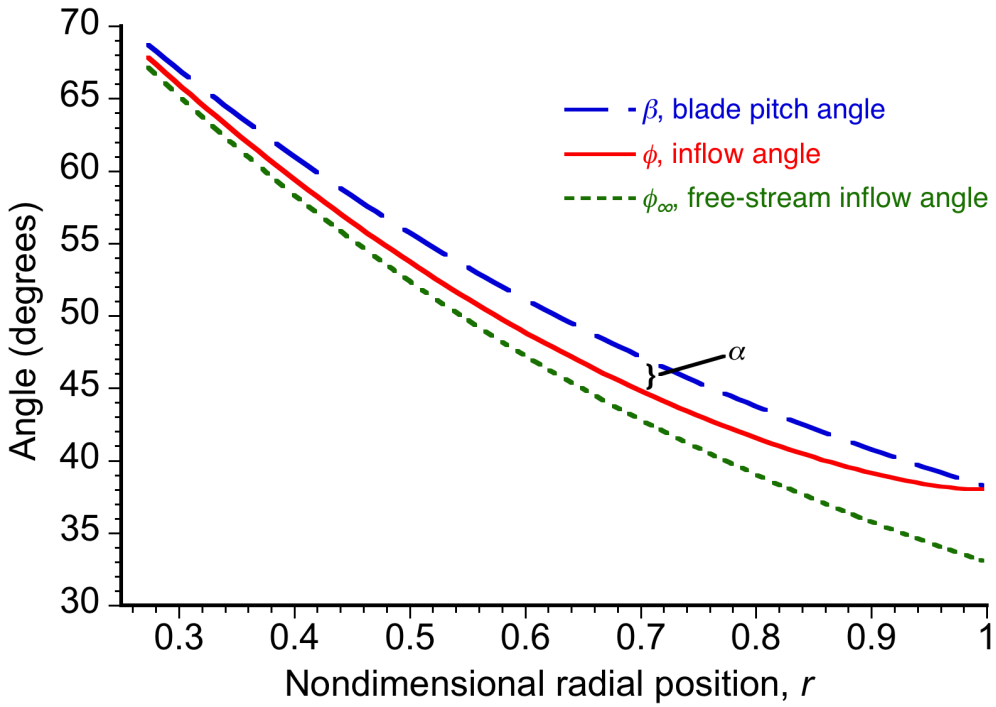

Figure 3.13: Example of the distribution of inflow across the blade span. NACA 3-bladed propeller at 315 kts.

and β across the entire blade, and approaches β near the tips because of the induced effects of the tip vortices (i.e., no lift is generated at the blade tips). The assumption that $\phi = \phi_\infty$ results in overpredictions of the angles of attack, and consequently overpredictions of both thrust and power occur. Ignoring only the swirl velocity, u_i, also results in overpredictions of sectional angle of attack, which in this case increase with increasing advance ratio. As advance ratio increases, so also does the component of lift that is parallel to the plane of rotation, which means that the inclusion of the swirl velocity becomes increasingly important under these conditions.

Spanwise loadings were also calculated to gain further insight into the overall aerodynamic behavior of the propellers, and to check that the results from the modeling were in accordance with physical expectations based on the sectional aerodynamic models. For

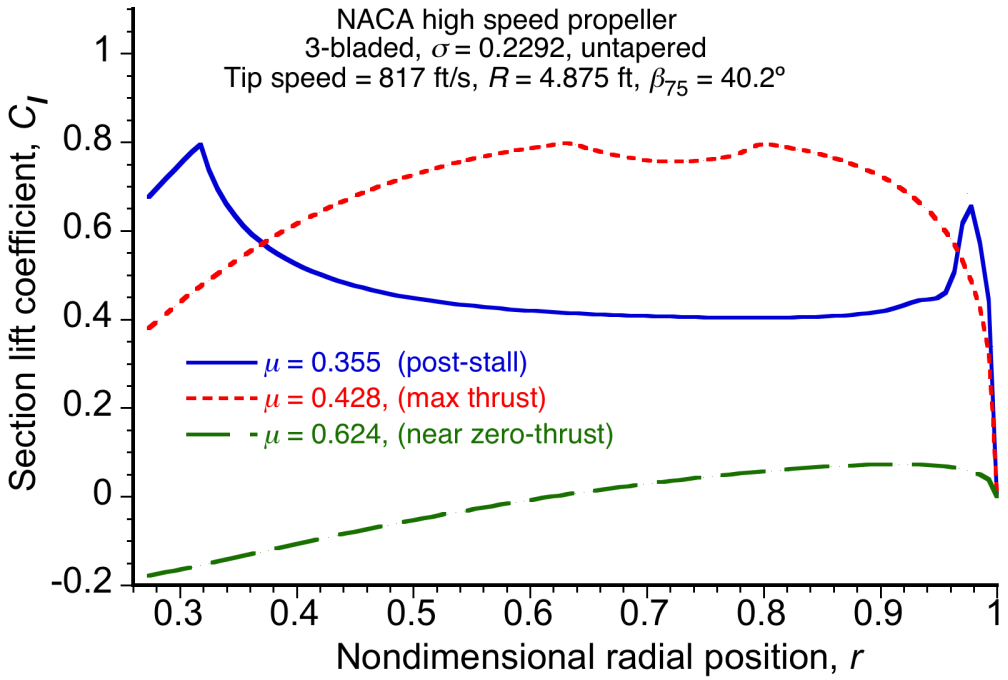

Figure 3.14: Spanwise distributions of sectional lift coefficients on the NACA 3-bladed propeller at three operating states.

example, Figs. 3.14–3.16 show the spanwise lift coefficients, thrust gradings, and power gradings for the 3-bladed propeller at a specific blade pitch and for three different vehicle advance ratios.

Under normal operating conditions the loadings over the blade are smooth, peaking up toward the tip region. When operating closer to maximum thrust conditions, the blades in this case can be seen to be stalled between radial stations $0.63R$ and $0.79R$, as indicated by the loss of sectional thrust and a corresponding increase in sectional power. For the post-stall condition, the entire blade is stalled except for small regions near the root and tip where the induced inflow is high. Interestingly enough, the stalled sections actually experience a reduction in power required, which arises because of the large decreases in the sectional components of induced drag at this stalled operating condition.

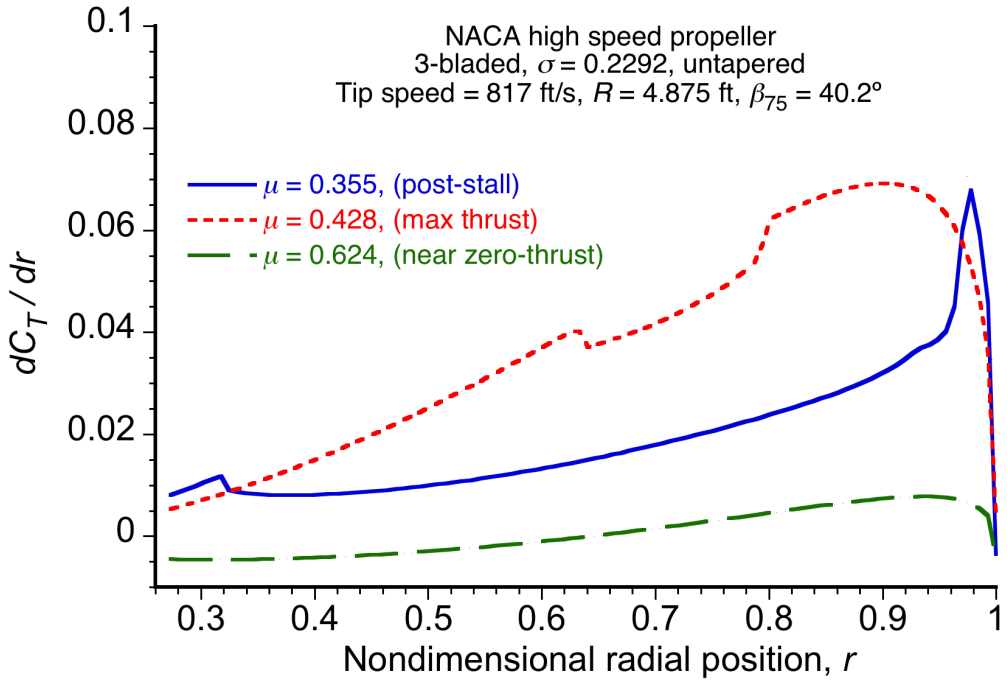

Figure 3.15: Spanwise distributions of thrust on the NACA 3-bladed propeller at three operating states.

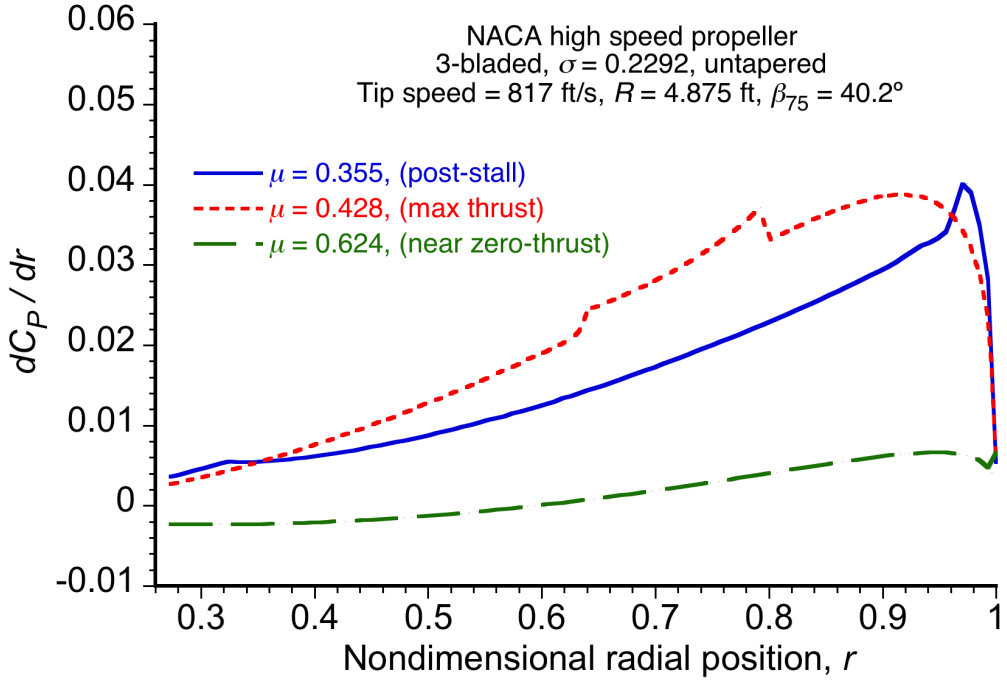

Figure 3.16: Spanwise distributions of power on the NACA 3-bladed propeller at three operating states.

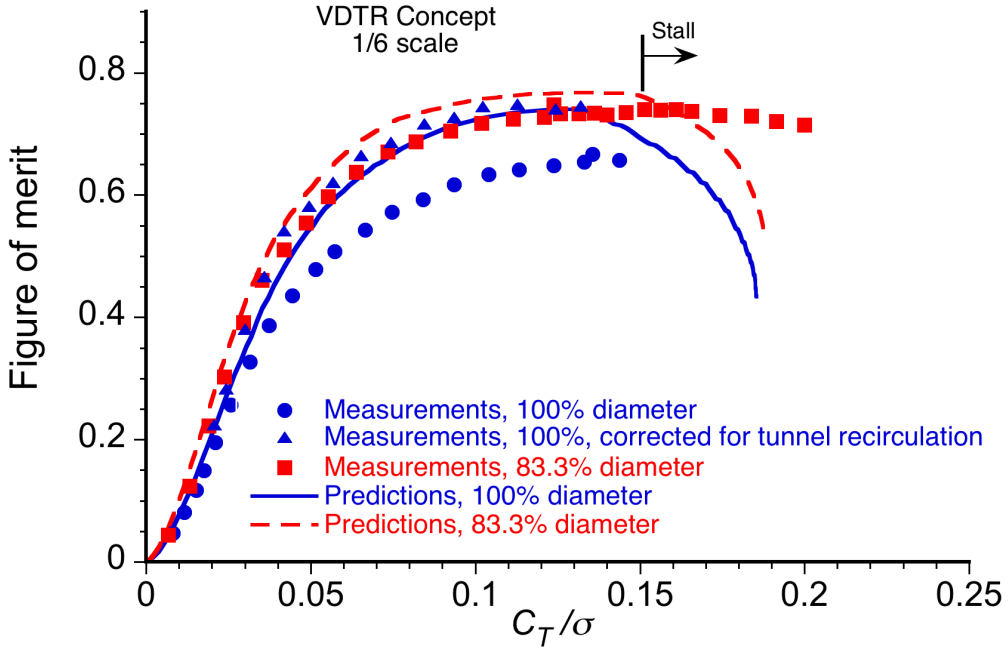

Figure 3.17: *FM* versus C_T/σ for the VDTR concept.

3.2.2 Validation for the VDTR Proprotor

Relatively little published data are available that document measured proprotor performance over the broad range of forward flight conditions that was used previously for the NACA high-speed propellers. Wind tunnel tests of the 1/6-scaled proprotor of the Sikorsky VDTR concept [28] are the only source of variable diameter proprotor data available to date. As shown in Fig. 3.17, predictions obtained using the present model were found to overpredict the figure of merit of the scaled VDTR proprotor in hover. However, after being corrected for recirculation effects in the wind tunnel by subtracting climb power increments from the measured power (see Ref. 28 for details), the measurements agreed much better with the predictions.

A comparison of the predictions of propulsive efficiency against the measured data is shown in Fig. 3.18. The model agrees with the measured data at lower values of thrust

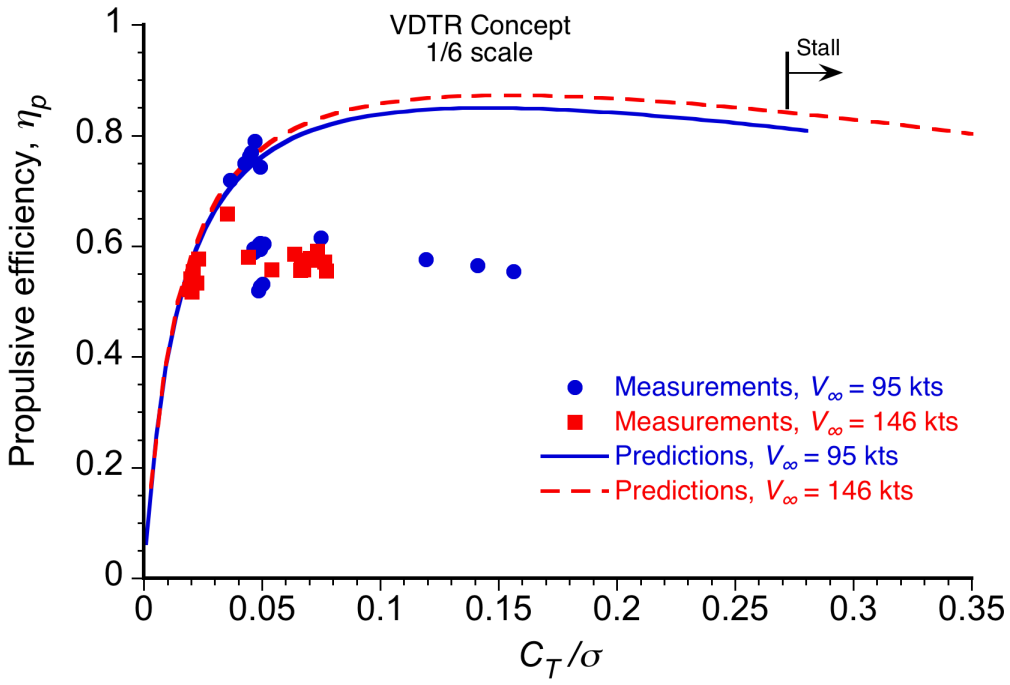

Figure 3.18: Propulsive efficiency versus C_T/σ for the VDTR concept.

(or C_T/σ), but overpredicts efficiency at higher levels of C_T/σ. However, there remains some concern as to whether the measured data for forward flight conditions is entirely correct and consistent. For example, some of the published data in Ref. 28 reports propulsive efficiencies in excess of unity, which is obviously incorrect. To this end, further work must be done to reconcile these particular experimental results before further comparisons of the measurements with the modeling would be productive.

3.2.3 Validation with CR Vehicle Performance

To examine the ability of the proprotor model to calculate performance data when coupled to an airframe, the model was validated against available performance charts for a medium-lift tiltrotor [55]. Comparisons of the published data against predictions using the present model for hover ceiling, cruise flight envelope, and payload/range are shown

in Figs. 3.19 through 3.21. The airframe and wing characteristics, as well as the engine and transmission operational states, were all estimated from the available data. Some of the characteristics of this configuration are shown in Table 3.1. Recognizing that most of the vehicle characteristics could only be estimated, the predictions made by the present model were found to be in good agreement with the available data.

In the validation conducted for the medium-lift tiltrotor, atmospheric conditions were modeled as functions of altitude to obtain the correct air density. In the International Standard Atmosphere (ISA), the air pressure, p is calculated according to

$$\frac{p}{p_0} = \left(1 - 6.876 \times 10^{-6} h\right)^{5.265} \tag{3.6}$$

where h is the altitude in feet and $p_0 = 2116.4$ lb/ft^2 is the pressure at mean sea level (MSL). Temperature in the standard atmosphere is a linear function of altitude and is expressed as

$$T = 59 - 0.00357\,h \tag{3.7}$$

where T is in °F and h is in feet. From Eqs. 3.6 and 3.7, the air density, ρ, can be calculated according to the ideal gas law, i.e.,

$$\rho = \frac{p}{RT} \tag{3.8}$$

where R is the gas constant for air, and is equal to 1,716.5 ft·lb/slug°R. Although air density in the standard atmosphere can be calculated directly as a function of altitude, Eqs. 3.6–3.8 allow density to easily be found for instances where the temperature varies from ISA conditions.

Some interesting general characteristics of CR vehicle performance are exposed in these results. For the speed/density altitude flight envelope chart shown in Fig. 3.19, there

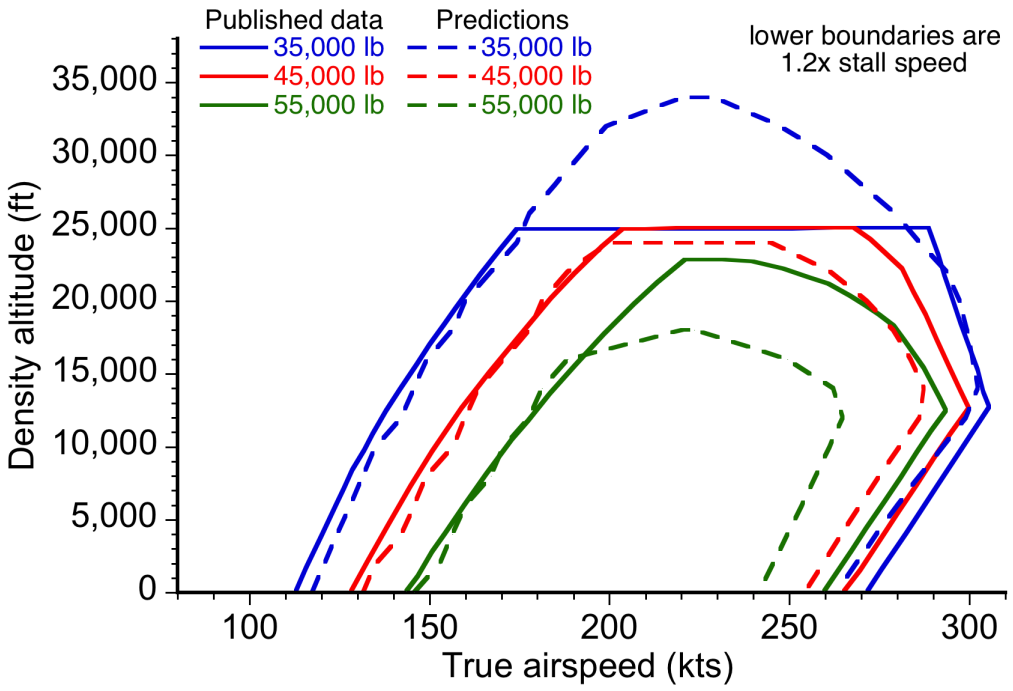

Figure 3.19: Cruise flight envelope of the medium-lift tiltrotor.

is a knee in the curves at the high-speed boundaries, indicating by which mechanism the maximum level flight speed of the aircraft becomes limited. At lower altitudes, the maximum speed is limited by reaching the transmission torque limit. At higher altitudes, the maximum speed of the aircraft becomes limited simply by the maximum continuous (installed) power that is available from the engines.

The predictions for payload/range also show good agreement with the available data, as shown in Fig. 3.20. The range predictions were generated according to the Breguét range equation [64], which defines the flight range, $\mathcal{R}$, as

$$\mathcal{R} = \int_{W_1}^{W_0} \frac{\eta_p}{\mathrm{SFC}} \left(\frac{L}{D}\right)_{\mathrm{veh}} \frac{dW}{W} \tag{3.9}$$

where W_0 is the initial gross weight and W_1 is the weight after fuel is burned off. Vehicle weight and the speed for best range both change during flight as fuel is burned off, making the solution to Eq. 3.9 complicated because propulsive efficiency, SFC, and L/D are not

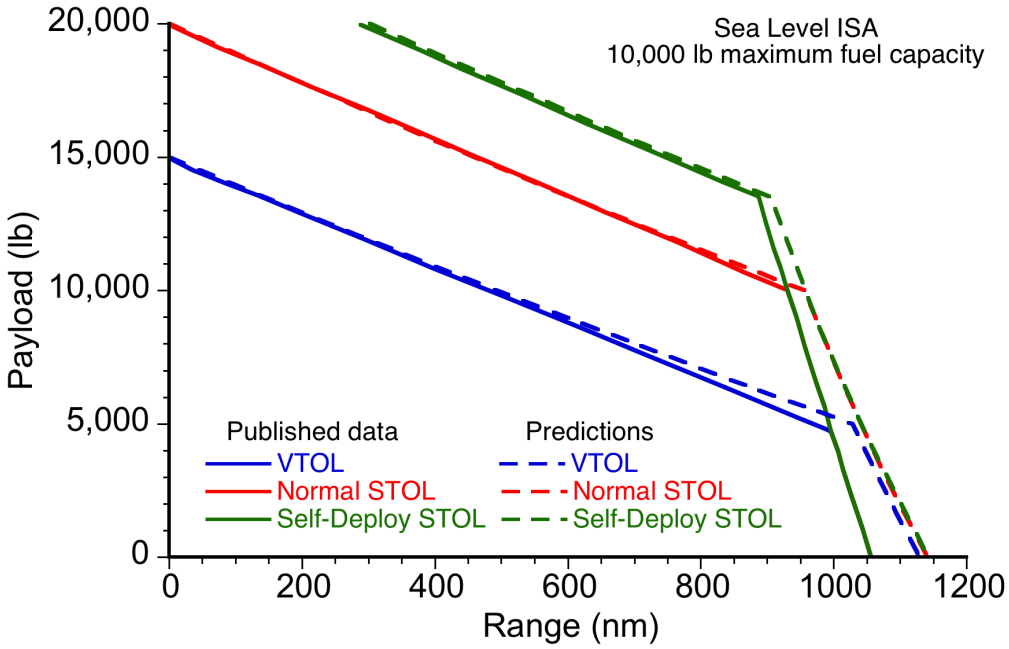

Figure 3.20: Payload/range of the medium-lift tiltrotor.

constant with speed and weight. Equation 3.9 can be approximated numerically as a sum, i.e.,

$$\mathcal{R} = \sum_{i=1}^{n} \left(\frac{V_\infty}{\mathrm{SFC}\, P} \right)_i \frac{W_0 - W_1}{n} \tag{3.10}$$

where n is the number of divisions for total fuel weight; a higher value of n results in a better approximation to the integral. Engine SFC was estimated at a fixed value of 0.35 $\mathrm{lb\,hp^{-1}hr^{-1}}$ for the predictions in Fig. 3.20, but the results show the ability of the present model to predict the power requirements and fuel burn in forward flight.

For the hover ceiling performance shown in Fig. 3.21, the knee in the predicted curve delineates two performance limits: one at lower gross weights where the maximum hovering altitude corresponds to the maximum thrust achievable by the proprotor before it begins to stall, and one at higher gross weights where the hover ceiling is determined by reaching a power limit. Such characteristics are not necessarily demonstrated by all CR aircraft and/or proprotor designs, but they do show how the maximum hover altitude on a

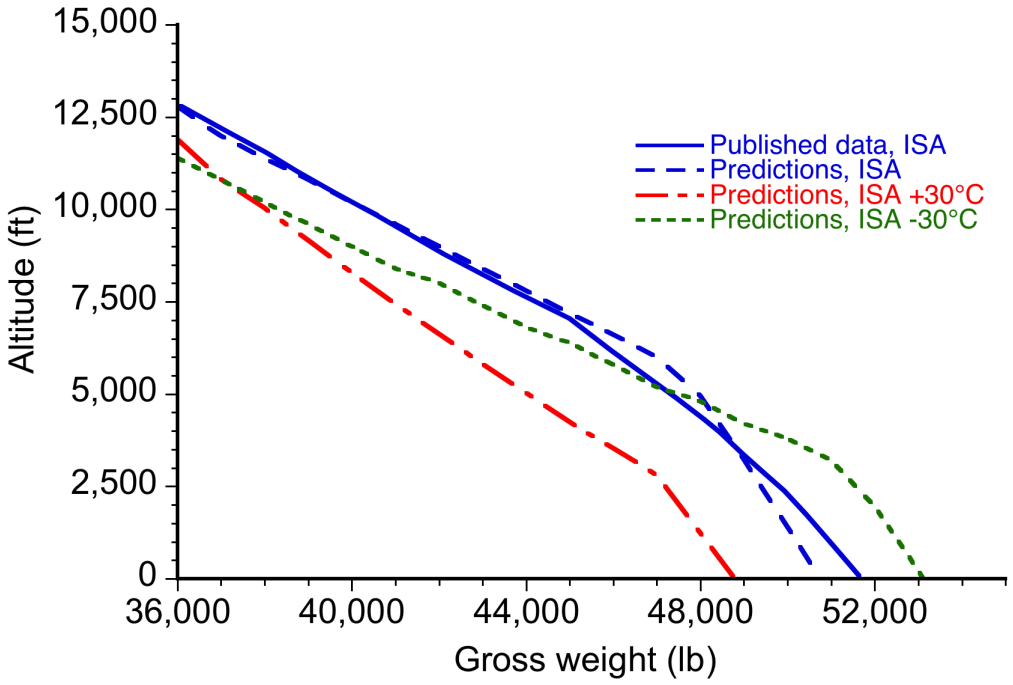

Figure 3.21: Hover ceiling of the medium-lift tiltrotor.

CR aircraft can be limited by two different mechanisms, depending on the vehicle gross weight. The trades between solidity (to improve hovering performance at higher density altitudes) and required engine power are considered later in Section 3.3.1.

Figure 3.22 shows the blade lift distributions for the medium-lift tiltrotor when at a gross weight of 38,000 lb, where the maximum hover altitude is stall limited. As altitude increases, the air density decreases, requiring higher lift coefficients to produce the same thrust. There is a stalled region on the inboard area of the blade that becomes larger as altitude increases and more blade sections begin to exceed their maximum lift coefficients. As the hover ceiling is approached, a small section near the blade tip also begins to stall. For the higher gross weights shown in Fig. 3.21, the power required exceeds the power available before the proprotor experiences significant stall.

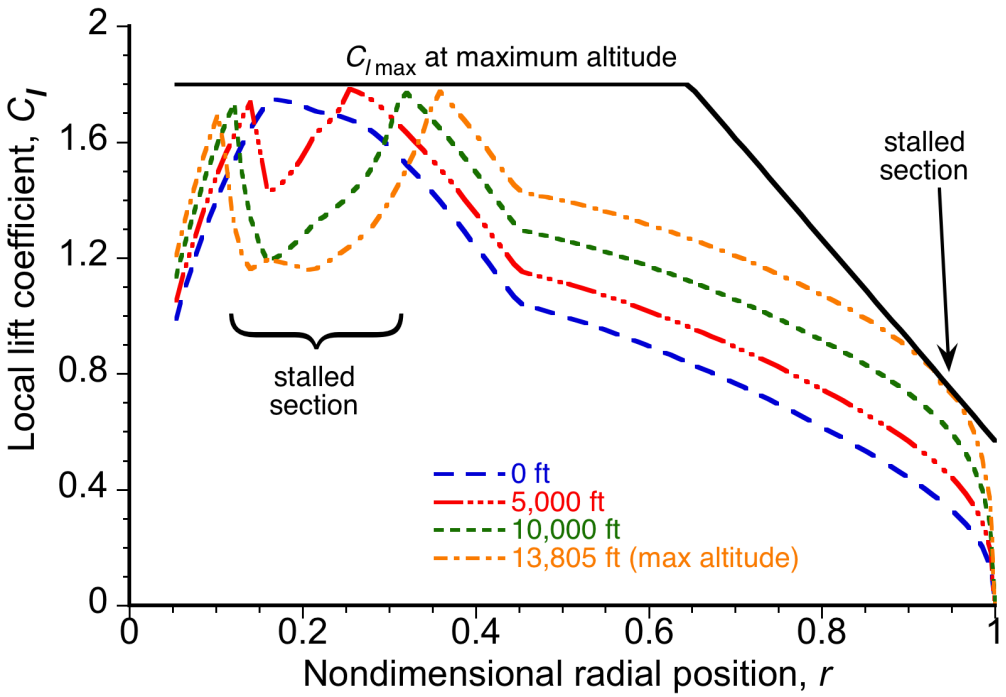

Figure 3.22: Spanwise distribution of lift coefficients for the medium-lift tiltrotor. 38,000 lb gross weight. ISA conditions.

3.3 Parametric Studies

Parametric studies were performed to determine the effects of the various proprotor blade design parameters on overall vehicle performance. While parametric variations of the design trades needed for aspects of isolated proprotor performance are also useful, ultimately the actual performance of any proprotor needs to be assessed in proper context with the flight vehicle to which it is attached.

The results in this thesis are shown primarily for the *Excalibur* CR configuration (Fig. 3.23), and also for the representative medium-lift tiltrotor considered previously, where appropriate. The essential specifications for these aircraft have been given in Table 3.1.

Variations in proprotor solidity, blade taper, number of blades, blade twist, rota-

Figure 3.23: The University of Maryland's *Excalibur* concept [56].

tional speed, diameter, blade tip sweep, and airfoil characteristics were all studied. Results were obtained for hover and forward flight over a range of vehicle airspeeds, including those in the extended regions of the expected operational and/or vehicle performance envelope. The calculations were all performed at the stated maximum vertical gross take-off weight for each vehicle.

3.3.1 Solidity

The effects of proprotor solidity on the cruise propulsive efficiency and hover power loading of the *Excalibur* concept are shown in Figs. 3.24 and 3.25, respectively. Solidity in this case was varied by changing the blade chord while keeping the diameter of the proprotor constant. Propulsive efficiency was clearly improved by decreasing the solidity, while hovering efficiency was improved by increasing the solidity. These conflicting characteristics illustrate one fundamental issue in CR design. In hover the blade sections

are operating at angles of attack above those for their best lift-to-drag ratio, $(C_l/C_d)_{\max}$, or in some cases too close to stall, i.e., at an angle of attack approaching the critical angle of attack for a given sectional Mach number. Therefore, an increase in solidity allows the blades to operate at lower angles of attack and lower lift coefficients to generate the same thrust, which improves the power loading (i.e., the overall hovering efficiency) of the proprotor.

In cruise, the proprotor is more lightly loaded relative to the hover condition (its thrust may be an order of magnitude lower near the best vehicle L/D), and generally the blades are operating at much lower average angles of attack (but not lower pitch angles). A tiltrotor may have a vehicle L/D of 10 to 12, or even more if carefully designed. Therefore, propulsive efficiency can benefit substantially by using lower values of solidity, which decreases profile power requirements (induced losses are small in this case). However, notice that decreasing solidity also decreases the airspeed at which blade stall first begins, which occurs because there is less blade area available to produce thrust and so overcome the drag of the aircraft at higher airspeeds.

Figure 3.26 shows the thrust margins for the *Excalibur* in the hover state. If solidity becomes too low or the operating density altitude is too high, then the proprotor will stall before producing enough thrust for the vehicle to hover. Recall that a proprotor needs generous stall margins in hover because the proprotors are also used for control and maneuver, e.g., there is a need for significant differential thrust between the two proprotors.

Figure 3.27 further shows the thrust margins for this proprotor in cruise. It is apparent that decreasing solidity not only reduces the maximum speed of the aircraft but also

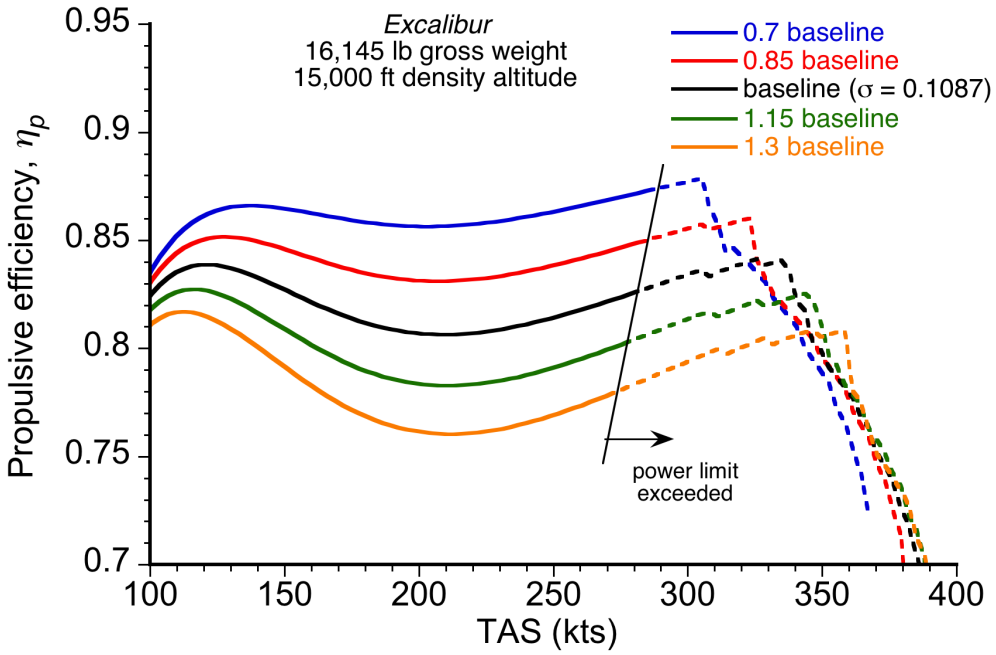

Figure 3.24: Effect of variations in solidity on the propulsive efficiency of the *Excalibur*.

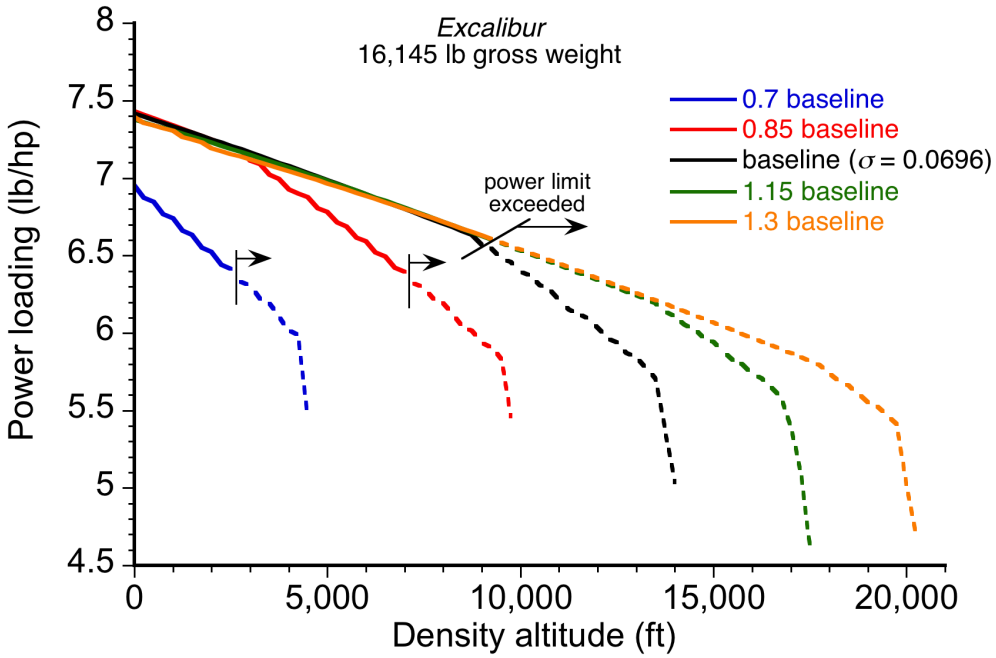

Figure 3.25: Effect of variations in solidity on the hover power loading of the *Excalibur*.

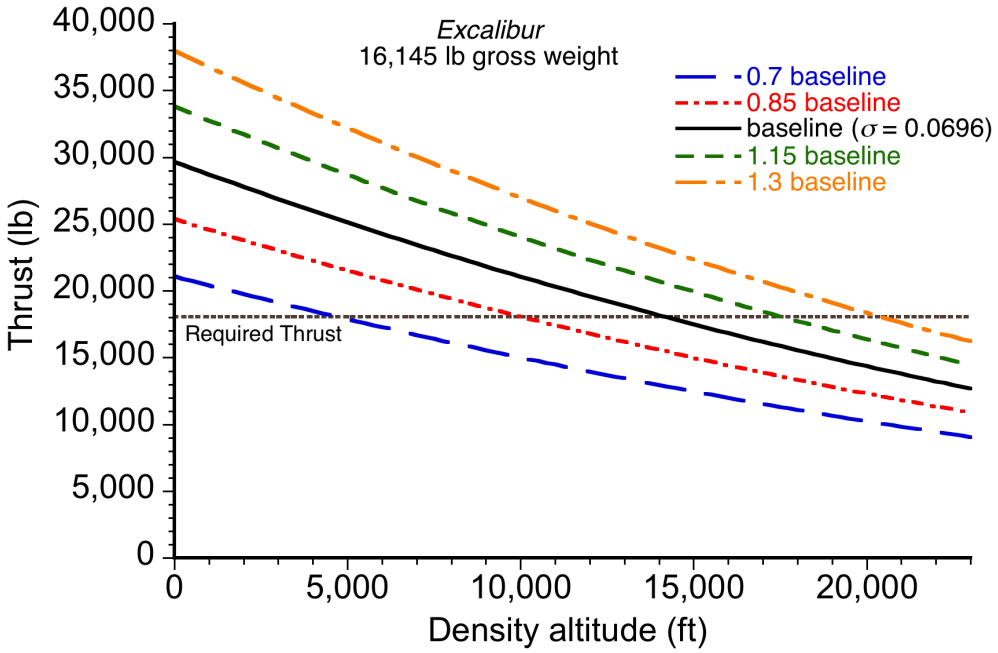

Figure 3.26: Effect of variations in solidity on the hover thrust margins of the *Excalibur*.

reduces the thrust margins when operating close to its maximum speed. Although the attainable thrust margins in both hover and cruise modes are improved markedly by increasing the solidity of the proprotor, sufficient power from the engine and/or sufficiently high transmission torque limits must also be available to allow the desired thrust margins from the proprotor to be achieved.

3.3.2 Blade Taper

The effect of blade taper ratio on cruise and hover performance is shown in Figs. 3.28 and 3.29 for the *Excalibur*. The results are all for a constant thrust-weighted solidity of $\sigma_e = 0.109$ in cruise and $\sigma_e = 0.0696$ in hover. Thrust-weighted solidities provide a way to compare proprotors with different blade planforms on the basis of the effect of planform on thrust. They allow the effects of taper to be separated from the effects of varying

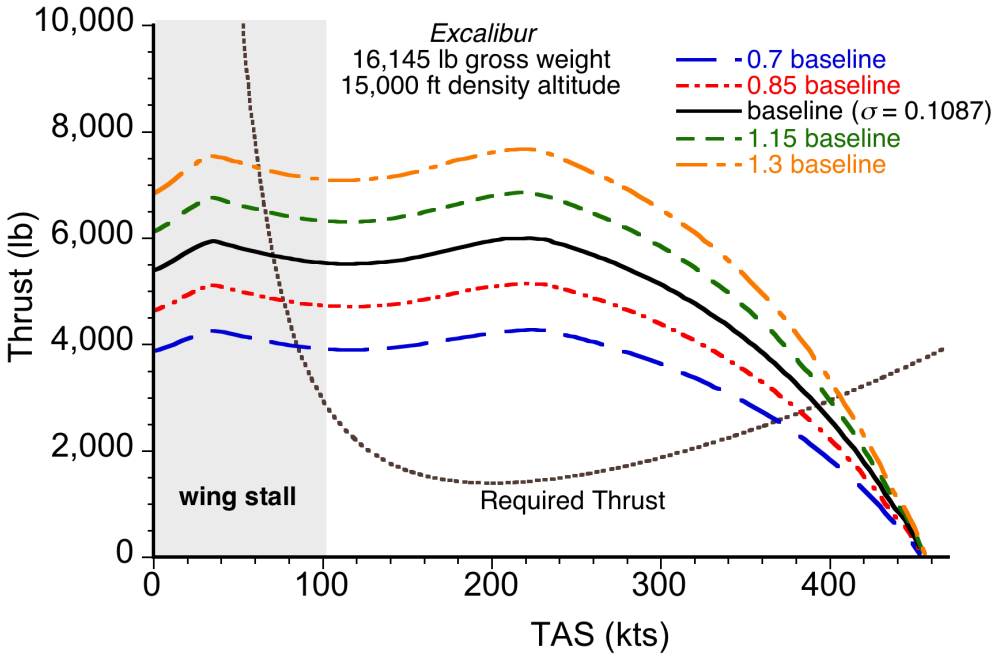

Figure 3.27: Effect of variations in solidity on the cruise thrust margins of the *Excalibur*.

blade chord. Thrust-weighted solidity is calculated as

$$\sigma_e = 3\int_0^1 \sigma r^2\, dr \tag{3.11}$$

Clearly, the r^2 term serves to weigh the solidities of the outboard blade sections more heavily than those further inboard.

Notice in Figs. 3.28 and 3.29 that an increase in blade taper ratio results in small increases in propulsive efficiency and modest improvements in power loading. Decreasing the taper ratio allows higher forward speeds to be reached before blade stall occurs. However, these results are not necessarily the best indicator of the effects of taper on proprotor performance because only the outboard region (i.e., $r > 0.84$ with the blades extended) of the blades is actually tapered; for the blade retraction mechanism to operate the inboard sections must obviously be untapered.

A better CR vehicle to illustrate the effects of blade taper is the medium-lift tiltro-

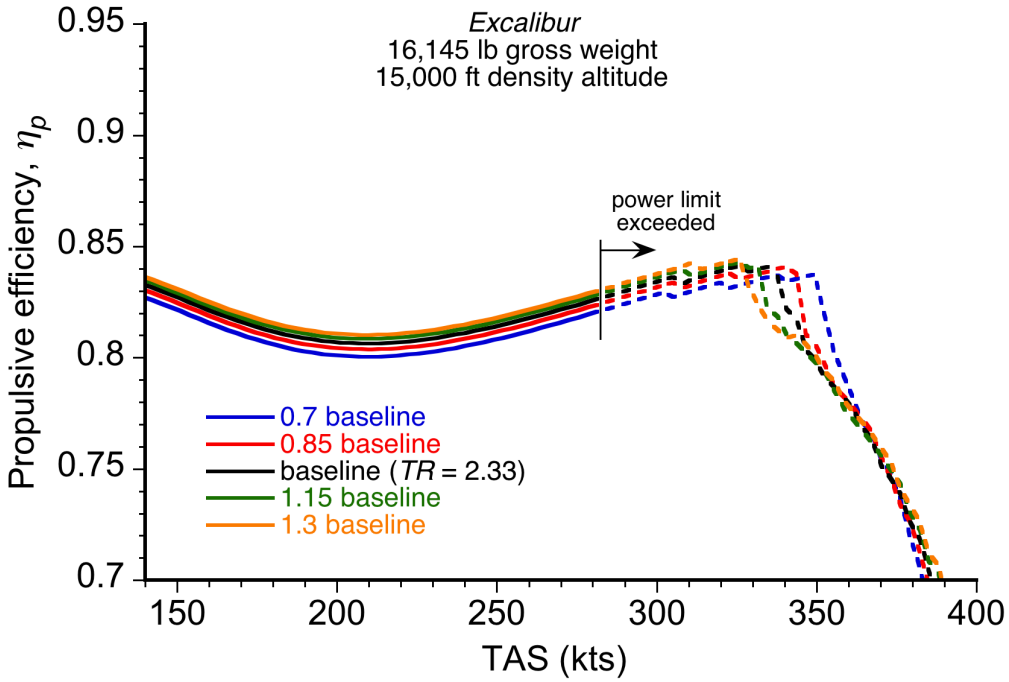

Figure 3.28: Effect of variations in blade taper ratio on the propulsive efficiency of the *Excalibur*.

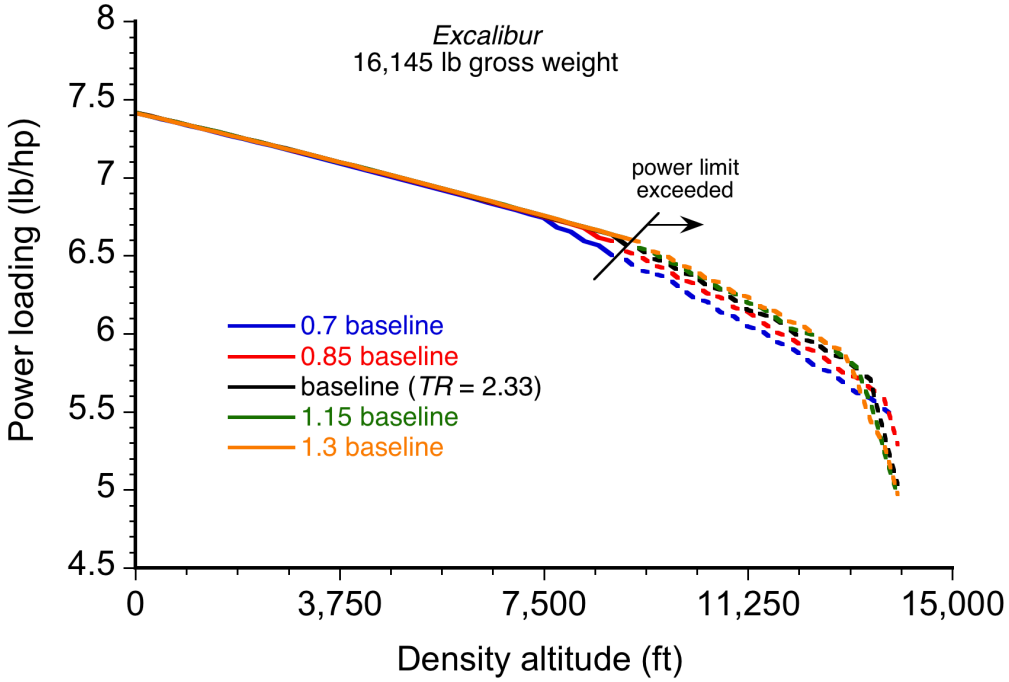

Figure 3.29: Effect of variations in blade taper ratio on the hover power loading of the *Excalibur*.

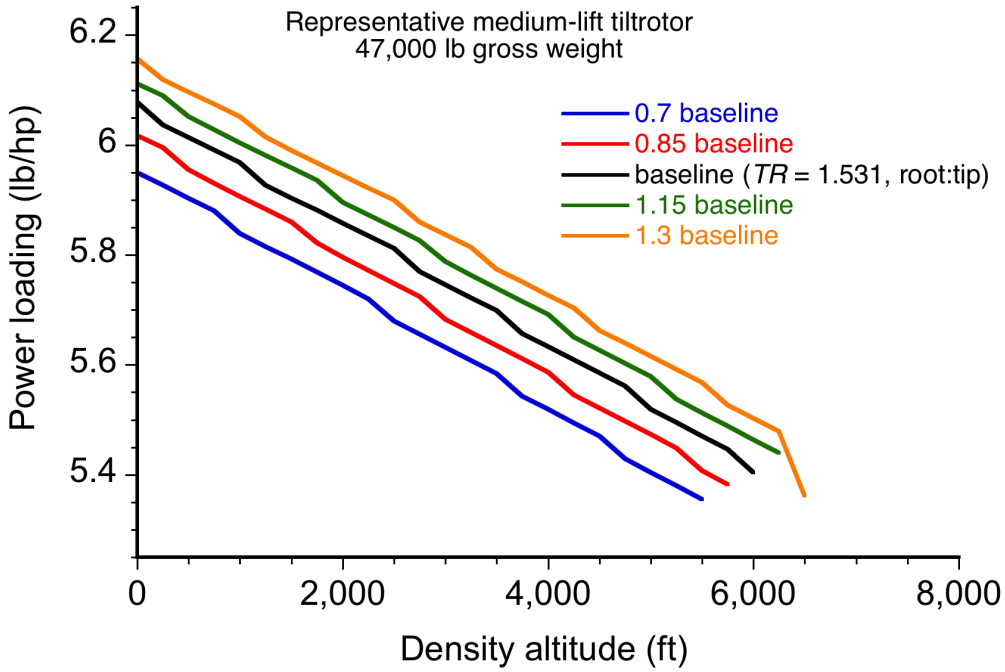

Figure 3.30: Effect of variations in blade taper ratio on the power loading of the representative medium-lift tiltrotor.

tor, results for which are shown in Fig. 3.30. For this vehicle, an increase in blade taper ratio results in more significant improvements in hover power loading. Reviewing the outcomes for the three CR configurations as a whole, increasing blade taper was found to result in only small changes in propulsive efficiency but gave more moderate improvements in hover performance. This outcome occurs because taper helps to decrease the values of C_l inboard, and brings the sections closer to their best C_l/C_d ratios and away from stall.

3.3.3 Blade Twist

Figures 3.31 and 3.32 show the effect of blade twist relative to the baseline used for the *Excalibur* design. The use of different values of blade twist clearly makes a large

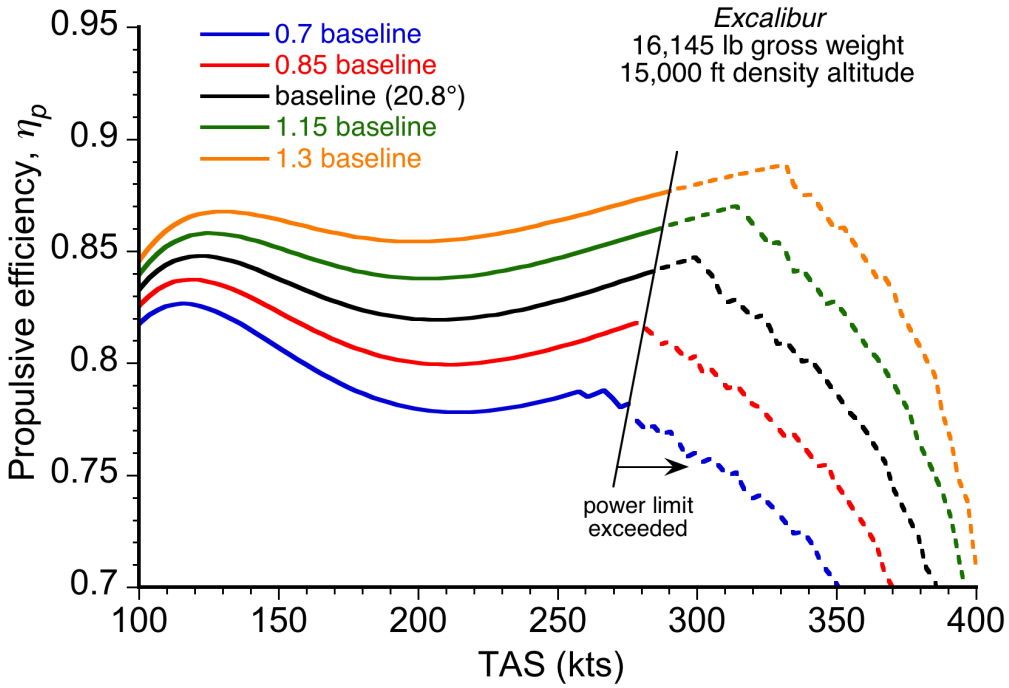

Figure 3.31: Effect of variations in blade twist on the propulsive efficiency of the *Excalibur*.

difference to both the propulsive efficiency and the hover power loading, and illustrates another significant trade in proprotor design. Using more blade twist on the proprotor allows the vehicle to fly faster and more efficiently, whereas less blade twist increases the hovering efficiency. Although a decrease in blade twist in hover increases the altitude at which the engine power limits are reached, it also decreases the density altitude at which the proprotor begins to reach its stall limits.

3.3.4 Blade Tip Sweep

Figure 3.33 shows the effect of blade tip sweep on the propulsive efficiency of the *Excalibur* concept. This blade has swept tips outboard of $r = 0.84$ in extended mode operation and outboard of $r = 0.76$ in retracted mode. Increasing tip sweep allows a moderate

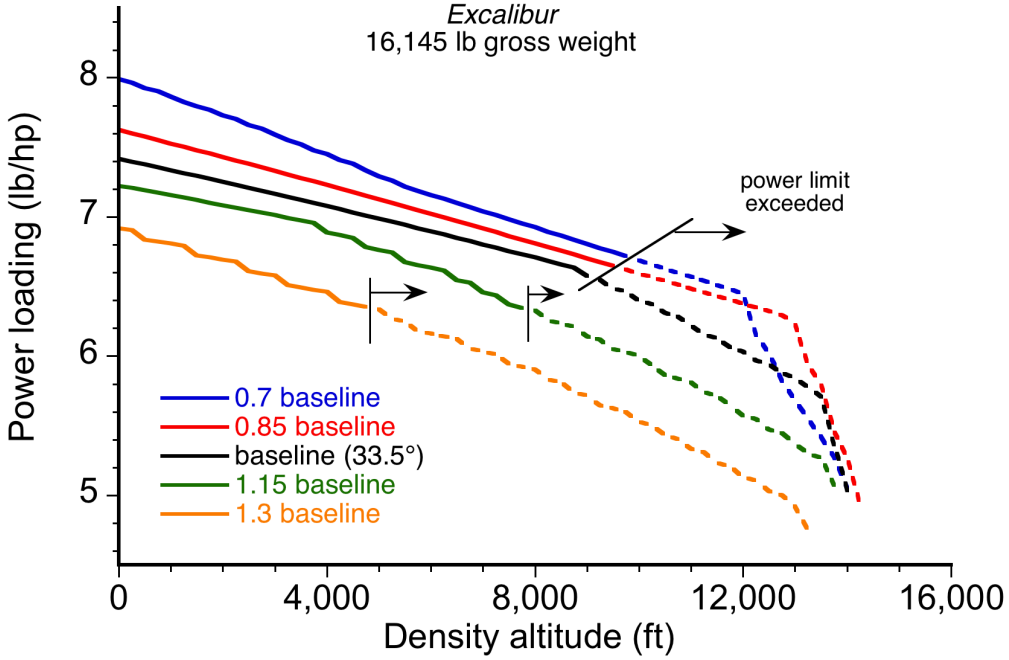

Figure 3.32: Effect of variations in blade twist on the hover power loading of the *Excalibur*.

delay in the build up of compressibility effects. However, there is not enough available power in this case to take advantage of delays in the onset of compressibility losses from the use of tip sweep. To capitalize on any potential benefits of delayed compressibility effects, the engines installed on this concept would need to be more powerful, but with the trade of driving up the empty weight fraction of the vehicle and so reducing its useful load (all other factors being held constant).

Figure 3.34 shows the effect of tip sweep on hover power loading. Increasing blade tip sweep allows the aircraft to operate at higher altitudes where the speed of sound is lower. However, as discussed previously, there is not enough available power in this case to realize this benefit.

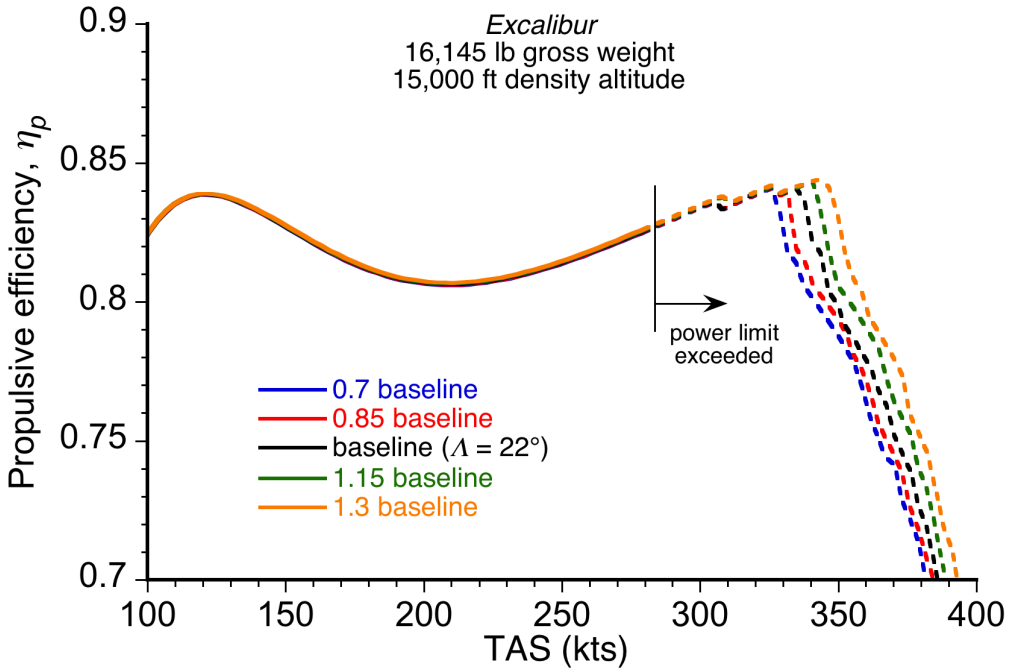

Figure 3.33: Effect of variations in tip sweep on the propulsive efficiency of the *Excalibur*.

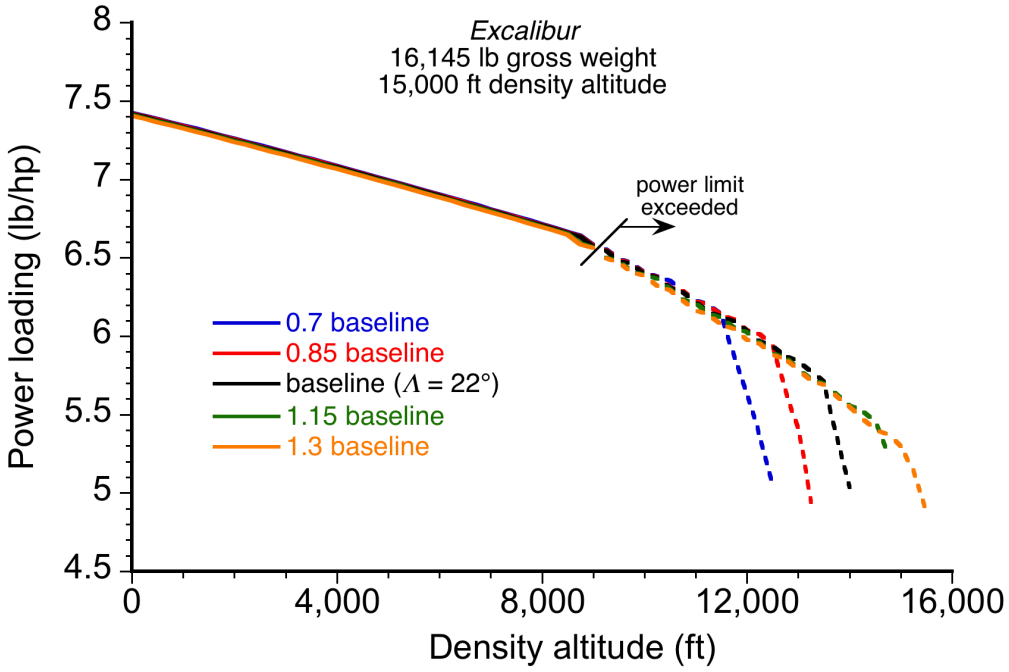

Figure 3.34: Effect of variations in tip sweep on the hover power loading of the *Excalibur*.

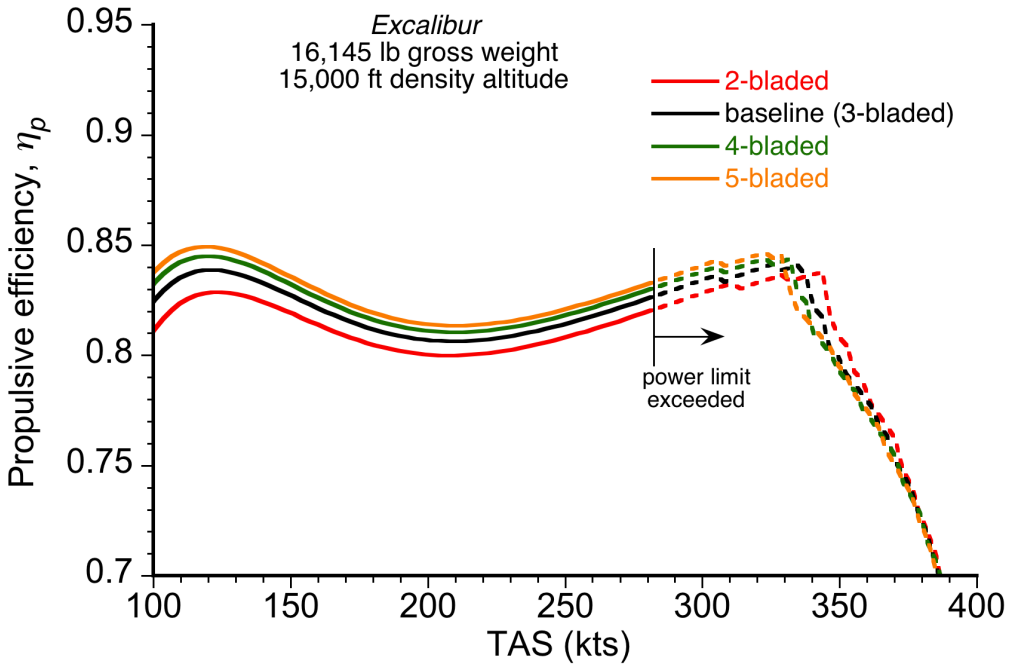

Figure 3.35: Effect of number of blades on the propulsive efficiency of the *Excalibur*.

3.3.5 Number of Blades

The effect of number of blades on proprotor performance is shown in Figs. 3.35 and 3.36. Increasing the number of blades was found to give relatively small improvements to both the hover and cruise efficiencies. Increasing the number of blades and, therefore, decreasing the spacing between adjacent vortex elements in the wake of the proprotor, will tend to reduce the tip-loss effects and so improve the overall performance of the proprotor, albeit with progressively diminishing returns. For example, there seems to be little aerodynamic advantage in using four versus three blades. This result does not necessarily mean, however, that there would not be a preference for using a larger number of blades for other reasons (e.g., dynamics, reducing vibrations, etc.).

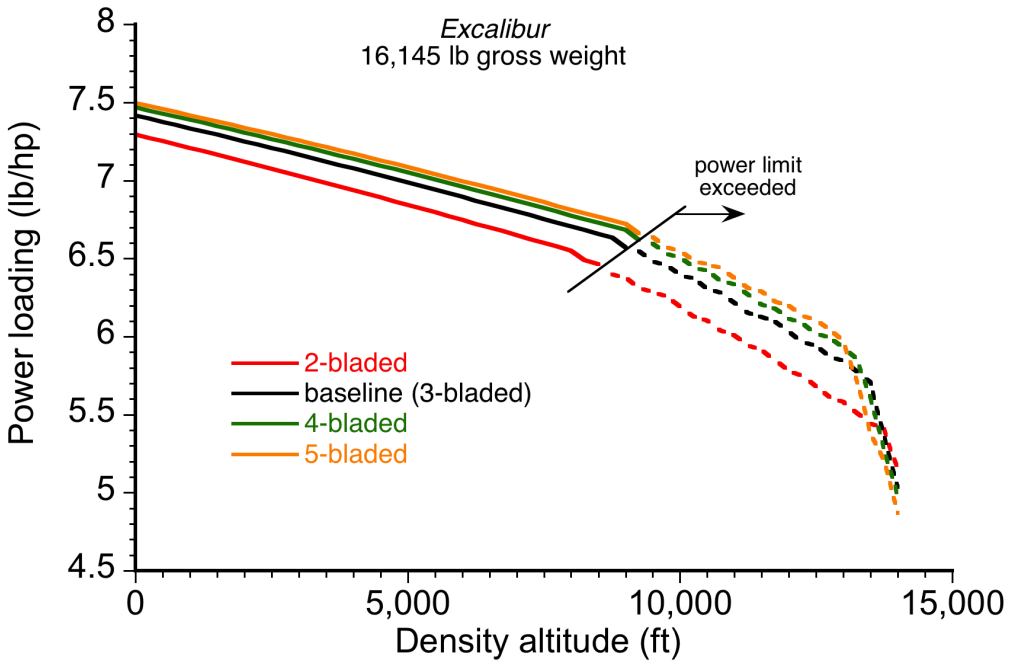

Figure 3.36: Effect of number of blades on the hover power loading of the *Excalibur*.

3.3.6 Rotational Speed

Results from the parametric study of proprotor rotational speed for the *Excalibur* CR aircraft are shown in Figs. 3.37 and 3.38. Decreasing rotational speed clearly produces a significant increase in propulsive efficiency and delays the onset of compressibility effects to higher maximum airspeeds. Figure 3.38, however, shows that reducing rotational speed can have an adverse effect on hover performance (in this case, the hover ceiling). It is also shown that increasing rotational speed decreases the hover ceiling at lower gross weights, but can extend the hover ceiling to higher maximum gross weights. In this regard, the increase in tip Mach number is a disadvantage at higher altitudes where compressibility effects manifest earlier because of the somewhat lower speed of sound (i.e., $a = 1,117$ fts^{-1} at MSL and $a = 1,037$ fts^{-1} at 20,000 ft).

While reducing the rotational speed of the proprotor can improve its propulsive

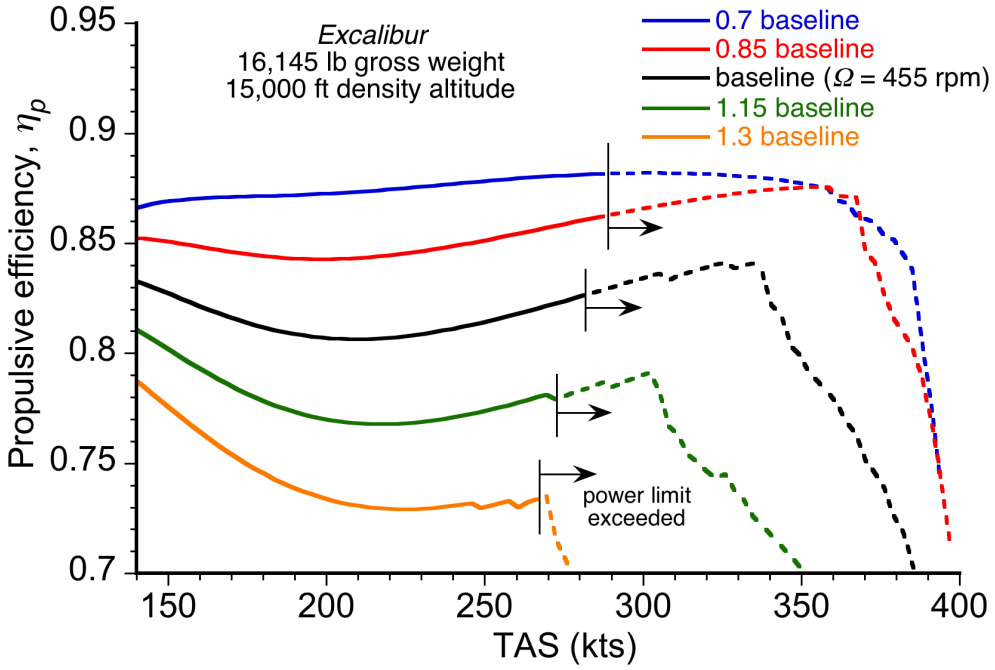

Figure 3.37: Effect of rotational speed on the propulsive efficiency of the *Excalibur*.

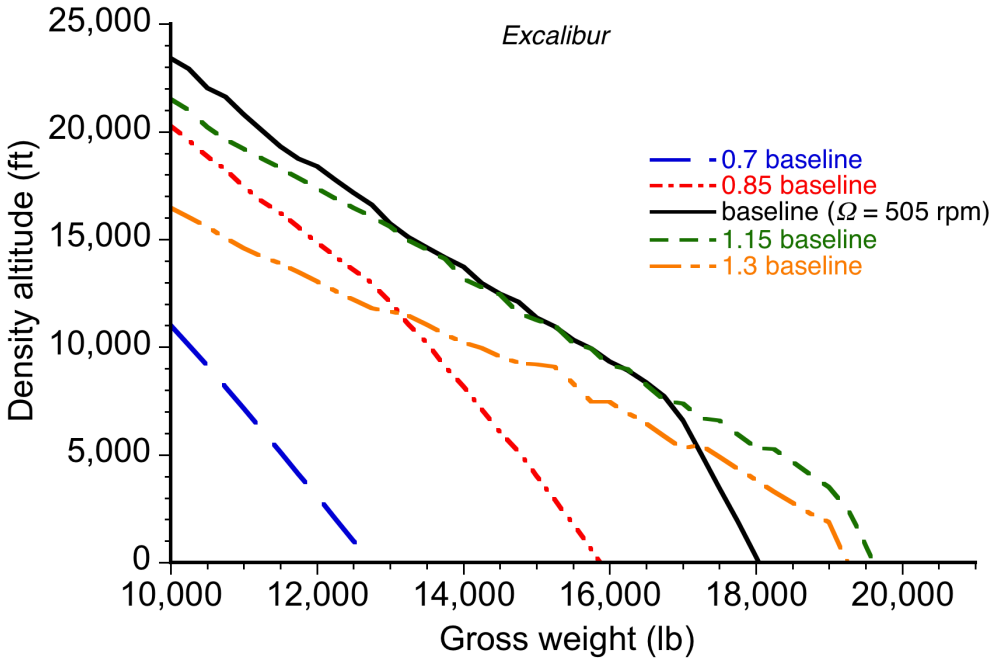

Figure 3.38: Effect of rotational speed on the hover ceiling of the *Excalibur*.

efficiency, it also increases the shaft torque for a given power requirement. Therefore, the trades in efficiency need to be examined in conjunction with any transmission limits. The representative medium-lift tiltrotor, in contrast to the *Excalibur*, has a relatively low transmission limit compared to its available engine power, which is mainly an outcome of the trade with vehicle weight.

Figure 3.39 shows that the highest aerodynamic efficiencies that are achievable by this proprotor by the use of varying rotational speed are constrained by the transmission torque limits. However, improvements are obviously possible if higher transmission torque limits were available, which must be traded against transmission weight. Reducing the rotational speed of the proprotor may also become more feasible at higher altitudes where the power available from the engine, rather than the torque on the transmission, tends to be the limiting factor that determines vehicle performance.

Although decreasing rotational speed (or tip speed in general) can increase the maximum speed of a CR aircraft by delaying the onset of compressibility to higher airspeeds, doing so also brings the proprotor closer to blade stall and decreases the proprotor thrust margins. As airspeed increases, the operating margins of the proprotor become significantly constrained between losses in performance from blade stall and the onset of compressibility, i.e., the proprotor begins to approach the "coffin-corner" operating state that was discussed in Ref. 26. In this regard, a "coffin-corner" can be reached when the boundaries between the onset of stall from changes in angle of attack and the onset of stall from increases in Mach number (i.e., shock stall) become very small. Figure 3.40 shows the upper and lower stall boundaries for variations in rotational speed, i.e., a reduction in $C_{l_{\max}}$ caused by compressibility at the upper boundary, and an increase in required lift co-

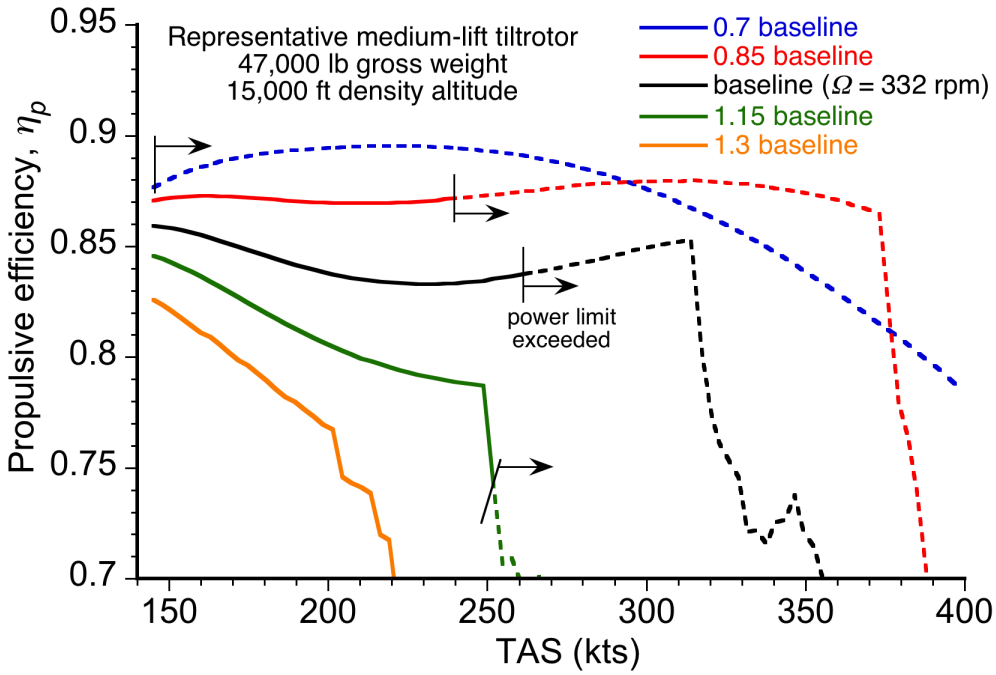

Figure 3.39: Effect of rotational speed on the propulsive efficiency of the representative medium-lift tiltrotor.

efficients at the lower boundary. Clearly, the range of feasible rotational speeds becomes smaller (and ultimately vanishes) as airspeed increases and the proprotor operates further into the "coffin-corner."

Figure 3.41 shows the proprotor rotational speeds that result in the best propulsive efficiencies. These most efficient rotational speeds are bracketed between the stall boundaries shown in Fig. 3.40, and tend to be located closer to the lower boundary.

3.3.7 Diameter

Figures 3.42 and 3.43 show the propulsive efficiency and hover ceiling of the *Excalibur* when the diameter of its proprotor is varied. For this vehicle, reducing diameter has a smaller effect on propulsive efficiency than does reducing the rotational speed. Fur-

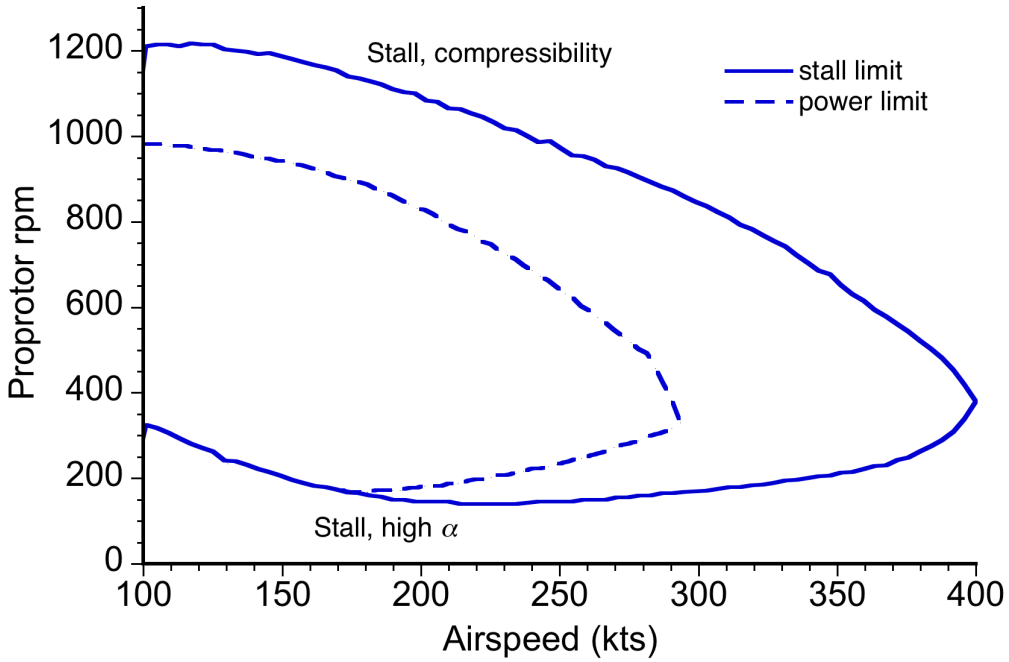

Figure 3.40: The range of feasible rotational speeds becomes increasingly constrained at higher airspeeds. Data shown for the *Excalibur* at 15,000 ft ISA.

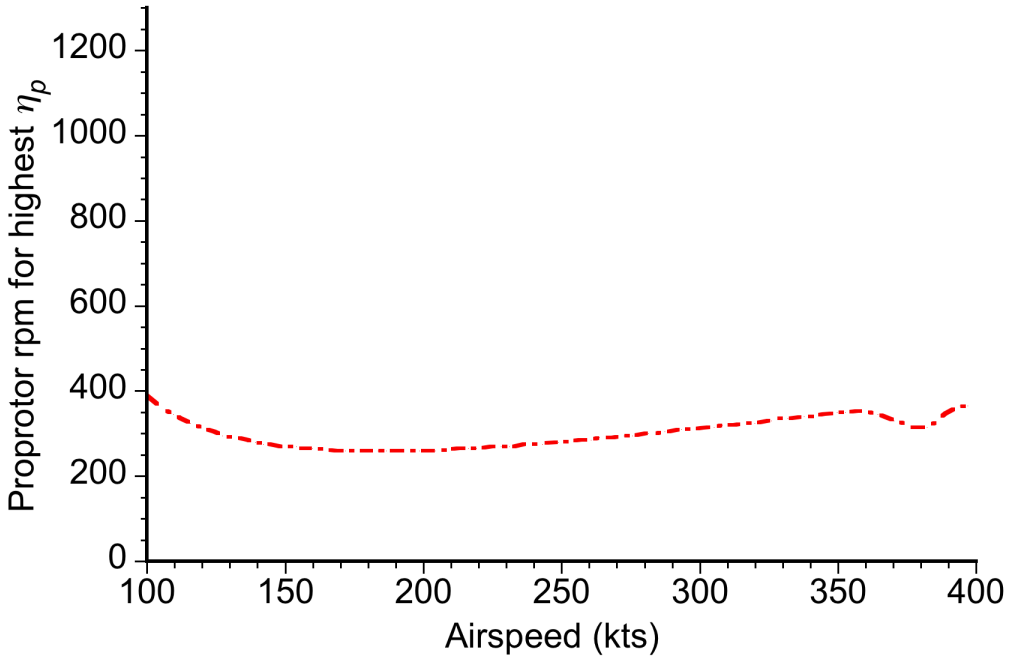

Figure 3.41: The rotational speed that results in the highest propulsive efficiency is a function of airspeed. Data shown for the *Excalibur* at 15,000 ft ISA.

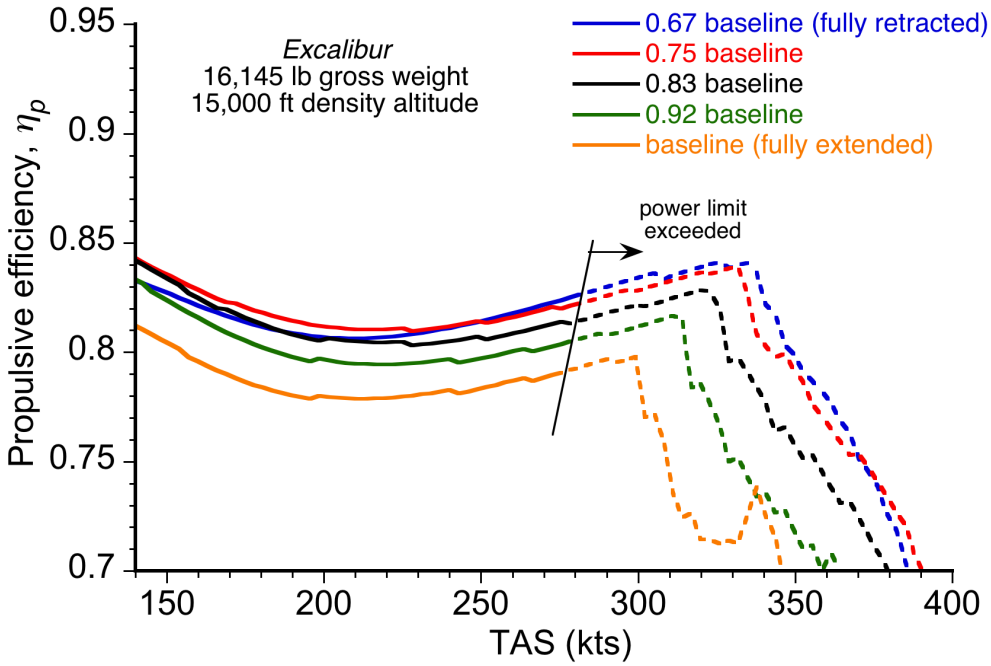

Figure 3.42: Propulsive efficiency of the *Excalibur* across its range of proprotor diameters.

thermore, the decrease in tip speed, coupled with the decrease in blade area, adversely affects performance at lower cruise speeds where the induced drag on the wings is higher, thus requiring higher thrust production from the proprotors. At these lower speeds, the fully retracted state produces lower efficiency than in the partially retracted state. This outcome occurs because to generate the required thrust some blade sections must operate at less efficient section values of C_l/C_d and in some cases closer to stall. However, increasing the diameter of the proprotor clearly improves the hover performance and gives an ability to hover at higher density altitudes and at higher gross vehicle weights.

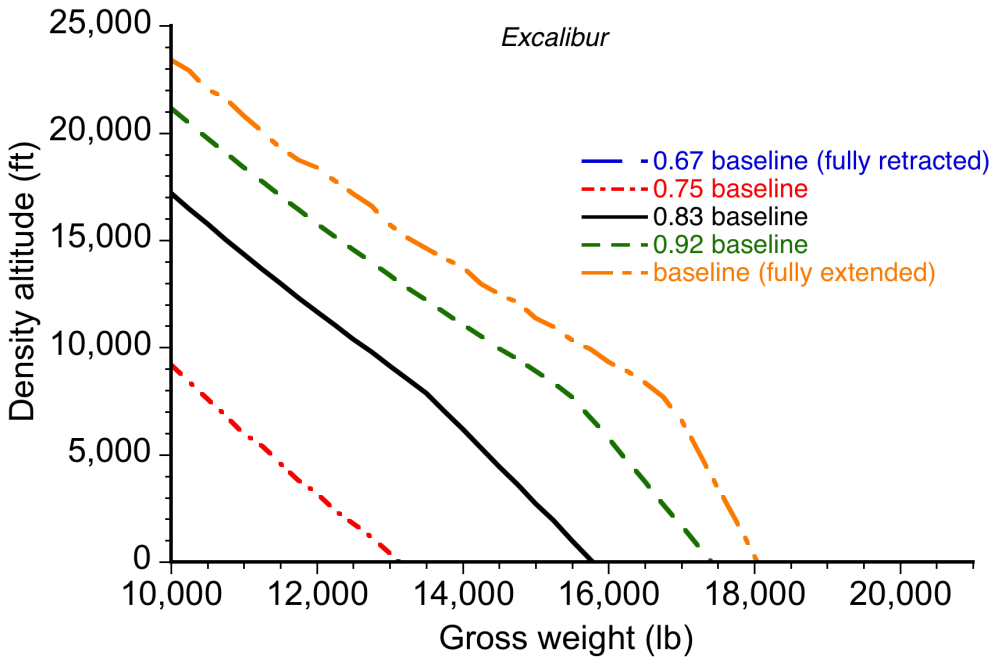

Figure 3.43: Hover ceiling of the *Excalibur* across its range of proprotor diameters.

3.3.8 Maximum Lift Coefficient

The effect of the maximum attainable lift coefficient, $C_{l_{\max}}$, of the blade sections on vehicle performance is shown in Figs. 3.44 and 3.45. In these calculations, it was assumed that the values of $C_{l_{\max}}$ could be adjusted independently while keeping constant all of the other sectional airfoil characteristics. It is recognized, however, that such aerodynamic improvements may not be possible in practice. The propulsive efficiency curves in Fig. 3.44 all follow the same behavior until, for a particular case, the blade sections begin to exceed $C_{l_{\max}}$ and the proprotor begins to stall. The power loading, as shown in Fig. 3.45, is clearly improved at all operational density altitudes by increasing the maximum attainable lift coefficients of the airfoil sections.

Notice in Fig. 3.44 that even with a $C_{l_{\max}}$ high enough to prevent blade stall at very high airspeeds, the propulsive efficiency will reach a peak at a certain airspeed and

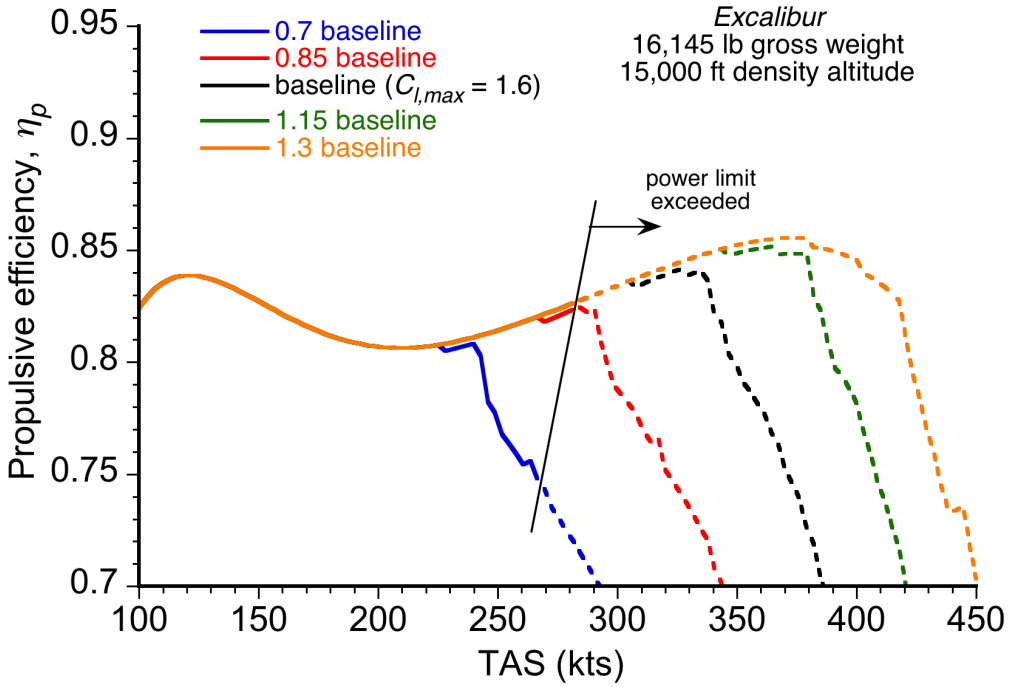

Figure 3.44: Effect of $C_{l_{\max}}$ on the propulsive efficiency of the *Excalibur*.

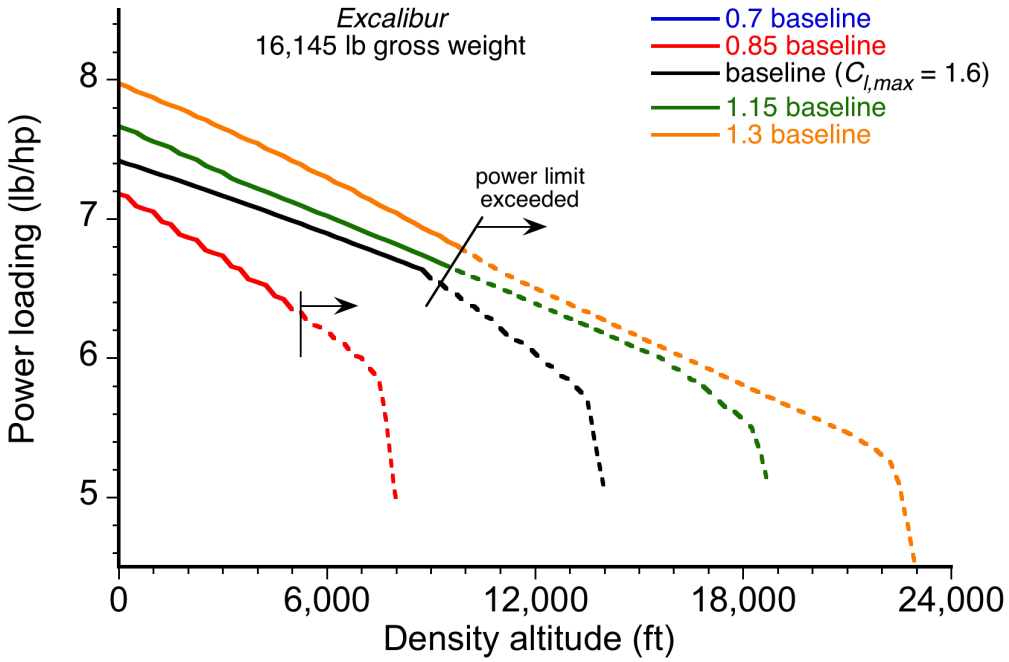

Figure 3.45: Effect of $C_{l_{\max}}$ on the hover power loading of the *Excalibur*.

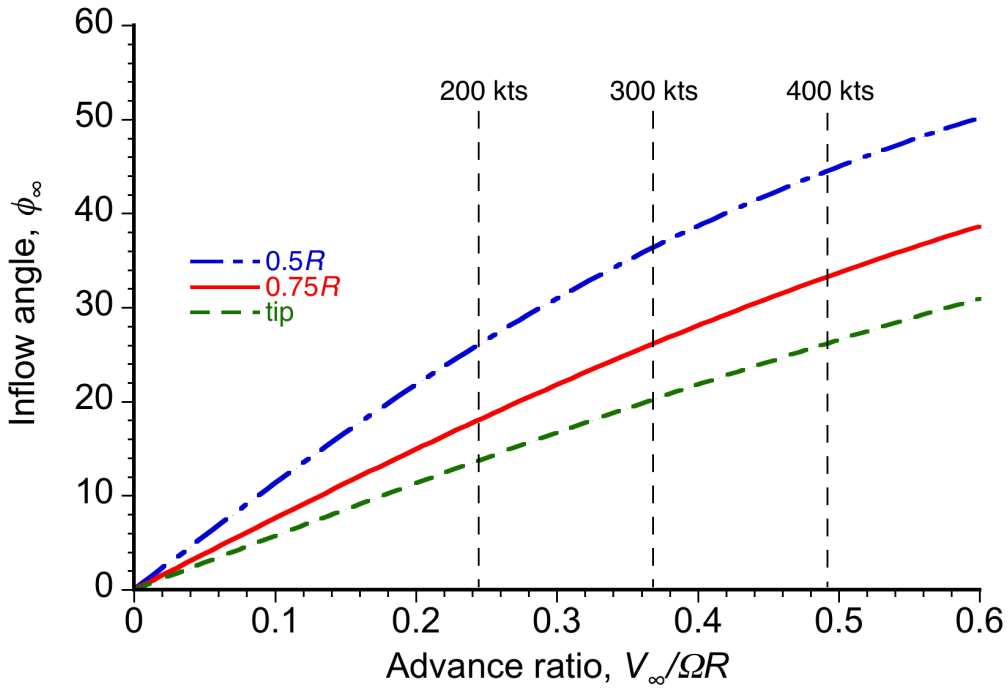

Figure 3.46: Inflow angle versus vehicle advance ratio for the *Excalibur*.

then show a decrease with further increases in airspeed. This outcome occurs because as advance ratio increases, the sectional lift vectors become inclined further away from the rotational axis and so act to reduce propulsive capabilities. In this case, the propulsive efficiency reaches its peak at about 380 kts.

Figure 3.46 shows how the inflow angle, which is equal to the angle between the lift vector and the rotational axis (refer to Fig. 2.1), increases with both advance ratio and distance inboard from the blade tips. Notice that at higher airspeeds, the mid-section of the blade can reach an inflow angle of 45°, i.e., the sectional lift contributes as much to rotor torque as it does to thrust.

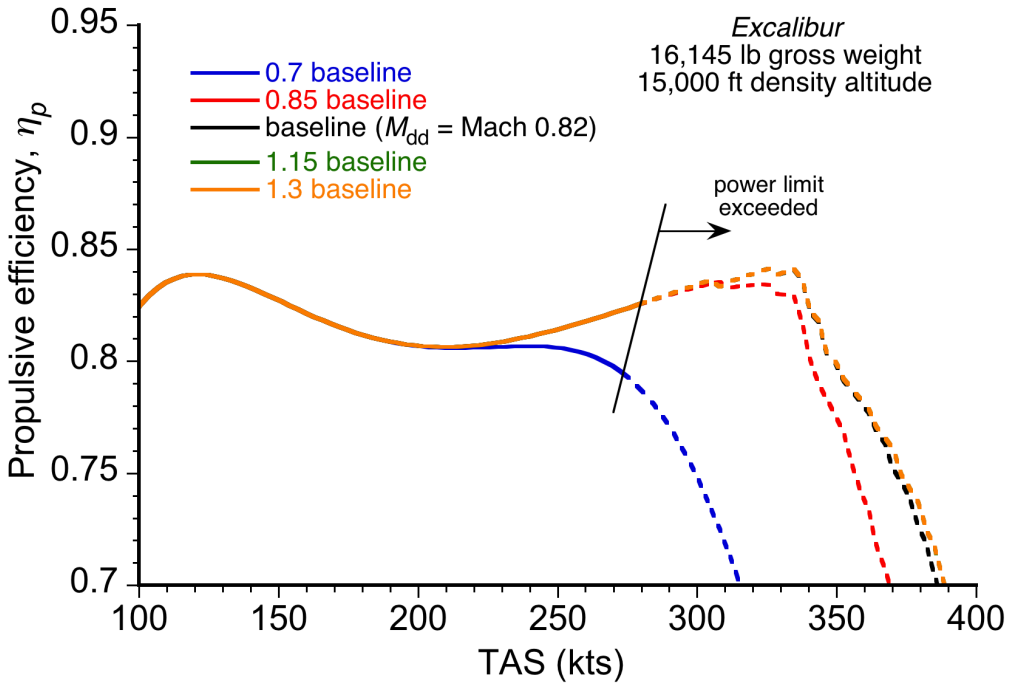

Figure 3.47: Effect of M_{dd} on the propulsive efficiency of the *Excalibur*.

3.3.9 Drag Divergence Mach Number

Figures 3.47 and 3.48 show the effects of variations in M_{dd} on the cruise and hover efficiencies of the *Excalibur*. As performed previously for $C_{l_{max}}$, it has been assumed for this study that M_{dd} can be varied while keeping all of the other airfoil characteristics constant. Notice that the value of M_{dd} has little or no effect on vehicle performance as long as it reaches a certain minimum threshold. The required value of M_{dd} is obviously higher for forward flight operations than for hovering flight because of the higher helical section velocities experienced in forward flight, and the need to limit the buildup of compressibility over more substantial parts of the blade (they are not just limited to the tip region). Figure 3.49 shows how the middle and inboard sections of the blade can reach relatively high helical Mach numbers when the proprotor operates at higher airspeeds.

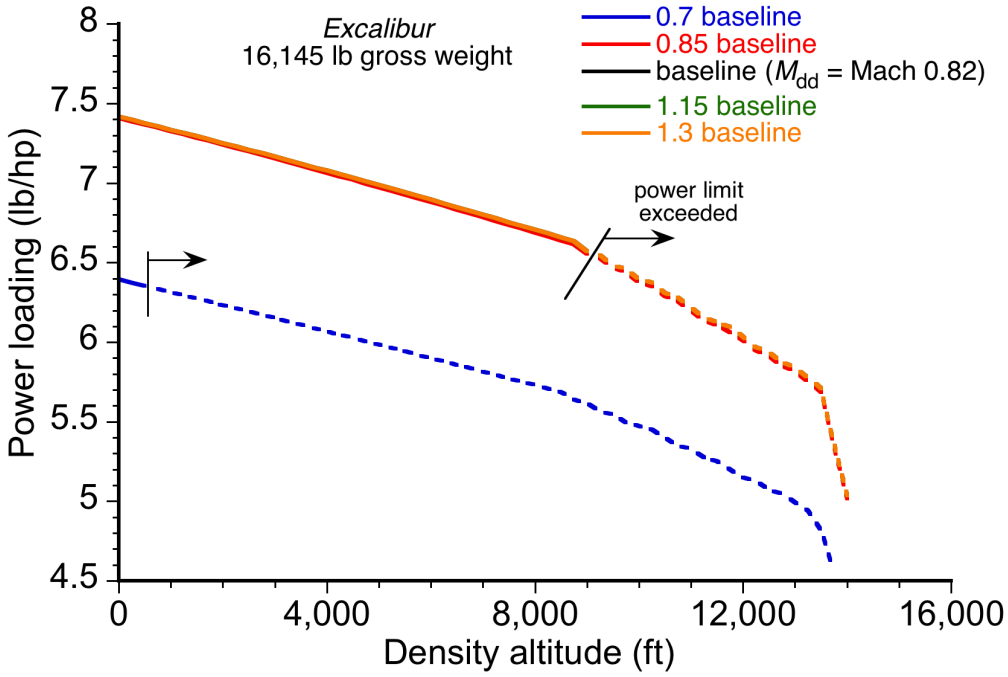

Figure 3.48: Effect of M_{dd} on the hover power loading of the *Excalibur*.

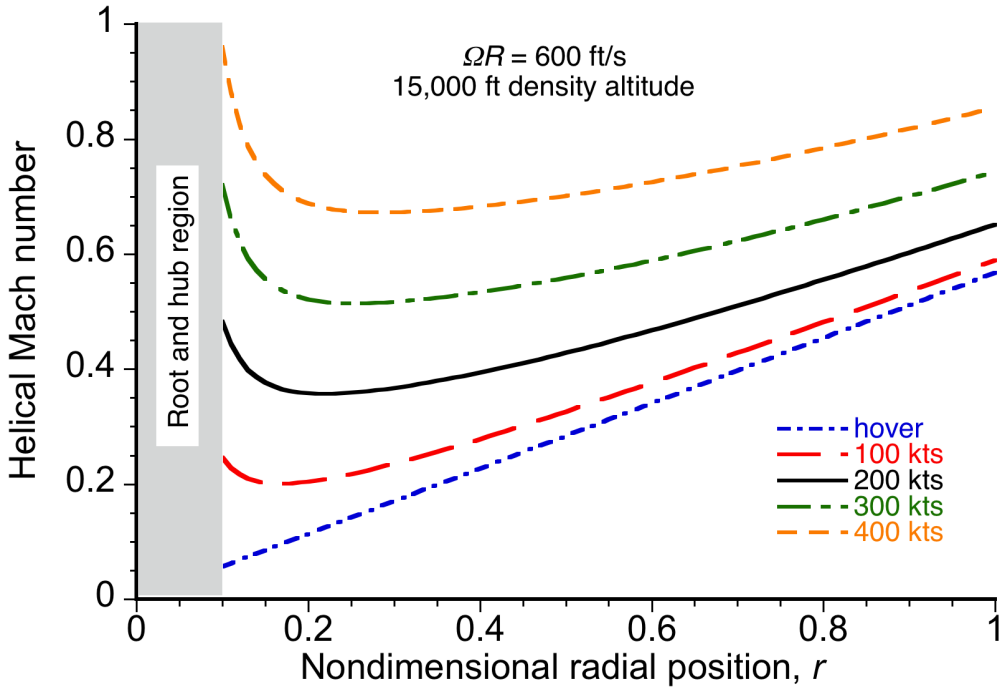

Figure 3.49: Helical Mach number distribution as a function of airspeed.

3.4 Alternative Efficiency Metrics

In the previous section, proprotor efficiency was expressed in terms of power loading in hover and propulsive efficiency in forward flight. However, proprotor performance can also be examined using alternative efficiency metrics; for example, figure of merit may be used to compare relative hovering efficiency, as shown by Fig. 3.50, which summarizes outcomes from the parametric study on solidity. Notice that figure of merit tends to increase with density altitude. This outcome is in contrast to the trend shown with hover power loading, which decreases with density altitude, as shown previously by the results in Fig. 3.25.

The explanation for the foregoing behavior can be attributed to the definition of figure of merit, which is defined as the ratio of ideal hover power to actual hover power, i.e.,

$$FM = \frac{P_{\text{ideal}}}{P} = \frac{C_T^{3/2}/\sqrt{2}}{C_P} = \frac{T^{3/2}}{\sqrt{2\pi\rho}\,PR} \tag{3.12}$$

From Eq. 3.12, it is apparent that figure of merit is inversely proportional to the square root of the air density. The results in Fig. 3.50 are therefore misleading because, although the power required to hover is greater at higher altitudes, the figure of merit increases with altitude simply because the air density decreases. Figure of merit is particularly unsuitable for examining the benefits of variations in rotor diameter because of the radius, R, in the denominator of Eq. 3.12. This radius term causes the value of FM to increase or decrease for no reason other than with variations in proprotor diameter. Therefore, the use of FM as an efficiency metric must be considered carefully.

An alternative metric for evaluating cruise efficiency is the power loading in forward

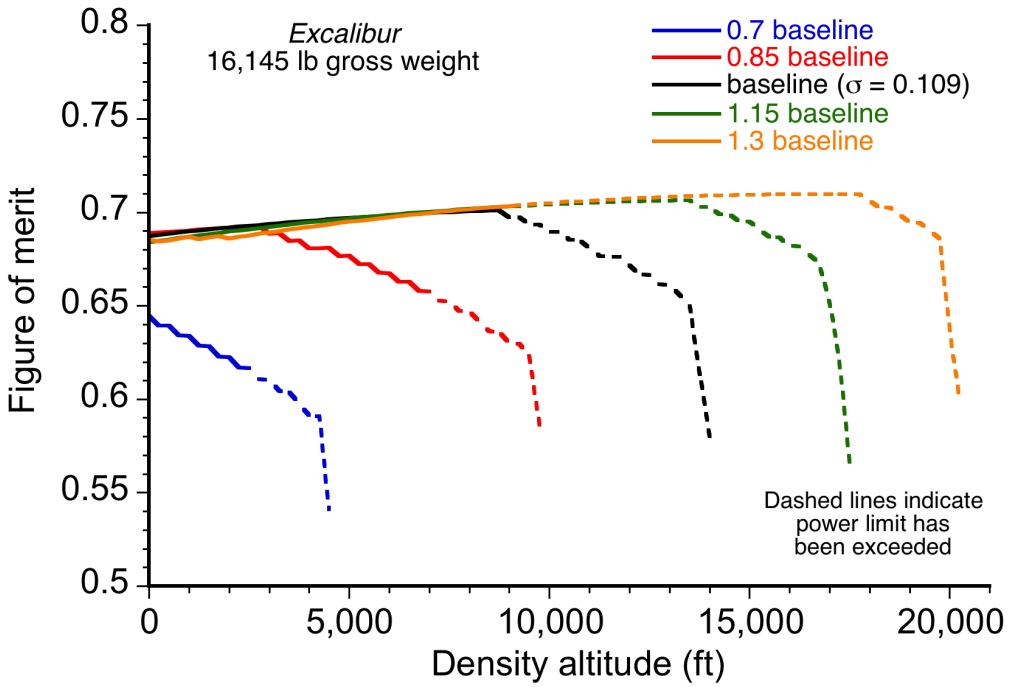

Figure 3.50: Parametric study of the effect of proprotor solidity on figure of merit.

flight, i.e., the ratio of vehicle gross weight to proprotor power required. Power loading in forward flight is defined as

$$PL_{\text{cruise}} = \frac{W}{P} = \frac{\left(\frac{L}{D}\right)_{\text{veh}} \eta_p}{V_\infty} \tag{3.13}$$

Figure 3.51 shows that the cruise power loading for the *Excalibur* peaks at 150 kts and then sees a rapid reduction at higher airspeeds. However, this trend is also misleading because, although power requirements increase substantially at higher airspeeds, the fact that the aircraft is traveling at a high airspeed itself makes such operating conditions desirable. Equation 3.13 indicates that the cruise power loading is dependent on the vehicle lift-to-drag ratio (see Fig. 3.63 in Section 3.7). Propulsive efficiency, as shown previously in Fig. 3.24, takes airspeed into account and is a much better efficiency metric in this case. Productivity metrics, such as those discussed in Ref. 65, may also be useful for

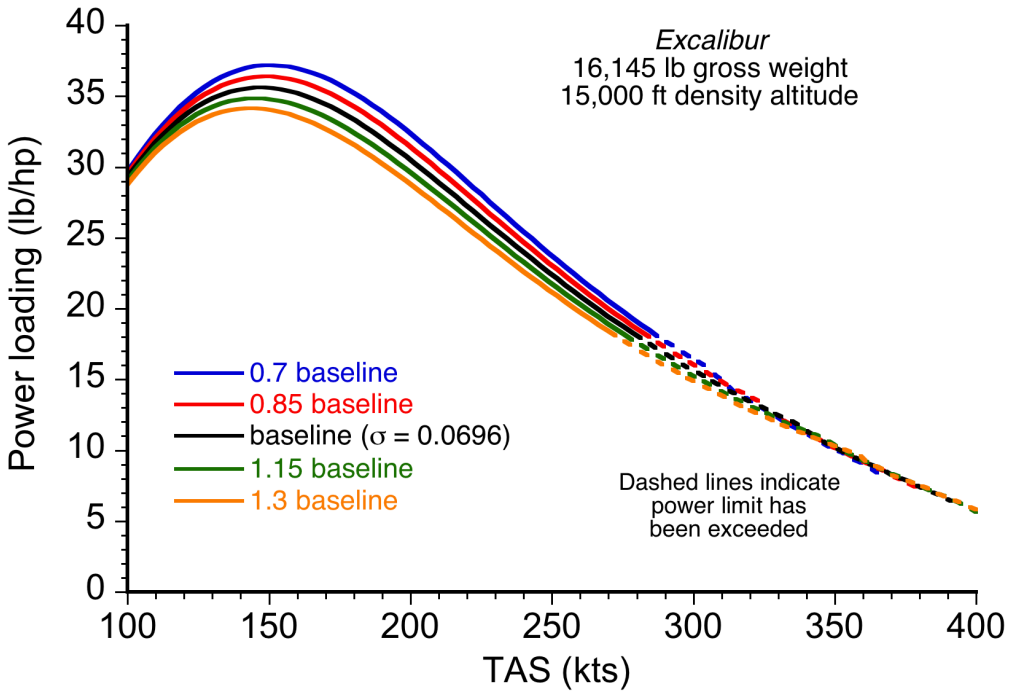

Figure 3.51: Parametric study of the effect of proprotor solidity on power loading in forward flight.

quantifying aspects of flight performance.

3.5 Validation of the Optimizer

Many of the remaining results in this chapter were obtained using formal optimization methods, as described in Section 2.8. The optimizer was validated to ensure that it was able to correctly iterate to the optimum value of the objective function, i.e., the highest values of proprotor aerodynamic efficiency. Figure 3.52 shows a validation of the optimizer with three design variables for a representative proprotor with bilinear blade twist. The curves represent parametric variations in the design variables from their optimum values. The efficacy of the optimizer is confirmed by the fact that the figure of merit decreases when the design variables are varied in either direction from the values

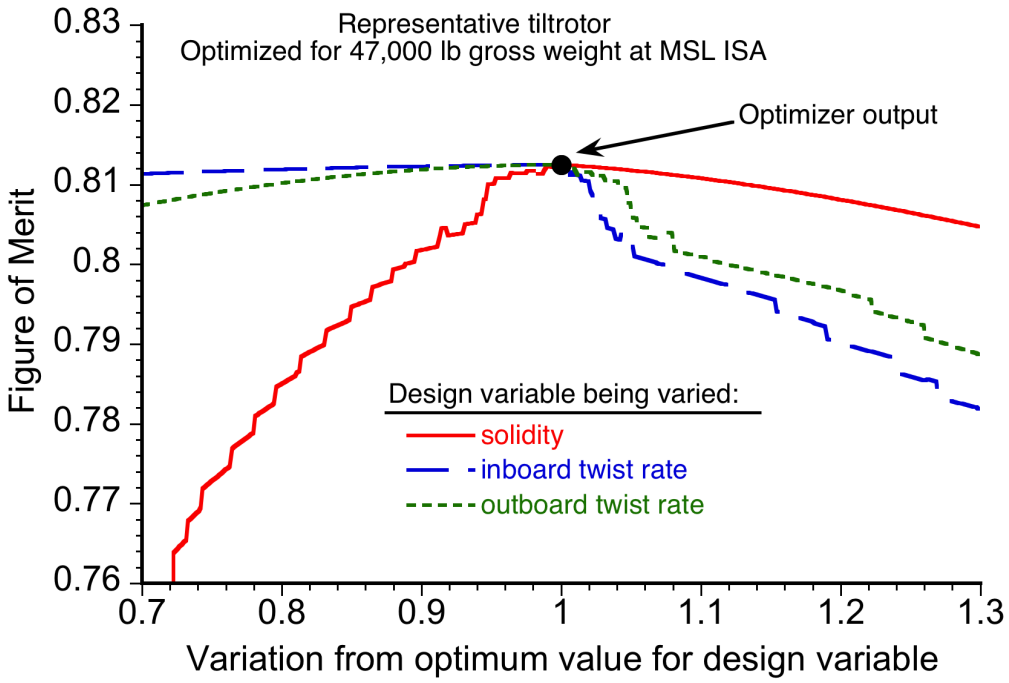

Figure 3.52: Validation of the optimizer for three design variables.

obtained from the optimizer.

Figure 3.53 shows a validation for six design variables, including a constraint to keep the transmission power limit above a certain value (effectively a lower limit on rotational speed). Again, the optimizer is validated by the fact that the power loading cannot be improved by varying the design variables from their optimized values, with the exception of rotational speed, which would encounter the constraint if lowered from the optimized value. Notice that the power loading experiences a steep decrease if the design variables are varied slightly in certain directions. This outcome occurs because when optimizing for a single design point (in this case, hover efficiency at MSL ISA), the resulting optimum configuration does not necessarily generate the needed thrust margins for off-design operation. When using an optimization approach to improve proprotor

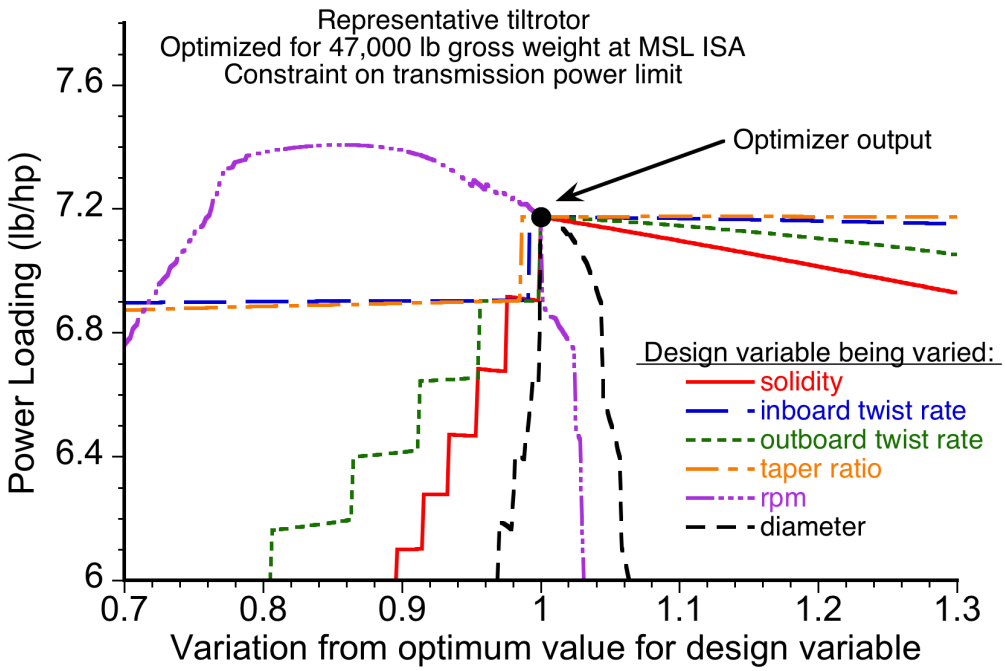

Figure 3.53: Validation of the optimizer for six design variables plus an inequality constraint.

performance, careful consideration must be given to the specific design point(s) being optimized for, and how the results affect performance across the entire spectrum of flight conditions.

To further illustrate the importance of the selection of the objective function, consider the results in Fig. 3.54, which shows a series of hover ceilings that were obtained by optimizing different design variables for hovering efficiency at 47,000 lb gross weight and 5,000 ft density altitude. As shown, when outboard blade twist or rotational speed are optimized to give the best hovering efficiency at this design point, performance at higher altitudes is degraded and the hover ceiling is also decreased. Additionally, optimizing solidity by itself results in a higher hover ceiling over the majority of the range of gross weights than does optimizing all four of the design variables at once. A better strat-

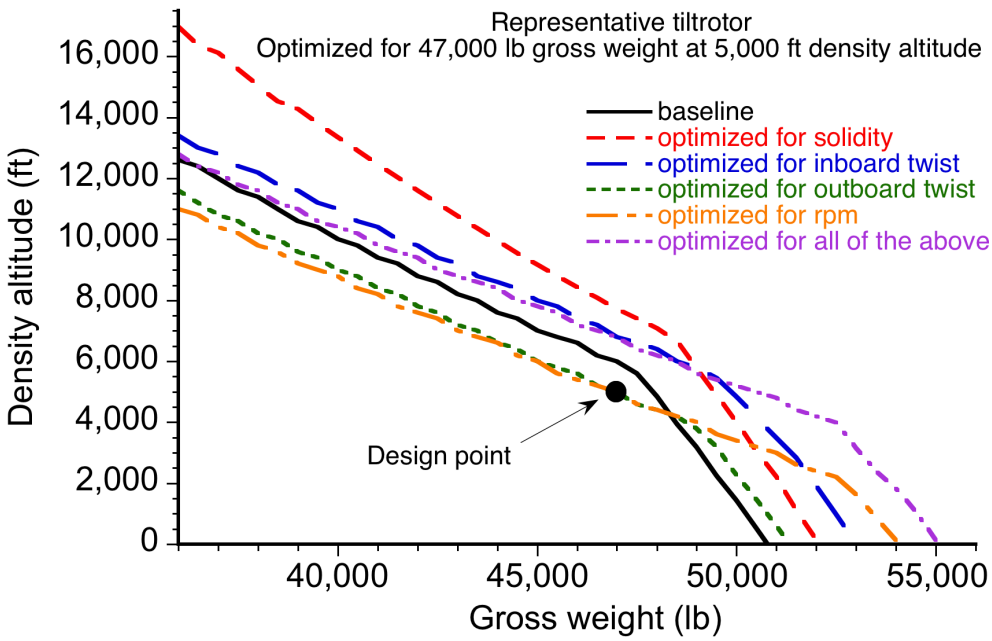

Figure 3.54: The effect on hover ceiling when the representative tiltrotor is optimized for a single design point.

egy for improving proprotor efficiency is to optimize a weighted average of the separate efficiencies at several different operating conditions.

3.6 Airfoil Requirements

As shown previously in the parametric studies, the choice of airfoils (and their spanwise placement on the blade) is obviously an important consideration in the design of all types of proprotor blades. To explore the effect that the choice of the airfoils has on the performance of a CR aircraft, a formal optimization study was performed on the airfoil selection process for the representative medium-lift tiltrotor. To this end, the values of $C_{l_{\max}}$ and M_{dd} were each represented as functions of the airfoil thickness-to-chord ratio (t/c), which has a primary effect on both parameters.

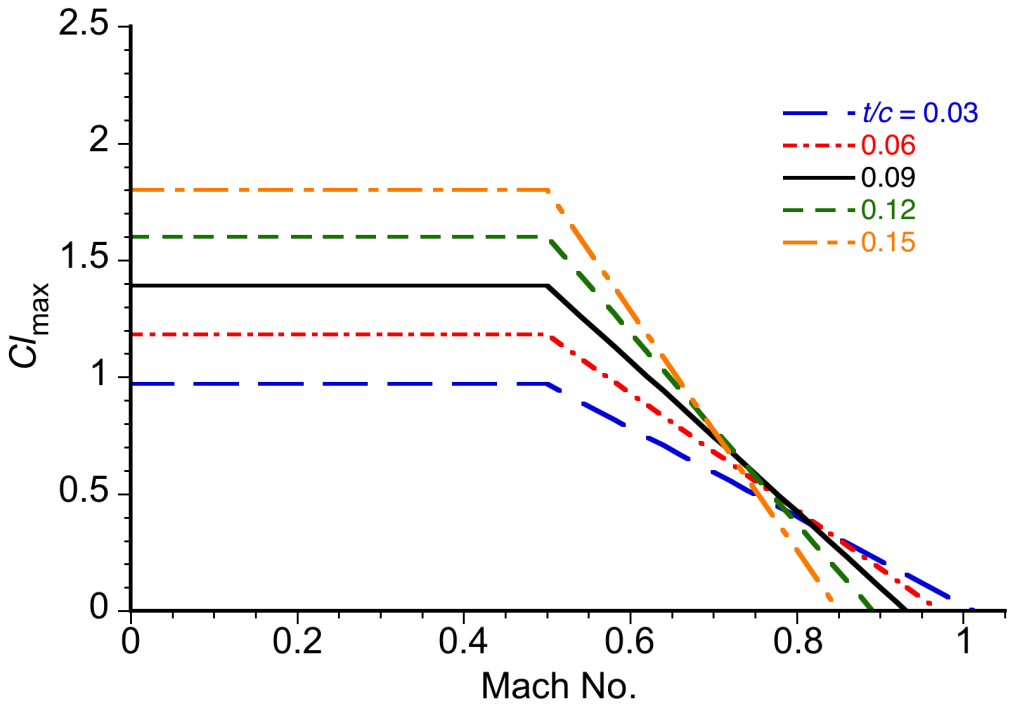

Figure 3.55: Effect of airfoil thickness on $C_{l_{\max}}$ distribution for the assumed canonical model.

Figure 3.55 shows how the $C_{l_{\max}}$ distribution changes with t/c. For the optimization, the blades were divided into twenty segments and the value of t/c for each segment was adjusted to maximize one of three objective functions: propulsive efficiency, figure of merit, and a balance between the maximum values of η_p and FM.

Figure 3.56 shows the outcomes from this optimization, which used a baseline airfoil t/c of 0.12. Maximizing hover efficiency demands thicker airfoil sections near the root so as to increase $C_{l_{\max}}$ and hence prevent these root sections from stalling. The compromised twist inherent to most proprotors is the main reason that the blade root sections operate at higher angles of attack in hover and so very high values of $C_{l_{\max}}$ are needed here to prevent stall. Maximizing both FM and η_p also requires a blade root section with relatively high values of $C_{l_{\max}}$, which is also good for structural reasons. Near the tip,

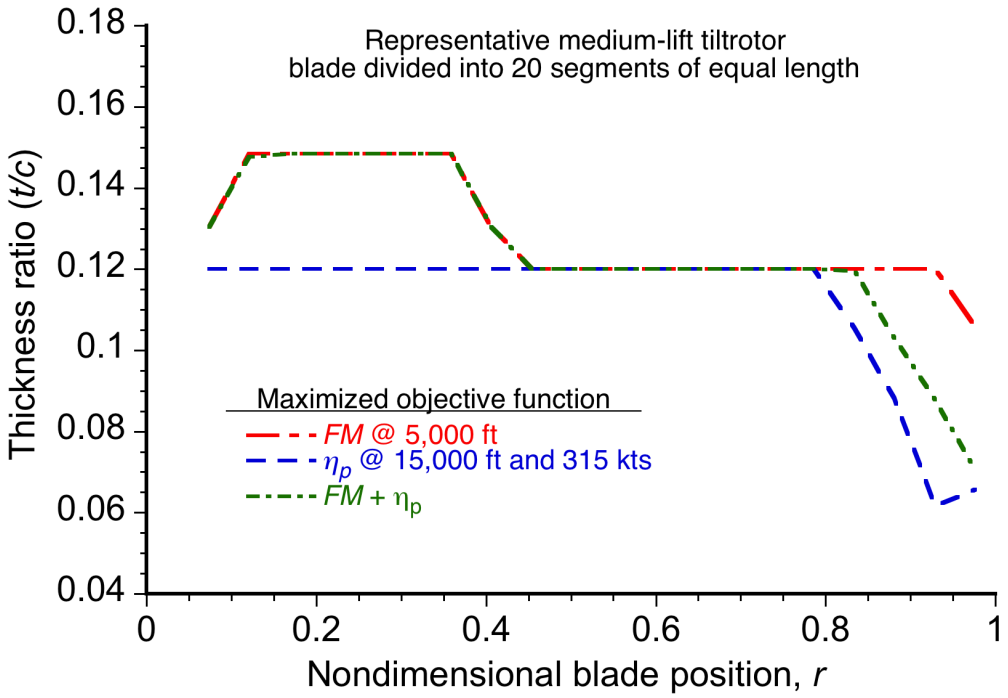

Figure 3.56: Airfoil thickness optimized for figure of merit, propulsive efficiency, and both.

however, maximizing η_p demands significantly thinner blade sections, while maximizing *FM* suggests that a smaller reduction in t/c needs to occur there.

The airfoil selection process also requires that hover and cruise performance be examined using the resulting t/c distributions from Fig. 3.56. Figure 3.57 shows the effect of optimization of airfoil requirements on propulsive efficiency. The airfoil characteristics in this case, only have an effect on the propulsive efficiency at higher forward speeds. Interestingly, the compromised case shows better efficiency than when η_p is maximized by itself; this is an outcome of optimizing propulsive efficiency for a single airspeed (i.e., 315 kts in this case). However, improvements in airfoil properties lead only to modest improvements in overall forward flight performance; the difference between the compromised blade and the blade optimized for hover is a delay in the onset of compressibility

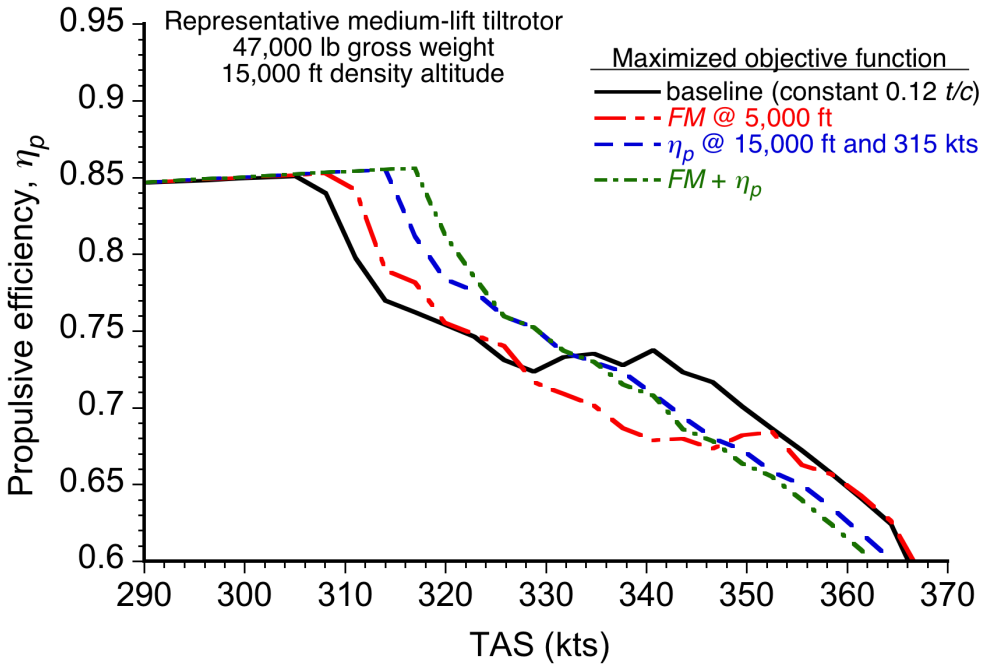

Figure 3.57: The effect of airfoil requirement optimization on forward flight efficiency.

effects of only 9 kts of airspeed.

Figure 3.58 shows the effect that the optimization of airfoil requirements has on the figure of merit of the proprotor. Optimizing for hover results in an increase in figure of merit of about 0.03, although this value is still significant because it would represent a 2–6% increase in payload. Optimizing for forward flight not only decreases the figure of merit, but also decreases the maximum operational altitude by about 2,500 ft. For the most part, the case where the airfoil requirements were optimized for a compromise between *FM* and η_p mirrors the results for when the blades were optimized for hover. The only difference is a decrease in the maximum operational density altitude of 1,000 ft, indicating that the use of thinner airfoils near the tip only become a concern for the compromised optimization at higher altitudes where higher $C_{l_{\max}}$ values are needed to avoid stall over the blade tip.

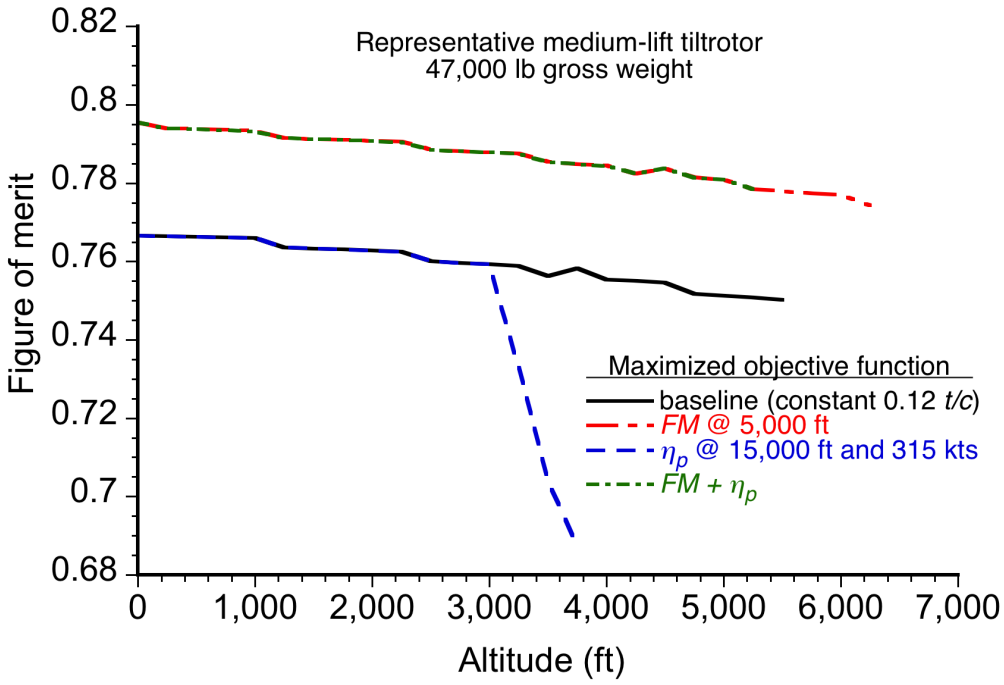

Figure 3.58: The effect of airfoil requirement optimization on hover figure of merit.

Overall, the results in Figs. 3.57 and 3.58 show that, at least for this vehicle configuration, the best gains in overall performance can be made when the airfoils are optimized for efficiency in hover rather than in forward flight.

3.7 Variable Tip Speed Operation

To further explore the effects of variable tip speed, a study was performed on the representative medium-lift tiltrotor to optimize its performance by using either of the VSPR and VDPR designs. A third "modified" VDPR design was also considered, which is an approach where the total blade twist per radius is preserved when the diameter of the proprotor is reduced; in practice this outcome can only be achieved by using a variable twist mechanism. The assumed proprotor in this case had a bilinear blade twist and a maximum tip speed reduction of 33%. For the VDPR concept, the inboard blade section

(which is sheathed inside the outboard section during retraction) had a chord equal to 1/3 of the root chord of the main blade.

For the baseline and the VDPR cases, it was assumed that the shaft speed could be reduced by 10% by using the power turbine alone; the shaft speed can be expected to be reduced by at least this amount without significantly increasing engine SFC [34, 35]. The design variables used were diameter, rotational speed, root chord, taper ratio, inboard and outboard twist, the radial position where twist changes, and the tip speed reduction. The flight conditions considered were cruise at 15,000 ft density altitude and 280 kts, and hovering flight at 6,000 ft density altitude.

The objective function needed for the optimization is not immediately apparent in this case. It is not acceptable to use *FM* and η_p together (as was used in the airfoil optimization study) because *FM* is dependent on diameter, and so the optimizer would not necessarily try to maximize absolute hovering efficiency (i.e., the power loading). Instead, a baseline proprotor design without variable tip speed was established to evaluate the VSPR and VDPR designs. The objective function was selected to be the sum of the ratio of the baseline cruise power to the cruise power and the ratio of the baseline hover power to the hover power.

Figures 3.59 and 3.60 show the cruise and hover efficiencies for the optimized variable tip speed proprotor designs. On one hand, the VSPR design offers large improvements in both propulsive efficiency and power loading over those of the baseline proprotor, although it soon exceeds the transmission torque limits when its shaft speed is reduced significantly in forward flight. On the other hand, the VDPR design gives lower propulsive efficiencies than for the baseline design. While this concept also achieves

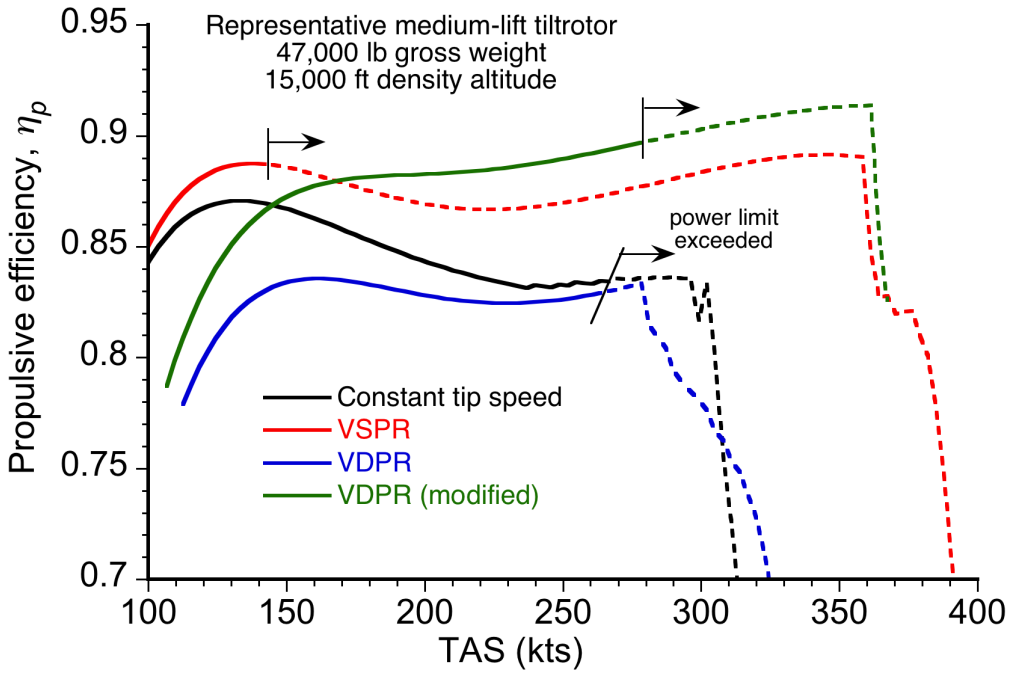

Figure 3.59: Propulsive efficiency for the optimized variable tip speed proprotor designs

.

higher power loadings than for the baseline, it does so at the expense of a lower hovering efficiency at higher altitudes. The results for the modified VDPR are much better than for the standard VDPR, indicating that the performance degradation shown with the VDPR design is largely attributable to the reduction in effective blade twist when the diameter of the proprotor is reduced.

Similar trends to those shown for the medium-lift tiltrotor were also found for a proprotor that is representative of the proposed Large Civil Tilt Rotor (LCTR) convertible-rotor concept. Figure 3.61 shows the peak propulsive efficiency of the LCTR concept as a function of airspeed, and Fig. 3.62 shows the propulsive efficiency when the thrust on the proprotors is determined by the vehicle drag by using Eq. 3.5. These results were not obtained through an optimization analysis as was performed for the medium-lift tiltro-

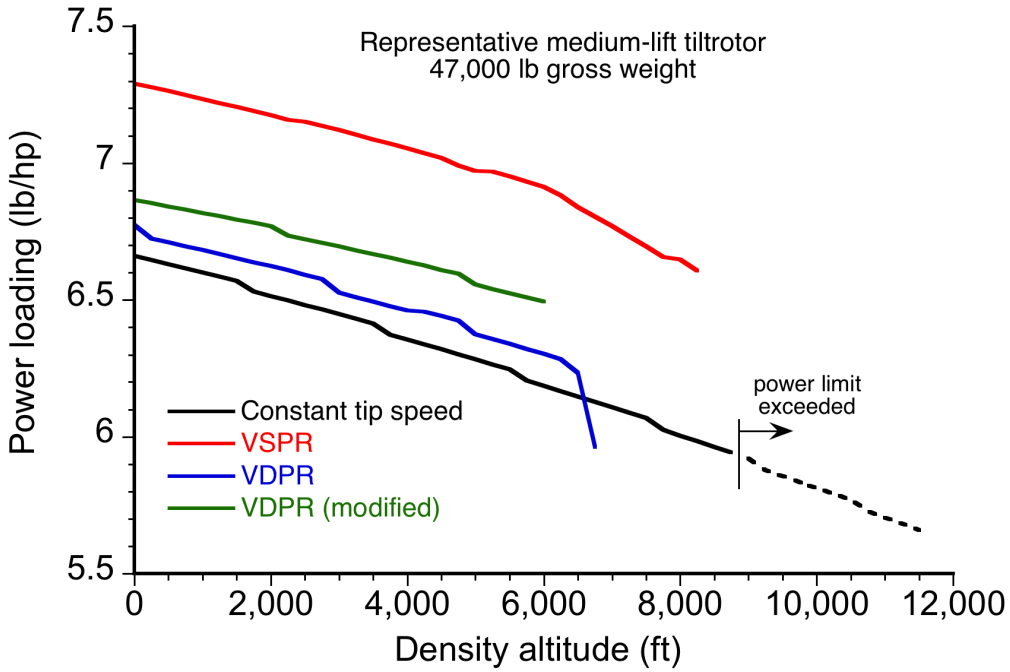

Figure 3.60: Hover power loading for the optimized variable tip speed proprotor designs.

tor, but simply by taking the baseline proprotor and reducing both its diameter and its rotational speed. As before, varying diameter gives a lower propulsive efficiency than varying rotational speed. However, unlike the outcomes found for the medium-lift tiltrotor, a VDPR design improves forward flight performance over that of the baseline, as shown in Fig. 3.62.

The foregoing comparison of the reduced tip speed methods for the medium-lift tiltrotor and the LCTR should not be taken to imply that reducing the rotational (shaft) speed is always the preferred approach to design. The LCTR concept, in particular, was designed specifically from the outset to exploit the benefits of reduced rotational speed in forward flight, so it is not surprising that this approach produces the best performance in this case. The parametric studies shown previously for the *Excalibur*, which is a VDPR design, indicate that reducing diameter is also a viable method for improving proprotor

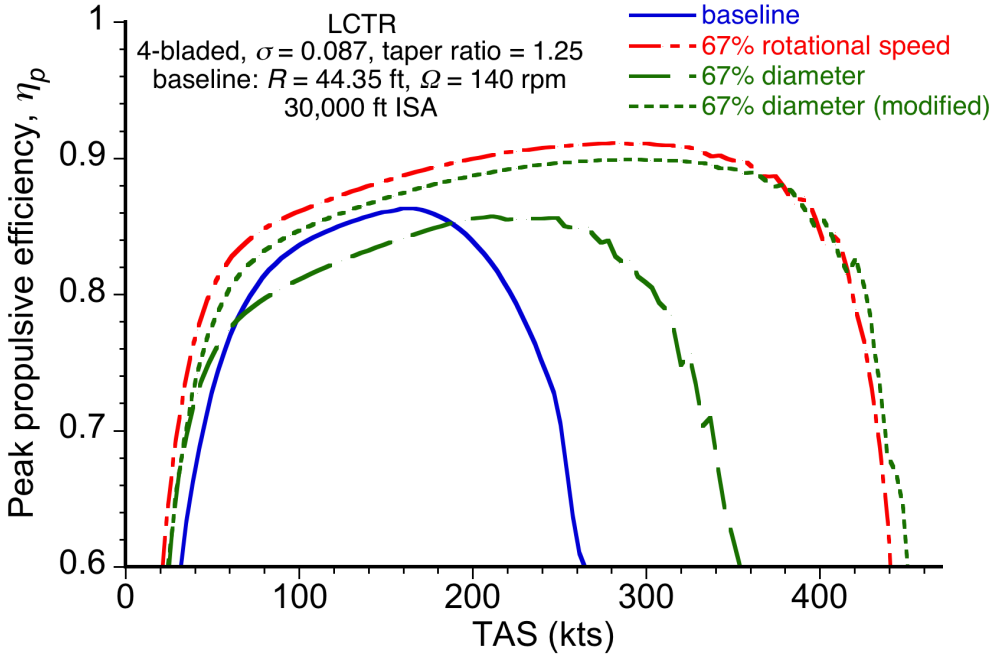

Figure 3.61: Effect of reduced tip speed methods on the peak propulsive efficiency of the LCTR.

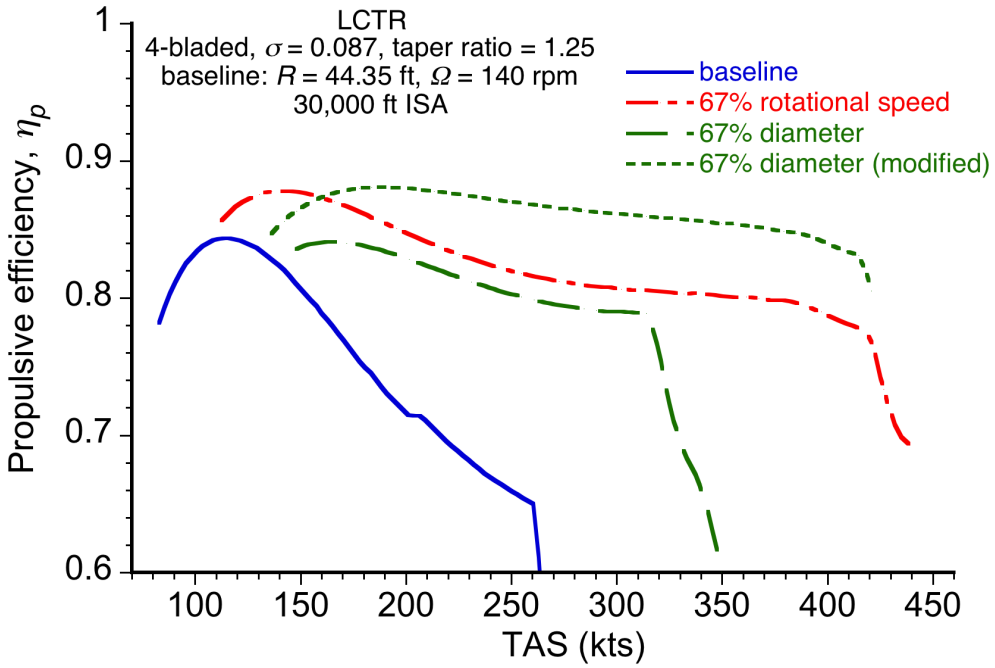

Figure 3.62: Effect of reduced tip speed methods on the propulsive efficiency of the LCTR.

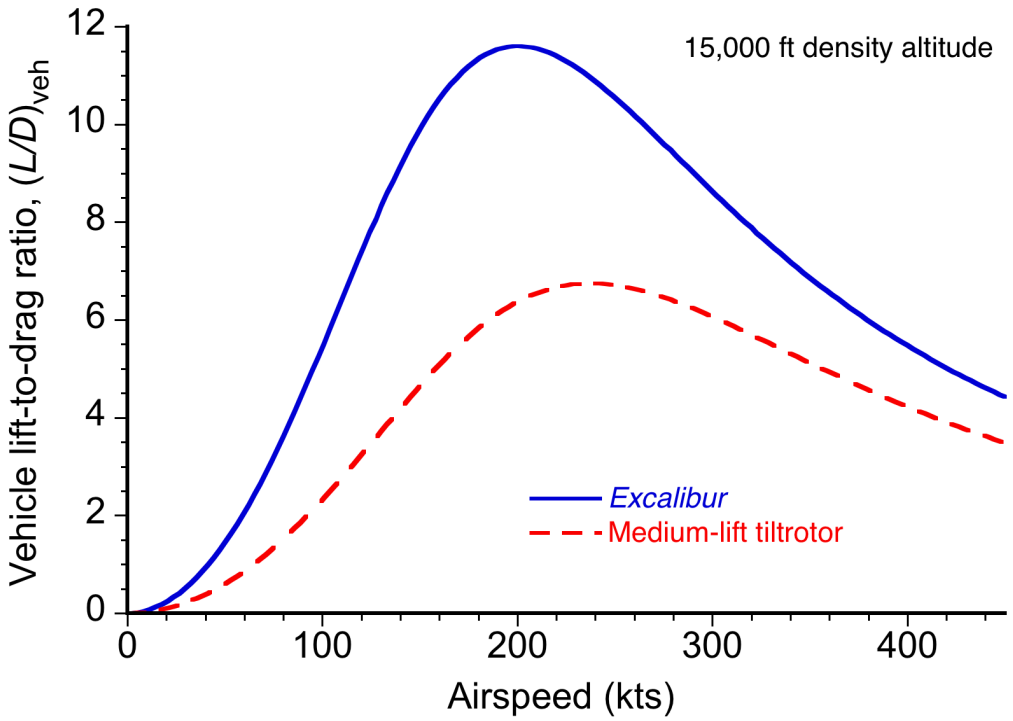

Figure 3.63: Vehicle lift-to-drag ratios for the *Excalibur* and representative medium-lift tiltrotor.

performance. Compared to the medium-lift tiltrotor, the *Excalibur* has much higher maximum and overall L/D ratios, as shown in Fig. 3.63. It seems that CR aircraft that can attain relatively low values of L/D compared to turboprop airplanes will have little to gain by using a VDPR concept because the combination of relatively higher thrust and smaller blade area in forward flight causes the proprotor to operate at lower propulsive efficiencies.

The importance of vehicle L/D in determining the advantages of the VSPR versus the VDPR designs can be further explained in terms of the blade loading coefficient, i.e.,

$$\frac{C_T}{\sigma} = \frac{T}{\frac{\rho A (\Omega R)^2}{\frac{N_b c}{\pi R}}} = \frac{T}{\rho R^3 \Omega^2 N_b c} \tag{3.14}$$

Higher thrust and lower tip speeds increase the blade loading coefficient, forcing the pro-

protor to operate with larger blade section angles of attack to obtain the required thrust. For a proprotor in forward flight, operation at higher angles of attack generally leads to improved values of propulsive efficiency; however, angles that are too high can reduce efficiency or cause the blade sections to stall. Notice that C_T/σ is proportional to $1/\Omega^2$ and to $1/R^3$, i.e., achieving a lower tip speed by reducing diameter results in a considerably higher blade loading coefficient than would be obtained by reducing rotational speed. Clearly, a variable diameter CR aircraft with relatively poor L/D may have inferior cruise performance because of an excessively high blade loading coefficient, resulting in higher and more inefficient angles of attack during normal operation. This behavior is shown in Fig. 3.64 for the Sikorsky VDTR concept, which can reduce its diameter by 33% for forward flight. Clearly, a reduction in diameter is much less attractive at higher thrust levels.

3.8 Variable Blade Twist

Variable blade twist is another way of improving proprotor performance by obviating the need to compromise the twist rate between the hover and cruise modes of flight operation. As noted in Section 3.3.3, less blade twist is beneficial for improving hover performance, while higher levels of twist are beneficial for improving forward flight efficiency. The extent to which the blade twist becomes compromised between the hover and cruise flight modes is mostly a function of the design cruise speed. As shown in Fig. 3.65, the optimized blade twist for forward flight may actually approach the twist needed for best hovering efficiency when the design cruise speed is increased to higher values. In this

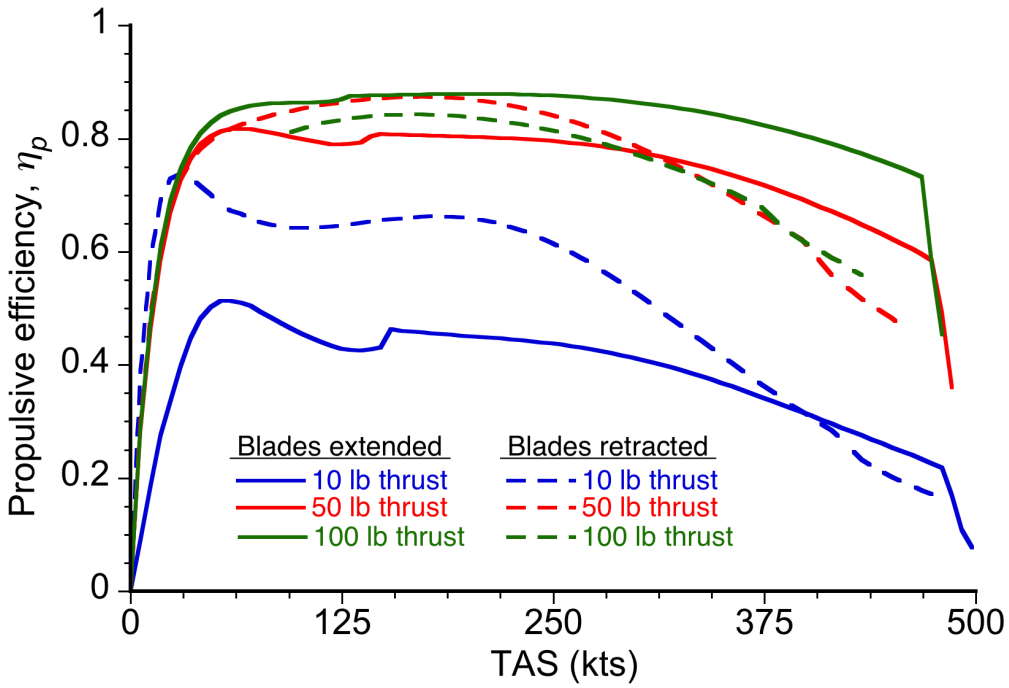

Figure 3.64: Propulsive efficiency for the 1/6-scaled Sikorsky VDTR, while varying diameter and thrust. MSL ISA.

example, the blade twist needed for forward flight better matches the ideal twist needed for hover over the outboard section of the blade when the desired cruise speed is increased from 300 kts to 450 kts.

In general, the ideal blade twist needed for different airspeeds will be fairly similar over the outboard region of the blade, but will differ more significantly inboard; this outcome indicates that the main downside to operating at off-design airspeeds is the propensity of the inboard sections of the blade to stall.

To explore the benefits of a proprotor that can change its twist during flight, an optimization study was performed on the representative medium-lift tiltrotor. The procedure was similar to that described previously in Section 3.7. The proprotor, with an assumed bilinear twist, was optimized to give balanced performance between hover at 6,000 ft ISA

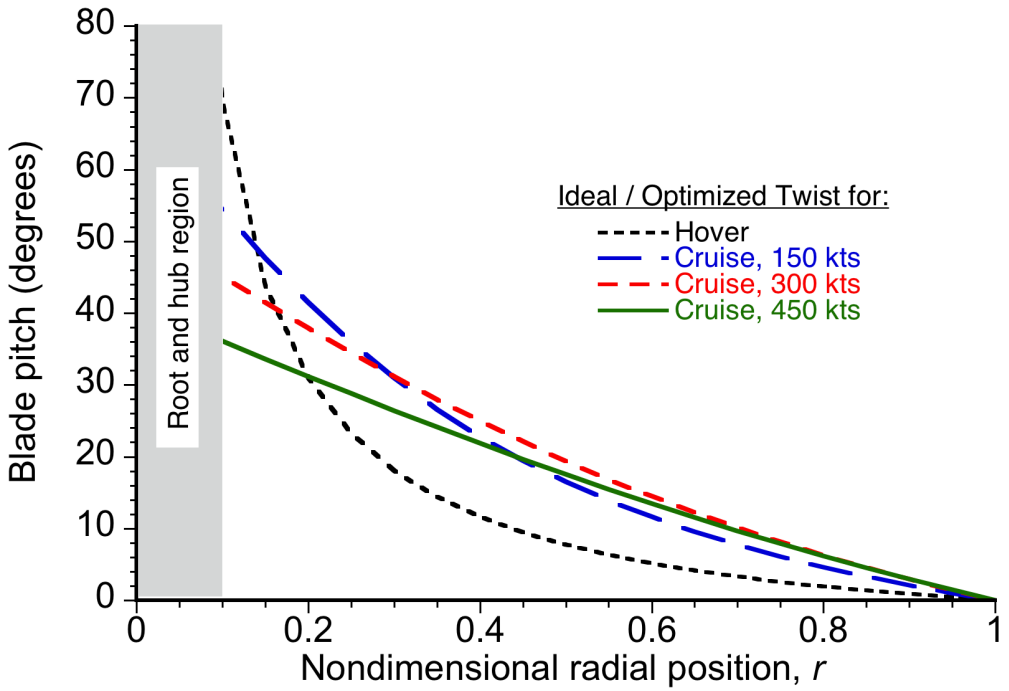

Figure 3.65: Hover and cruise modes demand significantly different blade twist distributions for efficient proprotor operation.

and cruise at 15,000 ft ISA; several design cruise speeds were examined. The proprotor geometry was allowed to be completely optimized, with the flexibility of allowing the inboard and outboard blade twist to be different for hover and for forward flight. A baseline case was also considered where the blade twist was held constant.

Figure 3.66 shows the resulting blade twists when a variable twist proprotor is optimized for different design cruise speeds. Notice that efficient operation in forward flight requires significantly higher blade twist than is required for efficient hover performance. Also notice that the smallest difference between the blade twist in hover and cruise occurs at the lowest and highest design cruise speeds; this outcome reinforces the concept shown in Fig. 3.65, i.e., the ideal blade twist for forward flight differs most from the ideal blade twist for hover at an airspeed of about 250–300 kts.

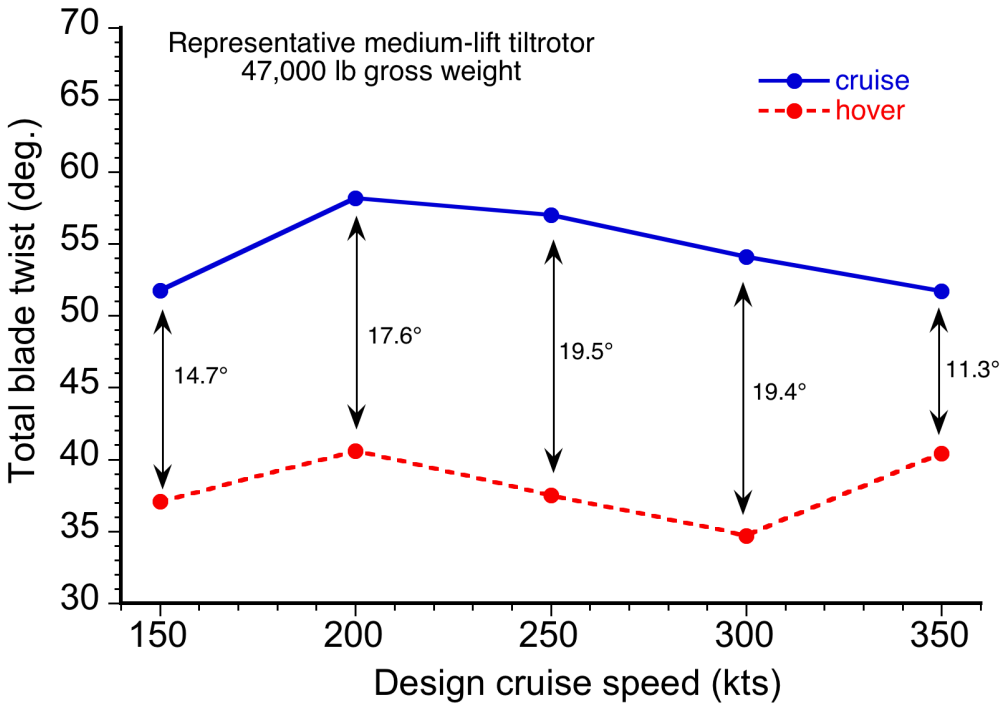

Figure 3.66: Variable twist proprotors need greater blade twist in cruise than in hover.

Figures 3.67 and 3.68 show the cruise and hover efficiencies for variable twist proprotors with different design cruise speeds. Notice that in this study, it was assumed that the proprotor could transition between two discrete twist distributions; in reality, a variable twist proprotor may be able to gradually vary its blade twist across a range of distributions using the methods discussed in Section 1.4. Clearly, at lower design airspeeds a proprotor with variable twist capabilities can realize greater overall performance by improving hover efficiency at the expense of cruise efficiency. At higher design airspeeds, more performance benefits can be obtained by improving cruise efficiency at the expense of some hovering efficiency. Notice, however, that although a variable twist proprotor can increase the propulsive efficiency at higher airspeeds, the maximum speed of the aircraft is still ultimately limited by the onset of compressibility losses; in this case, compressibility effects cause the propulsive efficiency to drop sharply at roughly 360 kts, regardless of

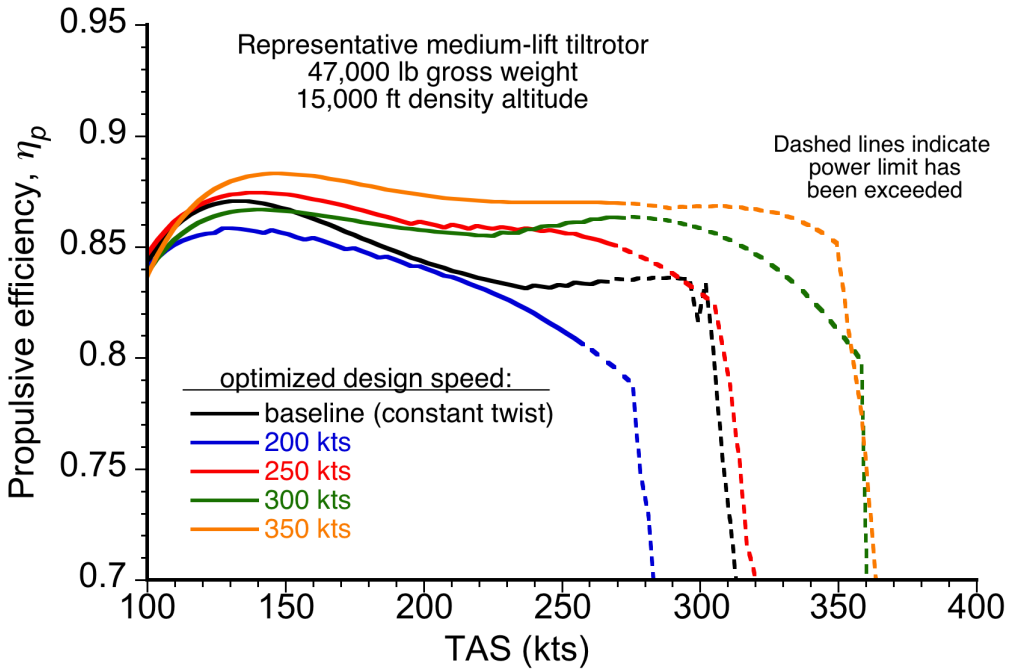

Figure 3.67: Propulsive efficiency for the optimized variable twist proprotors.

the blade twist selected. In general, however, a variable twist proprotor blade can achieve significant improvements over the baseline proprotor.

Compared to the variable tip speed proprotors shown previously in Figs. 3.59 and 3.60, a variable twist proprotor tends to achieve higher hover efficiencies when optimized for reaching a compromise between hover and cruise modes of flight operation. This outcome indicates that a proprotor with variable blade twist may be preferable to a variable tip speed design if hover efficiency is the most important design goal. However, by delaying the onset of adverse compressibility effects, variable tip speed designs can apparently achieve higher propulsive efficiencies at higher airspeeds than can a variable twist design.

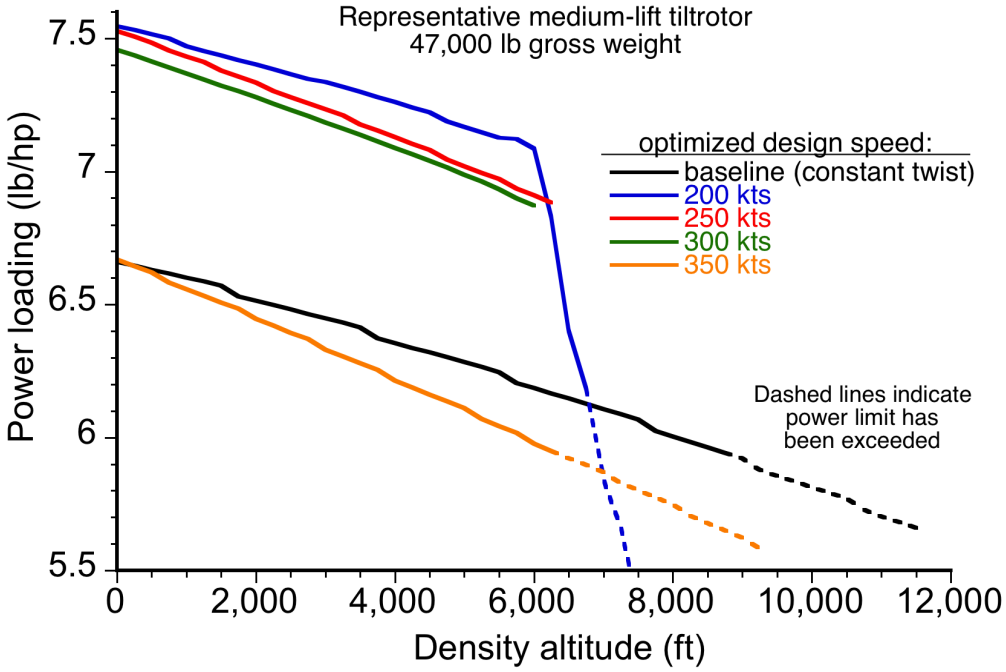

Figure 3.68: Hover power loading for the optimized variable twist proprotors.

Chapter 4

Conclusions

4.1 Summary

The effects of proprotor design parameters and operational characteristics on both hovering and forward flight performance have been examined in this thesis. A new methodology, based on blade element momentum theory, was developed to predict proprotor and convertible-rotor vehicle performance characteristics over a wide range of operating conditions, including forward flight at very high advance ratios and tip Mach numbers up to supersonic. The methodology was validated against performance measurements for high-speed propellers and proprotors, and also against published flight performance data for a contemporary tiltrotor aircraft. A series of parametric studies and optimization studies were performed to help generate a deeper understanding of proprotor aerodynamics and methods that could be used for improving proprotor efficiency. The effects on performance and efficiency that were produced by variable tip speed and variable twist operations were examined in detail.

A main contribution of this research to the knowledge on proprotor aerodynamics is the extensive validation of the predictive model against experimental measurements. The validation is more comprehensive than what has been performed in any work, and establishes a strong level of confidence in the model to predict the aerodynamic loads on proprotors or propellers in forward flight. Another important contribution is the extent of

the parametric studies and optimization studies, which demonstrate clearly the effects of different geometric and operational parameters on proprotor efficiency, both in hover and forward flight. The benefits of different methods for significantly improving proprotor performance are compared and contrasted; these results should serve as a springboard for future proprotor work.

4.2 Specific Conclusions

The following conclusions have been drawn from the studies conducted in this research:

1. The blade element momentum theory with "large angle" modifications was shown to be able to model the thrust and power characteristics of high speed propellers in forward flight. The inclusion of the swirl velocity into the calculations was found to be necessary to obtain satisfactory predictions of the propulsive efficiency at higher values of advance ratio, especially closer to unity.

2. Decreasing the solidity of the proprotor produced significant improvements in propulsive efficiency at the expense of degraded hover performance and reduced stall margins. Reductions in solidity also caused the proprotor to stall at lower forward speeds as propulsive thrust demands increased to overcome vehicle drag. However, using blade twist values that were more suitable for forward flight conditions (rather than hover) helped to delay the onset of blade stall to higher airspeeds.

3. Increased blade twist generally improved propulsive efficiency while decreasing

hover efficiency. There appeared to be no single optimum blade twist that simultaneously maximized both hovering efficiency and propulsive efficiency, except if the proprotor were to be designed for extremely high advance ratios, which in this case means that the needed twist distributions become more and more similar. Compared to the effects of varying twist and solidity, the effects of blade taper and number of blades appeared to have a secondary significance on performance. In some cases, however, more blade taper was shown to moderately improve the hovering efficiency of the proprotor.

4. As a proprotor becomes increasingly optimized for best propulsive efficiency, its design must be balanced between losses in performance from blade stall and losses from the onset of compressibility. Adequate margins must also be allowed for so as to avoid a "coffin-corner" operating state, which is where small excursions in operating conditions may cause a catastrophic loss of thrust, rapid increases in power required, and an overall performance degradation. In this respect, there is a necessary trade between the attainable propulsive efficiency and the stall margins when flying near these constrained operating states.

5. Optimization of the airfoil requirements for cruise conditions resulted in only small improvements in performance, namely small increases in maximum attainable airspeed. More significant gains in overall proprotor performance can be obtained by focusing airfoil design efforts toward meeting hovering flight requirements, especially for the inboard sections of the blade where very high maximum lift coefficients are generally required on proprotors.

6. Variable tip speed proprotor designs were shown to give large improvements in performance in both hovering and cruise modes of flight operation. The results suggested that a variable speed proprotor (VSPR) will have better performance characteristics than a variable diameter proprotor (VDPR). The main drawback to the VDPR concept is the reduction in effective blade twist when the blades are retracted inward for forward flight operation, coupled with the reduction in blade area. However, the VDPR concept becomes more attractive as the required thrust for forward flight decreases, i.e., with improvements to the vehicle lift-to-drag ratio. Ultimately, the preference for either of the VSPR or VDPR designs will depend on the vehicle to which the proprotor is attached, but the VSPR design appears to be the preferred choice for CR aircraft that achieve lower overall lift-to-drag ratios.

7. Variable twist proprotor concepts can also give large improvements in performance over that of a baseline design, i.e., a proprotor where blade twist is compromised between hover and forward flight requirements. The exact performance benefits depend greatly on the cruise speed that the blade twist needs to be optimized for. Variable twist designs can provide increased propulsive efficiencies at higher airspeeds, although the maximum airspeed is ultimately limited by the tip speed used on the proprotor. Raising the maximum attainable airspeed of the proprotor even higher requires significantly reduced tip speed operations so as to delay the onset of compressibility effects.

8. Ultimately, significant improvements to proprotor efficiency may not be practically achieved by using fixed blade geometries and rotational speeds that are unchanged

(or only changed slightly) between hover and forward flight modes of operation. To maximize the aerodynamic performance in both flight modes, it will be necessary to have full authority over the tip speed, solidity, and blade twist during flight. Such a proprotor design may be prohibitively complex and expensive, and perhaps difficult to practically realize. Nevertheless, the desired quantum improvements in performance of future proprotors may only be realized with designs that incorporate full authority over at least one or perhaps two of the critical parameters that affect its performance.

4.3 Suggestions for Future Work

This thesis has described a methodology for predicting the aerodynamic loads on proprotors in hover and in forward flight at high advance ratios. This predictive model has been used to explore some key characteristics of proprotor performance, and to demonstrate the benefits of different potential methods for improving proprotor efficiency. However, there are subjects that could be addressed by future work to gain a further understanding of the aerodynamic performance, efficiency, and design trades needed with advanced proprotors.

The following suggestions are offered:

1. There is a need for further validation of the model against experimental measurements for proprotors at operating conditions representative of both current and expected CR aircraft technology, i.e., advance ratios from 0.25–1.3, airspeeds up to 400 kts, and helical tip Mach numbers approaching supersonic. There is a relative

dearth of comprehensive wind-tunnel data for proprotors in forward flight; the most useful validations of the model described in this thesis were against measurements of high-speed propellers. Additional comprehensive wind-tunnel measurements of proprotors, and covering a wide range of operating conditions, would allow for validations more applicable to a model for proprotor aerodynamics and so increase the predictive confidence with the present model and with other models.

2. Validation with measurements shown in the present work indicated that the model has more limited predictive capabilities at lower blade chord Reynolds numbers. More work will be required to determine the range of Reynolds numbers over which the model has the best and most robust predictive capabilities, and how (perhaps) to modify the model to improve its effectiveness at lower chord Reynolds numbers. This will be a necessary step before the model can be used to confidently predict blade loadings for smaller-scale proprotors, such as those on unmanned CR aircraft.

3. In the present work, optimization studies were performed for proprotor concepts with variable tip speed and variable blade twist. In these studies, it was assumed that each parameter could only be altered between two discrete values, one for hover and one for cruise. In reality, it may be possible to achieve a design where the proprotor diameter, rotational speed, or blade twist are continuously varied. With such a design, a proprotor may be able to reach significantly improved levels of performance by judicious tuning of its shape or rotational speed, depending on the airspeed and atmospheric conditions. Future work could examine continuously variable proprotor designs in more detail, and so determine if they will provide

significant benefits over designs that can vary shape and/or operating state only between two discrete values. For a proprotor with variable blade twist, two types of continuously variable twist could be considered: one where the blade twist rate is coupled to the proprotor rotational speed (such as might be achieved structurally through an extension-twist-coupling effect), or one where the blade twist can be set by inputs specified by the pilot or a flight control or vehicle management system (such as might be achieved using shape memory alloys).

4. The optimization studies performed in the present work used relatively simple objective functions as metrics to describe proprotor performance; typically, cruise and hover efficiencies at specific design points were given equal weighting. This approach demonstrated the usefulness of optimization techniques for proprotor design and has generated some interesting results. However, future work should use objective functions that are more representative of expected CR aircraft mission profiles. For example, objective functions that minimize total fuel burn for an allotted hover duration, range, and time spent at best endurance speed, with constraints being required on stall margins, could provide some interesting results that will expose the potential capabilities of future CR aircraft.

Appendix A

In helicopter analysis the rotor thrust coefficient is formally defined as

$$C_T = \frac{T}{\rho A \Omega^2 R^2} \tag{4.1}$$

where the reference area is the rotor disk area A ($= \pi R^2$)and the reference speed is the blade tip speed, ΩR. The rotor power coefficient is defined as

$$C_P = \frac{P}{\rho A \Omega^3 R^3} \tag{4.2}$$

The corresponding rotor shaft torque coefficient is defined as

$$C_Q = \frac{Q}{\rho A \Omega^2 R^3} \tag{4.3}$$

Notice that because power is related to torque by $P = \Omega Q$, then numerically $C_P \equiv C_Q$. It is important to note that the US customary definition of the thrust, torque and power coefficients is different to that used in some parts of the world (mainly in Britain, most of Europe and Russia), where a factor of one half is used in the denominator giving the set:

$$C_T = \frac{T}{\frac{1}{2}\rho A (\Omega R)^2} \tag{4.4}$$

$$C_Q = \frac{Q}{\frac{1}{2}\rho A (\Omega R)^2 R} \tag{4.5}$$

$$C_P = \frac{P}{\frac{1}{2}\rho A (\Omega R)^3} \tag{4.6}$$

This means that the values of thrust, torque and power coefficients are all a factor of two greater than the values obtained with the US customary definition.

In propeller theory, the values of C_T, C_P are defined differently to those used for helicopter rotors. In this regard, all of the early NACA literature on propeller contain

measurements of performance coefficients that are determined using the following definitions, and caution should be used when manipulating any data. For the thrust coefficient for a propeller, then

$$C_T' = \frac{T}{\rho n^2 D^4} \tag{4.7}$$

where n is the rotational speed of the propeller in revolutions per second, and D is the propeller diameter. Notice that C_T' has been used to distinguish the value of the coefficient from the one used in the helicopter definition. Similarly, the propeller power and torque coefficients are defined as

$$C_P' = \frac{P}{\rho n^3 D^5} \tag{4.8}$$

and

$$C_Q' = \frac{Q}{\rho n^2 D^5} \tag{4.9}$$

Proceeding further by noting that

$$\Omega = 2\pi n \tag{4.10}$$

and

$$D = 2R \tag{4.11}$$

then the propeller performance coefficients can be redefined in terms of Ω and R. For the thrust coefficient then

$$C_T' = \frac{T}{\rho n^2 D^4} = \frac{T}{\rho(\Omega/2\pi)^2(2R)^4} = \frac{4\pi^2 T}{16\rho\Omega^2 R^4} = \left(\frac{4\pi^3}{16}\right)\frac{T}{\rho A \Omega^2 R^2} \tag{4.12}$$

which means that C_T' and C_T are simply related by

$$C_T' = \left(\frac{4\pi^3}{16}\right) C_T \quad (= 7.75 C_T) \tag{4.13}$$

Proceeding in a similar manner for C'_P gives

$$C'_P = \frac{P}{\rho n^3 D^5} = \frac{P}{\rho(\Omega/2\pi)^3(2R)^5} = \frac{8\pi^3 P}{32\rho\Omega^3 R^5} = \left(\frac{8\pi^4}{32}\right)\frac{P}{\rho A\Omega^3 R^3} \tag{4.14}$$

which means that C'_P and C_P are related by

$$C'_P = \left(\frac{8\pi^4}{32}\right) C_P \quad (= 24.35 C_P) \tag{4.15}$$

Finally, for the torque coefficients then

$$C'_Q = \frac{Q}{\rho n^2 D^5} = \frac{Q}{\rho(\Omega/2\pi)^2(2R)^5} = \frac{4\pi^2 Q}{32\rho\Omega^3 R^5} = \left(\frac{4\pi^3}{32}\right)\frac{Q}{\rho A\Omega^3 R^3} \tag{4.16}$$

which means that C'_Q and C_Q are related by

$$C'_Q = \left(\frac{4\pi^3}{32}\right) C_Q \quad (= 3.876 C_Q) \tag{4.17}$$

Appendix B

This appendix contains a paper from the Proceedings of the 68th Annual Forum of the American Helicopter Society, and serves as an abridged version of the information contained within this thesis.

Aerodynamic Design Optimization of Proprotors for Convertible-Rotor Concepts

Conor Stahlhut* J. Gordon Leishman†
Department of Aerospace Engineering
University of Maryland, College Park, MD 20742

Trades in the aerodynamic design of proprotors to power convertible-rotor aircraft have been examined. The most important design challenges are to maximize overall aerodynamic efficiency in both hover and forward flight, as well as preserving adequate stall margins for maneuvering flight. To better assess proprotor performance, a new formulation of the blade element momentum theory for high-speed propellers and proprotors was developed. The approach uses an efficient and robust numerical method to solve simultaneously for the axial and swirl induced velocity components. The efficacy of the approach was validated against measurements of the performance of two NACA high-speed propellers at advance ratios up to 2.5 and tip Mach numbers up to supersonic conditions. The importance of calculating accurately the swirl component of the induced velocity is emphasized. Parametric studies and design optimization studies were performed for different convertible rotor aircraft platforms with the end goal of developing a better understanding of the tradeoff that would be needed for the development of advanced proprotors to power such aircraft. The effects that solidity, diameter, rotational speed, blade twist and taper, number of blades, tip sweep, and airfoil characteristics have on proprotor performance were all explored. Particular importance was given to proprotors with variable tip speed, and the relative advantages of variable diameter versus variable rotational shaft speed concepts.

Nomenclature

a	Speed of sound
A	Rotor disk area
AR	Wing aspect ratio
c	Blade chord
C_d	Sectional drag coefficient
C_{D_0}	Average zero-lift drag coefficient
C_l	Sectional lift coefficient
C_{l_α}	Sectional lift curve slope
C_P	Rotor power coefficient, $= P/\rho A\Omega^3 R^3$
C_T	Rotor thrust coefficient, $= T/\rho A\Omega^2 R^2$
D	Drag
e	Oswald's spanwise efficiency factor
f_e	Effective parasitic drag area
F	Prandtl's tip-loss factor
FM	Figure of merit
L	Sectional lift
$\dot{m}$	Mass flow rate through rotor annulus
M	Mach number
M_{dd}	Drag divergence Mach number
N_b	Number of blades
r	Nondimensional radial position, $= y/R$
R	Rotor radius
P	Rotor power
q_∞	Free-stream dynamic pressure
s_p	Distance between vortex sheets in rotor wake
S	Wing area
T	Rotor thrust
u_i	Induced swirl velocity at rotor disk
u_w	Induced swirl velocity in rotor wake
U	Sectional resultant velocity
U_P	Sectional out-of-plane velocity, $= V_\infty + w_i$
U_T	Sectional in-plane velocity, $= \Omega y - u_i$
V_∞	Free-stream velocity or true airspeed
V_i	Resultant induced velocity at rotor disk
V_w	Resultant induced velocity in rotor wake
w_i	Induced axial velocity at rotor disk
w_w	Induced axial velocity in rotor wake
W	Vehicle weight
y	Distance along blade from rotor axis
α	Angle of attack
β	Blade pitch angle
γ	$\tan^{-1}(C_d/C_l)$
Γ	Circulation
η_p	Propulsive efficiency
λ	Inflow ratio, $= U_P/\Omega R$

*Graduate Research Assistant. email: **stahlhut@umd.edu**
†Minta Martin Professor. email: **leishman@umd.edu**
Presented at the 68th Annual Forum of the American Helicopter Society, Fort Worth, TX, May 1–3, 2012.

λ_i	Induced inflow ratio, = $w_i/\Omega R$
Λ	Tip sweep angle
μ	Advance ratio, = $V_\infty/\Omega R$
ξ	Azimuthal flow ratio, = $U_T/\Omega R$
ξ_i	Induced azimuthal flow ratio, = $u_i/\Omega R$
ρ	Air density
σ	Solidity, = $N_b c/\pi R$
ϕ	Inflow angle
ϕ_∞	Free-stream inflow angle, = $\tan^{-1}(V_\infty/\Omega y)$
Ω	Rotational speed

Introduction

Demanding military and civil vertical lift requirements often lead to the consideration of hybrid, convertible rotor (CR) aircraft concepts such as tiltrotors and tiltwings (Refs. 1–6). In principle, CR aircraft can take off vertically like a helicopter, convert, and then fly at forward speeds approaching those of turboprop airplanes. CR aircraft rely on one or two pairs of rotor-propeller concepts, called proprotors, to sustain flight. When tilted level the proprotors provide lift to overcome aircraft weight and allow for hovering flight, and when tilted forward the proprotors provide propulsion with the lift being carried on a fixed-wing.

The numerous challenges encountered during the design of CR aircraft mean that in practice they can become rather compromised aircraft, severe design trades often adversely impacting their desired fight capabilities, e.g., see Refs. 7–11. While CR aircraft may not necessarily ever attain the high levels of hovering efficiency of helicopters or reach the same speed, payload, and range capabilities of airplanes, they offer the ability to vertically lift payload to greater distances and at higher cruise speeds than helicopters. Civil CR aircraft concepts also continue to be examined to meet certain regional transportation requirements (Refs. 11, 12), where they may be able to operate closer to city centers and help to reduce congestion at larger hub airports. However, even if they are technically realizable, it is the economics of operation and passenger acceptance that will be the ultimate tests for a civil CR aircraft.

The two primary CR configurations are the tiltrotor and tiltwing, although other varieties of the CR concept have been proposed (Ref. 13). With a tiltrotor, the proprotors are tilted relative to the wing to convert between hover and cruise modes of operation. On a tiltwing, both the wings and the rotors are tilted together in unison. From an aerodynamic perspective, tiltrotors generally have a lower hovering efficiency because of the aerodynamic download and other flow interactions on the airframe produced by the wakes from the proprotors. Tiltwing aircraft experience lower download penalties and interactional effects, but they can show adverse susceptibility to crosswinds and ground effect conditions when in helicopter or transition mode. During conversion from helicopter to airplane mode operation, tiltwings tend to have narrower conversion corridors to avoid aeroelastic instabilities such as pylon whirl flutter (Ref. 14). Tiltwings also have a structural advantage over tiltrotors because they can be designed with thinner and more aerodynamically efficient wings for cruising flight (Ref. 1). In practice, however, the tiltrotor configuration has been a preferred design option, with the military V-22 Osprey and the civil AW-609 being the only two CR aircraft currently flying.

Proprotors are required to have high levels of aerodynamic performance over much broader ranges of flight conditions than would be encountered with either a helicopter rotor or with a propeller. Consequently, their performance can become compromised between their two primary modes of operation (Refs. 15–19). For example, a proprotor operating in hover is generally less efficient than a helicopter rotor (i.e., lower power loading and lower figure of merit), and a proprotor operating in forward flight is typically less efficient than a propeller (i.e., lower propulsive efficiency). In hover, the proprotors provide thrust to match the weight of the vehicle (plus any airframe download), and generous blade areas and higher tip speeds are needed. In cruise mode, the thrust must only overcome the drag of the aircraft; good propulsive efficiency requires low profile losses and the minimization of adverse compressibility effects, which demands the use of less blade area and lower tip speeds. Blade twist is also a trade between the two primary modes of flight operation, with significantly less blade twist being needed in hover to avoid reducing the stall margins; generous stall margins are always needed with proprotors so that they can provide the aircraft with sufficient control and maneuverability at low airspeeds.

Therefore, it is not unexpected that a proprotor designed for high cruise speeds, which unlike a propeller must have good static thrust efficiency, will be more difficult to design to avoid significantly compromised levels of performance. It has been suggested that the productivity of a civil tiltrotor will be maximized at cruise speeds of between 360 to 380 kts (Ref. 24), which is near the speeds of contemporary turboprop airplanes. However, the compendium of results shown in Fig. 1 suggests that there are substantial improvements to be realized if new generations of proprotors are to approach the propulsive efficiencies of the best propellers, especially at cruise speeds in excess of 350 kts. Therefore, increasing the efficiency of CR aircraft at airspeeds where contemporary turboprop aircraft currently fly will be critical for establishing their performance and economic viability as civil transport vehicles. Reaching this goal clearly sets down many technical challenges, aerodynamic and otherwise.

Another aspect of the design of proprotors is the need to include high levels of robustness for off-design operations (Ref. 25). To this end, the proprotor design must include good operating margins to allow for maneuvers, gusts, altitude effects, vehicle empty weight growth, and uncertainties in aerodynamic prediction. The robustness

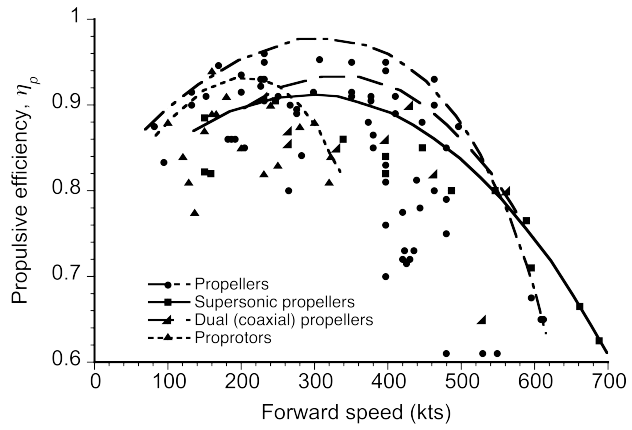

Fig. 1: Measurements of the propulsive efficiencies of propellers and proprotors as a function of forward speed. The lines shown represent the estimated envelope of maximum efficiency for each concept. (Results are from various published sources including NACA, NASA and the RAE, e.g., Refs. 20–23.)

in design philosophy applies particularly to proprotors because of higher overall uncertainties in their predicted performance compared to either helicopter rotors or to airplane propellers. Specifically, the proprotors must achieve high efficiencies and good operating margins even if the performance of the vehicle to which they are attached has been overestimated. To this end, design parameters such as disk loading, solidity, twist, and rotational speed, all need to be balanced between the performance requirements of both hovering and high-speed forward flight.

One approach to significantly increasing the performance of CR aircraft is to judiciously control the tip speed of the proprotors by varying either their rotational speed or diameter, or perhaps both together. Variable speed proprotor (VSPR) or variable diameter proprotor (VDPR) concepts can significantly delay the onset of compressibility effects to higher forward speeds by reducing the helical Mach numbers on the blades as airspeed increases. On one hand, the VSPR concept uses a gearbox to reduce the rotational speed, which maintains engine speed and propulsive efficiency. The so-called Optimum Speed Tilt Rotor (OSTR) is one type of VSPR design that allows for continuously variable rotational speeds to better optimize aerodynamic efficiency over the flight envelope (Ref. 26). On the other hand, the VDPR concept maintains shaft speed and uses a retraction mechanism to draw the blades in toward the hub (Refs. 27–29). After retraction, the blade root is sheathed inside the outboard blade sections, reducing the blade area. However, in either case, reducing tip speed by too much can erode the compressibility/stall margins for the proprotor and produce a "coffin-corner" effect (Ref. 25) similar to that experienced on high performance airplanes at transonic speeds and high altitudes. This latter problem is known to occur on some propellers, which can have very narrow operating margins near their peak propulsive efficiency, e.g., Refs. 30, 31.

The ability to confidently achieve better design compromises with proprotors will be fundamental to realizing future CR aircraft concepts that can operate at higher cruise speeds, have increased flight range, and offer better payloads. At the very least, achieving much better hovering efficiency (i.e., higher power loading approaching the values for a helicopter) simultaneously with better cruise efficiency (i.e., approaching the values of efficiency of contemporary turboprop-powered airplanes) must be a fundamental goal. In this regard, it is not necessarily inevitable that the proprotor that subsequently materializes is as much of an aerodynamic compromise as it has been in the past. While at least some compromises in proprotor performance may still be inevitable, they obviously cannot be allowed to manifest as unanticipated shortcomings in aircraft flight capabilities. Ultimately, it may be that the judicious tuning of vehicle speed, proprotor tip speed, blade pitch (perhaps also blade twist), and engine power setting by a vehicle management system will be needed to extract the best levels of performance from future CR aircraft.

The foregoing design challenges can only be solved successfully by using modeling tools with properly verified predictive capabilities (Ref. 25). To this end, the present paper discusses a numerically efficient approach that can be used to predict proprotor performance over broad ranges of operating conditions. The model is validated against wind-tunnel data for high-speed propellers, as well as against published performance data for CR aircraft. It is then used within the framework of a formal optimization approach to investigate trades in the various design parameters as they will affect both the hovering and propulsive performance of the proprotor. The sensitivity of the resulting levels of performance to the design parameters was also examined.

The overall goal of the work was to develop a modeling framework to expeditiously find the blade and proprotor designs that would give the highest levels of efficiency to meet the requirements of the vehicle, as well as the constraints imposed by practical flight operations. The results show that there are still many challenges in proprotor design but also exciting opportunities in the development of proprotors with substantially improved capabilities that can be used to power new generations of CR aircraft.

Methodology

Validated mathematical models can be used to help understand the limiting performance issues encountered by proprotors and to expose the levels of performance expected from new proprotor designs. To this end, validation with measurements of propeller and/or proprotor performance characteristics over appropriately broad ranges of operating conditions is critical.

The method used in the present work is a new development of the well-known blade element momentum theory

(BEMT), but specifically formulated for propellers and proprotors. In general, the BEMT is mathematically parsimonious and computationally expedient, but has been previously validated only to a limited extent for propellers and proprotors (Refs. 18, 25, 32). The BEMT combines the principles of the blade element and momentum theory approaches of lift (Refs. 33–36). The sectional aerodynamics are modeled using tables of coefficients, for which several optional sets of airfoils can be incorporated. In the present work, the BEMT approach was formally generalized to large angles and included a better method for simultaneously solving for the inflow and swirl induced velocity components in the wake.

Large Angle Approach

Figure 2 shows the angles, velocities, and force vectors acting on a blade element of a proprotor. The airfoil sections, which are at pitch angles β to the rotor plane, are at effective angles of attack α to the local flow, which has a relative velocity of U to the blade sections. The blade pitch varies along the span of the blade, and is normally defined relative to the zero-lift angle of the airfoil(s) being used. The out-of-plane velocity component, U_P, is the sum of the forward velocity, V_∞, and the induced axial velocity, w_i. The in-plane velocity component, U_T, is the difference between the rotational tangential speed, Ωy, and the induced swirl velocity, u_i. All of the velocity components are defined with respect to the leading edge of the blade, which may be swept with respect to a spanwise reference axis. It is apparent that the inflow angle, ϕ, is affected by both the w_i and u_i components of the induced velocity.

For a proprotor in high-speed forward flight the inflow angles can be large, often exceeding 45° near the blade tips. Therefore, the lift vectors on the blade sections may induce flow velocities in the in-plane direction that are even greater than the inflow components, so both the thrust and torque components will determine the induced flow field. The approach used in the present study differs from the classical approach in three ways: 1. The removal of all small angle assumptions, 2. Formal inclusion of the in-plane or swirl velocity components, and 3. A large angle modification to the classic Prandtl tip loss function.

Without using any small angle assumptions, the incremental thrust coefficient generated by a blade element is

$$dC_T = \frac{dT}{\rho A (\Omega R)^2} = \frac{N_b (dL\cos\phi - dD\sin\phi)}{\rho A (\Omega R)^2} \quad (1)$$

$$= \frac{N_b \left(\frac{1}{2}\rho U^2 c\right)(C_l\cos\phi - C_d\sin\phi)\,dy}{\rho A (\Omega R)^2} \quad (2)$$

$$= \frac{1}{2}\sigma\frac{\sqrt{U_T^2+U_P^2}\,(C_l U_T - C_d U_P)}{(\Omega R)^2}\,d\left(\frac{y}{R}\right) \quad (3)$$

$$\text{i.e.,}\quad dC_T = \frac{1}{2}\sigma\sqrt{\xi^2+\lambda^2}\,(C_l\xi - C_d\lambda)\,dr \quad (4)$$

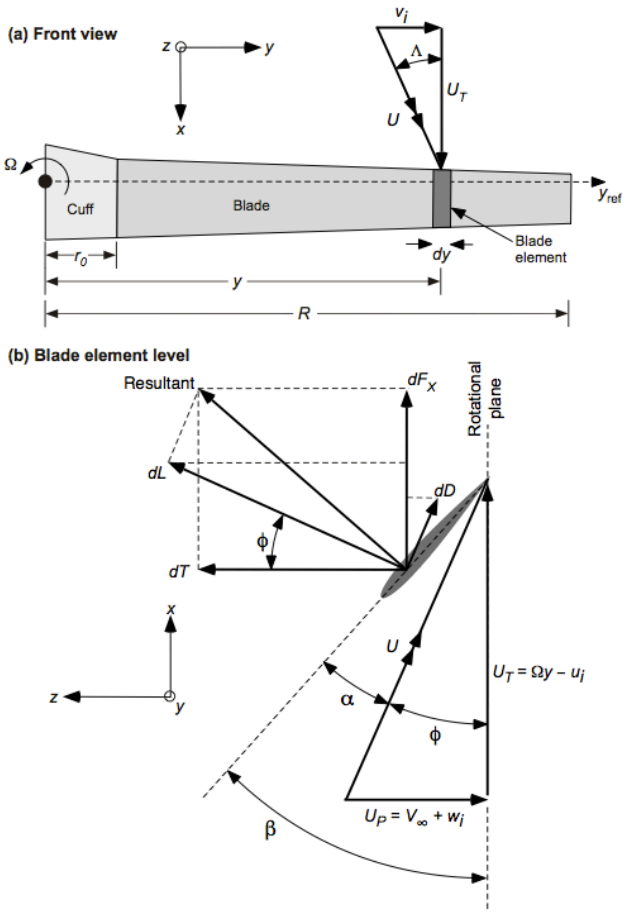

Fig. 2: The blade element convention used for proprotor analysis.

The inflow ratio $\lambda = (V_\infty + w_i)/\Omega R$ and azimuthal flow ratio $\xi = (\Omega y - u_i)/\Omega R$ are the components of the total velocity perpendicular and parallel to the rotor plane, respectively, both being nondimensionalized by tip speed. The incremental power coefficient required by a blade element is

$$dC_P = \frac{dP}{\rho A (\Omega R)^3} = \frac{N_b (dL\sin\phi + dD\cos\phi)\,\Omega y}{\rho A (\Omega R)^3} \quad (5)$$

$$= \frac{N_b \left(\frac{1}{2}\rho U^2 c\right)(C_l\sin\phi + C_d\cos\phi)\,\Omega y\,dy}{\rho A (\Omega R)^3} \quad (6)$$

$$= \frac{1}{2}\sigma\frac{\sqrt{U_T^2+U_P^2}\,(C_l U_P + C_d U_T)}{(\Omega R)^2}\,\frac{y}{R}\,d\left(\frac{y}{R}\right) \quad (7)$$

$$\text{i.e.,}\quad dC_P = \frac{1}{2}\sigma\sqrt{\xi^2+\lambda^2}\,(C_l\lambda + C_d\xi)\,r\,dr \quad (8)$$

Table 1 summarizes the blade element equations with and without the small angle assumptions and the swirl velocity.

The BEMT also uses differential momentum theory to determine the aerodynamics at the blade element. The rotor disk is divided into a number of annuli of area $2\pi y dy$. Conservation of momentum gives $dT = \dot{m} w_w$ and $dF_X = \dot{m} u_w$, where $\dot{m}$ is the mass flow rate through the annulus, and w_w and u_w are the induced axial and azimuthal velocities in the

Table 1: Comparison of blade element terms with and without the small angle assumption and swirl velocity.

Large angle assumptions	dT	$N_b\left(dL\cos\phi - dD\sin\phi\right)$
	dP	$N_b\left(dL\sin\phi + dD\cos\phi\right)\Omega y$
	dC_T	$\frac{1}{2}\sigma\sqrt{\xi^2+\lambda^2}\left(C_l\xi - C_d\lambda\right)dr$
	dC_P	$\frac{1}{2}\sigma\sqrt{\xi^2+\lambda^2}\left(C_l\lambda + C_d\xi\right)r\,dr$
	ϕ	$\tan^{-1}\left(\lambda/\xi\right)$
Small angle assumptions	dT	$N_b dL$
	dP	$N_b\left(\phi dL + dD\right)\Omega y$
	dC_T	$\frac{1}{2}\sigma C_l r^2 dr$
	dC_P	$\frac{1}{2}\sigma\left(C_l\lambda + C_d r\right)r^2 dr$
	ϕ	λ/r

wake. The conservation of energy is also applied, giving the result that $w_w = 2w_i$ and $u_w = 2u_i$. The thrust and power coefficients at each annulus then become

$$dC_T = 4\left|\lambda\right|\lambda_i r\,dr \tag{9}$$

and

$$dC_P = 4\left|\lambda\right|\xi_i r^2\,dr, \tag{10}$$

respectively, where $\lambda_i = w_i/\Omega R$ and $\xi_i = u_i/\Omega R$. The absolute values in Eqs. 9 and 10 are necessary for the case where an upflow through the rotor annulus is predicted, which can sometimes occur on a proprotor in the normal working state, such as in hover or at low forward speeds.

Tip-Loss for Large Angles

A Goldstein/Prandtl tip-loss model was used to account for the increased induced losses at the blade tips. Goldstein (Ref. 37) established a method for tip-loss by using the velocity potential of a series of helical vortex sheets in the rotor wake. The vortex sheets form a pitch helical angle ϕ with the rotor plane. The sheets move perpendicular to their plane at a speed V_w, where $V_w = \sqrt{w_w^2 + u_w^2}$ is the resultant induced velocity in the wake. A simplified version of the Goldstein result was first developed by Prandtl (Ref. 38), who approximated the helical surface as a series of two-dimensional planar sheets that convect at the slipstream velocity, which is a more practical realization of Goldstein's approach (Ref. 39).

Assuming the flow around the blade is irrotational, then the bound circulation Γ of a blade element is equal to the difference in velocity potential between the top and bottom surfaces of the blade section (Ref. 40). For a series of two-dimensional sheets then

$$\Gamma = \frac{2V_w s_p}{\pi}\cos^{-1}\left[\exp\left(\frac{-\pi a}{s_p}\right)\right] \tag{11}$$

where a is the distance between a blade section and the blade tip and $s_p = \left(2\pi y/N_b\right)\sin\phi$ is the normal distance between adjacent sheets. Defining $V_w = 2V_i$, where $V_i = \sqrt{w_i^2 + u_i^2}$ is the resultant induced velocity at the rotor plane, then

$$\Gamma = \frac{4\pi y V_i F}{N_b}\sin\phi \tag{12}$$

where

$$F = \frac{2}{\pi}\cos^{-1}\left[\exp\left(\frac{N_b\left(r-1\right)}{2r\sin\phi}\right)\right] \tag{13}$$

Notice that F, Prandtl's tip-loss factor, decreases with increases in r, indicating that the tip vortices have a greater effect closer to the blade tip. The value of F also decreases as ϕ is increased and N_b is reduced, showing that the effect of the tip vortices becomes stronger as the spacing decreases between the vortex sheets. However, Prandtl's assumption of two-dimensional vortex sheets becomes less accurate as s_p increases. Strictly speaking, F should be a function of the vortex sheet spacing at the blade tip, i.e., the term in the exponent in Eq. 13 should be $N_b(r-1)/(2\sin\phi_{\text{tip}})$. However, it is sufficiently accurate to use the local inflow angles, which are more convenient (Ref. 41).

To incorporate tip-loss effects, the Kutta-Joukowski theorem is used with the blade element expressions in Eqs. 4 and 8, i.e.,

$$\frac{1}{2}\rho U^2 c\left(C_l\cos\phi - C_d\sin\phi\right) = \rho U_T\Gamma \tag{14}$$

and

$$\frac{1}{2}\rho U^2 c\left(C_l\sin\phi + C_d\cos\phi\right) = \rho U_P\Gamma \tag{15}$$

Using the relations from Eqs. 12, 14, and 15, the circulation, Γ, is then substituted into Eqs. 4 and 8 to give

$$dC_T = \frac{1}{2}\left(\frac{N_b c}{\pi R}\right)\frac{U^2\left(C_l\cos\phi - C_d\sin\phi\right)}{\left(\Omega R\right)^2}dr \tag{16}$$

$$= \frac{N_b U_T\Gamma}{\pi R\left(\Omega R\right)^2}dr = \frac{4FV_i U_T r\sin\phi}{\left(\Omega R\right)^2}dr \tag{17}$$

$$\text{i.e.,}\quad dC_T = 4F\lambda\frac{V_i\cos\phi}{\Omega R}r dr \tag{18}$$

and

$$dC_P = \frac{1}{2}\left(\frac{N_b c}{\pi R}\right)\frac{U^2\left(C_l\sin\phi + C_d\cos\phi\right)\Omega y}{\left(\Omega R\right)^3}dr \tag{19}$$

$$= \frac{N_b U_P\Gamma\Omega y}{\pi R\left(\Omega R\right)^3}dr = \frac{4FV_i U_P r^2\sin\phi}{\left(\Omega R\right)^2}dr \tag{20}$$

$$\text{i.e.,}\quad dC_P = 4F\lambda\frac{V_i\sin\phi}{\Omega R}r^2 dr \tag{21}$$

Equations 18 and 21 are the same as Eqs. 9 and 10 except for the inclusion of the tip-loss factor F and the replacement of λ_i with $V_i\cos\phi/\Omega R$ and ξ_i with $V_i\sin\phi/\Omega R$.

Because an inviscid theory is used to obtain Eqs. 18 and 21, they are only completely valid when the directions of

w_i and u_i are opposite to that of the corresponding force vectors. Equation 18 is only strictly valid when $\phi = 0^\circ$, and Eq. 21 is only valid when ϕ=90°. At ϕ=90° for dC_T and ϕ=0° for dC_P, the tip vortices do not contribute to the induced velocities w_i and u_i.

To reconcile Eqs. 18 and 21 with the expected physical behavior, the expressions for the decreases in thrust and power, the terms $4\lambda\lambda_i r dr(1-F)$ and $4\lambda\xi_i r^2 dr(1-F)$, should gradually decrease to zero as the angles increase between the tip vortices and the blade force vectors. To model this behavior, the differential momentum theory equations for the thrust and power coefficients can be modified to read

$$dC_T = 4K_T\,|\lambda|\,\lambda_i r\,dr \tag{22}$$

and

$$dC_P = 4K_P\,|\lambda|\,\xi_i r^2\,dr, \tag{23}$$

respectively, where $K_T = [1-(1-F)\cos\phi]$ and $K_P = [1-(1-F)\sin\phi]$.

It is necessary to account for tip-loss effects because only some of the induced flow arises from momentum conservation, the remainder being from the presence of the tip vortices. The value of F can be viewed as the ratio of V_i that is directly induced by the rotor to the total V_i. Likewise, K_T and K_P are the ratios of the w_i and u_i that are directly induced by the rotor to the total w_i and u_i, respectively.

Numerical Solution for Inflow Components

To solve for the induced flow components, the blade element expressions for the incremental thrust and power coefficients are equated to those from momentum theory, i.e.,

$$\begin{aligned} dC_T &= \frac{1}{2}\sigma\sqrt{\xi^2+\lambda^2}\,(C_l\xi - C_d\lambda)\,dr \\ &= 4K_T\,|\lambda|\,\lambda_i r\,dr \end{aligned} \tag{24}$$

and

$$\begin{aligned} dC_P &= \frac{1}{2}\sigma\sqrt{\xi^2+\lambda^2}\,(C_l\lambda + C_d\xi)\,r\,dr \\ &= 4K_P\,|\lambda|\,\xi_i r^2 dr \end{aligned} \tag{25}$$

One way to solve this system of equations for λ and ξ is by fixed-point iteration. However, convergence is usually slow and relaxation tends to be necessary. Alternatively, the thrust and power equations can be expressed in terms of the inflow angle ϕ and combined into a single transcendental equation, as shown by Winarto (Ref. 42). In this case, only one equation needs to be solved.

Recognizing that $\lambda = U\sin\phi/\Omega R$ and $\xi = U\cos\phi/\Omega R$, Eq. 24 can be rewritten as

$$\frac{1}{2}\sigma\frac{U^2\,(C_l\cos\phi - C_d\sin\phi)}{(\Omega R)^2}dr = 4K_T\,|\lambda|\,\lambda_i r\,dr \tag{26}$$

Defining $\tan\gamma = C_d/C_l$ and substituting $C_l\tan\gamma$ for C_d, while also dimensionalizing by $(\Omega R)^2$ gives

$$\frac{1}{2}\sigma U^2 C_l\sec\gamma(\cos\gamma\cos\phi - \sin\gamma\sin\phi) = 4K_T U\sin|\phi|\,w_i r \tag{27}$$

Using the identity $\cos(\phi+\gamma) = \cos\phi\cos\gamma - \sin\phi\sin\gamma$, and recognizing that $w_i = U\sin\phi - V_\infty$, the above equation can be rearranged into

$$\frac{1}{8K_T}\sigma\frac{1}{r}UC_l\sec\gamma\csc|\phi|\cos(\phi+\gamma) = U\sin\phi - V_\infty \tag{28}$$

A function $B_1(\phi)$ is now defined as

$$B_1(\phi) = \frac{V_\infty}{U} = \sin\phi - \frac{1}{8K_T}\sigma\frac{1}{r}C_l\sec\gamma\csc|\phi|\cos(\phi+\gamma) \tag{29}$$

A similar method is used rewrite Eq. 25 to obtain a function $B_2(\phi)$, i.e.,

$$B_2(\phi) = \frac{\Omega y}{U} = \cos\phi + \frac{1}{8K_P}\sigma\frac{1}{r}C_l\sec\gamma\csc|\phi|\sin(\phi+\gamma) \tag{30}$$

Equations 29 and 30 can then be combined into a single transcendental equation, i.e.,

$$g(\phi) = [B_1(\phi)\,\Omega y - B_2(\phi)\,V_\infty]\sin\phi = 0 \tag{31}$$

or

$$\begin{aligned} g(\phi) = {} & (\Omega y\sin\phi - V_\infty\cos\phi)\sin\phi \\ & -\mathrm{sgn}(\phi)\,\frac{\sigma C_l\sec\gamma}{8r}\left[\frac{\Omega y}{K_T}\cos(\phi+\gamma) + \frac{V_\infty}{K_P}\sin(\phi+\gamma)\right] \end{aligned} \tag{32}$$

The signum function is introduced into Eq. 32 because the absolute values in Eqs. 29 and 30 were cancelled out in the derivation of $g(\phi)$.

In Eq. 32, the inflow angle, ϕ, is the only unknown. The values of C_l, C_d, K_T, and K_P are themselves functions of several variables of which ϕ is the only unknown. If the lift coefficient is zero, then $g(\phi) = (\Omega y\sin\phi - V_\infty\cos\phi)$ should be solved instead of Eq. 32. The inflow ratio and azimuthal flow ratio can then be calculated and introduced into Eqs. 4 and 8 to obtain the incremental thrust and power at that particular blade section. The inflow and swirl velocity ratios can be obtained using

$$\xi = r\frac{\cos\phi}{G(\phi)} \tag{33}$$

and

$$\lambda = \xi\tan\phi, \tag{34}$$

respectively.

Equation 32 cannot be solved using a fixed-point iterative method because of poor convergence characteristics and the existence of a range of ϕ that result in undefined solutions. However, the solution to this transcendental equation can be found using other root-finding methods, although derivative-based methods such as Newton's method

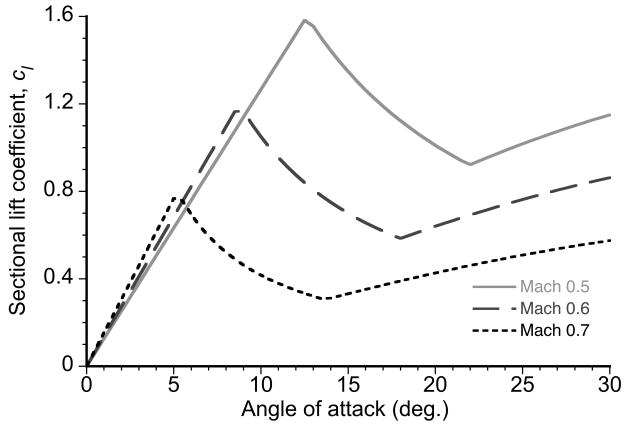

Fig. 3: Representation of sectional airfoil lift coefficients at different Mach numbers.

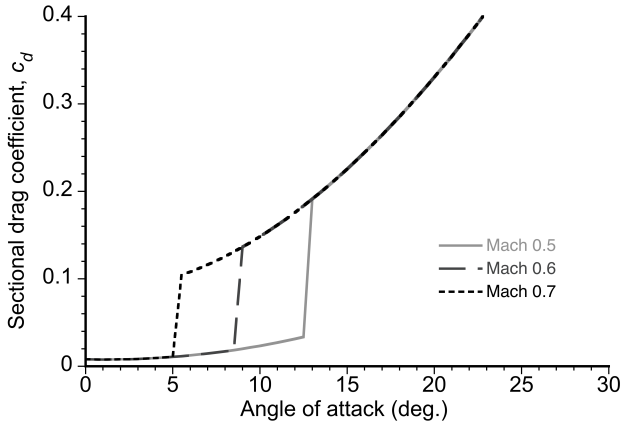

Fig. 4: Representation of sectional airfoil drag coefficients at different Mach numbers.

are not helpful either because the derivative of Eq. 32 has a nonlinearity from the C_l and C_d terms; if reading data from airfoil tables then the derivative can only be approximated.

The bracketed bisection method was found to be suitable for solving Eq. 32 because of its guaranteed convergence. This method works by realizing that a single solution for ϕ is located within a range bracketed between two points, and then halving this range with each iteration. Although the bisection method is among the slowest of root-finding methods, it can solve for ϕ roughly three times faster than solving for the induced velocity components separately. The bisection method is also very robust, and if there is only one solution it is impossible for the method to fail to converge.

A complication arises in the implementation of the bisection method for a hovering rotor, as occasionally there are multiple solutions to ϕ, one positive and one negative. To determine the correct solution, $g(\phi)$ in Eq. 32 is first calculated for $\phi = 0$. If $g(0) > 0$, then ϕ is negative. If $g(0) \leq 0$, then ϕ is positive. The boundaries for the bracketed solution are then adjusted accordingly.

Airfoil Characteristics

Airfoil characteristics can be read in the conventional way from a collection of "C-81" like tables listing values of sectional C_l and C_d for ranges of angles of attack, Mach numbers, and Reynolds numbers. However, such data is often not available and other approaches must be used to define the airfoil characteristics. Whatever models are used, it is imperative that they include stall and post-stall characteristics; in this regard, the compromised blade twist used on proprotors means that a significant portion of the blade may stall in hover and/or over some range of forward flight speeds. The sectional lift and drag model assumed in the present study are shown in Figs. 3 and 4. After the blade stalls, drag increases as flow separation occurs. Lift decreases with further increases in angle of attack until the airfoil begins to act more as a flat plate.

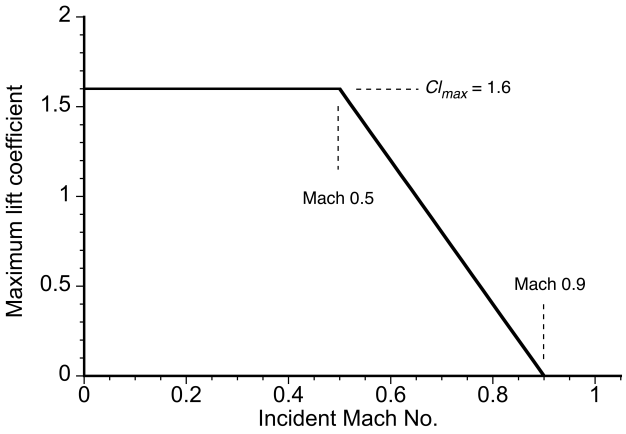

Fig. 5: Model for maximum lift coefficient versus Mach number.

Modeling compressibility effects at higher Mach numbers is also necessary. In the attached flow regime, the lift curve slope, C_{l_α}, can be adjusted by the Glauert rule, i.e.,

$$C_{l_\alpha} = \frac{C_{l_\alpha}|_{M=0.1}}{\sqrt{1-M^2}} \tag{35}$$

where $C_{l_\alpha}|_{M=0.1}$ is the lowest value for the lift curve slope. The maximum lift coefficient of an airfoil is also a function of Mach number. One representation, shown in Fig. 5, is that $C_{l_{\max}}$ remains constant up to a certain value of M, at which point it decreases linearly with further increases in M.

Compressibility also has an effect on drag. In particular, the drag on an airfoil begins to increase rapidly as the oncoming flow reaches the drag divergence Mach number, $M_{\rm dd}$. One approximation that has been used for the increase in drag approaching drag divergence is (Ref. 43)

$$\Delta C_d = \begin{cases} 12.5\,(M - M_{\rm dd} + 0.08) & \text{if} \quad M \geq (M_{\rm dd} - 0.08) \\ 0 & \text{otherwise} \end{cases}$$

Tip Relief

A compressibility tip relief model was used, which acts to delay the onset of drag divergence at the blade tip sections. Because of three-dimensional flow at the tip, the effects of compressibility are relaxed. When a blade section within one chord-length of the tip exceeds $M_{\rm dd}$, there is a reduced effective local Mach number, which can be approximated by (Ref. 43), i.e.,

$$M_{\rm eff} = M\left[\frac{M_{\rm dd2}}{M_{\rm dd3}} + \left(1 - \frac{M_{\rm dd2}}{M_{\rm dd3}}\right)(1-r)AR_{\rm blade}\right] \quad (36)$$

where $AR_{\rm blade}$ is the blade aspect ratio, $M_{\rm dd2}$ is the 2-dimensional drag divergence Mach number, and $M_{\rm dd3}$ is the assumed 3-dimensional drag divergence Mach number.

Spinner Effects

The presence of a spinner can result in high supervelocities near the blade roots, which are caused by the oncoming flow accelerating as it passes over the spinner. For proprotors, where the spinner diameter can be a significant fraction of the proprotor diameter, the supervelocity can have a significant effect on the blade aerodynamics by increasing the Mach number and altering the inflow angle distribution. This effect can be an issue in particular with a variable diameter proprotor design because the rotor diameter is reduced in forward flight and the spinner needs to be large enough to contain the blade retraction mechanisms.

If the spinner effects are approximated as an equivalent sphere, then potential flow theory gives the supervelocity, $V_{\rm sup}$, as (Ref. 44)

$$V_{\rm sup} = \frac{V_\infty}{2}\left(\frac{R_{\rm rotor}}{R_{\rm spinner}}\right)^3 \quad (37)$$

The increment in supervelocity is equal to half the free-stream velocity where the spinner meets the blade root, and then drops off quickly with distance outboard of the spinner.

Tip Sweep

Tip sweep can be employed on proprotor blades to delay the onset of compressibility by reducing the effective Mach number normal to the blade leading edge. The sweep angle, Λ, is implemented into the calculations by multiplying $\cos\Lambda$ by the components of both U_T and U_P, which are perpendicular to the leading edge.

Ignoring the induced velocity but accounting for both sweep and supervelocities, the effective Mach number at a blade section is then

$$M = \frac{1}{\rm a}\sqrt{U_T^2 + U_P^2} \quad (38)$$

where

$$U_T^2 = (\Omega y)^2\left[\cos^2\beta\cos^2\Lambda + \sin^2\beta\right]$$

and

$$U_P^2 = V_\infty^2\left[1 + \frac{1}{2}\left(\frac{R_{\rm rotor}}{R_{\rm spinner}}\right)^3\right]^2\left[\cos^2\beta + \sin^2\beta\cos^2\Lambda\right]$$

Optimizer

Some of the results reported in this article were obtained using a formal optimization approach. The optimizer was validated by optimizing proprotor efficiency using up to six design variables. Parametric studies were performed to confirm that the optimizer gave physically correct results and successfully minimized the stated objective function(s).

At its most elementary level, the optimizer works by applying small perturbations to each of the design variables to obtain a profitable search direction, and then minimizes an objective function along this direction. This process continues until convergence occurs. Side constraints (i.e., the upper and lower boundaries of the design variables) are specified prior to the start of the optimization.

If no constraints are imposed, then the optimizer uses the Broydon-Fletcher-Goldfarb-Shanno algorithm. If constraints are imposed (e.g., engine power available or transmission limits), then the method of feasible directions (MFD) is used. The MFD seeks the lowest possible value of the objective function that does not violate the constraints.

Results and Discussion

The results in this article are discussed in four parts, which are preceded by a description of the proprotor designs and CR aircraft for which results were obtained: 1. Validation of the proprotor model with propeller measurements, isolated proprotor measurements, and CR vehicle performance; 2. Parametric studies of proprotor and vehicle performance; 3. Optimization of the proprotor airfoils, and 4. Optimization for variable tip speed operations.

CR Aircraft Used in this Study

The results discussed in the present article were obtained using proprotors designed for three different CR configurations, namely: 1. A representative medium-lift tiltrotor; 2. The Sikorsky VDTR concept; and 3. The *Excalibur*, which is also a VDTR concept and was the University of Maryland's winning entry in the 2011 Annual AHS Design Competition (Ref. 45). These proprotors were used for the purposes of validation of the modeling and also to show the sensitivities in performance to parametric variations in the design parameters.

Table 2: Essential characteristics of the three CR configurations used in the present study.

Characteristic	Medium-Lift Tiltrotor	VDTR	*Excalibur*
Max. VTOL GTOW	51,000 lb	–	18,000 lb
Installed power	2 x 6,150 hp	–	2 x 1,908 hp
Proprotor diameter	38.1 ft	49.2 ft	30.5 ft
Shaft speed	412 rpm	264 rpm	505 rpm
Proprotor solidity	0.102	0.085	0.070
Vehicle f_e	26.0 ft^2	–	6.0 ft^2
Wing AR	6.97	–	6.0
Wing C_{D_0}	0.01	–	0.008
e	0.8	–	0.87
S	301.6 ft^2	–	267.2 ft^2

Some of the relevant vehicle specifications are given in Table 2. Notice that the VDTR and *Excalibur* are both variable-diameter proprotor concepts, the blades retracting to 2/3 of their maximum diameter. The net performance of the medium-lift tiltrotor and *Excalibur* proprotors were evaluated when coupled to a representation of their respective airframes, including the performance limits imposed by the engine and/or the transmission.

The thrust needed from the proprotors in hover was assumed to be equal to vehicle weight plus a margin to account for download on the wings, this being 12% of weight. The thrust needed in forward flight depends on the vehicle drag (i.e., its lift-to-drag ratio), so the thrust required in this case becomes a function of forward speed. The vehicle drag, D_{veh}, was calculated using

$$D_{\text{veh}} = q_\infty (f_e + S C_{D_0}) + \frac{W^2}{q_\infty S \pi AR e} \tag{39}$$

Validation of the Modeling

Validation with Propeller Measurements

The proprotor model was validated against wind-tunnel data for two NACA "high-speed" propellers. While some proprotor measurements are also available (Refs. 15,46,47), such measurements do not cover the wide range of operating conditions that are needed to validate all aspects of the modeling. Therefore, the two propellers identified by Harris (Ref. 48), which are representative of both the geometry of a proprotor and of the wide operating conditions that may be encountered by an advanced high-speed proprotor, were used instead.

The performance characteristics of these two propellers were measured in the NACA wind tunnels, one propeller being 2-bladed with a 4 ft diameter (Ref. 49) and the other being 3-bladed with a 9.75 ft diameter (Ref. 50). The 2-bladed propeller had a 2:1 blade taper from root to tip, and the 3-bladed propeller had constant chord untapered blades. Each propeller had approximately 32° of nose-down twist over the blade, and the boss (for the spinner and blade attachments) in each case was 27% of radius.

Parametric measurements for the 2-bladed propeller were taken by varying rotational speed while keeping tunnel wind speed and blade pitch constant. For the 3-bladed propeller, the measurements were taken by fixing the rotational speed and blade pitch while the wind speed was varied. The net result in either case (i.e., of systematic variations of wind speed at a constant blade pitch and/or blade pitch variations at a constant wind speed) are sets of propeller thrust, power, and efficiency curves as a function of the operating advance ratio (Ref. 33). In some of the operating conditions for the 3-bladed propeller, the thinner blades were reported to have experienced stall flutter and so could not operate continuously at these conditions (Ref. 50).

Predictions from the present model versus the propeller measurements are shown in Figs. 6 through 9 for the 2-bladed propeller, and in Figs. 10 through 13 for the 3-bladed propeller, in each case as sets of thrust, power and propulsive efficiency curves. Actual sectional airfoil characteristics were not available for either propeller, so generic airfoil tables in the forms described previously were used to represent the lift and drag coefficients in the modeling.

The reported measurements in Refs. 49 and 50 were converted from conventional propeller nomenclature into conventional helicopter rotor nomenclature, in this case in the form of C_T/σ and C_P/σ coefficients. The advance ratio is defined conventionally for helicopters as $\mu = V_\infty/\Omega R$; when multiplied by a factor of π, the forward speed ratio is equivalent to the advance ratio "J" used for propeller performance evaluations. The propulsive efficiency is defined using the helicopter nomenclature as $\eta_p = C_T\mu/C_P$, which gives the same numerical result when using the conventional propeller nomenclature.

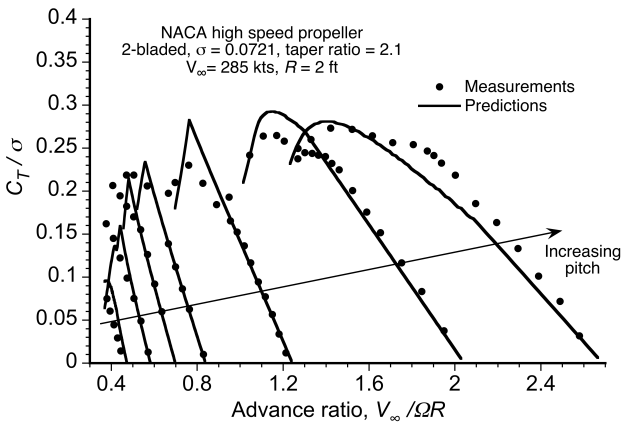

Fig. 6: Thrust in the form of C_T/σ versus advance ratio for the 2-bladed NACA propeller.

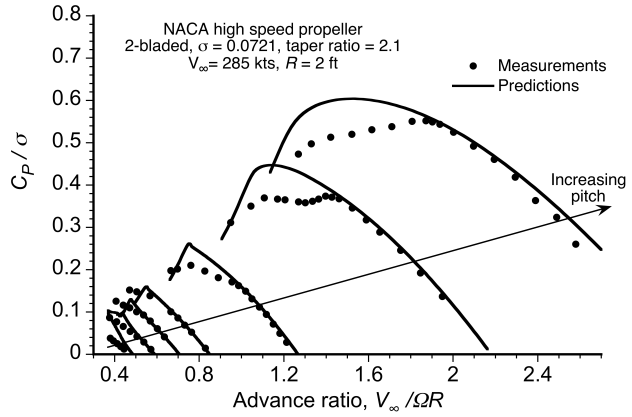

Fig. 7: Power in the form of C_P/σ versus advance ratio for the 2-bladed NACA propeller.

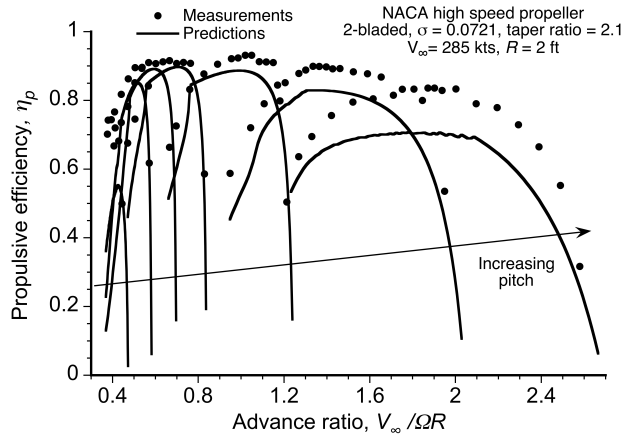

Fig. 8: Propulsive efficiency versus advance ratio for the 2-bladed NACA propeller.

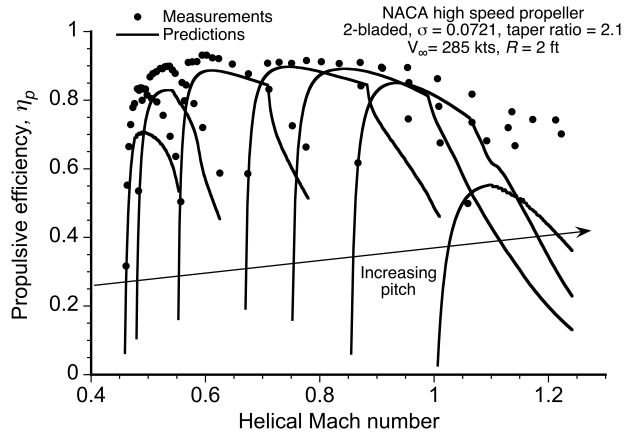

Fig. 9: Propulsive efficiency versus helical tip Mach number for the 2-bladed NACA propeller.

The results in Figs. 6 through 9 are for the 2-bladed propeller, which show good overall agreement between the model and the measurements. In many cases the agreement is excellent. General predictions of propeller performance over such wide ranges of operating conditions is very challenging, and the results shown here are actually very good relative to what would be obtained by using any model of propeller performance. Recall that these particular propeller data are useful for the validation of the present model because they encompass the operating conditions where an advanced proprotor may operate.

Figures 6 through 9 expose several general aspects of propeller performance. At low values of operating advance ratio the blades become partly stalled, so the propellers generate some thrust but need relatively high power. Increasing advance ratio for a fixed blade pitch causes the flow on the blades to progressively attach causing the propellers to produce more thrust, the corresponding initial power requirements also reaching a peak. Thereafter, the thrust and power both decrease with increasing values of advance ratio at a constant blade pitch. Eventually, as the advance ratio increases to higher values, the propeller produces near zero or negative thrust as the brake state is reached. Repeating the process for increasing values of blade pitch produces a set of curves where the brake state is reached at progressively higher advance ratios. Figure 9 illustrates how compressibility effects cause a rapid reduction in peak propulsive efficiency as the blade tips approach and exceed a Mach number of unity.

Overall, the predictions made for the 2-bladed propeller showed good agreement with the measurements except for at the very lowest and highest blade pitch settings. At the lowest blade pitch, this propeller actually operates with some supersonic flow, so at least some of the differences shown can be attributed to the efficacy of the assumed airfoil model in the transonic and supersonic flow regimes. The supersonic flow in this case arises because in the tunnel the wind speed was held constant while the rotational speed of the propeller was progressively increased to relatively high values, and so low pitch settings correspond to relatively high tip speeds that reach into the supersonic regime. At the highest blade pitch settings, it can be seen that the thrust on the propeller (see Fig. 6) was somewhat underpredicted and the power requirements (see Fig. 7) were overpredicted, which also causes the propulsive efficiency to be underpredicted (see Fig. 8). However, the overall performance trends shown for this 2-bladed propeller are quite well represented by the modeling.

In addition to operating partially in the supersonic range and also at very high advance ratios, which each pose challenges for the modeling, this propeller had sectional Reynolds numbers that were lower than for the 3-bladed propeller (considered next) and so uncertainties in the sectional characteristics are also higher. At lower chord Reynolds numbers, the effects of rotation of the three-dimensional boundary developments can be more pronounced, and tend to manifest as modeling deficiencies at the higher operating thrusts. However, no representation of rotational augmentation effects has been included into the present level of modeling.

In general, the results from the model were found to be in somewhat better overall agreement for the 3-bladed pro-

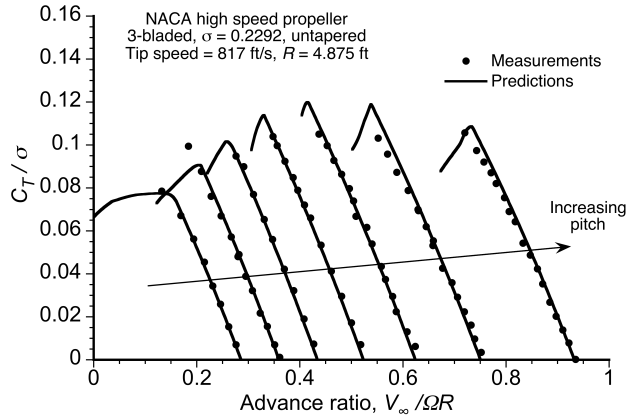

Fig. 10: Thrust in the form of C_T/σ versus advance ratio for the 3-bladed NACA propeller.

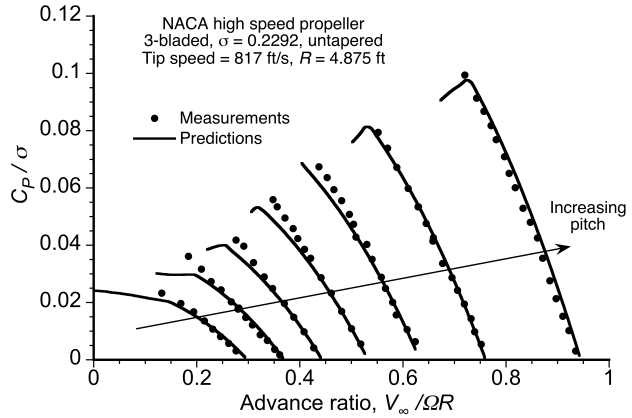

Fig. 11: Power in the form of C_P/σ versus advance ratio for the 3-bladed NACA propeller.

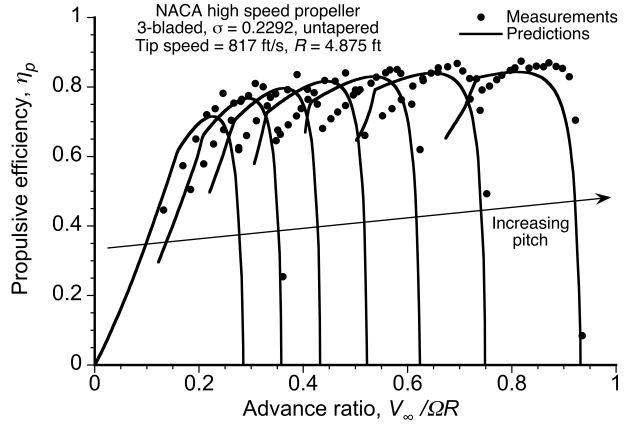

Fig. 12: Propulsive efficiency versus advance ratio for the 3-bladed NACA propeller.

peller, as shown in Figs. 10 through 13. In this case, the propeller operates at higher sectional Reynolds numbers, and was not tested such that it encountered significant supersonic flow at the blade tips. Therefore, the 3-bladed propeller measurements probably serve as a better indicator of the capabilities of the present model in the expected range of its normal usage.

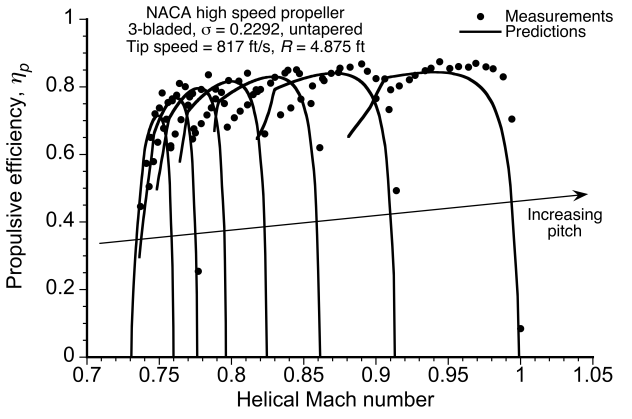

Fig. 13: Propulsive efficiency helical tip Mach number for the 3-bladed NACA propeller.

Notice again in this case the sensitivity of the propulsive efficiency (shown in Fig. 12) to small errors in the prediction of thrust and power. This outcome arises because the predictions of the sectional airloads are sensitive to the angles of attack of the local blade sections. It is also apparent that in this case the measured efficiency curves in Fig. 12 tend to be fairly peaky compared to those seen for the 2-bladed propeller (c.f., Fig. 8). For a fixed blade pitch, these peaks are bounded on one side (i.e., at lower values of advance ratio for a given blade pitch) by losses of efficiency resulting from some sections that operate away from their best lift-to-drag ratios and other sections that begin to encounter blade stall, and on the other side (i.e., at higher values of advance ratio) by the build up of compressibility effects from the growing helical Mach numbers over the blade tips.

The differences shown in the previous plots between the outcomes from the model and the measurements can be attributed to several sources, and are not just limited to the assumptions and/or simplifications involved in the aerodynamic modeling of the airfoil sections. For example, discrepancies can arise because of deficiencies in predicting the magnitude and distribution of inflow and swirl velocities, as well as tip loss and compressibility/tip relief effects. However, parametric studies and overall experience with the modeling has shown that the errors in the prediction of the inflow and swirl velocities will generally have the largest effects on overall performance.

For example, Figs. 14 and 15 show the effects on the thrust and power when the induced velocity components are systematically excluded. In this case, results for several values of blade pitch have been omitted to preserve clarity. When both the inflow, w_i, and the swirl, u_i, are removed from the inflow angle calculations, it is clear that both the thrust and power are significantly overpredicted at all advance ratios. At low advance ratios, the effects of the inflow velocities tend to be more important than swirl. However, at high advance ratios, the need to include both the inflow and the swirl velocity components is clearly critical if good quantitative predictions of performance are to

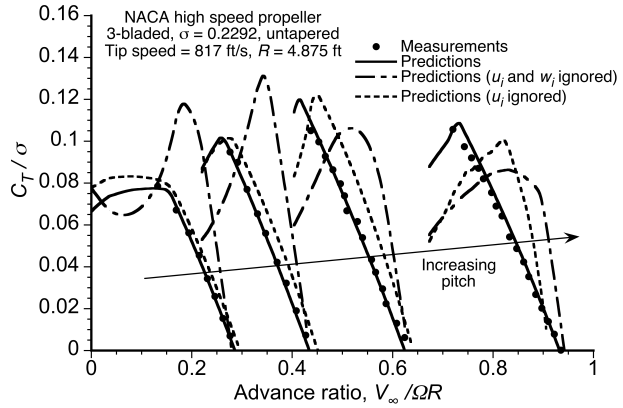

Fig. 14: Effect of inflow and swirl velocities on predicted thrust of the NACA 3-bladed propeller.

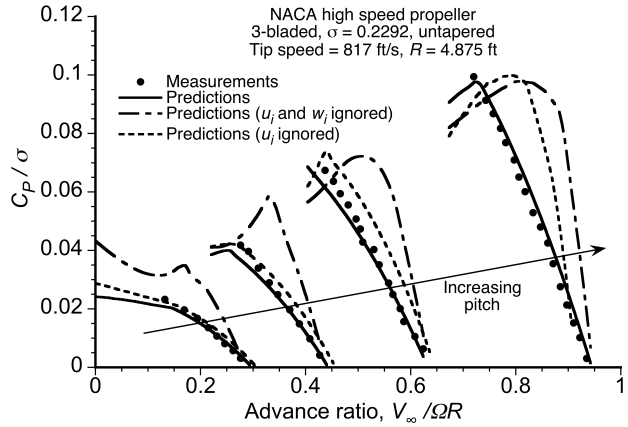

Fig. 15: Effect of inflow and swirl velocities on predicted power of the NACA 3-bladed propeller.

be obtained. In this regard, neglecting the swirl velocities (Ref. 25), or assuming uniform induced inflow velocity, or both (Ref. 51), is clearly inappropriate even at higher airspeeds where the induced velocities are a smaller fraction of the total sectional velocities.

Figure 16 helps to further explain this sensitivity. When the induced velocities are completely removed, the inflow angle at the blade is the free-stream inflow angle $\phi_\infty = \tan^{-1}(V_\infty/\Omega y)$. In practice, ϕ is between ϕ_∞ and β across the entirety of the blade, and approaches β near the tips because of the effects of the tip vortices. The assumption that $\phi = \phi_\infty$ results in overpredictions of angle of attack, and consequently overpredictions of both thrust and power. Ignoring the swirl velocity, u_i, also results in overpredictions of angle of attack, which in this case increases more with increasing advance ratio. As advance ratio increases, so also does the component of lift that contributes to the torque, so that the inclusion of the swirl velocity becomes increasingly important under these conditions.

Spanwise loadings were also calculated to gain further insight into the overall aerodynamic behavior of the propellers, and to check that the results from the modeling were in accordance with physical expectations based on the sectional aerodynamic models. For example, Figs. 17 and 18 show the spanwise thrust and power gradings, respectively, for three blade pitch values.

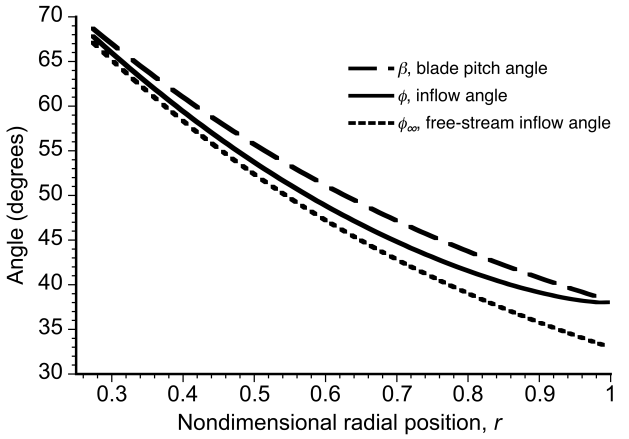

Fig. 16: Example of the distribution of inflow across the blade span. 3-bladed propeller at 315 kts.

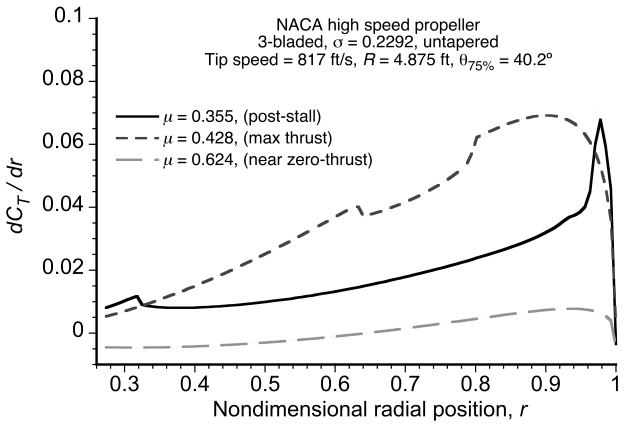

Fig. 17: Examples of the spanwise distribution of thrust on the NACA 3-bladed propeller for three blade pitch values.

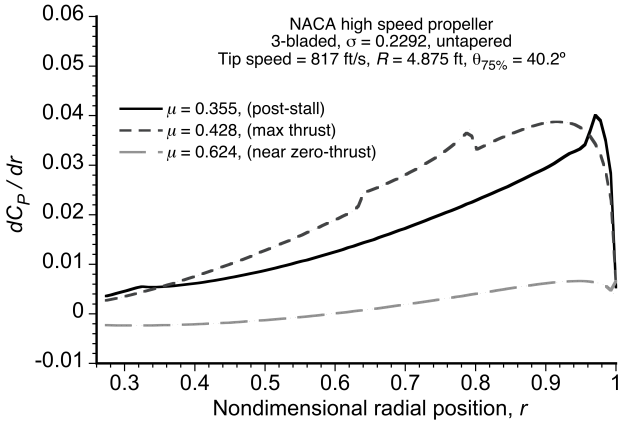

Fig. 18: Examples of the spanwise distribution of power on the NACA 3-bladed propeller for three blade pitch values.

Under normal operating conditions the loadings over the blade are smooth, peaking up toward the tip region. When operating closer to maximum thrust conditions,

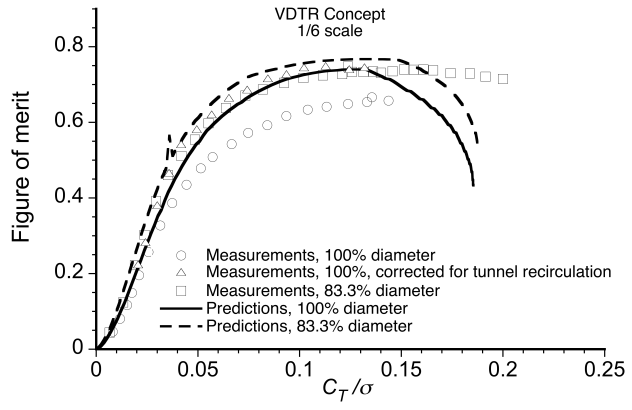

Fig. 19: FM versus C_T/σ for the VDTR concept.

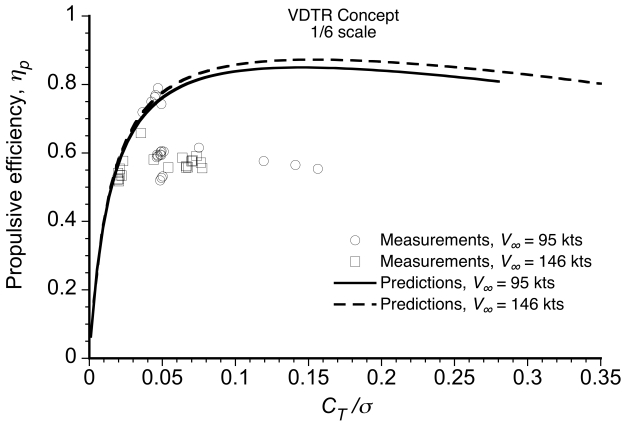

Fig. 20: Propulsive efficiency versus C_T/σ for the VDTR concept.

the blades in this case can be seen to be stalled between radial stations $0.63R$ and $0.79R$, as indicated by the loss of sectional thrust and a corresponding increase in power. For the post-stall condition, the entire blade is stalled except for small regions near the root and tip where induced inflow is high. Interestingly enough, the stalled sections actually experience a reduction in power required, which arises because of the large decreases in the sectional components of induced drag at this stalled operating condition.

Validation for the VDTR Proprotor

Relatively little published data is available that document measured proprotor performance over the broad range of forward flight conditions that was used previously for the NACA high-speed propellers. Wind tunnel tests of the 1/6 scaled proprotor for the Sikorsky VDTR concept (Ref. 27) are the only source of variable diameter proprotor data. Predictions obtained using the present model overpredict the figure of merit of the scaled VDTR proprotor in hover, as shown in Fig. 19. However, after corrected for tunnel recirculation effects, the measurements agree much better with the predictions. A comparison of propulsive efficiency predictions with measured data is shown in Fig. 20. The model agrees with the measured data at lower thrust values, but overpredicts efficiency at higher levels of C_T/σ.

However, there remains some concern as to whether the measured data for forward flight conditions is entirely consistent; for example, some of the published data in Ref. 27 records propulsive efficiencies in excess of unity, which is obviously incorrect. Further work must be done to reconcile the experimental results before further comparisons of the measurements with the modeling would be productive.

Validation with CR Vehicle Performance

To examine the ability of the proprotor model to calculate performance data when coupled to an airframe, the model was validated against available performance charts for a medium-lift tiltrotor (Ref. 52). Comparisons of the published data against predictions using the present model for hover ceiling, cruise flight envelope, and payload/range are shown in Figs. 21 through 23. The airframe and wing characteristics, as well as the engine and transmission operational states, were estimated from the available data. Some of the characteristics of this configuration are shown in Table 2. Recognizing that much of the vehicle characteristics could only be estimated, the predictions made by the model are in good agreements with the available data.

Some interesting characteristics of CR vehicle performance are exposed in these results. For the hover ceiling performance shown in Fig. 21, the knee in the predicted curve delineates two performance limits: one at lower gross weights where the maximum hovering altitude corresponds to the maximum thrust achievable by the proprotor before it begins to stall, and one at higher gross weights where the hover ceiling is determined by reaching a power limit. Such behaviors are not necessarily a characteristic of all CR aircraft and/or proprotor designs, but do show how the maximum hover altitude on a CR aircraft can be limited by either maximum attainable thrust or by power available, depending on the vehicle gross weight. The trades between solidity (to improve hovering performance at higher density altitudes) and power are considered later.

In the speed/density altitude flight envelope chart shown in Fig. 22, there is a similar knee in the curves for the high-speed boundaries. At lower altitudes, maximum speed is limited by the transmission torque limit. At higher altitudes, the maximum speed of the aircraft is limited by the maximum continuous power available.

The predictions for payload/range also show good agreement with the available data, as shown in Fig. 23. Engine SFC is this case was estimated, but the results show the ability of the model to predict the power requirements and fuel burn in forward flight.

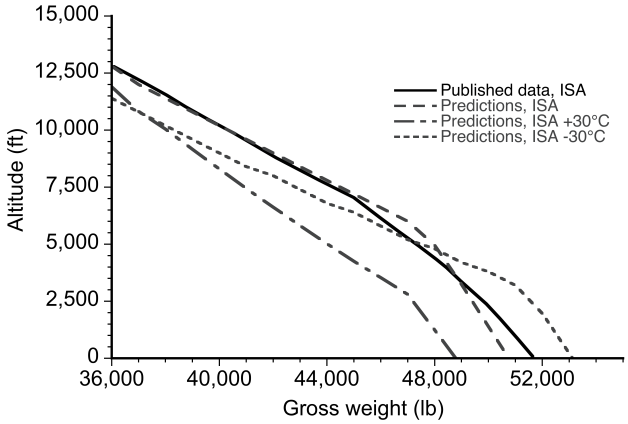

Fig. 21: Hover ceiling of medium-lift tiltrotor.

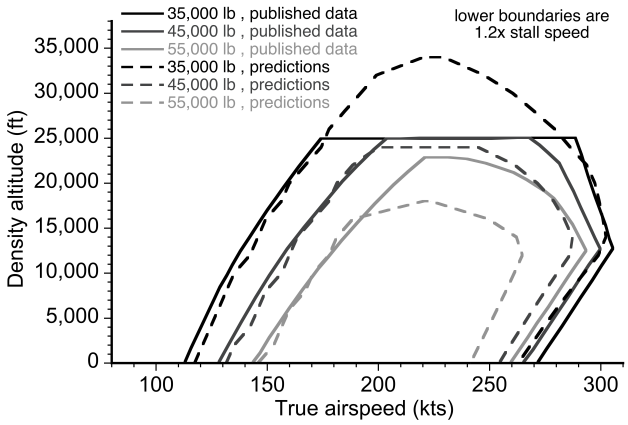

Fig. 22: Cruise flight envelope of medium-lift tiltrotor.

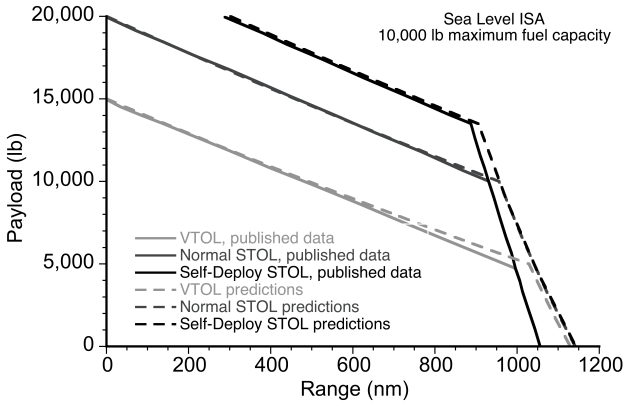

Fig. 23: Payload/range of medium-lift tiltrotor.

Parametric Studies

Parametric studies were performed to determine the effects of the various proprotor blade design parameters on overall vehicle performance. While parametric variations of the design trades needed for aspects of isolated proprotor performance are also useful, ultimately the actual performance of any proprotor needs to be assessed in context with the flight vehicle to which it is attached.

The results in the present work are shown primarily for the *Excalibur* CR configuration (Fig. 24), and also for the representative medium-lift tiltrotor where appropriate.

Fig. 24: The University of Maryland's *Excalibur* concept (Ref. 45).

Specifications for these vehicles have been given previously in Table 2.

Variations in proprotor solidity, blade taper, number of blades, blade twist, rotational speed, diameter, blade tip sweep, and airfoil characteristics were all studied. Results were obtained for hover and forward flight over a range of vehicle airspeeds, including those in the extended regions of the expected operational and/or vehicle performance envelope. The calculations were all performed at the stated maximum vertical gross takeoff weight for each vehicle.

Solidity

The effects of proprotor solidity on the cruise propulsive efficiency and hover power loading of the *Excalibur* concept are shown in Figs. 25 and 26. Solidity in this case was varied by changing the blade chord while keeping the diameter of the proprotor constant. Propulsive efficiency was clearly improved by decreasing the solidity, while hover efficiency was improved by increasing the solidity. In hover the blade sections are operating at angles of attack above those for their best ratio of C_l/C_d or in some cases too close to stall. Therefore, an increase in solidity allows the blades to operate at lower angles of attack and lower lift coefficients to generate the same thrust, which improves the power loading of the proprotor.

In cruise, the proprotor is more lightly loaded relative to the hover condition, and generally the blades are operating at much lower average angles of attack (but not lower pitch angles). Therefore, propulsive efficiency benefits substantially by using lower solidity, which decreases profile power requirements. However, notice that decreasing solidity also decreases the airspeed at which blade stall first begins to occur. This means that the operating margins of the proprotor between losses in performance from blade stall and the onset of compressibility become significantly constrained, i.e., the proprotor begins to approach the "coffin-corner" operating state that was discussed in Ref. 25.

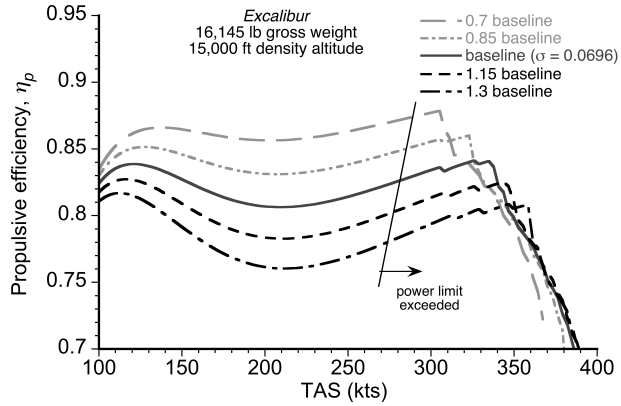

Fig. 25: Effect of variations in solidity on the propulsive efficiency of the *Excalibur*.

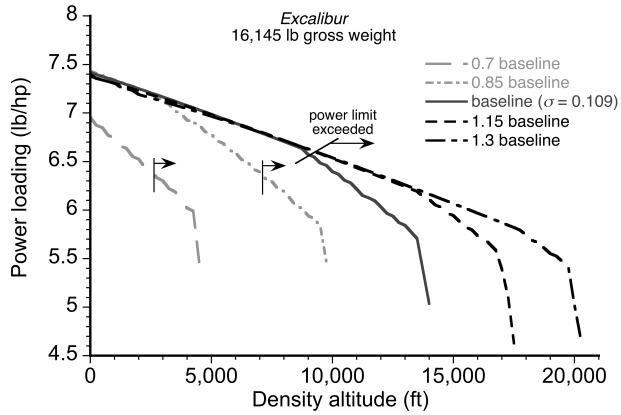

Fig. 26: Effect of variations in solidity on the power loading of the *Excalibur*.

Figure 27 further shows the thrust margins for this proprotor in the hover state. If solidity becomes too low or the operating density altitude is too high, then the proprotor will stall before producing enough thrust for the vehicle to hover. Recall that a proprotor needs generous stall margins in hover because the proprotors are used for control and maneuver, e.g., there is a need for significant differential thrust. Although attainable thrust margins in both hover and cruise modes are improved markedly by increasing the solidity, sufficient power from the engine and/or sufficiently high transmission torque limits must also be available to allow the desired thrust margins from the proprotor to be realistically achieved.

Blade Taper

The effect of blade taper ratio on cruise and hover performance is shown in Figs. 28 and 29 for the *Excalibur*. The results are all for a constant thrust-weighted solidity. Notice that an increase in taper ratio results in small increases in propulsive efficiency and modest improvements in power loading. Decreasing taper ratio allows higher forward speeds to be reached before blade stall occurs. However, these results are not necessarily the best indicator of the effects of taper on proprotor performance because only

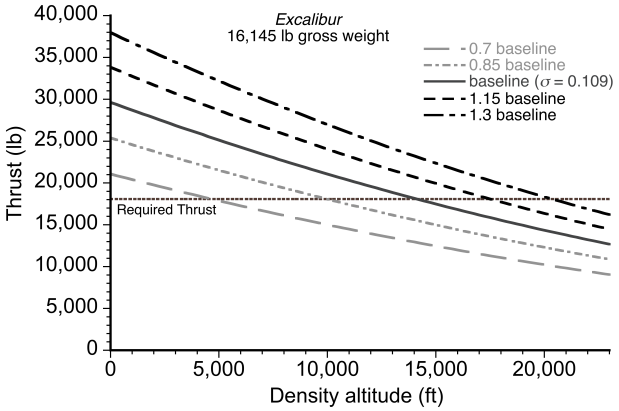

Fig. 27: Effect of variations in solidity on the hover thrust margins of the *Excalibur*.

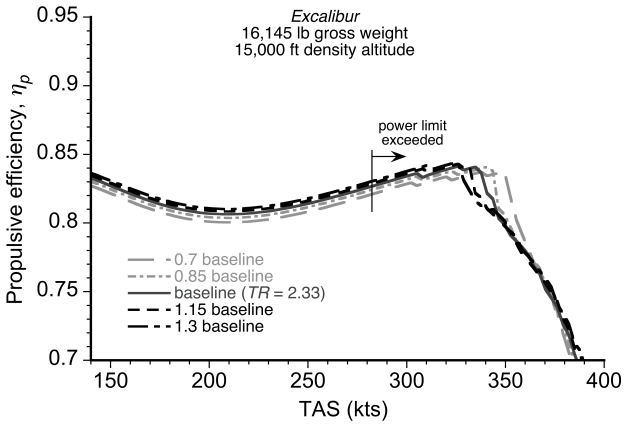

Fig. 28: Effect of variations in taper ratio on the propulsive efficiency of the *Excalibur*.

the outboard region (i.e., $r > 0.84$ with blades extended) of the blades is actually tapered; for the blade retraction mechanism to operate the inboard sections must be untapered.

A better vehicle to illustrate the effects of blade taper is the medium-lift tiltrotor, results for which are shown in Fig. 30. For this vehicle, an increase in blade taper ratio results in more significant improvements in hover power loading. Reviewing the outcomes for the three CR configurations as a whole, increasing blade taper was found to result in only small changes in propulsive efficiency but give more moderate improvements in hover performance.

Blade Twist

Figures 31 and 32 show the effect of blade twist relative to the baseline used for the *Excalibur* design. The use of different blade twist values clearly makes a large difference to both the propulsive efficiency and the hover power loading. Using more twist on the proprotor allows the vehicle to fly faster and more efficiently, whereas less blade twist increases the hovering efficiency. Although a decrease in blade twist in hover increases the altitude at which the engine power limits are reached, it also decreases the density altitude at which the proprotor begins to encounter its stall limits.

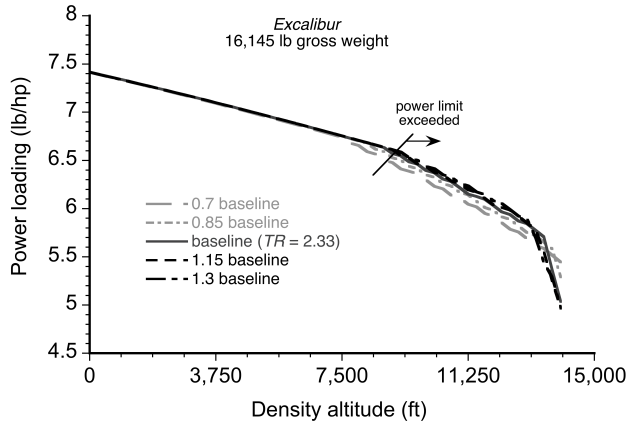

Fig. 29: Effect of variations in taper ratio on the power loading of the *Excalibur*.

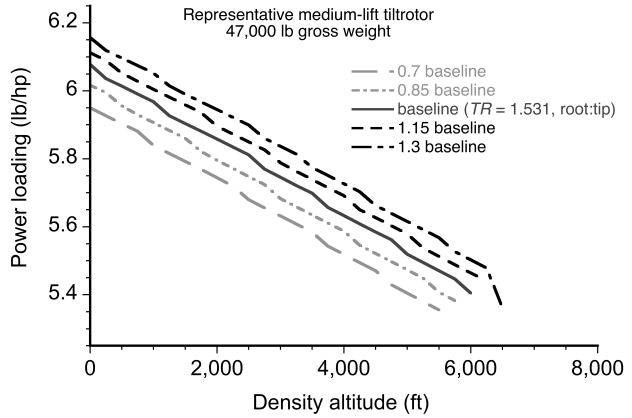

Fig. 30: Effect of variations in taper ratio on the power loading of the representative medium-lift tiltrotor.

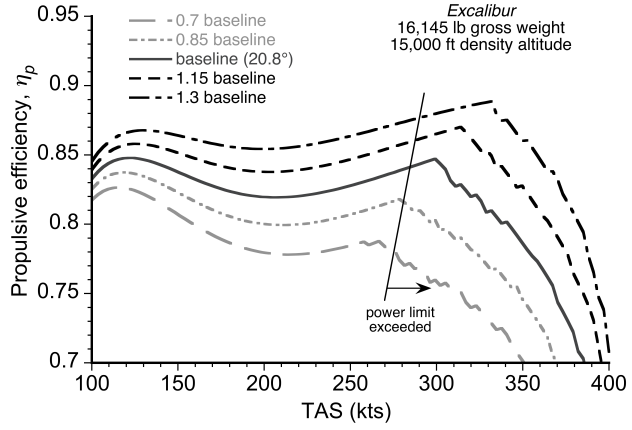

Fig. 31: Effect of variations in blade twist on the propulsive efficiency of the *Excalibur*.

The extent to which the blade twist becomes compromised between hover and cruise flight modes is mostly a function of the design cruise speed. As shown in Fig. 33, the optimized blade twist for forward flight may actually become closer to the twist needed for best hovering efficiency when the design cruise speed is increased to higher values. In this example, the blade twist rate needed for forward flight better matches the ideal twist needed for hover

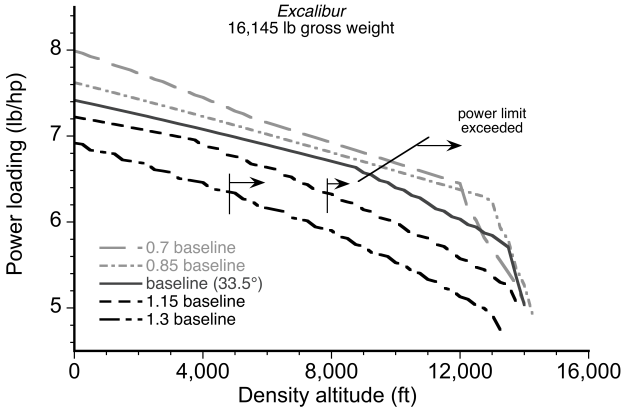

Fig. 32: Effect of variations in blade twist on the hover power loading of the *Excalibur*.

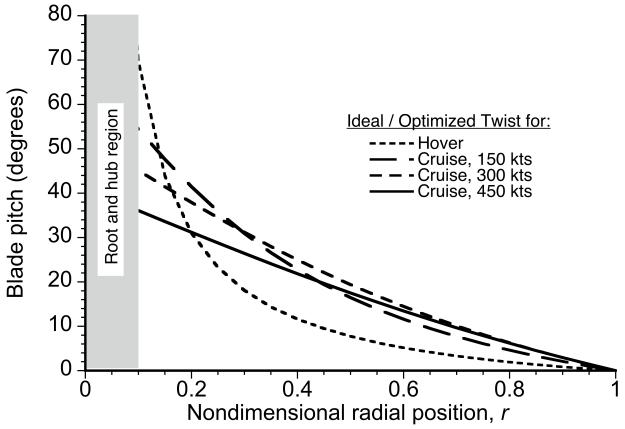

Fig. 33: Hover and cruise modes demand significantly different blade twist distributions for efficient proprotor operation.

over the outboard section of the blade when the desired forward speed is increased from 300 kts to 450 kts.

Blade Tip Sweep

Figure 34 shows the effect of blade tip sweep on the propulsive efficiency of the *Excalibur* concept. This blade has swept tips outboard of $r = 0.84$ in extended mode operation and outboard of $r = 0.76$ in retracted mode. Increasing tip sweep allows a moderate delay in the build up of compressibility effects. However, there is not enough available power in this case to take advantage of delays in the onset of compressibility losses from the use of tip sweep. To capitalize on any potential benefits of delayed compressibility effects, the engines installed on this concept would need to have greater continuous power ratings, with the trade of driving up the empty weight fraction of the vehicle and so reducing its useful load.

Number of Blades

The effect of number of blades on proprotor performance is shown in Figs. 35 and 36. Increasing the number of blades

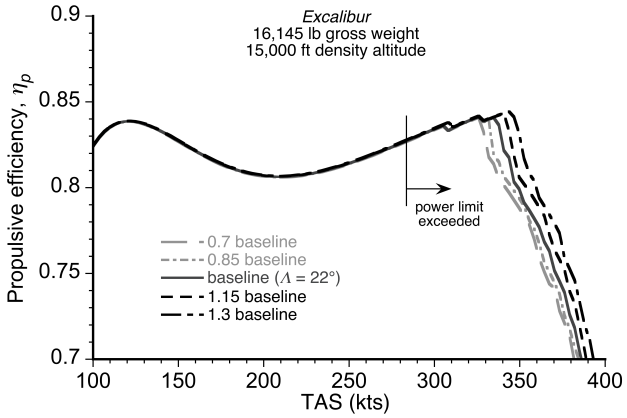

Fig. 34: Effect of variations in tip sweep on the propulsive efficiency of the *Excalibur*.

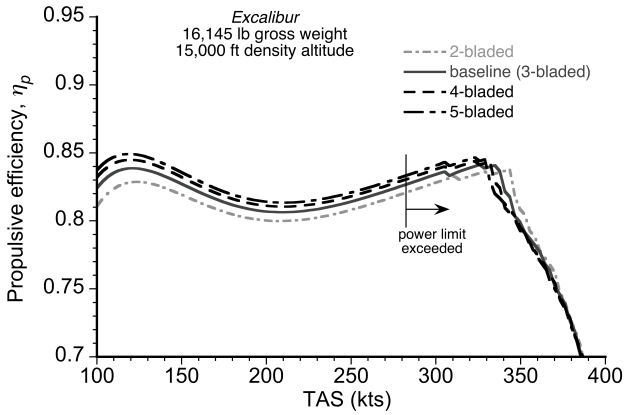

Fig. 35: Effect of number of blades on the propulsive efficiency of the *Excalibur*.

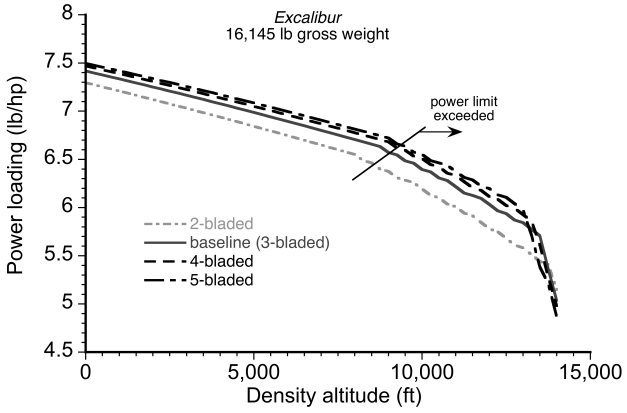

Fig. 36: Effect of number of blades on hover power loading of the *Excalibur*.

was found to give relatively small improvements to both the hover and cruise efficiencies. Increasing the number of blades and, therefore, decreasing the spacing between adjacent vortex elements, will tend to reduce the tip-loss effects and improve the performance of the proprotor, albeit with diminishing returns. For example, there seems little aerodynamic advantage in using 4 versus 3 blades. This does not necessarily mean, however, there would not be a preference for using a larger number of blades for other reasons.

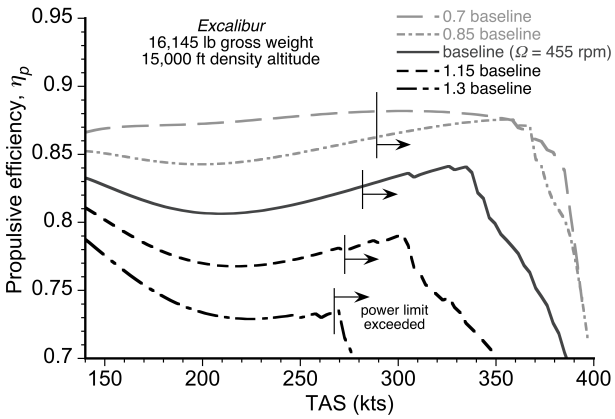

Fig. 37: Effect of rotational speed on the propulsive efficiency of the *Excalibur*.

Rotational Speed

Results from the parametric study of rotational speed effects for the *Excalibur* CR aircraft are shown in Figs. 37 and 38. Decreasing rotational speed clearly produces a significant increase in propulsive efficiency and delays the onset of compressibility effects to higher maximum forward speeds. Figure 38, however, shows that reducing rotational speed can have an adverse effect on hover performance (in this case, the hover ceiling). It is also shown that increasing rotational speed decreases the hover ceiling at lower gross weights, but can extend the hover ceiling to higher maximum gross weights. The increase in tip Mach number is a disadvantage at higher altitudes where compressibility effects manifest because of the somewhat lower speed of sound.

While reducing the rotational speed of the proprotor can improve its propulsive efficiency, it also increases the shaft torque for a given power requirement and so the results need to be examined in conjunction with transmission limits. The representative medium-lift tiltrotor, in contrast to the *Excalibur*, has a relatively low transmission limit compared to its available engine power.

Figure 39 shows that the highest aerodynamic efficiencies that are achievable by this proprotor by the use of varying rotational speed are constrained by the transmission torque limits. However, improvements are obviously achievable if higher transmission torque limits were available, which must be traded against transmission weight, or at higher altitudes where the power available is the limiting factor in determining the maximum attainable propulsive efficiency.

Diameter

Figures 40 and 41 show the propulsive efficiency and hover ceiling of the *Excalibur* when the diameter of the proprotor is varied. For this vehicle, reducing diameter has a smaller effect on propulsive efficiency than does reducing the rotational speed. Furthermore, the decrease in tip speed cou-

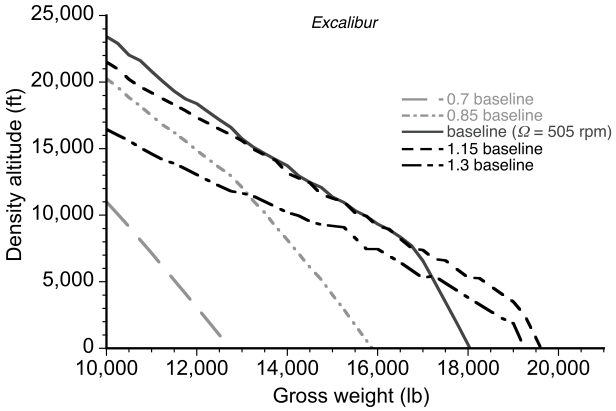

Fig. 38: Effect of rotational speed on the hover ceiling of the *Excalibur*.

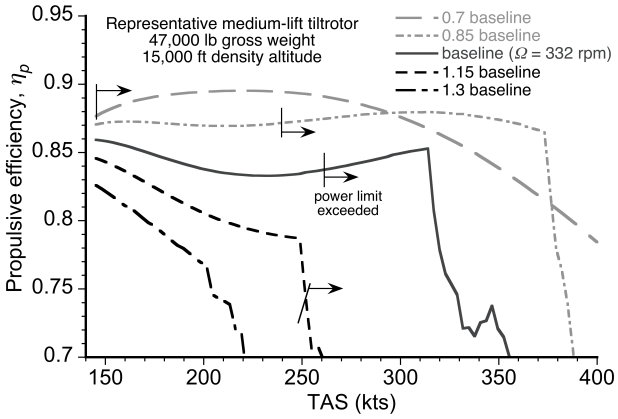

Fig. 39: Effect of rotational speed on the propulsive efficiency of the representative medium-lift tiltrotor.

pled with the decrease in blade area adversely affects performance at lower cruise speeds where the induced drag on the wings is higher, requiring higher thrust from the proprotors. At these lower speeds, the fully retracted state produces lower efficiency than in the partially retracted state because to generate the required thrust, some blade sections must operate closer to stall. However, increasing the diameter of the proprotor clearly improves the hover performance and gives an ability to hover at higher density altitudes and at higher gross vehicle weights.

Maximum Lift Coefficient

The effect of the maximum attainable lift coefficient, $C_{l_{\max}}$, of the blade sections on vehicle performance is shown in Figs. 42 and 43. In these calculations, it was assumed that $C_{l_{\max}}$ could be adjusted by itself while keeping constant all other sectional airfoil characteristics. It is recognized, however, that such improvements may not be possible in practice.

The curves in Fig. 42 all follow the same behavior until, for a particular case, the blade sections exceed $C_{l_{\max}}$ and the proprotor begins to stall. Even with a $C_{l_{\max}}$ high enough to prevent blade stall at very high airspeeds, the propulsive efficiency will reach a peak at a certain airspeed and then

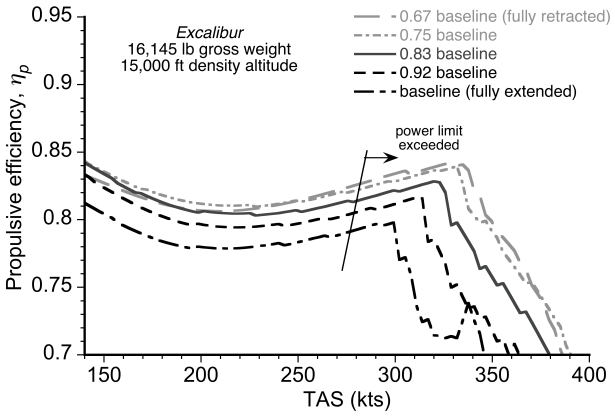

Fig. 40: Propulsive efficiency of the *Excalibur* across its range of operational diameters.

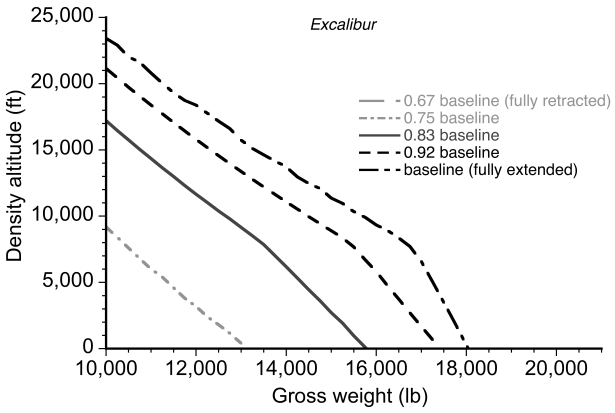

Fig. 41: Hover ceiling of the *Excalibur* across its range of operational diameters.

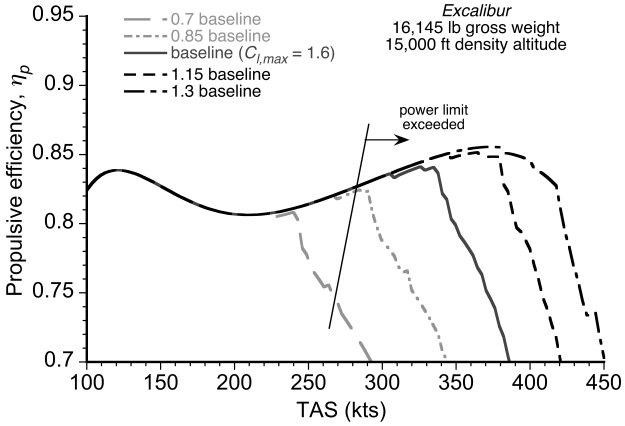

Fig. 42: Effect of $C_{l_{\max}}$ on the propulsive efficiency of the *Excalibur*.

decrease with further increases in airspeed. This outcome is because as advance ratio increases, the sectional lift vectors become inclined further away from the rotational plane and act to reduce propulsive capabilities. In this case, the propulsive efficiency reaches its peak at about 380 kts. The power loading, as shown in Fig. 43, is clearly improved at all operational density altitudes by increasing the maximum lift coefficient.

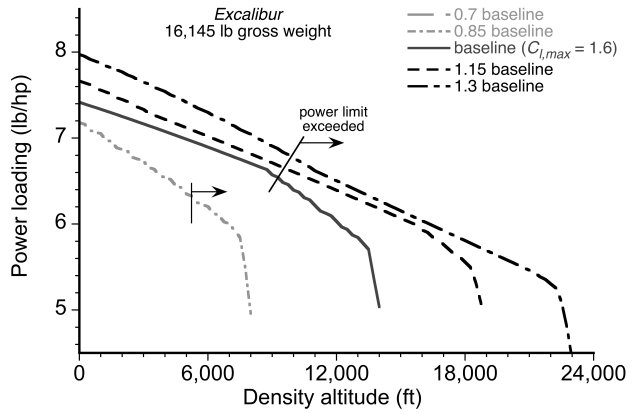

Fig. 43: Effect of $C_{l_{\max}}$ on the hover power loading of the *Excalibur*.

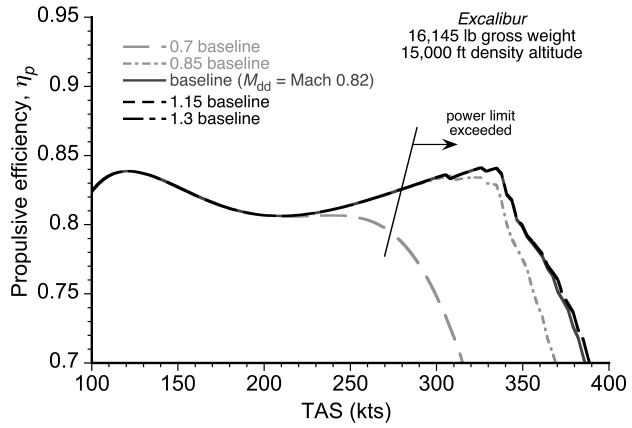

Fig. 44: Effect of M_{dd} on the propulsive efficiency of the *Excalibur*.

Drag Divergence Mach Number

Figures 44 and 45 show the effects of variations in M_{dd} on the cruise and hover efficiencies of the *Excalibur*. As done previously for $C_{l_{\max}}$, it has been assumed that M_{dd} can be varied while keeping all of the other airfoil characteristics constant. Notice that the value of M_{dd} has little or no effect on performance as long as it reaches a certain minimum threshold. The required value of M_{dd} is obviously higher for forward flight than for hover because of the higher helical section speeds experienced in forward flight and the need to limit the buildup of compressibility over more substantial parts of the blade that are not just limited to the tip region.

Airfoil Selection

As shown previously in the parametric studies, the choice of airfoils (and their spanwise placement on the blade) is obviously an important consideration in the design of proprotor blades. To explore the effect that the choice of the airfoils has on the performance of a CR aircraft, a formal optimization study was performed on airfoil selection for the representative medium-lift tiltrotor. The values of $C_{l_{\max}}$ and M_{dd} were each represented as functions of the airfoil thickness-to-chord ratio (t/c). For the optimization, these

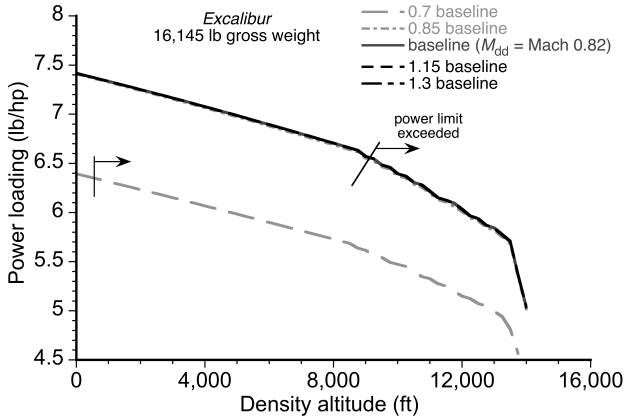

Fig. 45: Effect of M_{dd} on the hover power loading of the *Excalibur*.

blades were divided into twenty segments and the value of t/c for each segment was adjusted to maximize one of three objective functions: propulsive efficiency, figure of merit, and a compromise between the maximum values of η_p and FM.

Figure 46 shows the results of this optimization, which used a baseline t/c of 0.12. Maximizing hover efficiency demands thicker airfoil sections near the root to increase $C_{l_{\max}}$ and prevent these root sections from stalling. The compromised twist inherent to most proprotors is the main reason that the root sections operate at high angles of attack in hover and need very high values of $C_{l_{\max}}$. Maximizing both FM and η_p also requires a root section with high values of $C_{l_{\max}}$, which is also good for structural reasons. Near the tip, however, maximizing η_p demands significantly thinner blade sections, while maximizing FM suggests that a smaller reduction in t/c needs to occur there.

The airfoil selection process also requires that hover and cruise performance be examined with different t/c distributions. Figure 47 show the effect of airfoil optimization on propulsive efficiency. Airfoil characteristics in this case only have an effect on the propulsive efficiency at higher forward speeds. Interestingly, the compromised case shows better efficiency than when η_p is maximized by itself; this is an outcome of optimizing propulsive efficiency for a single airspeed (i.e., 315 kts in this case). However, improvements in airfoil properties lead to modest improvements in overall forward flight performance; the difference between the compromised blade and the blade optimized for hover is a delay in the onset of compressibility effects of only 9 kts of airspeed.

Figure 48 shows the effect of airfoil t/c optimization on the figure of merit of the proprotor. Optimizing for hover results in an increase in figure of merit of about 0.03, although this is still significant. Optimizing for forward flight not only decreases the figure of merit, but also decreases the maximum operational altitude by about 2,500 ft. For the most part, the case where the airfoils were optimized for a compromise between FM and η_p mirrors the results for

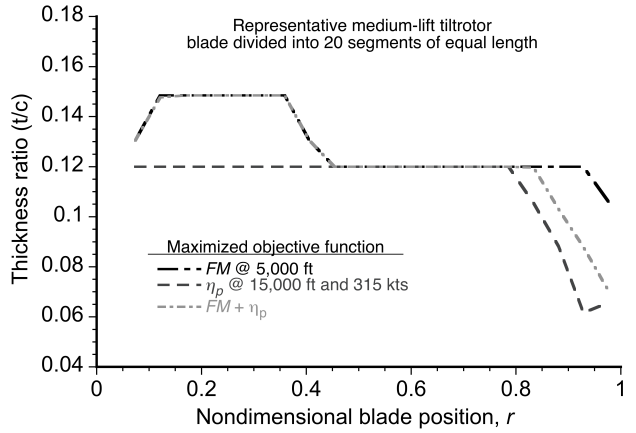

Fig. 46: Airfoil thickness optimized for figure of merit, propulsive efficiency, and both.

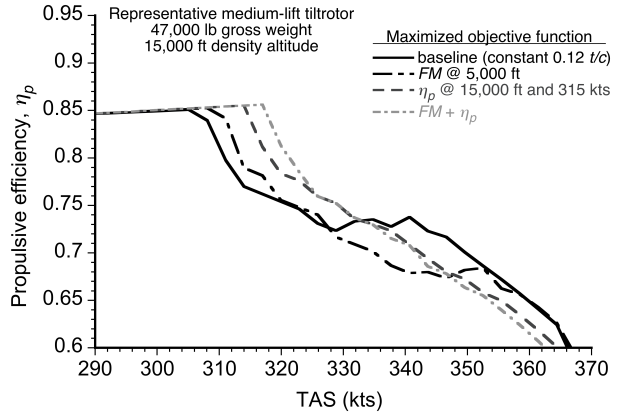

Fig. 47: The effect of airfoil optimization on forward flight efficiency.

when the blades are optimized for hover. The only difference is a decease in maximum operational density altitude of 1,000 ft, indicating that the use of thinner airfoils near the tip only become a concern for the compromised optimization at higher altitudes where higher $C_{l_{\max}}$ values are needed to avoid stall in the blade tip region.

Overall, the results in Figs. 47 and 48 show that, at least for this vehicle configuration, more important gains in overall performance can be made when the airfoils are optimized for efficiency in hover rather than in forward flight.

Variable Tip Speed Operation

To further explore the effects of variable tip speed, a study was performed on the representative medium-lift tiltrotor to optimize its performance using either of the VSPR and VDPR designs. A third "modified" VDPR design was also considered, which is an approach where the total blade twist per radius is preserved when diameter is reduced; in practice this outcome can only be achieved with a variable twist technique. The assumed proprotor in this case had a bilinear blade twist and a maximum tip speed reduction of 33%. For the VDPR concept, the inboard blade section (which is

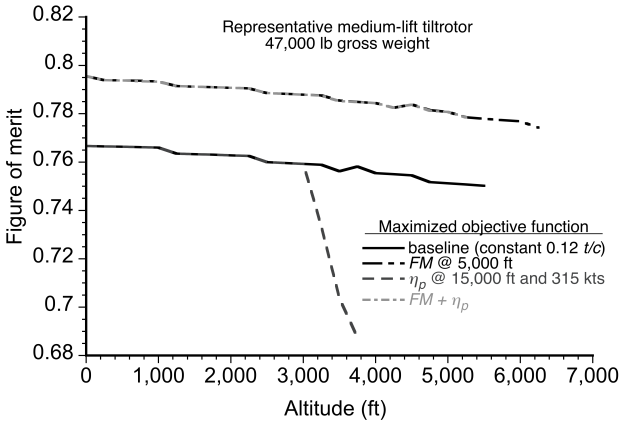

Fig. 48: The effect of airfoil optimization on hover figure of merit.

sheathed inside the outboard section during retraction) had a chord equal to 1/3 the root chord of the main blade.

For the baseline and VDPR cases, it was assumed that the shaft speed could be reduced by 10% by using the power turbine alone; the shaft speed can be expected to be reduced by at least this amount without significantly increasing engine SFC (Refs. 53, 54). The design variables used were diameter, rotational speed, root chord, taper ratio, inboard and outboard twist, the radial position where twist changes, and the tip speed reduction. The flight conditions considered were cruise at 15,000 ft density altitude and 280 kts, and hovering flight at 6,000 ft density altitude.

The objective function needed for the optimization is not immediately apparent in this case. It is not acceptable to use FM and η_p together (as was used in the airfoil optimization study) because FM is dependent on diameter, and so the optimizer would not necessarily try to maximize absolute hovering efficiency (i.e., the power loading). Instead, a baseline proprotor design without variable tip speed was established to evaluate the VSPR and VDPR designs. The objective function was selected to be the sum of the ratio of the baseline cruise power to the cruise power and the ratio of the baseline hover power to the hover power.

Figures 49 and 50 show the cruise and hover efficiencies for the optimized variable tip speed proprotor designs. On one hand, the VSPR design offers large improvements to both propulsive efficiency and power loading over those of the baseline proprotor, although it soon exceeds the transmission torque limits when its shaft speed is reduced significantly in forward flight. On the other hand, the VDPR design gives lower propulsive efficiencies than the baseline design. While this concept also achieves higher power loadings than the baseline, it does so at the expense of lower hover efficiency at higher altitudes. The results for the modified VDPR are much better than for the standard VDPR, indicating that the performance degradation of the VDPR design is because of the reduction in effective blade twist when the diameter is reduced.

Similar trends shown for the medium-lift tiltrotor were

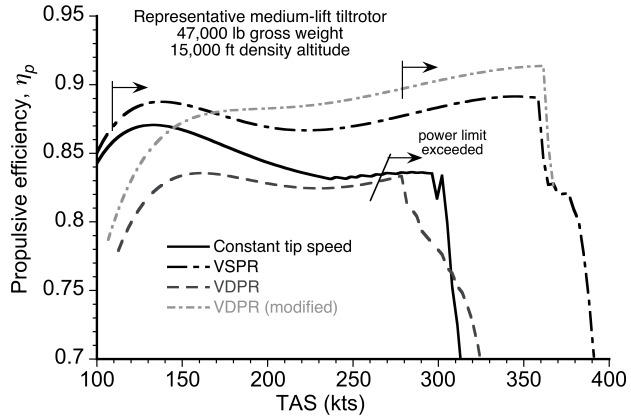

Fig. 49: Propulsive efficiency for the optimized variable tip speed proprotor designs .

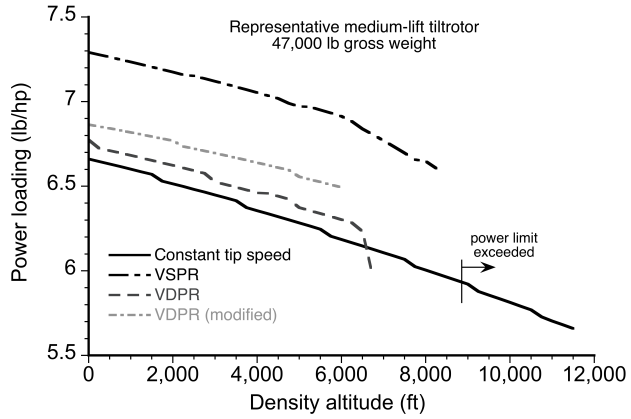

Fig. 50: Hover power loading for the optimized variable tip speed proprotor designs.

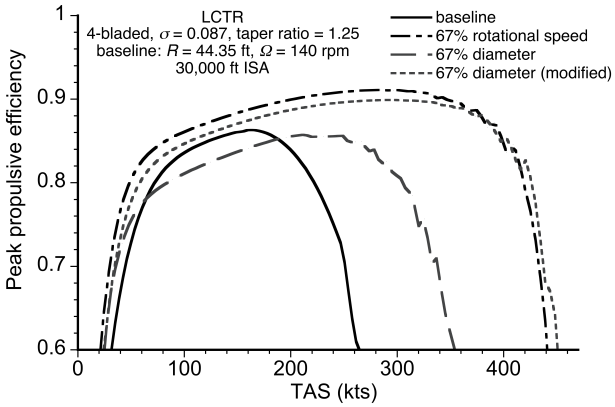

Fig. 51: Effect of reduced tip speed methods on the peak propulsive efficiency of the LCTR.

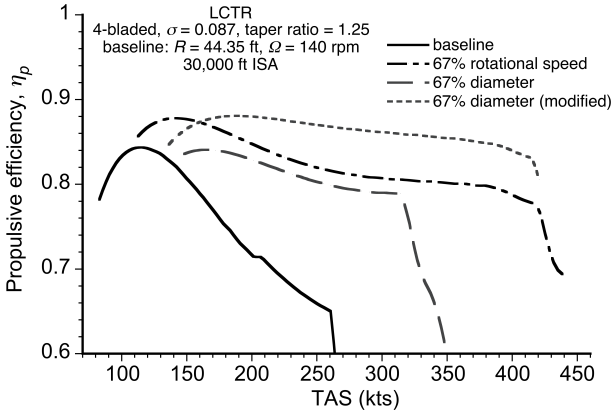

Fig. 52: Effect of reduced tip speed methods on the propulsive efficiency of the LCTR.

also found for a proprotor representative of that for the proposed Large Civil Tilt Rotor (LCTR) convertible-rotor concept. Figure 51 shows the peak propulsive efficiency of the LCTR concept as a function of airspeed, and Fig. 52 shows the propulsive efficiency when proprotor thrust is determined by the vehicle drag using Eq. 39. These results were not obtained through an optimization analysis as performed for the medium-lift tiltrotor, but simply by taking the LCTR proprotor and reducing its diameter and rotational speed. As before, varying diameter gives a lower propulsive efficiency than varying rotational speed. However, unlike that found for the medium-lift tiltrotor, a VDPR design improves forward flight performance over that of the baseline, as shown in Fig. 52.

The foregoing comparison of the reduced tip speed methods for the medium-lift tiltrotor and the LCTR should not be taken to imply that reducing the rotational (shaft) speed is the preferred approach. The LCTR concept, in particular, was designed specifically to exploit the benefits of reduced rotational speed in forward flight, so it is not surprising that this approach produces the best results in this case. The parametric studies shown previously for the *Excalibur*, which is a VDPR design, indicate that reducing diameter is also a viable method for improving proprotor performance. Compared to the medium-lift tiltrotor, the *Excalibur* has a much higher L/D ratio. It seems that CR aircraft that can attain relatively low values of L/D compared to turboprop airplanes will have little to gain by using a VDPR because the combination of relatively higher thrust and smaller blade area in forward flight causes the proprotor to operate at lower propulsive efficiencies. Therefore, a major factor in determining the advantages of the VSPR versus the VDPR designs will be the actual L/D of the vehicle to which the proprotor is attached.

Conclusions

The effects of proprotor design parameters and operational characteristics on hovering and forward flight performance were examined. A new methodology was developed to predict proprotor and convertible rotor vehicle performance characteristics over a wide range of operating conditions, including forward flight at very high advance ratios and tip Mach numbers up to supersonic. The methodology was validated against performance measurements for high-speed propellers and proprotors, and also against published flight characteristics of a contemporary tiltrotor aircraft. The effects on performance and efficiency produced by variable tip speed operations were examined in detail.

The following conclusions have been drawn from the study:

1. The blade element momentum theory with large angle modifications was shown to be able to model the thrust and power characteristics of high speed propellers in forward flight. The inclusion of the swirl velocity into the calculations was found to be necessary to obtain satisfactory predictions of the propulsive efficiency at higher advance ratios, especially closer to 2.

2. Decreasing solidity produced significant improvements in propulsive efficiency at the expense of degraded hover performance and reduced stall margins. Reductions in solidity also caused the proprotor to stall at lower forward speeds as propulsive thrust demands increased to overcome vehicle drag. However, using blade twist rates more suitable for forward flight conditions (rather than hover) helped to delay the onset of blade stall to higher airspeeds.

3. Increased blade twist generally improved propulsive efficiency but while decreasing hover efficiency. There appear to be no single optimum blade twist rate that simultaneously maximized both hovering efficiency and propulsive efficiency, except if the proprotor is designed for extremely high advance ratios where the needed twist distributions become more similar. Compared to the effects of twist and solidity, the effects of blade taper and number of blades appeared to have secondary significance on performance. In some cases, however, increased blade taper moderately improved the hovering efficiency of the proprotor.

4. As a proprotor becomes increasingly optimized for best propulsive efficiency, its design must be balanced between losses in performance from blade stall and the onset of compressibility. Adequate margins must be allowed for so as to avoid a "coffin-corner" operating state where small excursions in operating conditions may cause a catastrophic loss of thrust, rapid increases in power required and overall performance degradation.

5. Optimization of the airfoil sections for cruise conditions resulted in only small improvements in performance. More significant gains in overall proprotor performance can be obtained by focusing airfoil design efforts toward meeting hovering flight requirements, especially for the inboard sections of the blade where very high maximum lift coefficients are required.

6. Variable tip speed proprotor designs were shown to give large improvements in performance in both the hover and cruise modes of operation. The results suggested that a variable speed proprotor (VSPR) will have better performance characteristics than a variable diameter proprotor (VDPR). The main drawback to the VDPR concept is the reduction in effective blade twist when the blades are retracted for forward flight. Ultimately, the preference for either of the VSPR or VDPR designs will depend on the vehicle to which the proprotor is attached.

Acknowledgements

This work has been partly supported by the Office of Naval Research (ONR). Judah Milgram was the technical monitor. Any opinions, findings, conclusions, or recommendations expressed in this paper are those of the authors alone and do not necessarily reflect the views of the University of Maryland, the sponsoring agencies, or any other organization or persons with which the authors may have been associated.

References

[1]Hafner, R., "The Case for the Convertible Rotor," 10th Cierva Memorial Lecture, *The Aeronautical Journal*, Vol. 75, Nos. 728 & 729, August & September, 1971, pp. 505–528, pp. 610–624.

[2]DeTore, J., and Conway, S., "Technology Needs for High Speed Rotorcraft," NASA Contractor Report 177592, October 1991.

[3]Spivey, D., "Runway Independent Aircraft," AIAA Paper 2002-5958, International Powered Lift Conference and Exhibit, Williamsburg, VA, November 5–7, 2002.

[4]Spivey, D., "The Need for Tactical, High Speed, Long Range, Vertical Envelopment Transport Development," AIAA Paper 2002-6022, International Powered Lift Conference and Exhibit, Williamsburg, VA, November 5–7, 2002.

[5]Foster, M., "The Future Evolution of the Tiltrotor," AIAA Paper 2003-2652, AIAA/ICAS International Air and Symposium and Exposition: The Next 100 Years of Flight, Dayton, OH, July 14–17, 2003.

[6]Howard, W. B., Jr., and Pilling, D. L., "Defense Science Board Task Force on Future Need for VTOL/STOL Aircraft," Defense Science Board, Washington DC, July 2007.

[7]Talbot, P. D., Philips, J. D., and Totah, J. J., "Selected Design Issues of Some High Speed Rotorcraft Concepts," *Journal of Aircraft*, Vol. 30, (6), 1993, pp. 864–871.

[8]Manley, D. J., and von Klein, W., "Design and Development of a Super-Short Takeoff and Landing Transport Aircraft," AIAA Paper 2002-6023, 2002 Biennial International Powered Lift Conference and Exhibit, Williamsburg, VA, November 5–7, 2002.

[9]Johnson, W., Yamauchi, G. K., and Watts, M. E., "Heavy Lift Rotorcraft Systems Investigation," NASA/TP-2005-213467, December 2005. See also: Johnson, W., Yamauchi, G. K., and Watts, M. E., "Design and Technology Requirements for Civil Heavy Lift Rotorcraft," American Helicopter Society Vertical Lift Aircraft Design Conference Proceedings, San Francisco, CA, January 18–20, 2006.

[10]Sinsay, J. D., "The Path to Turboprop Competitive Rotorcraft: Aerodynamic Challenges," American Helicopter Society Specialist's Conference on Aeromechanics, San Francisco, CA, January 23–25, 2008.

[11]Cicalé, M., "ERICA: The European Tiltrotor," Presented at the 2005 Europe/US International Aviation Safety Conference, Cologne, Germany, 7–9 June, 2005.

[12]Acree, C. W., Jr., and Johnson, W., "Performance, Loads and Stability of Heavy Lift Tiltrotors," AHS Vertical Lift Aircraft Design Conference, American Helicopter Society International, Inc., San Francisco, CA, January 2006.

[13]Preator, R., Leishman, J. G., and Baldwin, G. D., "Performance and Trade Studies of the Mono Tiltrotor Design," American Helicopter Society 61st Annual Forum Proceedings, Grapevine, TX, June 1–3, 2005.

[14]Nixon, M. W., "Aeroelastic Response and Stability of Tiltrotors with Elastically-Coupled Composite Rotor Blades," Ph.D. Dissertation, Department of Aerospace Engineering, University of Maryland, College Park, MD, 1993.

[15]Wernike, K. G., and Edenborough, H. K., "Full-Scale Proprotor Development," *Journal of the American Helicopter Society*, Vol. 17, (1), January 1972, pp. 31–40.

[16]Paisley, D. J., "Rotor Aerodynamic Optimization for High-Speed Tiltrotors," American Helicopter Society 43rd Annual Forum Proceedings, St. Louis, MO, May 18–20, 1987.

[17]Farrell, M. K. "Aerodynamic Design of the V-22 Osprey Proprotor," American Helicopter Society 45th Annual Forum Proceedings, Boston, MA, May 22–24, 1989.

[18]Liu, J., Paisley, D. J., and Hirsh, J., "Tiltrotor Aerodynamic Blade Design by Numerical Optimization," American Helicopter Society 46th Annual Forum Proceedings, Washington DC, May 21–23, 1990.

[19]Dadone, L., Liu, J., Wilkerson, J., and Acree, C. W., "Proprotor Design Issues for High Speed Tiltrotors," American Helicopter Society 50th Annual Forum Proceedings, Washington DC, May 11–13, 1994.

[20]Platt, R. J., Jr., and Shumaker, R. A., "Investigation of the NACA 3-(3)(05)-05 Eight-Blade Dual-Rotating Propeller at Forward Mach Numbers to 0.925," NACA RM L50D21, June 1950.

[21]Hammack, J. B., and O'Bryan, T. C., "Effect of Advance Ratio on Flight Performance of a Modified Supersonic Propeller," NACA TN 4389, September 1958.

[22]Maynard, J. D., and Salters, L. B., Jr., "Aerodynamic Characteristics at High Speeds of Related Full-Scale Propellers Having Different Blade-Section Cambers," NACA Report 1309, 1948.

[23]Booth, E. R., Jr., Botha, G., Dawson, S., Yamauchi, G. K., and Young, L. A, "Overview of the Testing of a Small-Scale Proprotor," American Helicopter Society 55th Annual Forum Proceedings, Montréal, Canada, May 25–27, 1999.

[24]Aguilera, F., Brender, S., and Mark, H., "The Attributes of a Variable-Diameter Rotor System Applied to Civil Tiltrotor Aircraft," NASA CR 203092, 1997.

[25]Leishman, J. G., and Rosen, K. M., "Challenges in the Aerodynamic Optimization of High-Efficiency Proprotors," *Journal of the American Helicopter Society*, Vol. 56, (1), October 2010, pp. 568–596.

[26]Karem, A. E., "Optimum Speed Tilt Rotor," U.S. Patent Number 6,641,365, November 4, 2003.

[27]Matuska, D., Dale, A., and Lorber, P., "Wind Tunnel Test of a Variable-Diameter (VDTR) Model," NASA CR 177629, January 1994.

[28]Wang, J. M., Jones, C. T., and Nixon, M. W., "A Variable Diameter Short-Haul Civil Tiltrotor," American Helicopter Society 55th Annual Forum Proceedings, Montréal, Canada, May 25–27, 1999.

[29]Fradenburgh, E., and Matuska, D., "Advancing Tiltrotor State-of-the-Art with Variable Diameter Rotors," American Helicopter Society 48th Annual Forum Proceedings, Washington, D.C., June 3–5, 1992.

[30]Stack, J., Draley, E. C., Delano, J. B., and Feldman, L., "Investigation of the NACA 4-(3)(08)-03 and NACA 4-(3)(08)-045 Two-Blade Propellers at Forward Mach Numbers to 0.725 to Determine the Effects of Compressibility and Solidity on Performance," NACA Report 999, January 1944.

[31]Carmel, M. M., and Robinson, H. L., "Further Investigation of NACA 4-(5)(08)-03 Two-Blade Propeller at High Forward Speeds," NACA-RM-L7E12, Declassified, December 14, 1953 as NACA Research Memorandum L7E12.

[32]Gur, O., and Rosen, A., "Comparison Between Blade-Element Models," *The Aeronautical Journal*, Vol. 112, (1138), December 2008, pp. 689–704.

[33]Weick, F. E., *Aircraft Propeller Design*, McGraw-Hill Book Company, Inc., York, PA, 1930.

[34]Froude, W., "On the Elementary Relation Between Pitch, Slip and Propulsive Efficiency," *Transactions of the Institute of Naval Architects*, 19, 1878, pp. 47–57.

[35]Gessow, A., "Effect of Rotor-Blade Twist and Plan-Form Taper on Helicopter Hovering Performance," NACA Technical Note 1542, 1948.

[36]Gessow, A., and Myers, G. C., *Aerodynamics of the Helicopter*, MacMillan Co., New York, NY, 1952, pp. 73–75.

[37]Goldstein, S., "On the Vortex Theory of Screw Propellers," Proceedings of the Royal Society, Vol. 123, (792), 1929.

[38]Betz, A., *Schraubenpropeller mit geringstem Energieverlust*, Göttingen Nachrichten, 1919.

[39]Bradley, T. H., Mavris, D., Moffitt, B. A., and Parkh, D. E., "Validation of Vortex Propeller Theory for UAV Design with Uncertainty Analysis," 46th AIAA Aerospace Sciences Meeting and Exhibit, Reno, NV, January 2008.

[40]Balmford, D., and Done, G., *Bramwell's Helicopter Dynamics* (2nd ed.), American Institute of Aeronautics and Astronautics, Inc., Oxford, UK, and Butterworth-Heinemann, Reston, VA, 2001.

[41]Lissaman, P. B. S., Walker, S. N., and Wilson, R. E., "Aerodynamic Performance of Wind Turbines," Oregon State University, Corvallis, OR, 1976.

[42]Winarto, H., "BEMT Algorithm for the Prediction of the Performance of Arbitrary Propellers," CR CoE-AL 2004-HW3-01, Centre of Expertise in Aerodynamic Loads, Royal Melbourne Institute of Technology, Australia, March 2004.

[43]Prouty, R. W., *Helicopter Performance, Stability, and Control*, PWS Engineering Publishing, Boston, MA, 1986.

[44]Anderson, J. D., Jr., *Fundamentals of Aerodynamics*, 4th ed., McGraw-Hill, New York, NY, 2007.

[45]Eide, K., Harrington, A. M., Kalra, T. S., Milluzzo, J., and Seshadri, P., "Excalibur: The Cutting Edge in Tiltrotor Technology," 2011 Annual AHS International Student Design Competition Report, Graduate Category, University of Maryland, College Park, June 2011.

[46]Johnson, J. L., and McCluer, M. S., "Full-Span Tiltrotor Aeroacoustic Model (FS TRAM) Overview and Initial Testing," American Helicopter Society Aerodynamics, Acoustics, and Test and Evaluation Technical Specialists' Meeting Proceedings, San Francisco, CA, January 2002.

[47]Acree, C. W., Jr., "JVX Proprotor Performance Calculations and Comparisons with Hover and Airplane-Mode Test Data," NASA TM 215380, April 2009.

[48]Harris, F. D., "Performance Analysis of Two Early NACA High Speed Propellers with Application to Civil Tiltrotor Configurations," NASA CR 196702, August 1996.

[49]Carmel, M. M., and Delano, J. B., "Investigation of the NACA 4-(5)(08)-03 Two-Bladed Propeller at Forward Mach Numbers to 0.925," NACA RM L9G06a, September 1949.

[50]Evans, A. J., and Liner, G., "A Wind Tunnel Investigation of the Aerodynamic Characteristics of a Full-Scale Supersonic-Type Three-Bladed Propeller at Mach Numbers to 0.96," NACA TR 1375, 1958.

[51]Liu, J., and McVeigh, M. A., "Design of Swept Blade Rotors for High Speed Tiltrotor Applications," AIAA Paper 91-3147, AIAA Aircraft Design Systems and Operations Meeting, September 23–25, 1991.

[52]*V-22 Osprey Guidebook*, Published by the Naval Air Systems Command, United States Navy, 2011/2012.

[53]Rosen, K. M., "A Prospective: The Importance of Propulsion Technology to the Development of Helicopter Systems with a Vision of the Future – The 27th Alexander A. Nikolsky Lecture," *Journal of the American Helicopter Society*, Vol. 53, (4), October 2008, pp. 307–337.

[54]d'Angelo, M., "Wide Speed Range Turboshaft Study," NASA Contractor Report 198380, August 1995.

Bibliography

[1] Hafner, R., "The Case for the Convertible Rotor," 10th Cierva Memorial Lecture, *The Aeronautical Journal*, Vol. 75, Nos. 728 & 729, August & September, 1971, pp. 505–528, pp. 610–624.

[2] DeTore, J., and Conway, S., "Technology Needs for High Speed Rotorcraft," NASA Contractor Report 177592, October 1991.

[3] Spivey, D., "Runway Independent Aircraft," AIAA Paper 2002-5958, International Powered Lift Conference and Exhibit, Williamsburg, VA, November 5–7, 2002.

[4] Spivey, D., "The Need for Tactical, High Speed, Long Range, Vertical Envelopment Transport Development," AIAA Paper 2002-6022, International Powered Lift Conference and Exhibit, Williamsburg, VA, November 5–7, 2002.

[5] Foster, M., "The Future Evolution of the Tiltrotor," AIAA Paper 2003-2652, AIAA/ICAS International Air and Symposium and Exposition: The Next 100 Years of Flight, Dayton, OH, July 14–17, 2003.

[6] Howard, W. B., Jr., and Pilling, D. L., "Defense Science Board Task Force on Future Need for VTOL/STOL Aircraft," Defense Science Board, Washington DC, July 2007.

[7] Acree, C. W., Jr., and Johnson, W., "Performance, Loads and Stability of Heavy Lift Tiltrotors," AHS Vertical Lift Aircraft Design Conference Proceedings, American Helicopter Society International, Inc., San Francisco, CA, January 2006.

[8] Cicalé, M., "ERICA: The European Tiltrotor," 2005 Europe/US International Aviation Safety Conference Proceedings, Cologne, Germany, 7–9 June, 2005.

[9] Talbot, P. D., Philips, J. D., and Totah, J. J., "Selected Design Issues of Some High Speed Rotorcraft Concepts," *Journal of Aircraft*, Vol. 30, (6), 1993, pp. 864–871.

[10] Manley, D. J., and von Klein, W., "Design and Development of a Super-Short Takeoff and Landing Transport Aircraft," AIAA Paper 2002-6023, 2002 Biennial International Powered Lift Conference and Exhibit, Williamsburg, VA, November 5–7, 2002.

[11] Johnson, W., Yamauchi, G. K., and Watts, M. E., "Heavy Lift Rotorcraft Systems Investigation," NASA/TP-2005-213467, December 2005. See also: Johnson, W., Yamauchi, G. K., and Watts, M. E., "Design and Technology Requirements for Civil Heavy Lift Rotorcraft," American Helicopter Society Vertical Lift Aircraft Design Conference Proceedings, San Francisco, CA, January 18–20, 2006.

[12] Sinsay, J. D., "The Path to Turboprop Competitive Rotorcraft: Aerodynamic Challenges," American Helicopter Society Specialist's Conference on Aeromechanics, San Francisco, CA, January 23–25, 2008.

[13] Nixon, M. W., "Aeroelastic Response and Stability of Tiltrotors with Elastically-Coupled Composite Rotor Blades," Ph.D. Dissertation, Department of Aerospace Engineering, University of Maryland, College Park, MD, 1993.

[14] Moore, M. D., "NASA Puffin Electric Tailsitter VTOL Concept," NASA NF1676L-11227, September 2010.

[15] Preator, R., Leishman, J. G., and Baldwin, G. D., "Performance and Trade Studies of the Mono Tiltrotor Design," American Helicopter Society 61st Annual Forum Proceedings, Grapevine, TX, June 1–3, 2005.

[16] Wernike, K. G., and Edenborough, H. K., "Full-Scale Proprotor Development," *Journal of the American Helicopter Society*, Vol. 17, (1), January 1972, pp. 31–40.

[17] Paisley, D. J., "Rotor Aerodynamic Optimization for High-Speed Tiltrotors," American Helicopter Society 43rd Annual Forum Proceedings, St. Louis, MO, May 18–20, 1987.

[18] Farrell, M. K. "Aerodynamic Design of the V-22 Osprey Proprotor," American Helicopter Society 45th Annual Forum Proceedings, Boston, MA, May 22–24, 1989.

[19] Liu, J., Paisley, D. J., and Hirsh, J., "Tiltrotor Aerodynamic Blade Design by Numerical Optimization," American Helicopter Society 46th Annual Forum Proceedings, Washington DC, May 21–23, 1990.

[20] Dadone, L., Liu, J., Wilkerson, J., and Acree, C. W., "Proprotor Design Issues for High Speed Tiltrotors," American Helicopter Society 50th Annual Forum Proceedings, Washington DC, May 11–13, 1994.

[21] Aguilera, F., Brender, S., and Mark, H., "The Attributes of a Variable-Diameter Rotor System Applied to Civil Tiltrotor Aircraft," NASA CR 203092, 1997.

[22] Platt, R. J., Jr., and Shumaker, R. A., "Investigation of the NACA 3-(3)(05)-05 Eight-Blade Dual-Rotating Propeller at Forward Mach Numbers to 0.925," NACA RM L50D21, June 1950.

[23] Hammack, J. B., and O'Bryan, T. C., "Effect of Advance Ratio on Flight Performance of a Modified Supersonic Propeller," NACA TN 4389, September 1958.

[24] Maynard, J. D., and Salters, L. B., Jr., "Aerodynamic Characteristics at High Speeds of Related Full-Scale Propellers Having Different Blade-Section Cambers," NACA Report 1309, 1948.

[25] Booth, E. R., Jr., Botha, G., Dawson, S., Yamauchi, G. K., and Young, L. A, "Overview of the Testing of a Small-Scale Proprotor," American Helicopter Society 55th Annual Forum Proceedings, Montréal, Canada, May 25–27, 1999.

[26] Leishman, J. G., and Rosen, K. M., "Challenges in the Aerodynamic Optimization of High-Efficiency Proprotors," *Journal of the American Helicopter Society*, Vol. 56, (1), October 2010, pp. 568–596.

[27] Karem, A. E., "Optimum Speed Tilt Rotor," U.S. Patent Number 6,641,365, November 4, 2003.

[28] Matuska, D., Dale, A., and Lorber, P., "Wind Tunnel Test of a Variable-Diameter (VDTR) Model," NASA CR 177629, January 1994.

[29] Wang, J. M., Jones, C. T., and Nixon, M. W., "A Variable Diameter Short-Haul Civil Tiltrotor," American Helicopter Society 55th Annual Forum Proceedings, Montréal, Canada, May 25–27, 1999.

[30] Fradenburgh, E., and Matuska, D., "Advancing Tiltrotor State-of-the-Art with Variable Diameter Rotors," American Helicopter Society 48th Annual Forum Proceedings, Washington, D.C., June 3–5, 1992.

[31] Stack, J., Draley, E. C., Delano, J. B., and Feldman, L., "Investigation of the NACA 4-(3)(08)-03 and NACA 4-(3)(08)-045 Two-Blade Propellers at Forward Mach Numbers to 0.725 to Determine the Effects of Compressibility and Solidity on Performance," NACA Report 999, January 1944.

[32] Carmel, M. M., and Robinson, H. L., "Further Investigation of NACA 4-(5)(08)-03 Two-Blade Propeller at High Forward Speeds," NACA-RM-L7E12, Declassified, December 14, 1953 as NACA Research Memorandum L7E12.

[33] Nixon, M. W., "Improvements to Tilt Rotor Performance Through Passive Blade Twist Control," NASA TM 100583, April 1988.

[34] Rosen, K. M., "A Prospective: The Importance of Propulsion Technology to the Development of Helicopter Systems with a Vision of the Future – The 27th Alexander A. Nikolsky Lecture," *Journal of the American Helicopter Society*, Vol. 53, (4), October 2008, pp. 307–337.

[35] d'Angelo, M., "Wide Speed Range Turboshaft Study," NASA Contractor Report 198380, August 1995.

[36] Park, J., Kim, S., Jung, S. N., and Lee, M., "Design and Analysis of Variable-Twist Tiltrotor Blades Using Shape Memory Alloy Hybrid Composites," *Smart Materials and Structures*, Vol. 20, (1), January 2011.

[37] Acree, C. W., Jr., Sinsay, J. D., and Yeo, H., "Performance Optimization of the NASA Large Civil Tiltrotor," Presented at the International Powered Lift Conference, London, UK, July 22–24, 2008.

[38] Gur, O., and Rosen, A., "Comparison Between Blade-Element Models," *The Aeronautical Journal*, Vol. 112, (1138), December 2008, pp. 689–704.

[39] Weick, F. E., *Aircraft Propeller Design*, McGraw-Hill Book Company, Inc., York, PA, 1930.

[40] Froude, W., "On the Elementary Relation Between Pitch, Slip and Propulsive Efficiency," *Transactions of the Institute of Naval Architects*, 19, 1878, pp. 47–57.

[41] Gessow, A., "Effect of Rotor-Blade Twist and Plan-Form Taper on Helicopter Hovering Performance," NACA Technical Note 1542, 1948.

[42] Gessow, A., and Myers, G. C., *Aerodynamics of the Helicopter*, MacMillan Co., New York, NY, 1952, pp. 73–75.

[43] Lissaman, P. B. S., Walker, S. N., and Wilson, R. E., "Aerodynamic Performance of Wind Turbines," Oregon State University, Corvallis, OR, 1976.

[44] Deilmann, C., "Passive Aeroelastic Tailoring of Wind Turbine Blades — A Numerical Analysis," M.S. Thesis, Department of Mechanical Engineering, Massachusetts Institute of Technology, 2009.

[45] Hansen, A. C., and Moriarty, P. J., "AeroDyn Theory Manual," NREL/TP-500-36881, January 2005.

[46] Goldstein, S., "On the Vortex Theory of Screw Propellers," Proceedings of the Royal Society, Vol. 123, (792), 1929, pp. 440–465.

[47] Betz, A., *Schraubenpropeller mit geringstem Energieverlust*, Göttingen Nachrichten, 1919.

[48] Bradley, T. H., Mavris, D., Moffitt, B. A., and Parkh, D. E., "Validation of Vortex Propeller Theory for UAV Design with Uncertainty Analysis," 46th AIAA Aerospace Sciences Meeting and Exhibit, Reno, NV, January 2008.

[49] Balmford, D., and Done, G., *Bramwell's Helicopter Dynamics* (2nd ed.), American Institute of Aeronautics and Astronautics, Inc., Oxford, UK, and Butterworth-Heinemann, Reston, VA, 2001.

[50] Winarto, H., "BEMT Algorithm for the Prediction of the Performance of Arbitrary Propellers," CR CoE-AL 2004-HW3-01, Centre of Expertise in Aerodynamic Loads, Royal Melbourne Institute of Technology, Australia, March 2004.

[51] Mayda, E. A., "A CFD-Based Methodology to Automate the Generation of C81 Airfoil Performance Tables," M.S. Thesis, University of California, Davis, December 2003.

[52] Prouty, R. W., *Helicopter Performance, Stability, and Control*, PWS Engineering Publishing, Boston, MA, 1986.

[53] Anderson, J. D., Jr., *Fundamentals of Aerodynamics*, 4th ed., McGraw-Hill, New York, NY, 2007.

[54] Vanderplaats, G. N., *Numerical Optimization Techniques for Engineering Design*, McGraw-Hill, Inc., 1984.

[55] *V-22 Osprey Guidebook*, Published by the Naval Air Systems Command, United States Navy, 2011/2012.

[56] Eide, K., Harrington, A. M., Kalra, T. S., Milluzzo, J., and Seshadri, P., "Excalibur: The Cutting Edge in Tiltrotor Technology," 2011 Annual AHS International Student Design Competition Report, Graduate Category, University of Maryland, College Park, June 2011.

[57] Johnson, J. L., and McCluer, M. S., "Full-Span Tiltrotor Aeroacoustic Model (FS TRAM) Overview and Initial Testing," American Helicopter Society Aerodynamics, Acoustics, and Test and Evaluation Technical Specialists' Meeting Proceedings, San Francisco, CA, January 2002.

[58] Acree, C. W., Jr., "JVX Proprotor Performance Calculations and Comparisons with Hover and Airplane-Mode Test Data," NASA TM 215380, April 2009.

[59] Harris, F. D., "Performance Analysis of Two Early NACA High Speed Propellers with Application to Civil Tiltrotor Configurations," NASA CR 196702, August 1996.

[60] Carmel, M. M., and Delano, J. B., "Investigation of the NACA 4-(5)(08)-03 Two-Bladed Propeller at Forward Mach Numbers to 0.925," NACA RM L9G06a, September 1949.

[61] Evans, A. J., and Liner, G., "A Wind Tunnel Investigation of the Aerodynamic Characteristics of a Full-Scale Supersonic-Type Three-Bladed Propeller at Mach Numbers to 0.96," NACA TR 1375, 1958.

[62] Du, Z., and Selig, M., "A 3-D Stall-Delay Model for Horizontal Axis Wind Turbine Performance Prediction," Proceedings of the 17th ASME Wind Energy Symposium and the 36th AIAA Aerospace Sciences Meeting and Exhibit, Reno, NV, January 12–15, 1998.

[63] Liu, J., and McVeigh, M. A., "Design of Swept Blade Rotors for High Speed Tiltrotor Applications," AIAA Paper 91-3147, AIAA Aircraft Design Systems and Operations Meeting, September 23–25, 1991.

[64] Anderson, J. D., *Introduction to Flight*, 5th ed., McGraw-Hill Professional, New York, NY, 2004.

[65] Leishman, J. G., *The Helicopter: Thinking Forward, Looking Back*, The College Park Press, College Park, MD, 2007.